Weather-Adaptive Noise Abatement Procedures

Using Optimal Control Theory

Co C. Petersen

Technische Universiteit Delft

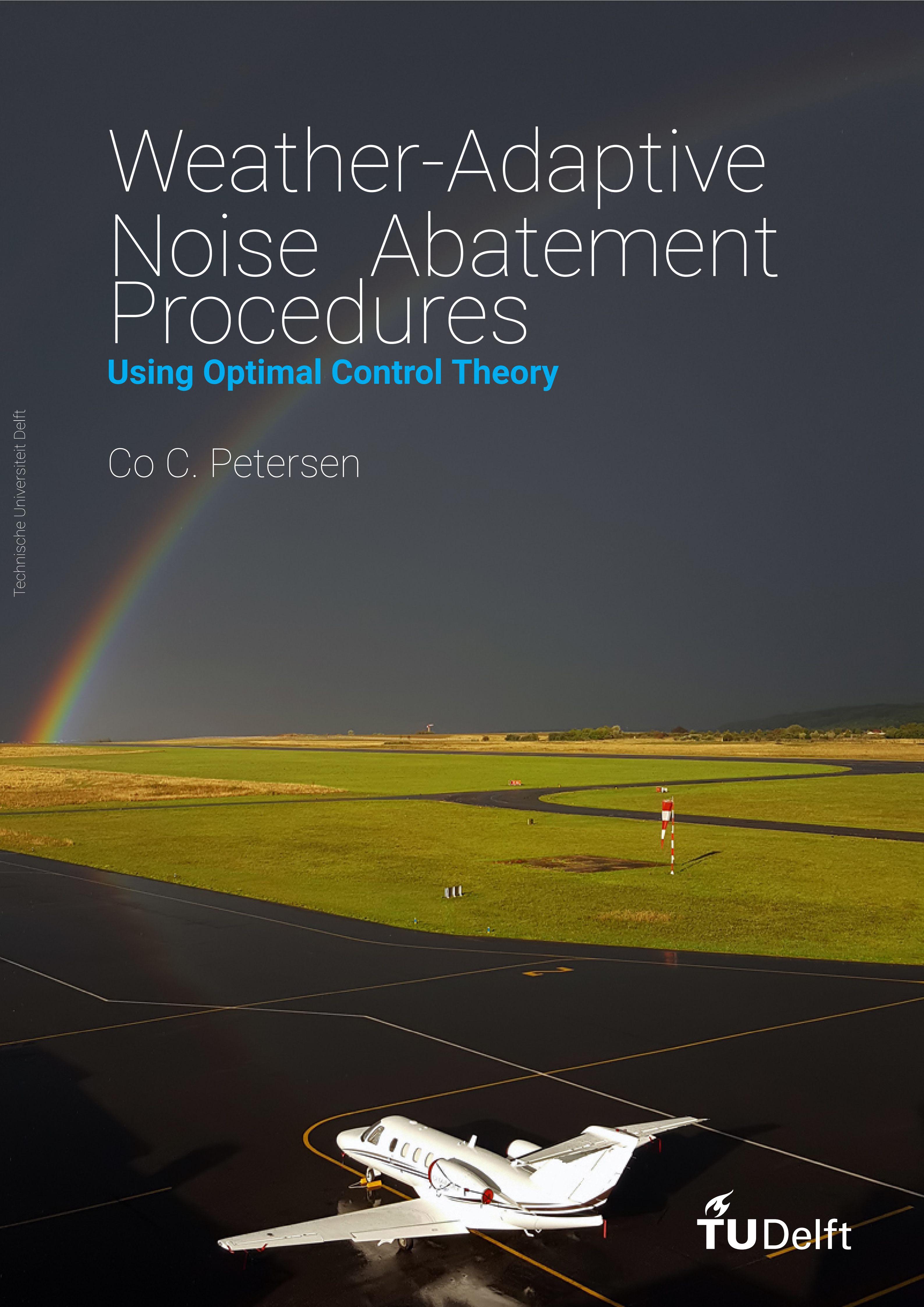

Cover photo: Cessna 525 Citation CJ1+ at Nancy - Essey (ENC / LFSN) - photo by Francois-Xavier Simon.
`https://www.airliners.net/`.

Weather-Adaptive Noise Abatement Procedures

Using Optimal Control Theory

by

Co C. Petersen

To obtain the degree of

Master of Science
in Aerospace Engineering

at the Delft University of Technology.
to be defended publicly on Friday October 19, 2018 at 14:30.

Student number:	4293657	
Thesis committee:	Prof. dr. R. Curran,	TU Delft, committee chair
	Dr. ir. S. Hartjes,	TU Delft, daily supervisor
	Dr. ir. J. Ellerbroek,	TU Delft, external committee member

TU Delft

Preface

This report is the result of the Master Thesis study at the department of Air Transport and Operations of the master track Control and Operations at the faculty of Aerospace Engineering of the Delft University of Technology.

In the past months, I have conducted research on the influence of various weather conditions on noise optimal departure procedures. To perform this analysis a trajectory optimisation tool has been developed. In its current form, the multiple objective optimisation takes into account the sound level observed on the ground, and the economical factor of fuel usage in its objective function.

As I grew up in the vicinity of Amsterdam Airport Schiphol, it was interesting to model the sound level observed in my hometown when aircraft fly by. Before starting this thesis, I noticed that there were some differences in the sound level observed when aircraft on take-off fly past my house depending on the season and the time of the day. Having analysed the sound propagation in various weather conditions, I can happily say that my ears did not deceive me.

With this report, it should become clear for the reader what the causes are of these variations in the sound level observed and how trajectories can be changed in order to reduces the sound levels at the observer depending on the actual weather conditions.

I could not have written this thesis without the help of many. First of all I would like to thank the members of my exam committee:

- Prof. dr. Ricky Curran
- Dr. ir. Sander Hartjes
- Dr. ir. Joost Ellerbroek

Special thanks go out to my daily supervisor, Sander Hartjes for the guidance during the thesis work. Thank you for reminding me to first take two steps backwards and analyse a basic problem, before jumping into complicated problems. Thank you for always having your office open in order for me to use your desktop to program in FORTRAN. I hope you enjoyed my company as well.

In addition I would like to thank dr. ir. H.G. Visser (Dries) for his attendance and feedback during the various presentations I have given discussing my progress. Please enjoy your retirement now. Thank you ir. P.C. Roling (Paul) for attending my green light presentation and the feedback.

Last but most certainly not least, I would like to thank my family and friends who have all contributed in various ways to the result now lying before us. Thank you mom and oma for the dinners on Mondays!

Co C. Petersen
Delft, October 2018

Summary

In the coming 20 years, air travel demand is forecasted to double the current demand. With the increased demand, flight movements at the airport will increase as well. Not only the maximum airport throughput capacity becomes a concern, also the (future) policies towards environmental pollution such as gaseous emissions and noise will form a major challenge.

If the sound is unwanted by the receiver, it is considered as noise. Aircraft noise is mainly regarded as annoying as it is represented by loud, single noise events of departing or landing aircraft. The harm caused to the health by noise as well as the symptoms observed are a function of sound level and exposure time. For example, noise in general can cause feelings of discomfort such as annoyance, an increased production of stress hormones and can cause deprivation of sleep.

Gaseous emission are related to the emission characteristics of the engine. Thus to reduce the gaseous emission, engine technology research is required. The negative effects of noise emissions can be reduced without the introduction of new technology: This can be achieved by introducing operational restrictions. The most common operational measure in aviation to reduce the effect of environmental noise pollution is noise abatement procedures. Noise abatement procedures are recommended flying techniques based on noise optimal trajectories, which aim at reducing the noise impact on local communities as much as possible.

Noise abatement procedures are based on noise optimal trajectories. The current noise abatement procedures are fixed and are used in any weather condition. However atmospheric conditions change with varying weather conditions. Thus the propagation of sound from the sound source at the aircraft to the observer also changes.

Previous research have analysed noise abatement procedures in International Standard Atmosphere (ISA) conditions in order to develop noise optimised trajectories for aircraft. Furthermore, the change in the observed sound levels on the ground in varying weather conditions have been analysed. However, the application of weather-adaptive noise abatement procedures have not been researched yet.

This research has been set up in order to analyse whether the implementation of weather-adaptive noise abatement procedures result in different noise optimal trajectories in different weather conditions. The research objective is *to assess the influence of weather on optimised noise abatement departure procedures for one fly over, by developing an optimisation tool that allows for the synthesis of weather-adaptive noise abatement procedures within the Terminal Manoeuvring Area (TMA).*

For this purpose, the Weather-Adaptive Flight Optimisation Research Tool (WAFORT) has been developed. Within this framework, an Aircraft Performance Model (APM), sound propagation model, noise impact model and Geographic Information System (GIS) is combined in the dynamic optimisation software GPOPS. Based on the problem statement, aircraft data, cost functional and initial guess, the noise optimal trajectory with the minimised maximum number of expected awakenings is obtained using the gradient-based optimisation technique Optimal Control Theory (OCT).

Weather variables that influence sound propagation are the air temperature, relative humidity and the wind.

The APM is modelled using BADA 4.0. The BADA holds a data base with performance characteristics of aircraft types. Furthermore the aerodynamic forces are related to the pressure and air temperature ratios to account for different atmospheric conditions. The aircraft mechanics is modelled as a point mass, reducing the number of variables in the optimisation.

The source noise level of the aircraft is derived from the ANP database. Combined with the Doppler frequency shift, the sound is propagated towards the observer. Sound propagation is modelled using geometric ray tracing. Ray tracing is independent of frequency, reducing computational time. Refraction is modelled by dividing the atmosphere is logarithmic spaced atmospheric layers. With the inclusion of wind, rays may be refracted upwards upwind of the aircraft due to decreasing effective speed of sound levels. Downwind, rays are bent downwards diminishing all shadow zones. The losses accounted for in the propagation model include spreading loss, atmospheric attenuation loss and ground reflection. Atmospheric attenuation loss is influenced by air temperature and relative humidity, with larger atmospheric attenuation loss at higher atmospheric attenuation coefficients. The atmospheric attenuation coefficient is frequency dependent. Ground reflection is influenced by the ground surface type and is frequency dependent as well. The shadow zones are modelled to ensure continuity for all observers, which is required for the gradient-based optimisation scheme.

Noise impact is evaluated using the FICAN dose-response relationship, relating Sound Exposure Level (SEL) to the maximum number of expected awakenings. The analysis is made site-specific by the GIS, using the latest data from 2017 published by Statistics Netherlands (CBS).

A gradient-based optimisation technique is used as it has a superior run time over other optimisation techniques. Using optimal control theory, one composite objective function is evaluated within a couple seconds to minutes. An initial guess is required to start the optimisation.

Verification and validation of the sound propagation model was performed by comparing the sound levels against the sound levels obtained using the Integrated Noise Model (INM), the current standard to evaluate aircraft noise. The new propagation model results in larger sound levels. This is caused by the different atmospheric attenuation loss obtained in each atmospheric layers. INM employs a constant, arithmetic atmosphere which does not take into account different atmospheric layers. Furthermore since INM does not model the shadow zone, large differences in sound levels are observed when the receiver is in the shadow zone.

In the new propagation model, larger sound levels are observed when the aircraft is flying away from the observer due to the Doppler frequency shift. Furthermore the shift in the shadow zone location is clearly observed with the inclusion of wind. Thin, narrow bands with varied sound levels are observed due to the ground reflection, caused by secondary sound rays interfering constructively or destructively with the direct sound ray. With softer ground surfaces, the effect of ground reflection is damped, resulting in lower overall sound levels and smaller ground reflection peaks.

The gradients of the noise impact model are obtained using the forward finite difference method as automatic derivatives with machine precision resulted in convergence difficulties.

To analyse the influence of the weather variables, simulations in various wind and atmospheric attenuation conditions have been performed on two different Standard Instrument Departure (SID) procedures from Amsterdam Airport Schiphol (AAS):

- *Spijkerboor 3K departure to way point ANDIK.* - Departure from runway 24 in southwestern direction, where after a sharp turn towards the right is made to continue flight in northeastern direction.
- *Arnem 3E departure to way point IVLUT.* - Departure from runway 18L in southern direction, followed by a left turn towards the east.

The two departure procedure differ mainly in the population density spread around the departure track and in length. Nearly all around the ground track of the Spijkerboor departure there is population while for the Arnem departure, the population is mainly located at the initial and final position of the simulation. The Arnem departure is also shorter in length, meaning reduced flight time.

To analyse the separate influences of the weather variables on the fuel usage, the sound propagation and the noise impact, first the weather variables have been analysed separately. The results obtained for the two departure procedures were compared to the results obtained in International Standard Atmosphere (ISA) conditions. This was followed by an analysis on actual weather conditions observed in the past months, which combines the different weather conditions.

It turned out that the difference in fuel usage, noise propagation and the noise impact in different atmospheric conditions can be predicted with respect to the values obtained in ISA conditions. However, the noise optimal trajectory is a trade-off between fuel usage and noise impact performed by the optimisation. Especially for the Spijkerboor departure, unexpected trajectories were obtained when the different weather variables were combined.

However, convergence difficulties for higher weighting factors for the noise impact in the objective function, k_{noise}, resulted in not entirely new noise optimal trajectories. Most of the obtained noise optimal trajectories can be considered as slight adaptations on the horizontal, vertical and velocity profile in ISA conditions.

The initial search range of the optimisation is based on the initial guess. Initial guesses of trajectories flying around cities with larger population density, converges towards either the solution presented in the specific case or the threshold of feasibility or optimally could not be obtained.

When analysing convergence behaviour, it is observed that for atmospheric conditions in which relatively high sound levels are obtained, the weighting value of noise in the objective function k_{noise} has been increased until the normalised Pareto fronts show a satisfactory curve in which awakenings are only slightly decreased with large increase in fuel usage. One reason for this behaviour might be the shape of the objective function. The higher sound levels are penalised more due to the increased number of awakenings in the objective function.

At lower sound levels, the optimisation might be deceived by the increased sound levels due to ground reflection. The ground reflection induces thin narrow bands with increasing or decreasing sound levels. When a large population grid point is located exactly within the peaks, the optimisation is stuck and convergence difficulties arise. With increasing k_{noise} values, this effect is strengthened.

For simulations with the inclusion of wind, the shadow zone might also be a source of the convergence difficulties. When entering the shadow zone, initially the sound level drops linearly. Although the loss is modelled continuously, the second order derivative, the Hessian, is not continuous. In case of stronger wind velocities, the shadow zone upwind of the aircraft moves closer to the aircraft due to the change in local speed of sound. Again when a large population grid point is located near the boundary of the illuminated and shadow zone, convergence issues might be encountered.

Furthermore the set-up of the cases influence the convergence. As the Arnem departure is very restricted by the population spread, noise optimal trajectories with lower k_{noise} value are also the noise optimal trajectory for larger k_{noise} values. This limits the number of data points on the Pareto front, resulting in non-smooth normalised Pareto fronts.

Based on these findings, it is concluded that the weather-adaptive noise abatement procedures will benefit the local community. It is noted that the fuel optimal trajectory evaluated in this study is more fuel efficient than the current procedures. Thus the limited increase in fuel usage over the fuel optimal trajectory does not necessarily increase the current fuel usage. Furthermore as no entire new trajectories are obtained, the implementation of weather-adaptive noise abatement procedures should not introduce many difficulties for both cockpit crew and air navigation service providers.

Limitations of the analysis performed in this research is that only one aircraft type has been simulated, no actual measurements in the field have been performed, the use of FICAN dose-response relationship as noise criterion, and the use of gradient-based optimisation in combination with an initial guess to start the optimisation. Different aircraft types have different source noise and performance, resulting in different noise optimal trajectories. Furthermore the noise impact is based on the maximum expected number of awakenings. As this is a fictional value, it might be difficult to communicate the value to outsiders.

Recommendations for further improvements to the WAFORT include more accurate and flyable trajectories, more accurate modelling of the atmosphere and atmospheric properties, modelling of the aircraft and sound source as rigid models and the modelling of more accurate flow resistivity per ground surface. Fly ability is improved by implementing area navigation.

For future work, it is interesting to enhance the WAFORT optimisation scheme with an evolutionary algorithm to obtain the global minimum, the definition of a multiple noise event problem and the creation of a runway allocation problem from an airport perspective. The WAFORT in its current form can be used to identify atmospheric conditions in which it is of interest to employ weather-adaptive noise abatement procedures. Using the evolutionary algorithm, the global optimum and thus the most noise optimal trajectories can be obtained. As the total number of awakenings are very much influenced by the atmospheric conditions, a runway allocation problem to minimise noise for the entire community around the airport might result in interesting new noise preventing findings.

Contents

List of Figures

List of Tables

Nomenclature

Acronym	**Description**
AAS	Amsterdam Airport Schiphol
AD	Automatic Differentiation
AEDT	Aircraft Environmental Design Tool
APM	Aircraft Performance Model
BADA	Base of Aircraft Data
CBS	Centraal Bureau voor de Statistiek (Statistics Netherlands)
CDA	Continuous Decent Approach
ECAC	European Civilian Aviation Conference
FFP	Fast Field Programme
FORT	Flight Optimisation Research Tool
GA	Genetic Algorithm
GIS	Geographic Information System
GPOPS	General Pseudospectral OPtimal control Software
ICAO	International Civil Aviation Organization
INM	Integrated Noise Model
ISA	International Standard Atmosphere
NADP	Noise Abatement Departure Procedure
NAP	Noise Abatement Procedure
ND	Numerical Differentiation
NLP	Non Linear Program
OCT	Optimal Control Theory
PE	Parabolic Equation
RNAV	Area Navigation
SEL	Sound Exposure Level
SID	Standard Instrument Departure
SPL	Sound Pressure Level
STAR	Standard Terminal Arrival Route
TMA	Terminal Manoeuvring Area
WAFORT	Weather-Adaptive Flight Optimisation Research Tool

Constant	**Description**	**Value**	**Units**
κ	Heat capacity ratio for air	1.4	-
ρ_0	Air density at at sea level	1.225	kg·m^{-3}
g_0	Gravitational acceleration	9.81	m·s^{-2}
p_0	Air pressure at sea level	101325	Pa
R	Specific gas constant for air	287.06	J·kg^{-1}·K^{-1}
T_0	Temperature at sea level	288.15	K

Symbol	**Description**	**Units**
α	Atmospheric attenuation coefficient	dB·100^{-1}m
$\bar{u}$	Control vector	-
$\bar{x}$	State vector	-
χ	Heading angle	°
$\dot{m}$	Mass flow	kg·s^{-1}
η	Throttle setting	-
γ	Flight path angle	°
λ	Temperature lapse rate	K·m^{-1}
μ	Bank angle	°
ψ_W	Wind direction (blowing to)	°
ρ	Air density	kg·m^{-3}
a	Acceleration	m·s^{-2}
c	Speed of sound	m·s^{-1}
D	Drag	N
f	Frequency	Hz
J	Cost functional	-
k	Weighting factor	-
L	Lift	N
M	Mach number	-
N_A	Total number of awakenings	-
p	Air pressure	Pa
T	Temperature	K
T	Thrust	N
t	Time	s
v	Aircraft velocity	m·s^{-1}
V_W	Total wind velocity	m·s^{-1}
W_{AC}	Weight of aircraft	N
xyz	Position coordinates	-
z	Altitude	m

1

Introduction

1.1. Background

With the increased competition between airlines, air fares have dropped and air travel has become more affordable for an increasing number of people. Combined with the increase in air travel demand in developed countries, it is expected that air travel demand in emerging countries will grow increasingly due to their rising Gross Domestic Product (GDP) per capita [1]. It is forecasted that in the coming 20 years, the air travel demand will double the current demand [2, 3].

Airports have to facilitate the increased number of flight movements at the airport, as well as to deal with the consequences. Not only the maximum airport throughput capacity becomes a concern, also the (future) policies towards environmental pollution such as gaseous emissions and noise will form a major challenge. Gaseous emission such as CO_2 and NO_x are very much related to the emission characteristics of the engine. Thus to reduce the gaseous emission, engine technology research is required [4]. In order to help creating effective noise pollution policies to eliminate the negative effects of noise towards populated communities, sound and the propagation of sound have to be analysed in more detail.

Sound is a propagating pressure disturbance. If the sound is unwanted by the receiver, it is considered as noise. Many background sound sources produce environmental noise. Examples are traffic noise and the conversations of people in crowded areas. Aircraft noise is one type of background noise and is mainly regarded as annoying as it is represented by loud, single noise events of departing or landing aircraft.

The harm caused on the health by noise as well as the symptoms observed, are a function of sound level and exposure time. For example, noise in general can cause feelings of discomfort such as annoyance, an increased production of stress hormones and can cause deprivation of sleep [5–7]. Studies performed in the field of medication use, annoyance and the economy in relation with aircraft noise all point to a beneficiary effect if noise at the observer is reduced [8–10].

To reduce aircraft noise received by the observer on the ground, generally new aircraft technologies are introduced or operational restrictions are set in place.

New aircraft technology. Newer generation aircraft are equipped with more quiet engines and low drag aerodynamic structures. Since the introduction of the turbofan engine, the overall trend in aircraft noise is reducing steadily due to the increased knowledge about turbo-machinery noise and improved design methods. Figure 1.1 illustrates that as of the start of the turbo-engine era, the average noise level has been reduced by nearly 20 dB.

While the noise at the source is reducing drastically, they are only introduced with the introduction of new aircraft types. Because aircraft are designed to be in service for over 20 years, the reduced source levels are not immediately noticeable for the observers on the ground.

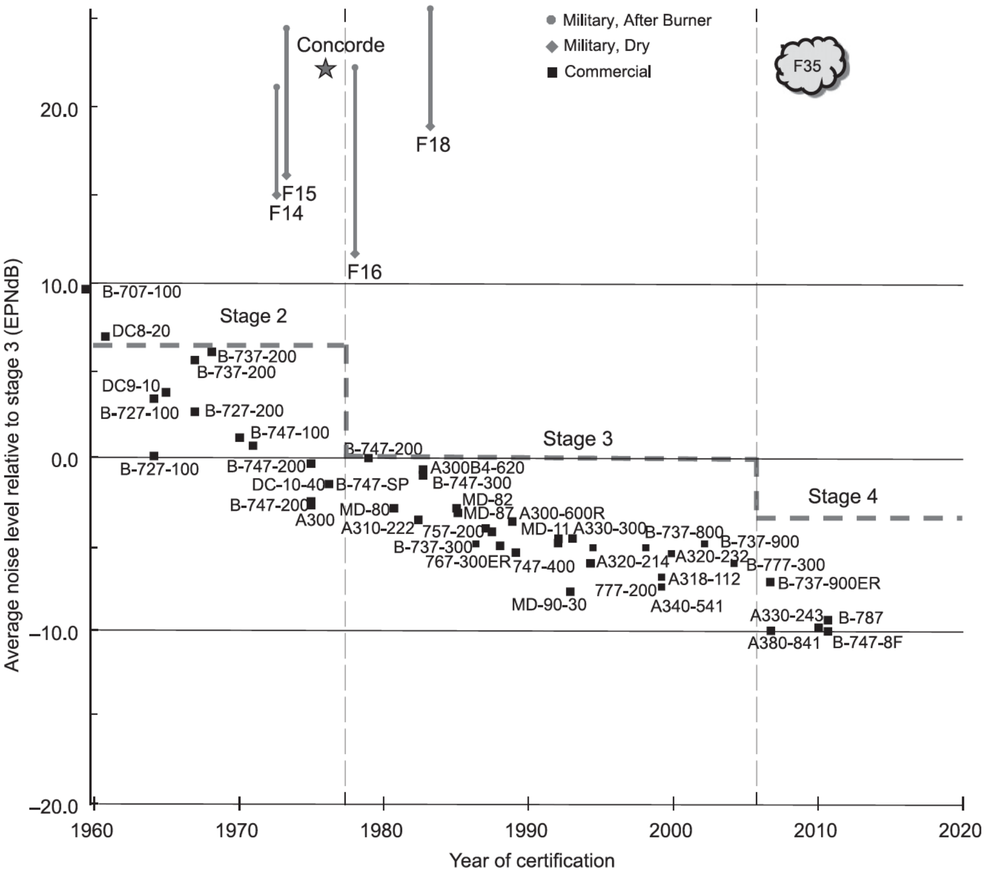

Figure 1.1: Average noise level of aircraft in relation to the year of certification of the aircraft type [11].

Airport operational restrictions. Every airport has its own set of operational restrictions on the ground and in the air to reduce the aircraft noise.

Examples of restrictions in the air are curfews, preferential runway use and noise abatement procedures [12]. With a curfew set in place, no scheduled flights are allowed to land or take-off within a certain time period. Especially at night, the curfew relieves the population underneath the departure and arrival trajectory of noise. With preferential runway usage, the runway with the least noise impact on the community is used for most of the time. Alternatively, runway usage is altered depending on the time of the day in order for the community to adapt their schedule to the expected noise.

Based on a study performed by Boeing[1] presented in Figure 1.2, it is observed that in particular Noise Abatement Procedures (NAPs) have been introduced at an increasing number of airports. Noise abatement procedures are procedures regarding recommended flying techniques of arrival and departure trajectories. Procedures are constructed based on a joint undertaking between the stakeholders of the airport, civil aviation authority and air navigation service providers.

Arrival noise abatement procedures are for instance the Continuous Decent Approach (CDA) and low power low drag approaches [13]. Departure noise abatement procedures are for example the Noise Abatement Departure Procedure-I (NADP-I) to mitigate noise near the airport, and the NADP-II to mitigate noise along the departure path [14]. Most noise abatement procedures hold for any weather condition, as long as safe operations can be maintained.

---

[1] https://www.boeing.com/commercial/noise/charts_all.page, accessed on 19 August 2018

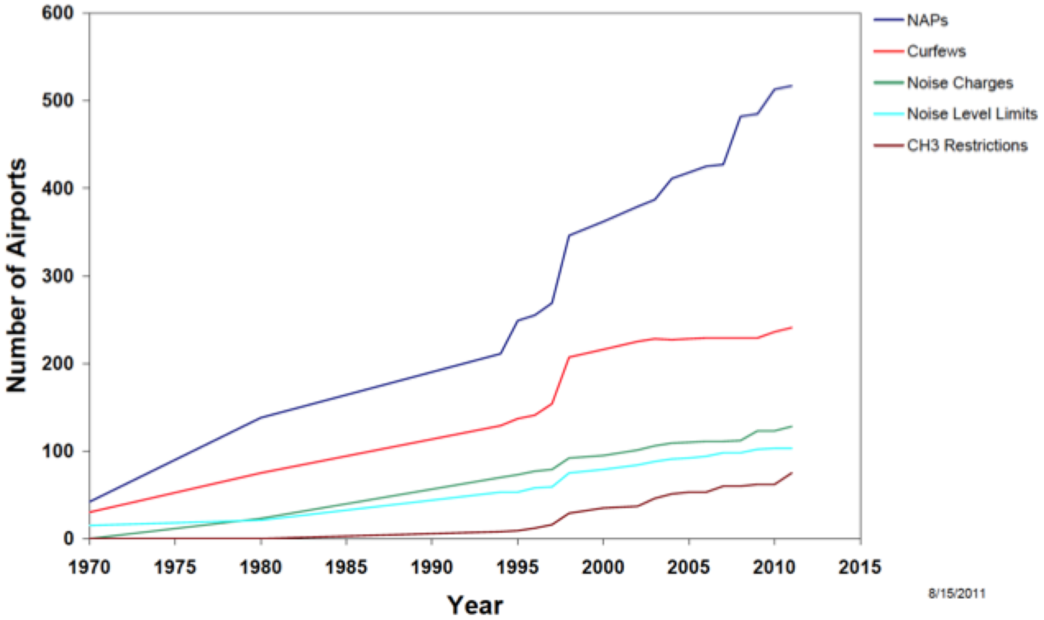

Figure 1.2: Time line of airport noise restriction according to Boeing, as of 15 August 2011[1].

From the sound source at the aircraft towards the observer on the ground, sound travels through the atmosphere. With varied weather conditions and season, the atmospheric conditions changes. This affects the propagation of sound through the atmosphere [15], implying that the noise received on the ground differs by the season and even by the time of the day.

In order to reduce noise annoyance with immediate effect, noise abatement procedures are required. In order to operate the procedures with the lowest noise impact in different weather conditions, different flight procedures might be required to the ones currently used. To analyse whether weather-adaptive noise abatement procedures are different to the current noise abatement procedures and their applicability to daily operations, research is required.

1.2. Previous Research and Research Gap

The trajectories defined in the noise abatement procedures are based on noise optimised trajectories. Previous research on noise optimised trajectories and trajectories taking into account varied weather conditions can be classified in the following three groups:

- Trajectory optimisation for noise in International Standard Atmosphere (ISA) conditions.
- Analysis of noise impact for fixed trajectories in non-ISA conditions.
- Trajectory optimisation for noise in non-ISA conditions.

Multiple studies have been performed for trajectory optimisation for noise in ISA conditions. For this research, the publications of *Visser and Wijnen* [16, 17], *Hartjes et. al* [18] and *Hogerhuis et. al* [19] are discussed in more detail.

The study performed by *Visser and Wijnen* focused on the development of a generic methodology for both departing and landing aircraft, applied at any given airport. It consists of an acoustic sound module, a trajectory optimisation module and a Geographic Information System (GIS) module. To minimise for the number of people affected, the GIS is used to identify population densities. Noise propagation is modelled using the Integrated Noise Model (INM) [20] and the noise performance is evaluated using a dose-response relationship [21].

This framework was altered by *Hartjes et. al* to include Area Navigation (RNAV) procedures for departing aircraft together with the addition of the evaluation of local emissions. *Hogerhuis et. al* implemented a similar technique for arriving aircraft. RNAV procedures allow for the use of area navigation procedures to fly lateral

2D trajectories. This means that trajectories are not flown using way points [22] but using satellite navigation systems. This results in aircraft flying more precise ground trajectories.

For fixed trajectories in non-ISA conditions, *Clarke* [23] and *Hubert et. al* [24] have developed a methodological framework consisting of a weather model, acoustic sound model and a GIS. The methodology has been used to analyse departures and arrivals using a variable wind model [24, 25].

The weather model is based on actual atmospheric measurements from a weather balloon to obtain the temperature, the dew temperature and the wind field at specified altitudes. Based on the readings, a horizontally homogeneous, equally thick atmosphere is generated. Multiple directional sound sources are modelled and the propagation is simulated by ray acoustics. The propagating rays are affected by the weather characteristics in each atmospheric layer. The resulting different noise contours for different weather conditions is illustrated by Figure 1.3.

While *Huber et. al* presented that in varying weather conditions, the noise contour differs and concluded that different weather specific trajectories might result in less noise impact, no further research has been performed to add a (simplified) trajectory optimisation technique to the model.

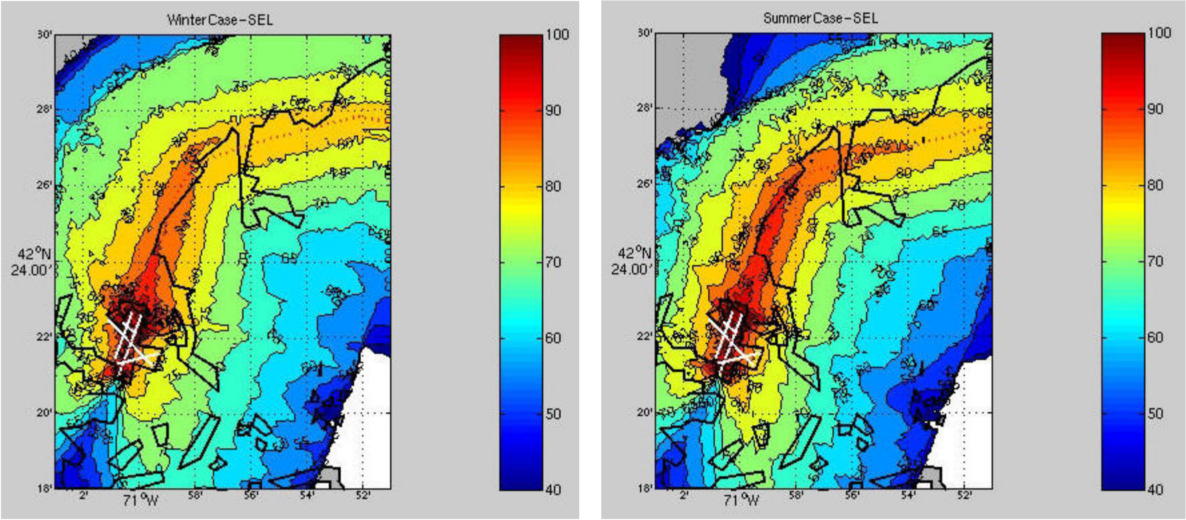

(a) Departure in the winter.

(b) Departure in the summer.

Figure 1.3: Fixed trajectory sound exposure levels in varied weather conditions in dBA [24].

In 1953, *Ingard* [15] presented that meteorological conditions do have an influence on the sound propagation. However, the author could not find any published research regarding trajectory optimisation for aircraft noise in non-ISA conditions. Although not for aircraft sound, *Hartjes* [26] discusses the application of weather-adaptive noise abatement procedures for helicopters.

Helicopter noise is highly directional and asymmetric thus the sound spectrum and directionality of helicopters are very different compared to aircraft. Due to this complicated emission of noise by helicopters and the difference in ground speed of aircraft and helicopters, the study could not be translated into aircraft. However the existence of a similar study suggests the feasibility to apply a similar method to develop a weather-adaptive noise abatement procedure tool for aircraft.

1.3. Problem Statement and Research Objective

To analyse the influence of the difference in season or time of the day on noise abatement procedures, this research develops a tool that can be used to synthesise noise abatement procedures in various weather conditions. Current noise abatement procedures are valid for certain fixed weather conditions, which do not exactly occur frequently.

The research mainly focus on the abatement of noise for the population living in the Terminal Manoeuvring Area (TMA) of an airport. The TMA is part of the airspace outlined around an airport, designed to facilitate climbing and descending aircraft along their Standard Instrument Departure (SID) and Standard Terminal

Arrival Route (STAR). The exact shape of the TMA varies per airport. As aircraft fly relatively close to the ground in the TMA, most noise is experienced by the population living in the TMA.

Besides the analysis of the received sound levels in various weather conditions, the research allows for future noise abatement procedures to take into account varying weather. The impact of the weather variables is currently known quantitatively, however it has not yet been applied to real aircraft procedures [27].

This research is not part of a funded research project, however the outcome will result in useful information towards a first step of a possible future, innovative new application to the flight management system that can determine the optimal departure, or arrival route during the pre-departure or pre-arrival checklist. The influence of (variable) weather conditions might be the source of variation in the flown trajectory.

The Research Objective.
In order to fill the previously mentioned research gap, the following research objective is formulated:

To assess the influence of weather on optimised noise abatement departure procedures for one fly over, by developing an optimisation tool that allows for the synthesis of weather-adaptive noise abatement procedures within the terminal manoeuvring area.

The influence of weather on arrival procedures is not discussed as it is already generally known that Continuous Decent Approach (CDA) with idle thrust setting result in lower noise levels on the ground. However, with the implementation of CDA, separation distances between aircraft becomes a problem for the throughput rate of the runway [13]. This is an entirely different study and is thus not considered.

In order to evaluate the research objective, the following research questions are posed:

- What are the influences of the weather variables on fuel usage, the sound propagation and the resulting noise impact?
    - Weather variables are varied in order to identify their general influence on the fuel usage and sound propagation. These general findings can then be employed to estimate how various weather conditions influences the noise impact and accordingly, how the noise optimal departure procedures will change in different weather conditions.
- What can be concluded from the comparison of noise optimal departure procedures in International Standard Atmosphere (ISA) conditions and the weather-adaptive noise optimal departure procedures?
    - This research question identifies the changes to the noise optimal departure procedures when the weather variables are altered to simulate different whether conditions. It concludes whether the introduction of weather-adaptive departure procedures is beneficiary or not. If so, in what weather conditions they should be employed.

The influence of the weather on noise optimised trajectories is measurable based on the parameters used in the objective function of the optimisation. By varying the weather variables influencing sound propagation independently, the influence of each variable is obtained. By varying multiple variables at a time, different realistic scenarios are simulated as well as the influence of the variation of multiple variables are analysed.

1.4. Thesis Structure

This is the thesis report for the research *"Weather-adaptive noise abatement procedures"* as the Master thesis assignment at the Air Transport and Operations track of the Control and Operations department at the Delft University of Technology.

This report first synthesises upon the research by discussing the necessary background knowledge of sound, identifying the modelling framework and the flight procedures and regulations in Chapter 2. In Chapter 3 the tool developed to evaluate the noise abatement procedures, the Weather-Adaptive Flight Optimisation Research Tool (WAFORT), is introduced and discussed in detail. Chapter 4 covers the verification and validation of sound propagation model within the WAFORT. This process is followed by Chapter 5, in which case studies are performed on departure procedures at Amsterdam Schiphol Airport in various atmospheric conditions in order evaluate the performance of the WAFORT and to answer the research objective. The report is concluded in Chapter 6 including a set of recommendation for future studies. Three appendices are included to provide more information about Amsterdam Airport Schiphol in Appendix A, Appendix B presenting supporting case study results and Appendix C tabulating all results of the simulations performed in Case 1 and Case 2, as well as presenting noise contour lines in fuel and noise optimal trajectories.

2

Problem Synthesis

2.1. Introduction

The initial step to approach the research objective is to identify the pieces of information that allow for the synthesises of the problem. In order to so, knowledge regarding the physical behaviour of sound when propagating through the atmosphere is required as well as an understanding of when sound levels are loud and harmful. Section 2.2 performs this basic analysis of aviation noise. In order to devise a tool to evaluate noise impact in different weather conditions, it is beneficial to identify how previous work have modelled similar tools. Based on the findings of previous work, a modelling framework for the tool is identified as well as pros and cons of different modelling schemes employed in previous studies are discussed in Section 2.3. This section also include an initial trade-off to determine what type of scheme is used in the tool. The weather adaptive noise abatement procedures need to be safe and realistic. Section 2.4 identifies what safe operations and restrictions are. Furthermore the current noise abatement procedures are discussed.

2.2. Basics of Aviation Noise

Aviation noise is a very broad topic, thus this section introduces the basics of aviation noise which is of interest for this research. In Section 2.2.1 the sound propagation is introduced by identifying the sound sources of an aircraft, identifying what atmospheric parameters influence the propagation and what transmission losses are generally accounted for when modelling the propagation of sound. To quantify the sound energy observed by the observer, Section 2.2.2 introduces comparative noise levels and basic noise metrics.

2.2.1. Sound Propagation

Sound is a propagating pressure disturbance that travels from the source towards the receiver through the atmosphere. The location of the observer relative to the sound source determines how much sound is received. This section elaborates on the basics of sound propagation of interest for this research. For a more detailed and elaborate explanation, please refer to *Ruijgrok* [27].

The main sound source of an aircraft is the propulsive system. The amount of sound produced is related to the amount of thrust produced by the engines. Another sound source is the airframe: the aerodynamic noise generated by turbulence in airflow over the outer surface of the aircraft. Airframe noise is especially dominant when the aerodynamic devices and landing gears are deployed; in other words, when the aircraft is in its landing or take-off configuration.

For modern turbofan propulsion systems with high bypass ratio, noise is generated by the fan, compressor, combustor, turbine and exhaust jet noise. The directions towards the noise is produced is illustrated by Figure 2.1. The fan noise radiates roughly equally to the front as well as to the aft of the engine, while the compressor noise radiates to the front. The jet noise, caused by the turbulent mixture of hot gas flow and ambient air radiates to the aft as well as the turbine and combustor noise.

The bypass ratio of the turbofan engine characterises the noise produced: the higher the ratio, the lower the exhaust velocity. This results in a reduced jet noise. Fan noise becomes dominant once the ratio is larger than four. Due to developments to reduce engine fan noise on newer generation engines, airframe noise is becoming the dominant noise source during landing [27].

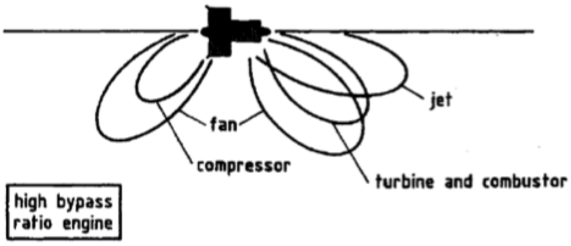

Figure 2.1: Turbofan engine directional of noise components [27].

The level of sound produced by the engines is closely related to the thrust level of the aircraft. Atmospheric conditions play a role in aircraft performance. For instance, in cold weather the engine performance is improved as the air density is higher resulting in higher fuel to air mixture and accordingly, more power can be produced improving for example climb performance. On the other hand with increasing relative humidity, the air pressure for a given volume of air goes down resulting in the adverse effect of cold weather conditions. Furthermore, the aircraft is generating less lift at the same velocity, resulting in higher take-off velocities and increased thrust levels [27].

From the sound source, the sound waves travel through the atmosphere towards the observer. In a quiet, homogeneous and isothermal atmosphere, the waves are not bent and are sent straight to the ground from the source following the emission angle.

In a non-homogenous atmosphere with varying local air temperature, relative humidity and wind velocities, the sound waves are bent, which is called refraction. Relative humidity is the ratio in percentage of the prevailing water vapour pressure in the air and the saturation vapour pressure. The direction of bending is influenced by the local speed of sound gradient. With decreasing temperatures with increasing altitudes, the sound waves are bent up while they are bent down when the temperature increases with altitude. This is illustrated by Figure 2.2.a and Figure 2.2.b. When the waves are bent upwards, areas where no direct waves are received are created. This is the so-called shadow zone. In the shadow zone, no direct sound waves are received and thus the received sound levels drop drastically. When waves are bent downwards, all shadow zones diminish.

The wind influences the effective speed of sound levels and accordingly the refraction of sound waves. For upwind observer locations, the sound waves are bent up while for the observer locations downwind, the sound waves are bent down. This results in a 'pushing' effect on the shadow zone. The shadow zone upwind is closer to the source while downwind, the shadow zone disappears. This effect is depicted in Figure 2.2.c for a typical positive wind gradient with altitude.

Weather conditions like rain, fog or snow have a negligible direct effect on sound propagation [15], however these conditions do influence the temperature, relative humidity and the ground surface type.

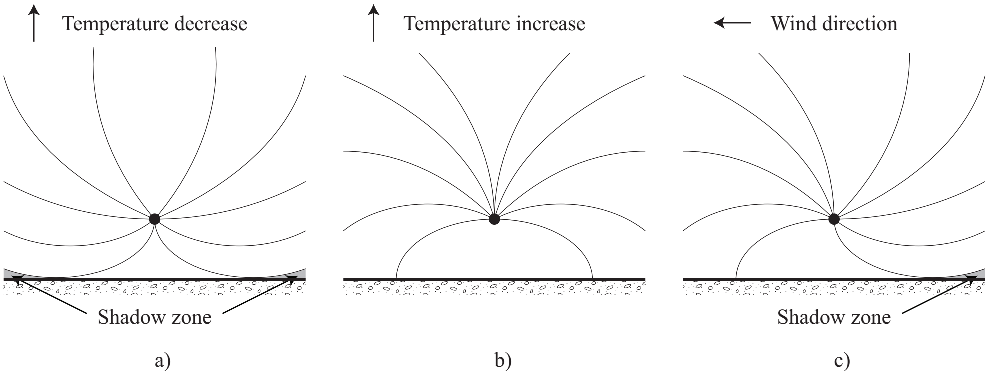

Figure 2.2: Refraction of sound: a) Negative temperature gradient, b) Positive temperature gradient, c) Wind [26].

For moving sound sources such as an aircraft, the tones observed by the receiver when an aircraft is flying towards the receiver, when the aircraft is directly overhead and when the aircraft is flying away from the observer is different from the actual tones emitted by the sound source. The shift in tones is caused by the Doppler effect and is caused by a time rate of change in the distance between the source and receiver.

Generally when modelling the loss of sound energy while travelling from the source to the observer, the spreading loss, atmospheric attenuation loss, ground reflection and the shadow zones are modelled [27]. In the following paragraphs, each phenomena is elaborated in more detail.

Spreading loss. While travelling through air, the sound wave spreads over an increasing area with increasing distance from the sound source. The reduction in sound intensity is called spreading loss. For non-directional sources, the sound is spread over a spherical surface with increasing distance, as illustrated by Figure 2.3.

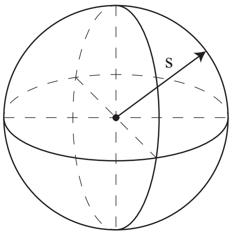

Figure 2.3: Spherical spreading of sound [26].

Atmospheric attenuation loss. The phenomenon of the sound energy being absorbed due to internal friction is called atmospheric attenuation. The degree of absorption is mainly influenced by the local air temperature and the relative humidity.

Ground reflection. The receiver on the ground receives both sounds from direct and indirect waves. The indirect waves result from ground reflections. Based on the location of the aircraft overhead, the sound received from the direct and indirect rays might amplify or cancel out depending on whether the waves arrive in- or out-of-phase.

Shadow zone. Shadow zones are the areas were no direct waves from the source are received. In the International Standard Atmosphere (ISA) the temperature decreases with altitude refracting the sound wave upward due to the increasing local speed of sound. The boundary between the illuminated zone and shadow zone is located where the sound just arrives on the ground. This is illustrated by Figure 2.4. For lower sound emission angles, the sound waves are travelling upwards again before reaching the ground.

A significant lower sound level is received in the shadow zone which consists of mainly sound caused by ground waves, scatter caused by turbulence and diffraction [27].

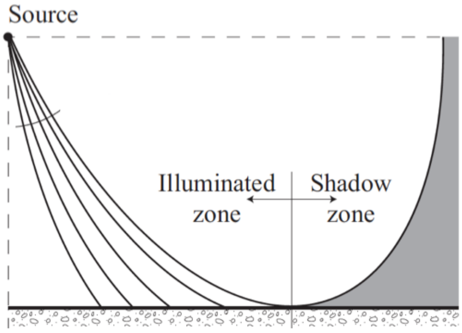

Figure 2.4: Refraction of the sound waves creating shadow zones. Adapted from [26].

2.2.2. Noise Metrics

Sound is expressed as sound intensity using the decibel scale (dB). Due to the logarithmic nature of the scale, the intensity doubles every 3 dB. Table 2.1[1] gives an indication of comparative noise levels. If one is exposed

---

[1] State of California, loudness comparison chart (www.dot.ca.gov/dist2/projects/sixer/loud.pdf), accessed on 11 August 2018.

to noise levels higher than 85 dB, the exposure time should be limited in order to avoid hearing loss. The exposure time before hearing loss is encountered halves with every 3 dB increase. At noise levels of 125 dB, one starts to feel pain.

Microphones in sound measuring systems respond to variations in pressure, resulting in the use of the Sound Pressure Level (SPL) or the effective pressure of sound as metric for sound levels. The audible range of sound for given frequencies varies with the SPL. An illustrative relation between frequency and SPL for the human audible sound range is presented in Figure 2.5.

Table 2.1: Comparative noise levels[1].

Noise level [dB]	Noise source
0	Threshold of hearing
10	Breathing
30	Whisper
40	Library, quiet residential area
50	Refrigerator
60	Normal conversation
80 - 90	City traffic
90	Shouting conversation
100	Factory machinery
110	Shouting in ear
140	Jet engine at take-off

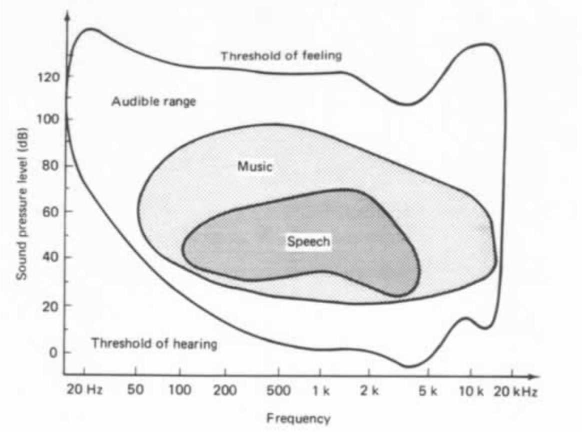

Figure 2.5: Human audible sound range [27].

The SPL is determined according to Equation (2.1), in which p_e is the effective free field sound pressure and p_0 the reference pressure ($2 \cdot 10^{-5} \mathrm{N} \cdot \mathrm{m}^{-2}$).

$$SPL = 10 \cdot \log_{10}\left(\frac{p_e^2}{p_0^2}\right) \tag{2.1}$$

To account for the human perception of noise due to the sensitivity of the human ear to certain pure tones, a frequency weighting correction is applied. The current correction factor standard for civil aviation measurements is the A-weighting factor in dBA. The A-weighted correction factor has been plotted for the centre frequencies of the third octave band in Figure 2.6. The human ear is less responsive to frequencies below 1000 and above 6000 Hz, resulting in a negative A-weighting correction.

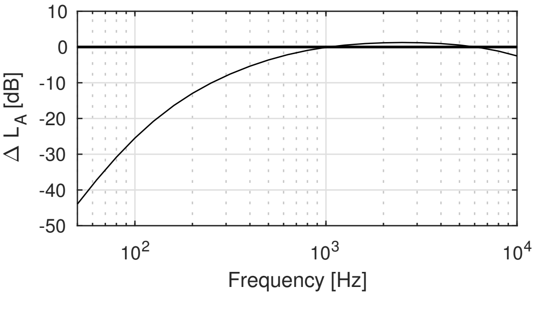

Figure 2.6: A-weighting frequency filter.

The L_{Amax} is the maximum A-weighted sound level during a noise event. In order to determine the total sound level of a noise event, the L_A values are integrated over time. To compare multiple events with different duration the Sound Exposure Level (SEL) or L_{AE} is used. The SEL contains as much energy as the varying noise level over the full event by normalised it to a time period of one second. The comparison between the total sound level and SEL is presented in Figure 2.7.

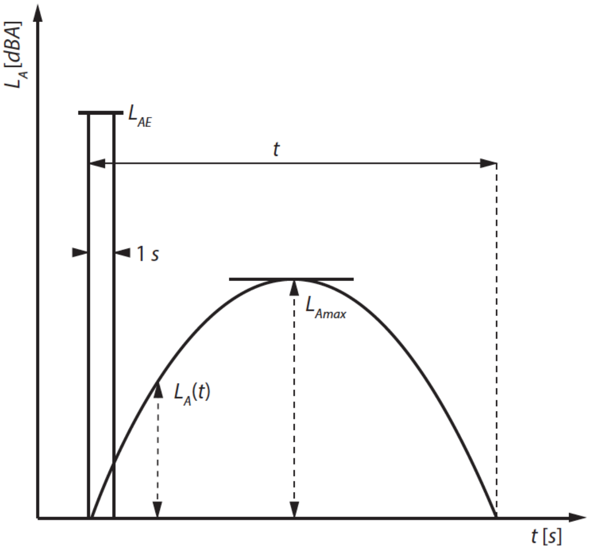

Figure 2.7: Time based ($L_A(t)$), maximum level based (L_{Amax}) and exposure based (L_{AE}) sound intensity measures [27].

2.3. Modelling Framework

To analyse the noise impact in the Terminal Manoeuvring Area (TMA) for different weather conditions, a tool that allows for the evaluation of sound received on the ground in different atmospheric conditions is to be developed. From the existing framework of trajectory optimisation for noise [16, 17] and the framework for noise evaluation for fixed trajectory [23], it can be deduced that a tool consisting of multiple modules is frequently employed. So to synthesise weather-adaptive noise abatement procedure the tool will consist of the following separate models:

- Optimisation scheme.
- Atmosphere and sound propagation model.
- Aircraft model.
- Noise impact model.

In the following sections, an introduction and an initial considerations for the optimisation scheme and atmosphere and sound propagation model is presented. Section 2.3.1 discusses different optimisation schemes and performs a trade-off to determine what scheme to be employed in the framework. The propagation of sound and the atmosphere in which it propagates are interrelated. Section 2.3.2 identifies the weather variables of influence on the propagation, furthermore different propagation techniques are introduced and a trade-off is performed to decide on the propagation scheme used in the framework.

The aircraft model and noise impact model are discussed in Section 3.3 and respectively Section 3.5 as these models do not require an initial trade-off to determining what modelling scheme is used in the framework.

2.3.1. Optimisation Scheme

To find the trajectory with the least noise impact, a trajectory optimisation scheme is employed. Commonly used trajectory optimisation schemes are evolutionary techniques and gradient-based methods. The application of evolutionary algorithms in the field of trajectory optimisation mainly deals with the Genetic Algorithm (GA) [28–30]. Gradient-based trajectory optimisation applications mainly make use of Optimal Control Theory (OCT) [16–19]. The main findings comparing the two schemes are presented in Table 2.2.

Table 2.2: Evaluation of the trajectory optimisation methods.

	Genetic Algorithm	**Optimal Control theory**
Accuracy	Global optimum	Local optimum
Computational time	Hours	Seconds/minutes
Objective function parameters	Multiple parameter objective	Single objective function, multiple parameter with weighting function

Both methods have their pros and cons. Evolutionary algorithms allow for the optimisation of a multiple parameter objective function at one time. The global optimum is found by analysing all possible solutions [31]. The program only needs to be one run once to obtain all optimal solutions for varying weighting function. In exchange, the computational time increases exponentially with increasing number of parameters to be evaluated in the objective function.

To use gradient-based methods, every function used within the modelling framework must be able to be expressed in terms of smooth differential equations. The technique is very efficient in finding the optimal trajectory for one single (composite) objective function. A weighting function subjective to the user determines the final trajectory. However, the objective function can be more complicated compared to the genetic algorithm by adding more parameters. Depending on an initial guess, optimal control theory finds a local minimum. The local minimum is not always the global minimum as the optimisation problem is highly likely to be of non-convex and nonlinear nature due to the interaction between the different models.

As multiple different weather conditions are evaluated in this research, computational time becomes expensive. Furthermore, the different optimised trajectories for different weather circumstances need to be compared with each other. This requires a somewhat equal weighting function to be used, and not all possible trajectories are of interest. Combined with the argument that continuous problems must be solved by continuous optimisation methods [32], optimal control theory is chosen as optimisation scheme.

Optimal control theory. An optimal control problem finds the most suitable control function subjected to all dynamic, initial and terminal constraints, that minimises the performance index [33].

In the context of trajectory optimisation, an aircraft flying a certain trajectory is the dynamic system. The aircraft is represented by the state of the system which describes the characteristics of the aircraft at certain moments in time. It is denoted as x_n with n being the number of state variables. The states can be manipulated through input by the control variables u_m, in which m is the number of control variables. The particular set of control variables that minimises the performance index is called the optimal control, and the corresponding set of state variables form the optimal trajectory.

Within optimal control theory, there are direct and indirect methods. The benefits and limitations of the two methods are summarised in Figure 2.8. The indirect method explicitly solves the optimality conditions while the direct method discretises the trajectory dynamics in order to formulate the problem as a Non-Linear Program (NLP) [34]. To use the indirect method, it is required to analytically determine the gradient of the performance index in order to identify the zero gradient [32]. This might be bothersome for non-linear functions. Advantage of the direct method is that large problems are redefined as finite dimensional NLP which can be solved using numerical solvers [26]. The NLP problems are large, but mainly sparse and thus efficient. Furthermore, constraints can be easily implemented along the trajectory [32]. Considering these advantages over indirect methods, direct optimal control is used.

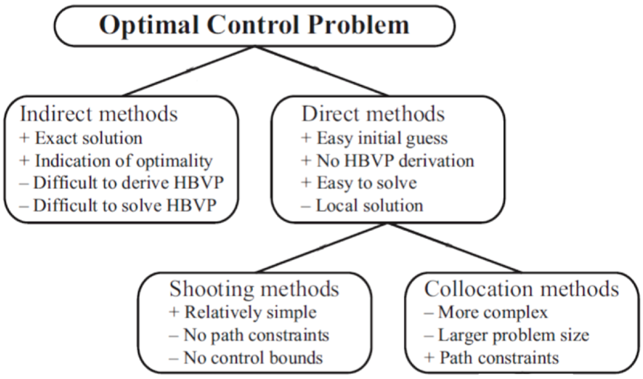

Figure 2.8: Overview of benefits and limitations of different optimal control problem optimisation methods. Adapted from [26].

Visser and Wijnen have implemented a direct collocation method in their research [16, 17, 35]. In their approach, the state and control variables are parameterised in order to divide the trajectory in multiple intervals or phases. By doing so, piecewise constant control and piecewise linear state histories are obtained [34]. Since different constraints hold for different phases in flight, i.e. turning constraints immediately after departure, it is of importance that the trajectory can be split into different phases of flight and that different path constraints can be set per flight phases. Thus the collocation method is preferred over the shooting method, as no path constraints and control bounds can be set in the latter method.

2.3.2. Atmosphere and Sound Propagation Model

The sound wave emitted by the sound source travels through the atmosphere to the observer. The transmission loss encountered while propagating is determined by the propagation loss model, while the atmosphere model crafts the characteristics of the atmosphere.

An adaptive atmosphere model enables the simulation of varied weather conditions. To simulate the atmosphere, actual weather balloon readings can be used. An alternative is to propagate the readings of weather stations on the ground near airports to higher altitudes. Weather stations can provide the wind profile (speed and direction), the temperature, the pressure and the dew temperature. The dew temperature can be used to determine the relative humidity.

Propagation modelling techniques commonly used are the Fast Field Programme (FFP), the Parabolic Equation (PE) and ray tracing. The FFP and PE are based on the wave equation. The FFP solves the wave equation by using the Fourier transform [36]. The PE makes use of the time-independent form of the wave equation and makes use of a finite spatially evolutionary scheme. The ray tracing method integrates sound rays by tracing parts of the sound wave front that is propagating in time [37, 38]. All make use of a horizontally stratified atmosphere to present vertical variation in speed of sound due to temperature and wind gradients. The main findings comparing the three methods are presented in Table 2.3.

In this study, hybrid methods combining multiple modelling techniques [39, 40] have not been considered due to the extensive work required to develop and validate the scheme. Furthermore, analytic sound propagation methods have not been considered as detailed Sound Pressure Levels (SPLs) and their respective directional of the noise sources of aircraft are required. This varies per specific case i.e. aircraft type and configuration, aircraft velocity and thrust setting. Next to this information not available to this research, also sufficiently accurate results can be obtained using the numerical methods. For analytic methods please refer to the Aircraft NOise Prediction Program (ANOPP) developed by the National Aeronautics and Space Administration (NASA) [41].

Table 2.3: Evaluation of the sound propagation methods.

	Fast Field Program	**Parabolic Equation**	**Ray tracing**
Accuracy	Very accurate	Limited elevation angle ±10 to ±35 degrees	Not accurate at very low frequency
Computational time	Very intensive	Intensive	Decent
Loss analysis	Per frequency	Per frequency	Per ray trace
Availability	Enough documentation	Enough documentation	Validated model [26]
Suitable trajectory optimisation scheme	Genetic Algorithm	Genetic Algorithm	Optimal Control Theory

The FFP generates very accurate results when the atmospheric layers near the ground become sufficiently thin. However this increased accuracy comes with increased computational intensity. The FFP method is frequency dependent meaning that it has to be evaluated for all frequencies individually to cover the complete frequency spectrum [37], increasing its computational intensity.

The PE generates varying accuracy depending on the elevation angle. Using the wide angle PE (the Crank Nicholson approximation [42, 43]), accurate results are obtained for elevation angles between ±10 to ±35 degrees of the horizontal. No accurate noise exposure can be evaluated exactly underneath the aircraft. As with the FFP method, the PE method is frequency dependent meaning that only one frequency is evaluated at a time, requiring each frequency to be evaluated before accurate noise footprints are generated.

Whilst ray tracing does not accurately model the losses of very low frequencies over a very large distance [37], the losses are determined while propagating towards the observer and is independent of frequency. By doing so, computational intensity is drastically reduced compared to the FFP and the PE. *Hartjes* [26] has modelled the propagation of helicopter sound using ray tracing. This model is available for this research.

For the FFP and the PE, transmission losses can be determined online i.e. in the program itself, or offline i.e. pre-run and stored in a database. To have an acceptable computational time, it is required for both methods to store the losses per frequency per distance per atmosphere condition in a database. Interpolation is used if a data point lies in between the stored values, creating discontinuities in the model. This is in objection with the gradient-based optimisation scheme. Ray tracing does not have this issue. Combined with the model of *Hartjes*, ray tracing does not only satisfy the continuity constraint of the model, as well reduces the workload of developing and modelling an own propagation model.

2.4. Flight Procedures and Regulations

The International Civil Aviation Organization (ICAO) has defined safety guidelines and regulations for defining instrument departure and arrival procedures in their Procedures for Air Navigation Services – Aircraft OPerationS (PANS-OPS) [14]. The procedures are designed such that it applies to all aircraft categories, unless stated otherwise. Primary goal is safe operations.

In this section, the most important general departure procedures are highlighted in Section 2.4.1 and the two different Noise Abatement Departure Procedures (NADPs) are introduced in Section 2.4.2. Regulations regarding safe operations during different meteorological conditions are discussed in Section 2.4.3.

2.4.1. General Departure Procedures

In order to have safe departure procedures, the PANS-OPS describe the vertical and horizontal departure profile [14]. Main focus points are obstacle clearance and turning after take-off.

Vertical procedure. The vertical departure procedure described by the PANS-OPS start 5 m above the end of the runway threshold, the so-called Departure End of Runway (DER). From the DER, the Obstacle Identification Surface (OIS) extends along a 2.5% gradient. Departure procedures always require an additional gradient of 0.8% on top of the OIS, resulting in a Procedure Design Gradient (PDG) of 3.3%. If there is an obstacle located within the OIS, a higher PDG must be used such that a Minimum Obstacle Clearance (MOC) of 0.8% is always achieved. After clearing the obstacle, the PDG is reduced to the minimum of 3.3%. Obstacles up to 60 m are required to be published, but the PDG does not have to be altered. The PDG ends when the aircraft has reached the minimum altitude to start the en-route climb, which is published as well. Figure 2.9 and Figure 2.10 elaborates further upon the PDG and MOC.

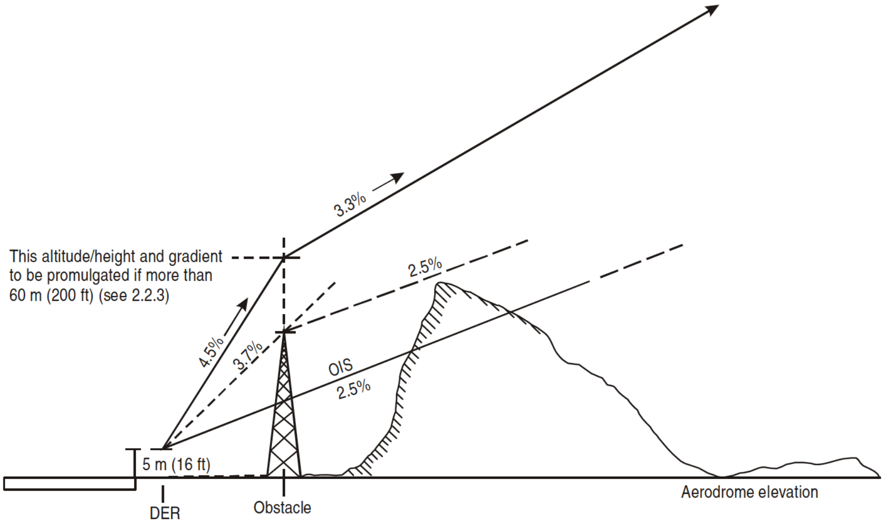

Figure 2.9: The procedure design gradient for departure procedures [14].

PDG P_1 due to obstacle A is not published because $H_1 \leq$ 60 m (200 ft).
PDG P_2 due to obstacle B is published because H2 > 60 m (200 ft).
Both obstacles A and B must be published.

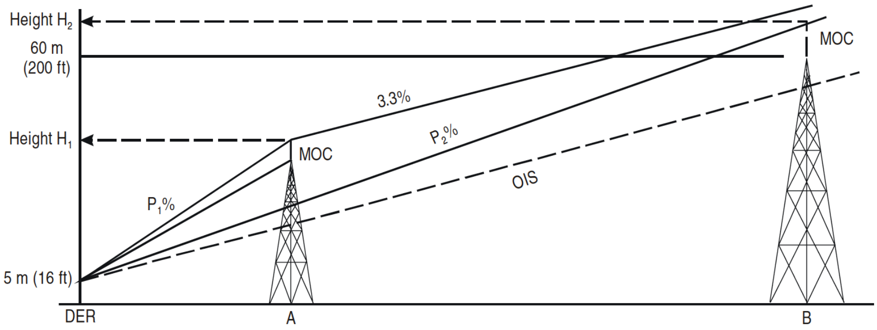

Figure 2.10: Close-in obstacles [14].

Horizontal procedure. The horizontal departure procedure is characterised by straight and turning departure procedures. Aircraft are not allowed to turn until the aircraft has reached a height of 400 ft or 120 m above the Final Approach and Take Off area (FATO). A straight departure is a departure where the aircraft is within 15° of the alignment of the runway centre line in its initial departure track. In turning departures, the aircraft makes a turn of 15° or more in its initial track. During the procedure, the bank angle is limited until a height of 300 ft above the DER is achieved. Table 2.4 presents the maximum bank angles per height above the DER.

Table 2.4: Bank angle limitation for different height above the end of the runway after take-off [14].

Bank angle (μ) [°]	**Height [ft]**	**Height [m]**
15	$400 \leq z < 1000$	$120 \leq z < 305$
20	$1000 \leq z < 3000$	$305 \leq z < 915$
25	$3000 \geq z$	$915 \geq h$

All procedures are described by the departure charts. Example departure charts for Amsterdam Airport Schiphol (AAS) is presented in Appendix A.

2.4.2. Noise Abatement Procedures

To minimise the noise received on the ground, the *ICAO* [14] has developed two different Noise Abatement Departure Procedures (NADPs) as guidance and are considered safe.The procedures can only be initiated once the aircraft has reached an height of at least 240 m (= 800 ft) above the ground and the velocity 20 km$\cdot h^{-1}$ (= 10 kts) larger than the safety take-off velocity v_2.

NADP-I. The first NADP is meant to reduce the noise near the end of the runway i.e. close to the airport. This is achieved by climbing to an altitude of 900 m (= 3000 ft) as quick as possible before changing to climb-out aircraft settings.

NADP-II. The second NADP reduces the noise received further away from the airport. Once the aircraft has reached a height above the ground of 240 m, the aircraft accelerates to a velocity of 20 to 40 km$\cdot h^{-1}$ (= 10 to 20 kts) above the aircraft velocity in clean configuration, while maintaining positive rate of climb. Once the aircraft reached an altitude of 900 m the aircraft setting is changed to climb-out mode.

2.4.3. Meteorological Conditions

The meteorological conditions play an important role in runway usage and runway throughput. Aircraft generally take-off and land using the runway directed against the wind to create headwind. The headwind component reduces the take-off distance and improves climbing performance of the aircraft. Crosswind and tailwind procedures are allowed under limiting conditions. Visibility constraints the throughput rate of the runway.

Aircraft manufactures have to demonstrate the crosswind capabilities of their aircraft types during certification. Aircraft with winglets are more subjective to crosswinds compared to their counterpart without winglets due to the increased vertical area.

Generally, take-off with slight tailwind is allowed under the following limitations: [44, 45]:

- Dry and clear runways.
- Anti-skid and thrust reversers are fully operational.
- Max takeoff rated thrust is used.
- Authorised pilot.

Airports also restrict certain runway usage at limiting crosswind values. For example, the primary runway at Schiphol is limited to 20 kts crosswind, while the secondary runway is allowed to have a larger crosswind component [2]. During operations at night, this is increased to 25 kts [46].

---

[2] https://www.lvnl.nl/veiligheid/realiseren-veiligheid/weersomstandigheden, accessed on 6 August 2018 (Dutch)

3

The Weather-Adaptive Flight Optimisation Research Tool

3.1. Introduction

The Weather-Adaptive Flight Optimisation Research Tool (WAFORT) framework is built on top of the Flight Optimisation Research Tool (FORT) developed by the Air Transport and Operations department of the Delft University of Technology. The WAFORT consists of a dynamic optimisation algorithm GPOPS, a sound propagation model, an Aircraft Performance Model (APM), a Geographic Information System (GIS) and a noise impact model. In this chapter, the modelling techniques of each model is discussed.

Section 3.2 discusses the dynamic optimisation tool by introducing the general problem formulation of an optimal control problem and the introduction of the GPOPS software. The aircraft mechanics and performance model is modelled by the APM and is discussed in Section 3.3. Section 3.4 discusses the propagation of sound from the aircraft towards the observer, and the resulting sound level at the observer. The noise impact model translates the sound level received by the observer to to a value that can be evaluated and compared. Section 3.5 discusses multiple schemes that can be used to quantify the noise impact. The GIS data used in the simulation is introduced in Section 3.6. A high level overview of the WAFORT model and its interaction between the problem statement, user inputs and the different models is presented in Section 3.7. The chapter is concluded by discussing the limitations of the WAFORT in Section 3.8.

3.2. Dynamic Optimisation Algorithm

Following an initial trade-off performed in Section 2.3.1, it is decided to use Optimal Control Theory (OCT), and more specifically collocation methods are chosen as it allows for the discretisation of the trajectory into segments.

To introduce OCT, the general formulation of a optimal control problem is presented in Section 3.2.1. This is followed by the introduction of the optimisation tool employed in the WAFORT and the considerations to use the General Pseudo-spectral OPtimal control Software (GPOPS) in Section 3.2.2.

3.2.1. General Optimal Control Theory Problem Formulation

For this research, the OCT problem is formulated as a continuous Bolza problem. The performance index J, also known as objective function or cost function, consists of both Mayer (Φ) and Lagrange ($\mathscr{L}$) form. A direct collocation method is used as optimisation scheme.

A basic control problem is defined like Equation (3.1), in which J is the performance index, $\bar{x}$ is a vector denoting all state variables n in $\mathbb{R}$, $\bar{u}$ is a vector for all control variables m in $\mathbb{R}$ and t_f is the final time. The aim is to minimise the performance index while satisfying the constraints.

If $\Phi = 0$, the problem is a Lagrange problem, while if $\mathscr{L} = 0$, the problem is a Mayer problem. A combination of both the Lagrange and Mayer problem is the so-called Bolza problem.

$$J = \Phi\left[\bar{x}(t_0), t_0, \bar{x}(t_f), t_f\right] + \int_{t_0}^{t_f} \mathscr{L}\left[\bar{x}(t), \bar{u}(t), t\right] dt \tag{3.1}$$

The problem is constrained by dynamic constraints $\bar{f}$, boundary conditions $\bar{\phi}$ and algebraic path constraints $\bar{C}$, as presented in Equation (3.2).

$$
\begin{aligned}
&\dot{\bar{x}}(t) = f\left[\bar{x}(t), \bar{u}(t), t\right] \\
&\bar{\phi}\left[\bar{x}(t_0), t_0, \bar{x}(t_f), t_f\right] = 0 \\
&\bar{C}\left[\bar{x}(t), \bar{u}(t), t\right] \leq 0
\end{aligned}
\tag{3.2}
$$

In multi-phase problems, the total cost function is the sum of the cost functional in each phase, $J = \sum_{p=1}^{P} J^p$ for P phases. Furthermore each phase might have its own differential equations $\dot{\bar{x}}^p$, boundary condition $\bar{\phi}^p$ and state constraint $\bar{C}^p$. The phases can be connected provided that the time variable t does not change direction. The linkage constraints ensure that the phases being connected are continuous for the state and time vector. The connection between different phases is illustrated by Figure 3.1. Equation (3.3) presents the linkage constraint $\bar{P}$ for multiple phases, in which p_l^s is the linkage point left of the linkage L, and p_u^s the linkage point to the right [26].

$$
\begin{aligned}
&\bar{P}\left[\bar{x}^{p_t^s}(t_f), t_f^{p_t^s}; \bar{P}\bar{x}^{p_u^s}(t_0), t_0^{p_u^s}\right] = 0, \\
&\text{with} \quad \left(p_l^s, p_u^s \in [1, \ldots P], s = 1, \ldots, L\right), \qquad \bar{x}^p \in \mathbb{R}^{n_p}, \quad t \in \mathbb{R}
\end{aligned}
\tag{3.3}
$$

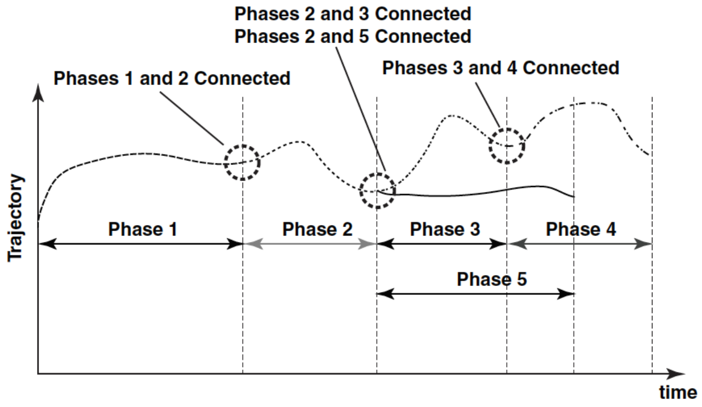

Figure 3.1: Multiple phases trajectory linkages [47].

3.2.2. General Pseudo-Spectral Optimal Control Software

The original FORT framework makes use of the dynamic optimisation algorithm General Pseudo-spectral OPtimal control Software, or GPOPS, to optimise the flight trajectory. GPOPS is an optimisation tool developed by the University of Florida. The tool is very useful due to its built in scaling option to reduce the effort to define problems and due to the availability of several different differentiation methods. Furthermore, the software is integrated in the MATLAB programming environment [47] which is advantageous for this research.

As the name of GPOPS suggests, it makes use of pseudo-spectral methods [48]. The pseudo-spectral method is one type of collocation method within the optimal control theory optimisation methods. Using collocation, the trajectory dynamics are discretised into segments transforming the optimisation problem into a parameter optimisation problem [16]. The use of pseudo-spectral methods over local collocation methods lies in the fact that higher accuracy can be obtained for smaller problem sizes [26]. Spectral convergence is achieved when pseudo-spectral methods are used, meaning faster convergence than any power of N^{-m}, in which N is the number of collocation points and m is any value [49].

Psuedo-spectral methods approximate the state and control vectors using global polynomials. At the orthogonal collocation points, collocation of the differential-algebraic equations is performed [48]. Pseudo-spectral methods often make use of the Gaussian quadrature to integrate the dynamics of the system. A high level of accuracy can be maintained with relatively low discretisation points.

There are multiple different Gaussian methods applicable to trajectory optimisation such as the Legendre-Gauss (LG), Legendre-Gauss-Lobatto (LGL) and the Legendre-Gauss-Radau (LGR) quadrature rules. The LGR quadrature rules show the best convergence behaviour [48] and allows for either one of the initial or final time point to be constrained at the boundary. The benefits and limitations of different collocation methods is presented in Figure 3.2.

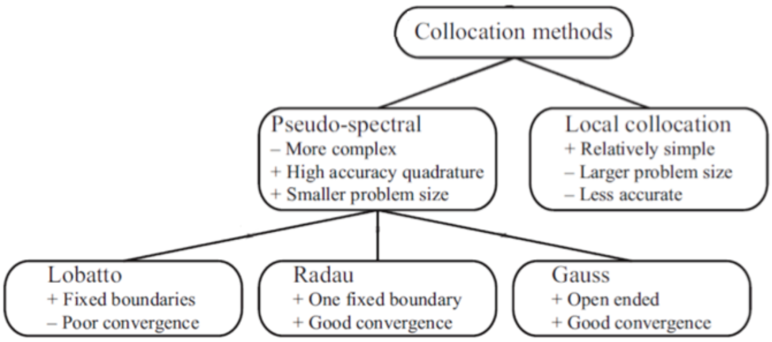

Figure 3.2: Overview of benefits and limitations of different optimal control collocation methods. Adapted from [26].

GPOPS is capable of solving multiple phase optimal control problems by discretising the cost functional J and the differential-algebraic equations $\dot{x}$ in each phase. Linkage conditions connect the different phases while boundary limits for the state and control variables limit the optimisation range. A NLP solver finds the optimal control starting from an initial guess to initiate the optimisation process. The algorithmic flow within GPOPS is depicted in Figure 3.3.

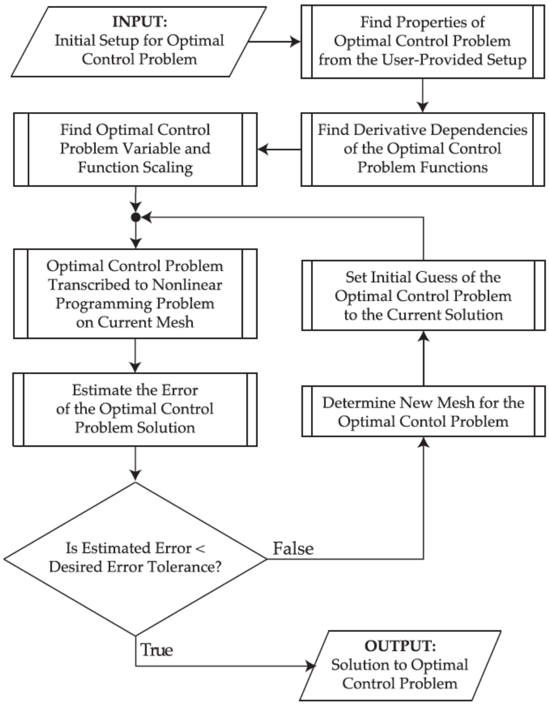

Figure 3.3: Flowchart of dynamic optimisation algorithm GPOPS [47].

As optimal control theory is a gradient-based technique, the NLP solver requires gradients of the cost functional and constraints. Due to the size of the problem and varying constraints per simulation, Automatic Differentiation (AD) is available to differentiate the flight mechanics model, path constraints and the noise model instead of analytically differentiation of the entire model. AD makes use of the chain rule and is repeatedly applied to the arithmetic activities performed by the computer. This results in derivatives with machine precision and is equal to its symbolic derivatives.

To solve the large NLP, Sparse Nonlinear OPTimizer (SNOPT) is used [50] as it is available within MATLAB and GPOPS. SNOPT makes use of Sequential Quadratic Programming (SQP) to solve the optimisation problem. GPOPS iterates until both feasibility and optimality threshold are achieved. For this research, the threshold is set at $\epsilon = 1 \cdot 10^{-6}$.

3.3. Aircraft Performance Model

The aircraft performance model consists of the flight mechanics model and the flight performance model. To reduce the number of parameters to optimise for, the aircraft mechanics is modelled as a point mass model. Section 3.3.1 discusses the mechanics model by introducing the assumptions made and the state and control variables used by the optimisation scheme. Furthermore, the derivatives of the states are determined in order to be used as algebraic differential equations in the optimisation scheme. In Section 3.3.2, the capabilities of the performance model is introduced.

3.3.1. Flight Mechanics

The flight mechanics model is modelled as a point mass model as a numerical sound propagation model is chosen with a point source, Discussed in Section 3.4. Main simplification over a rigid body model is that all forces exerted on and by the aircraft go through one point: the centre of gravity. Previous studies by *Hartjes et. al* and *Hogerhuis et. al* [18, 19] show that a point mass model returns satisfying results.

For the aircraft mechanics the following assumptions are made:

- *Flat, non-rotating Earth* - This assumption is valid as the total flight time in the simulation is short.
- *Coordinated flight* - The aircraft flies in the direction its nose is pointing. No side slipping allowed ($\beta = 0$).
- *The aircraft is modelled as a point mass model* - All forces act in the centre of gravity.
- *Thrust vector is aligned along the velocity vector.*
- *The atmosphere is horizontally stratified without vertical wind components* ($V_{W_z} = 0$) - The air is non-turbulent.
- *No wind shear* - Wind shears are sudden changes of wind direction and velocity which are hard to be predicted based on measurements.

In this research a horizontally stratified atmosphere is modelled as elaborated in Section 3.4.3. Within each layer, it is assumed that there is no vertical wind components. For optimisation using optimal control theory including turbulent air with wind shear, please refer to *Visser* [51].

The mechanics is described using 6 states and 3 control variables, as presented in Equation (3.4). The state variables xyz denote the position coordinate of the aircraft in an Earth-fixed reference frame. The angles χ for the azimuth angle or the heading angle, γ for the flight path angle and μ for the aerodynamic roll angle are fixed to the air-path fixed coordinate system. The heading angle matches the true compass i.e. 0° for the compass north, 180° for the compass south. W_{AC} is the weight of the aircraft while the control variable η is the normalised throttle setting.

$$\bar{x} = \begin{bmatrix} x \\ y \\ z \\ V \\ \chi \\ W_{AC} \end{bmatrix}, \qquad \bar{u} = \begin{bmatrix} \eta \\ \gamma \\ \mu \end{bmatrix} \tag{3.4}$$

The thrust level is related to the source noise level emitted by the aircraft. To determine the thrust level, the normalised throttle setting is multiplied by the total thrust available plus the idle thrust as presented by Equation (3.5).

$$T = (T_{max} - T_{idle}) \cdot \eta + T_{idle} \tag{3.5}$$

The algebraic differential of the states with the exclusion of the wind is presented in Equation (3.6). The set is obtained using equilibrium expressions: The derivative of the velocity is obtained using force equilibrium in climbing flight. The derivative of the heading is determined from the force equilibrium in a horizontal steady turn. The change in aircraft weight equals the negative fuel flow $\dot{m}_{fuel}$.

$$\dot{x} = \begin{bmatrix} x \\ y \\ z \\ V \\ \chi \\ W_{AC} \end{bmatrix}' = \begin{bmatrix} V \cdot cos(\gamma) \cdot sin(\chi) \\ V \cdot cos(\gamma) \cdot cos(\chi) \\ V \cdot sin(\gamma) \\ \frac{g_0}{W_{AC}} \cdot (T - D - W_{AC} \cdot sin(\gamma)) \\ \frac{g_0}{V} \cdot tan(\mu) \\ -\dot{m}_{fuel} \cdot g_0 \end{bmatrix} \tag{3.6}$$

Before identifying the algebraic differential equations with the inclusion of wind, first the modelling of the wind is elaborated.

Modelling of the wind. The wind V_W is modelled in a form of the logarithmic expression of the Hellman's exponential law, correlating wind speed readings at two different heights [52]. This is illustrated in Equation (3.7) with $v_0(z_v)$ the wind velocity at reference altitude z_v, z the altitude and z_0 the roughness length of the ground surface. The roughness length is roughly 10% of the surface roughness element [26]. Examples of the surface roughness elements are presented in Table 3.1. Figure 3.4 presents the increase of the wind velocity factor $ln\left(\frac{z}{z_0}+1\right) \cdot \left[ln\left(\frac{z_v}{z_0}+1\right)\right]^{-1}$ with increasing altitude.

$$V_W(z) = v_0(z_v) \cdot \frac{ln\left(\frac{z}{z_0}+1\right)}{ln\left(\frac{z_v}{z_0}+1\right)} \tag{3.7}$$

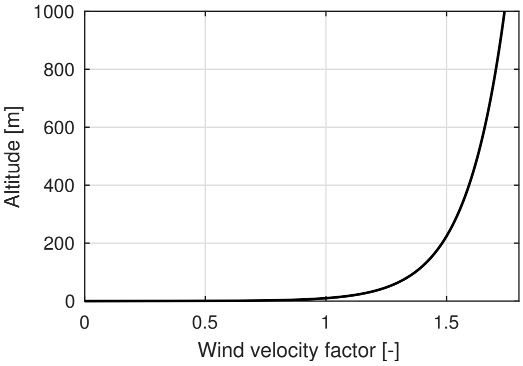

Figure 3.4: Wind velocity factor against altitude over crops and hedges (z_0 = 0.02 m).

Table 3.1: Roughness element of different terrains [52].

Terrain characteristics	Roughness element [-]
Smooth hard ground, cold water	0.1
Tall grass on level ground	0.15
High crops, hedges and shrubs	0.2
Wooded countryside, many trees	0.25
Small town with trees and shrubs	0.3
Large city with tall buildings	0.4

The wind alters the ground speed of the aircraft as illustrated by Equation (3.8), with $\vec{V_{GS}}$ the ground speed, $\vec{V}$ the velocity of the aircraft and $\vec{V_W}$ the wind velocity. The wind is characterised by its profile i.e. the magnitude and the direction it flows from. The wind direction is given in azimuth degrees from the direction it is blowing i.e. a west wind is a wind from 270° and blows from west to east. In Equation (3.8), ψ_W represents the direction the wind is **blowing to**, as represented by the wind geometry presented in Figure 3.5.

$$
\begin{aligned}
\vec{V_{GS}} &= \vec{V} + \vec{V_W} \\
V_{Wx} &= V_W \cdot \sin(\psi_W) \\
V_{Wy} &= V_W \cdot \cos(\psi_W)
\end{aligned}
\tag{3.8}
$$

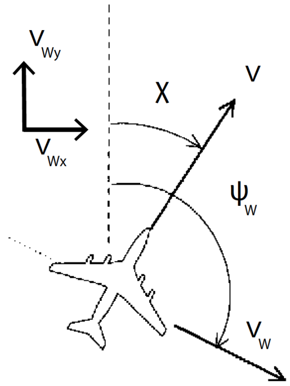

Figure 3.5: Geometry of the wind. Adapted from [51].

Algebraic differential equations with the inclusion of wind. The algebraic differentials determined in Equation (3.6) all require an additional wind term except for the vertical acceleration $\dot{z}$ and the change in aircraft weight $\dot{W}_{AC}$. The position differentials are presented in Equation (3.9).

$$
\begin{aligned}
\dot{x} &= V \cdot \cos(\gamma) \cdot \sin(\chi) + V_{Wx} \cdot \sin(\chi) - V_{Wy} \cdot \cos(\chi) \\
\dot{y} &= V \cdot \cos(\gamma) \cdot \cos(\chi) + V_{Wx} \cdot \cos(\chi) + V_{Wy} \cdot \sin(\chi) \\
\dot{z} &= V \cdot \sin(\gamma)
\end{aligned}
\tag{3.9}
$$

For the acceleration $\dot{V}$, the motion of an aircraft flying in the vertical plane is used, as illustrated by Figure 3.6.

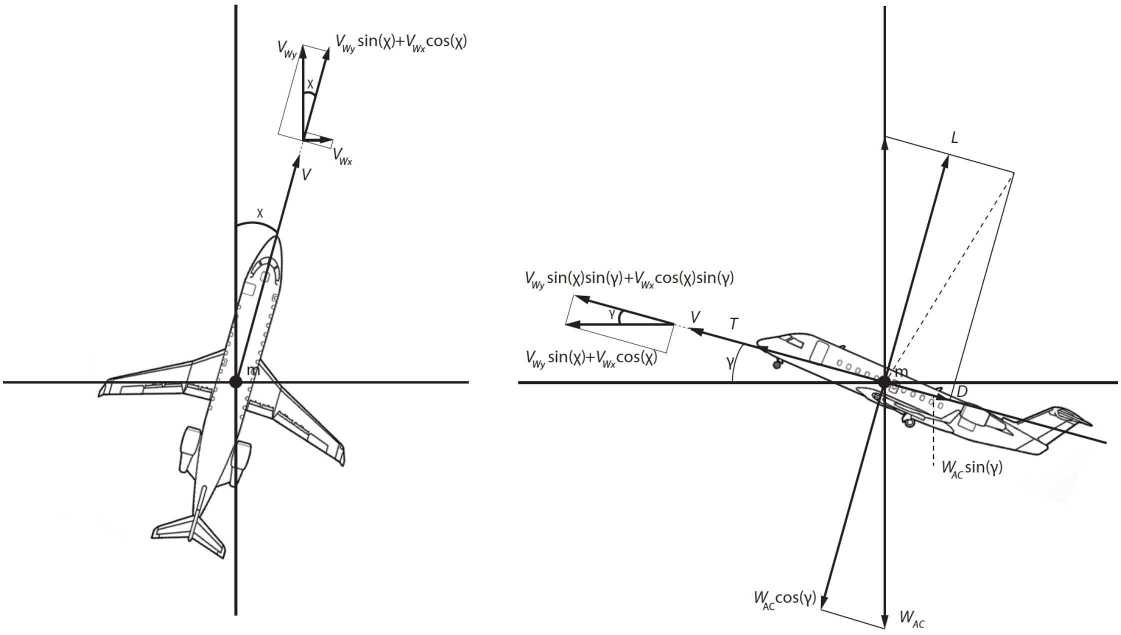

Figure 3.6: Top and side view of an aircraft in steady horizontal flight along the velocity vector. Adapted from [53].

Using Newton's second law of motion in the body reference frame of the aircraft, $F = m \cdot a$, the expressions in Equation (3.10) are obtained. Using $m = \frac{g_0}{W_{AC}}$, the derivative of the velocity is obtained in Equation (3.11).

$$
\begin{aligned}
F &= T - D - W_{AC} \cdot \sin(\gamma) \\
a &= \dot{V} + \dot{V}_{Wx} \cdot \sin(\gamma) \cdot \sin(\chi) + \dot{V}_{Wy} \cdot \cos(\gamma) \cdot \sin(\chi)
\end{aligned}
\tag{3.10}
$$

$$\dot{V} = \frac{g_0}{W_{AC}} \cdot (T - D - W_{AC} \cdot \sin(\gamma)) - \dot{V}_{Wx} \cdot \cos(\gamma) \cdot \sin(\chi) - \dot{V}_{Wy} \cdot \cos(\gamma) \cdot \cos(\chi) \tag{3.11}$$

A similar method is used to determine the derivative of the heading. In this case, an aircraft in a steady horizontal turn with radius R is considered, as depicted by Figure 3.7.

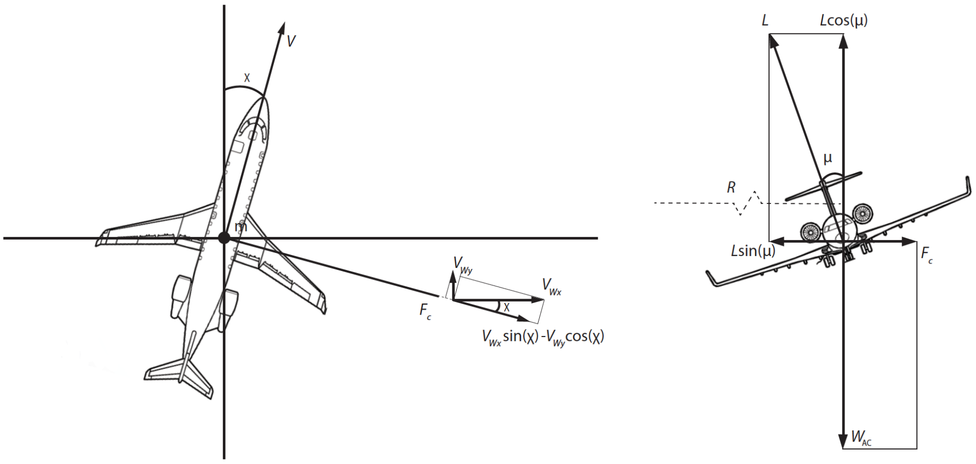

Figure 3.7: Top and front view of an aircraft in steady horizontal turn. Adapted from [53].

Again the Newton's law is applied in Equation (3.12). In this case, the force is the Coriolis force F_c. Combined with $\dot{\chi} = \frac{V}{R}$, the final expression for the angular velocity is obtained in Equation (3.13).

$$\begin{aligned} F =& F_c = L \cdot \sin(\mu) \\ a =& \frac{V^2}{R} + \dot{V}_{Wx} \cdot \cos(\chi) - \dot{V}_{Wy} \cdot \sin(\chi) \end{aligned} \tag{3.12}$$

$$\dot{\chi} = \frac{g_0}{V \cdot \cos(\gamma)} \cdot \tan(\mu) + \frac{1}{V \cdot \cos(\gamma)} \cdot (\dot{V}_{Wy} \cdot \sin(\chi) - \dot{V}_{Wx} \cdot \cos(\chi)) \tag{3.13}$$

Lastly, the unchanged derivative of the weight of the aircraft is presented by Equation (3.14).

$$\dot{W}_{AC} = -\dot{m}_{fuel} \cdot g_0 \tag{3.14}$$

The total set of algebraic differentials is presented in Equation (3.15).

$$\dot{\vec{x}} = \begin{bmatrix} x \\ y \\ z \\ V \\ \chi \\ W_{AC} \end{bmatrix}' = \begin{bmatrix} V \cdot \cos(\gamma) \cdot \sin(\chi) + V_{Wx} \\ V \cdot \cos(\gamma) \cdot \cos(\chi) + V_{Wy} \\ V \cdot \sin(\gamma) \\ \frac{g_0}{W_{AC}} \cdot (T - D - W_{AC} \cdot \sin(\gamma)) - \dot{V}_{Wx} \cdot \cos(\gamma) \cdot \sin(\chi) - \dot{V}_{Wy} \cdot \cos(\gamma) \cdot \cos(\chi) \\ \frac{g_0}{V \cdot \cos(\gamma)} \cdot \tan(\mu) + \frac{1}{V \cdot \cos(\gamma)} \cdot (\dot{V}_{Wy} \cdot \sin(\chi) - \dot{V}_{Wx} \cdot \cos(\chi)) \\ -\dot{m}_{fuel} \cdot g_0 \end{bmatrix} \tag{3.15}$$

3.3.2. Aircraft Performance

The aircraft performance depends on aircraft type specific data and on the current state of the aircraft in the simulation. A model that contains all these aircraft specific data is the Base of Aircraft Data (BADA), developed and maintained by Eurocontrol [54]. The BADA model is a widely used and recognised APM. The model is suitable for trajectory simulation used to support research and development, validation and assessment of new air traffic management concepts and air traffic control procedure, ground based trajectory prediction and aircraft emissions environmental assessment.

The BADA model holds performance and operating procedure coefficients to calculate thrust, drag and fuel flow for various aircraft and engine types for specific climb and descent velocities. The BADA technical manual elaborates upon what equations and functions have been implemented. Within the database, most common used aircraft type data is available [55].

The BADA distinguishes different maximum thrust ratings for cruise and climbing flight. Furthermore, it incorporates the effect of the engine operating in the flat-rated area, where the engine behaviour is limited by the internal pressure, and the temperature rated area, where the amount of fuel injected into the combustion chamber is reduced to control the turbine entry temperature [55]. The aircraft model is thus temperature related, but is not related to the relative humidity or wind.

3.4. Sound Propagation Model

The sound propagation model consists of the source noise modelling and the propagation loss modelling. The approach followed to model the noise in this thesis is based on the approach elaborated by *Hartjes* [26], in which helicopter noise in non-standard atmosphere was modelled using ray tracing. The research has been validated using the work of *Arntzen et. al* [56], which is by itself validated using the work computed using a FFP method [57].

The source noise emit by the aircraft is frequency dependent. The considerations taken and the method to determine the source noise is elaborated in Section 3.4.1. With the relative movement of the aircraft with respect to the fixed observer, the observed frequency of sound is shifted by the Doppler frequency shift. This frequency correction is discussed in Section 3.4.2. The sound ray travelling from the source to the observer is modelled using ray tracing, as previously determined in Section 2.3.2. This ray tracing method is elaborated in more detail in Section 3.4.3. Between the source and the observer, the sound energy is subjected to losses. The propagation losses generally accounted for are spreading loss, atmospheric attenuation loss, ground reflection and shadow zones. The modelling of these losses are discussed in detail in Section 3.4.4. All losses are combined to obtain the observed total sound levels. The section concludes with an discussion on the limitations of the propagation model

3.4.1. Source Noise Modelling

To model the source noise of an aircraft, a noise source simulation method or an integrated method can be employed. In a simulation method, the acoustics of each noise component are determined. In an integrated method, the noise is based on experimental data or the certified data of the complete aircraft. For the purpose of noise exposure on the ground for trajectory optimisation, generally the integrated method is employed as it does not matter specifically what noise component is contributing to the noise of the complete aircraft observed on the ground. So an integrated method is used in this research. Furthermore, in the far field i.e. the distance is large compared to the size of the source, the source can be treated as a point source.

This section first discusses the database from which source noise data is obtained. This is followed by the determination of the source noise level.

Source noise database. The noise emitted by aircraft varies per aircraft type and its thrust setting. Initially the *Society of Automotive Engineers* [58] made recommendations to bring standards to aircraft noise modelling. This report has been modernised by the *European Civilian Aviation Conference (ECAC)* Doc.29 publication [59]. ECAC is the largest and oldest aviation organisation in Europe and is part of the ICAO air transport global community. Since then, the Doc.29 has been incorporated by the ICAO [60].

Existing reference-day noise simulation models make use of databases with noise source information. Examples are the INM [20], the Aircraft Environmental Design Tool (AEDT) [61], which is INM's successor, and Doc.29. The INM has been developed by the FAA and was initially introduced in 1979. The ECAC/CEAC Doc.29 manual [59] recommends the use of the Aircraft Noise and Performance (ANP) database[1], which is endorsed by ECAC as the source for aircraft noise source reference. The ANP database is developed, hosted and maintained by Eurocontrol Experimental Center. The INM makes use of the same database. The data consists of mainly manufacturer supplied data.

In the database, the Noise Power Distance (NPD) can be found tabulated. The NPDs are source noise levels expressed as intensities at a certain distance away from the observer at a height of 1.2 m. It is defined for the Effective Perceived Noise Level (EPNL), LA_{max}, the maximum tone corrected perceived noise level (PNLTM)

---

[1] www.aircraftnoisemodel.org

and SEL at slant ranges of 200 to 25000 ft. Non-tabulated data points are obtained by interpolation. Furthermore, the unweighted reference sound spectrum defined per $\frac{1}{3}$ octave frequency bands at 1000 feet from the aircraft is defined as the spectral classes.

Using the NPD data, it is assumed that aircraft flies along a straight path of infinite length and parallel to the ground. The NPD and spectral class varies per specific aircraft type. The database is derived from noise certification tests in accordance with FAR Part 36.5(c)(1), stating that the test were performed at 101,315 Pa sea level pressure, a temperature of 25°C, a relative humidity of 70% and no wind. This is the so-called SAE-AIR-1845 atmosphere [58].

Calculating the source noise. The actual noise emitted is not present in the ANP database. All values in the ANP database are normalised to the AIR-1845 atmosphere. So it is required to estimate the normalisation factor used in the ANP database to determine the source noise based on the data in the ANP database.

To do so, first the spectral class values are propagated back to the source. Then a normalisation factor is determined in order to obtain a source noise level that matches the $L_{A,max}$ at 1000 ft.

When the aircraft is directly overhead, the $L_{A,max}$ can be considered identical to the noise received on the ground. Furthermore, if the aircraft is directly overhead, only spherical spreading loss ($20 \cdot log_{10}(s)$) and absorption loss ($\alpha \cdot s$) are taken into account by the ANP [59]. The propagation loss is discussed in more detail in Section 3.4.4.

Within the SAE AIR-1845 atmosphere, arithmetic averages are used for the atmospheric attenuation coefficient α, and are tabulated in Table 3.2.

Table 3.2: Atmospheric attenuation coefficient α used in SAE AIR-1845 atmosphere [59].

Frequency [Hz]	**50**	**63**	**80**	**100**	**125**	**160**	**200**	**250**	**315**	**400**	**500**	**630**
α [dB/100m]	0.033	0.033	0.033	0.066	0.066	0.098	0.131	0.131	0.197	0.230	0.295	0.361
Frequency [Hz]	**800**	**1000**	**1250**	**1600**	**2000**	**2500**	**3150**	**4000**	**5000**	**6300**	**8000**	**10000**
α [dB/100m]	0.459	0.590	0.754	0.983	1.311	1.705	2.295	3.115	3.607	5.246	7.213	9.836

In order to determine the normalisation factor, a minimisation problem is run in which the difference between the $L_{A,max}$ found in the the NPD and the $L_{A,max}$ found by backwards propagating the spectral classes and then propagated again with the inclusion of a normalisation factor is subtracted. This is illustrated by Equation (3.16).

First the emitted noise corrected by a normalisation factor (norm) is obtained. This source noise is than subtracted by the propagation losses and the sound is made A-weighted resulting in $SPL(f)$. The calculations are performed in the SAE AIR-1845 atmosphere and at a slant range s of 1000 feet as the spectral class (Spec) is defined at 1000 ft.

$$\begin{aligned} \text{minimise:} \quad & \Delta SPL = \sqrt{\left(10 \cdot 10 \cdot \log_{10}(\sum_{f=1}^{24}(10^{\frac{SPL(f)}{10}}) - L_{A,max,\text{NPD}}\right)^2} \\ \text{with:} \quad & SPL(f) = \frac{\text{Spec} + \alpha \cdot s + 20 \cdot \log_{10}(s)}{\text{norm}} + A_W - \alpha \cdot s - 20 \cdot \log_{10}(s) \end{aligned} \tag{3.16}$$

Using the normalisation factor, the source noise SPL_A is obtained using Equation (3.17). For each thrust level for which the $L_{A,max,\text{NPD}}$ is defined, a different normalisation factor is obtained. Interpolation between these source noise levels and the thrust level determines the actual source noise.

$$SPL_A(f) = \frac{\text{Spec} + \alpha \cdot s + 20 \cdot \log_{10}(r)}{\text{norm}} \tag{3.17}$$

The thrust levels in the ANP database are not the actual thrust level of the aircraft. It is the so-called net-corrected thrust level per engine T_n, or the value at sea level. The correction from thrust to net corrected thrust is presented by Equation (3.18), in which n_{eng} is the number of engines the aircraft is equipped. Using this variable, thrust at different power settings and altitudes can be compared [59].

$$T_n = \frac{T}{n_{eng}} \cdot \frac{p_0}{p} \tag{3.18}$$

3.4.2. Doppler Frequency Shift

For moving sound sources, the observed frequency differs to the emitted frequency. This is due to the Doppler effect. The effect is caused by a time rate of change in the distance between the moving source and receiver. When the aircraft is flying towards the observer, the observed frequency is higher, while when the aircraft is flying away from the observer the observed frequency is lower.

To determine the frequency shift, Figure 3.8 illustrates the problem geometry. The frequency shift $\frac{f'}{f}$ is given by Equation (3.19), in which M is the Mach number, θ the incidence angle, v the airspeed, c the speed of sound and r the slant range.

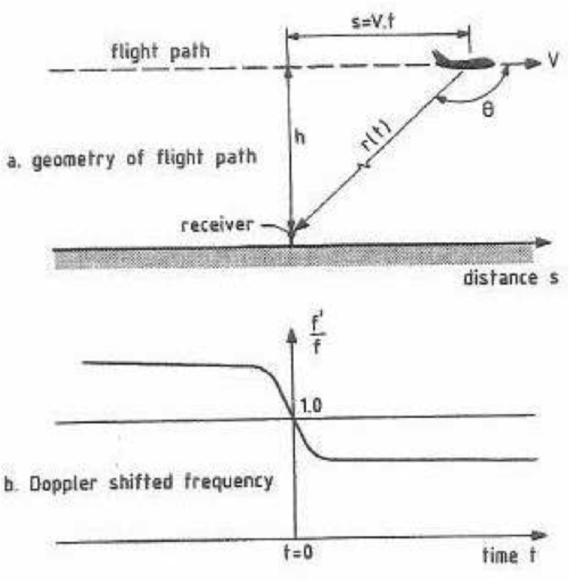

$$\frac{f'}{f} = \frac{1}{1 - M\cos(\theta)}, \qquad \text{with} \quad M = \frac{v}{c}, \quad r = -\frac{v \cdot t}{\cos(\theta)} \tag{3.19}$$

Figure 3.8: Doppler frequency shift geometry [27].

At any moment, if the velocity vector relative to the fixed observer is known, the Doppler frequency shift can be determined. In a layered atmosphere, it does not matter what atmospheric layer is chosen to evaluate the shift, as long as the local speed of sound and incidence angle θ is used. The frequencies used throughout the calculation of the propagation loss is the frequency shifted by the Doppler frequency shift.

3.4.3. Ray Path Modelling

For the sound propagation model, ray tracing is used as determined in Section 2.3.2. First the influence of the different atmospheric properties are discussed followed by the construction of the ray path.

For this study, a horizontally stratified atmosphere is assumed. This means that each layer has different atmospheric properties, but within the layer the temperature, relative humidity and the wind speed gradient does not change. The layers are divided logarithmic, in order to evaluate the logarithmic speed of sound profile when wind is included. This is important in order to accurately model refraction.

Atmospheric Propagation.

Under ISA conditions, the ISA relations is used to evaluate the temperature, pressure and density for different altitudes in the troposphere. The variation in temperature with height is described by Equation (3.20), in which T the temperature in Kelvin at the height z in meters, T_0 the ground temperature, λ the temperature gradient which is -0.0065 Km^{-1} in ISA conditions and z_0 is the height on the ground.

$$T = T_0 + \lambda(z - z_0), \qquad \text{with: } \lambda = \frac{dT}{dz} \tag{3.20}$$

Due to the temperature gradient, the effective speed of sound c varies per layer. With Snell's Law, refraction is calculated on the boundary of each atmospheric layer and is represented by Equation (3.21), in which θ is the incidence angle, κ is the heat capacity ratio of air and R the gas constant of air [27]. Figure 3.9 represents refraction towards an atmospheric layer (medium 2) with a lower speed of sound.

$$\frac{\cos(\theta_2)}{c_2} = \frac{\cos(\theta_1)}{c_1}, \quad \text{with} \quad c = \sqrt{\kappa R T} \tag{3.21}$$

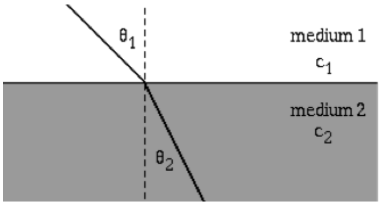

Figure 3.9: Snell's law [27].

In non-ISA conditions, the temperature on the ground can differ, or the temperature lapse is different. To model variation in temperature and the lapse, this research continuous to make use of the ISA relation of Equation (3.20). The relative humidity is kept constant in each layer.

Construction of Ray Paths.

The main principles of ray path methods is to numerically integrate the ray in time. In general this is performed along the wave direction as the sound wave travels from the source to the receiver, also known as the forward method. Figure 3.10 presents a refracted ray path, which is launched from the source with launch angle θ_0, covering distance s. Depending on the speed of sound in each layer i, Snell's law refracts the ray such that the incidence angle in the next layer becomes θ_i.

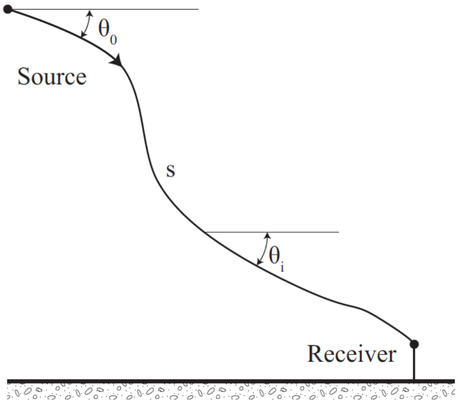

Figure 3.10: Refracted ray path from the source to the receiver [26].

However for this research, sound levels at fixed observer locations need to be evaluated. With the forward method, either many evaluations are required to find the ray paths that exactly arrive at the fixed observers or interpolation between different ray paths is required. It is more computational efficient to backward trace the ray from the receiver to the source. This is achieved by repeatably determining the refraction in each atmospheric layer i.

Within each atmospheric layer, the speed of sound is determined by combining Equation (3.7), Equation (3.20) and Equation (3.21) into Equation (3.22). Within the layers, the speed of sound is approximated using a constant speed of sound gradient G_{lin}, illustrated by Figure 3.11.

$$c(z) = \sqrt{\kappa \cdot R \cdot (T_0 + \lambda \cdot z)} + V_w(z) \tag{3.22}$$

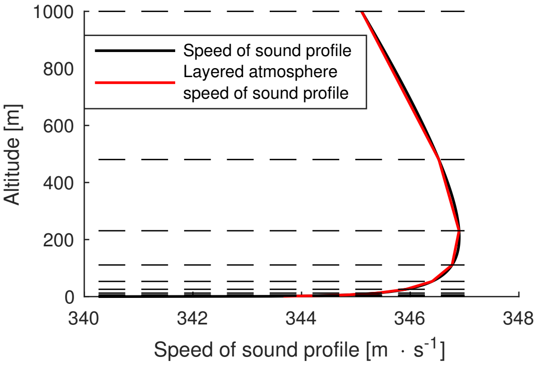

Figure 3.11: Linear approximation of the speed of sound in a layered atmosphere (v_0 = 5 m· s^{-1} and z_0 = 0.02 m).

Instead of using Snell's law, the constant speed of sound gradient G_{lin} is used to evaluate the refraction and to numerically determine the launch angle θ_0. The constant gradient refracts the ray with a constant rate of curvature. By determining the centre and the radius of curvature in each layer, the entire ray path is geometrically determined. This results in the total horizontal distance distance travelled x, the total ray path length s and the final incidence angle θ_f at which the ray arrives at the receiver. For a more elaborated discussion on this procedure please refer to *Ruijgrok* [27].

In the i^{th} layer, the radius of curvature is determined using Equation (3.23), in which c_i is the speed of sound at the top of the layer and $G_{lin,i}$ the linearised gradient in the layer. The centre of curvature is then defined by $(x_{c,i}, z_{c,i})$, and presented in Equation (3.24). Following these expressions, the final angle of incidence $\theta_{f,i}$, final distance $x_{f,i}$ and arc segment length s_i is determined accordingly by evaluating Equation (3.25) to Equation (3.27). Figure 3.12 illustrates the geometry of the process.

$$R_i = \frac{-c_i}{G_{lin,i} \cdot \cos(\theta_{0,i})} \tag{3.23}$$

$$\begin{aligned} x_{c,i} &= x_{0,i} + R_i \cdot \sin(\theta_{0,i}) \\ z_{c,i} &= z_{0,i} + R_i \cdot \cos(\theta_{0,i}) \end{aligned} \tag{3.24}$$

$$\theta_{f,i} = \cos^{-1}\left(\frac{z_c - z_{f,i}}{R_i}\right) \tag{3.25}$$

$$x_{f,i} = x_c - R_i \cdot \sin(\theta_{f,i}) \tag{3.26}$$

$$s_i = |R_i \cdot (\theta_{f,i} - \theta_{0,i})| \tag{3.27}$$

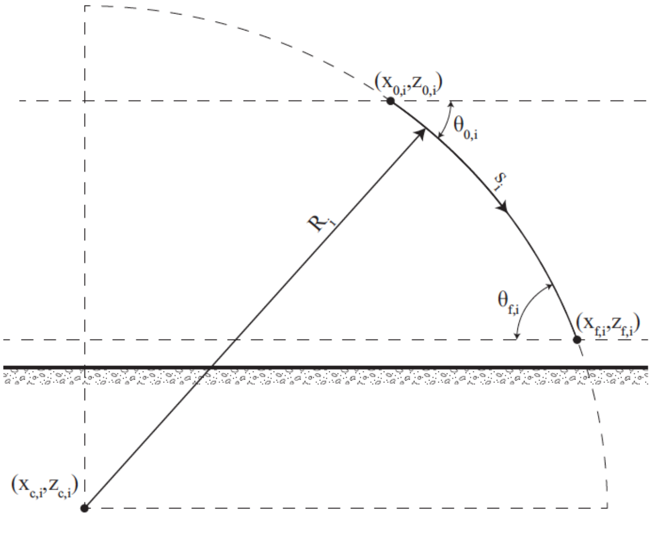

Figure 3.12: Refraction in a linear speed of sound profile [26].

3.4.4. Propagation Loss Modelling

From the source to the observer, sound energy is lost. Generally modelled losses in sound propagation are spreading loss, atmospheric attenuation, ground reflection and shadow zones. In this section, each are discussed in separate paragraphs. The paragraphs are followed by the determination of the total sound level at the observer. In order to understand the application of the propagation model, the limitations to the model are discussed in the final paragraph of this section.

Spreading Loss.

It is assumed that the point source emits in a non-directional fashion resulting in spherical spreading i.e. energy is equally emitted in any direction. In a homogeneous atmosphere, rays travel along a straight line and spreading loss is determined by Equation (3.28), the inverse distance law. Reference distance s_0 is typically 1 m [27].

$$TL_S = 20 \cdot log_{10}\left(\frac{s}{s_0}\right) \tag{3.28}$$

In non-homogeneous atmospheres rays either refract towards (focusing) or away (defocusing) from each other resulting in slightly different spreading losses than obtained by the inverse distance law. To account for this slight difference, an additional correction to the spreading loss is added to the inverse distance law. The effect of (de)focusing can be evaluated by comparing two rays launched at the same time in homogeneous, and non-homogeneous atmosphere. This is illustrated by Figure 3.13.

Ray tubes are evaluated by launching two rays with incremental different launch angle $\Delta\theta$. This results in increasing tube area A over time dt and distance s. As the ray tracing is only performed in two dimensions (x and z), the out-of-plane separation angle $\Delta\lambda$ remains constant.

Different ray tubes relate to each other by the Blokhintzev invariant [62] presented in Equation (3.29) in which p is the pressure, $|v_{ray}|$ is the velocity magnitude, A_{ray} is the ray tube area, ρ is the local air density, c is the local speed of sound and Ω is the wind vector. Using the geometry of Figure 3.13, the ray tube areas are defined as Equation (3.30) in which γ is the seperation distance determined by Equation (3.31).

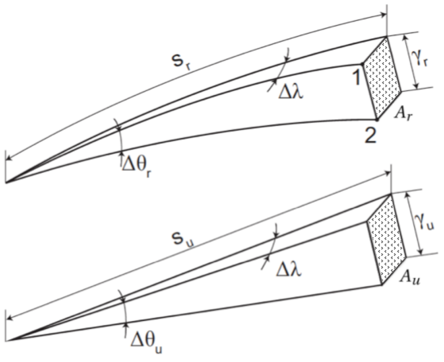

Figure 3.13: Geometry of refracted (r) and straight (u) ray tubes. Adapted from [26].

$$\frac{p^2 \cdot |v_{ray}| \cdot A_{ray}}{\rho \cdot c^2 \cdot \Omega} = \text{constant} \tag{3.29}$$

$$\begin{aligned} A_u &= \gamma_u \cdot s_u \cdot \Delta\lambda \\ A_r &= \gamma_r \cdot s_r \cdot \Delta\lambda \end{aligned} \tag{3.30}$$

$$\begin{aligned} \gamma_u &= 2 \cdot s_u \cdot \tan\left(\frac{\Delta\theta_u}{2}\right) \\ \gamma_r &= \sqrt{(x_1 - x_2)^2 + (y_1 - y_2)^2} \end{aligned} \tag{3.31}$$

From the Blokhintzev variant, the additional correction on the inverse distance law following the effect of refraction is presented in Equation (3.32) [27]. Although strictly speaking the expression is only valid for stationary atmosphere, for wind velocities under 15 kts (≈ 7.7 m·s^{-1}), this expression is still valid [62].

$$TL_{S_r} = 10 \cdot \log_{10}(\frac{\rho_u \cdot c_u^2 \cdot A_r}{\rho_r \cdot c_r^2 \cdot A_u}) \tag{3.32}$$

For refracting and straight ray tubes near the ground where the wind velocity $V_W \approx 0$, the local speed of sound and air density are taken equal for both refracting and straight ray tubes [62]. With this simplification, the total spreading loss in refracting atmosphere is expressed as Equation (3.33).

$$TL_S = 10 \cdot \log_{10}(\frac{A_r}{A_u}) + 20 \cdot \log_{10}\left(\frac{s}{s_0}\right) \tag{3.33}$$

In order to determine the ray tube area of the refracted ray A_r, the separation distance of the refracted ray tube γ_r is required. To determine this distance, two sound rays are shot until they both arrive at the receiver height. The direct shot arrives at the receiver, while the second ray is shot at incrementally larger launch angle below the direct ray, covering a shorter ground distance x. The second ray can also be launched at an incrementally smaller launch angle, however there is a chance that the second ray arrives in the shadow zone if the receiver is located on or very near the shadow zone.

Interpolation is used to find the ray location of the first ray at the time the second ray arrived at the receiver height. The j^{th} atmospheric layer in which the $t_{2,f} > t_{1,j}$ is used for the interpolation to determine the ground distance x_1 and altitude z_1 is expressed by Equation (3.34).

$$\begin{aligned} x_1 &= x_{1,j-1} + \left(x_{1,j} - x_{1,j-1}\right) \cdot \frac{t_{2,f} - t_{1,j-1}}{t_{1,j} - t_{1,j-1}} \\ z_1 &= z_{1,j-1} + \left(z_{1,j} - z_{1,j-1}\right) \cdot \frac{t_{2,f} - t_{1,j-1}}{t_{1,j} - t_{1,j-1}} \end{aligned} \tag{3.34}$$

The arrival time of the ray is determined by defining the travel time along the ray in the i^{th} atmospheric layer, as presented by Equation (3.35) in which with $c_i(z)$ is the linearised speed of sound profile in the layer. Rewriting this equation as a function of incidence angle θ, Equation (3.36) is obtained. Evaluating the integral within the layer i, Equation (3.37) is obtained.

$$t_i = \int_0^{s_i} \frac{1}{c_i(z)} ds_i, \qquad \text{with} \quad c_i(z) = c_{0,i} + G_{lin,i} \cdot z, \quad ds_i = R_i d\theta \tag{3.35}$$

$$t_i = \int_{\theta_{0,i}}^{\theta_{f,i}} \frac{R_i}{c_{0,i} - G_{lin,i} \cdot z_{c,i} - G_{lin,i} \cdot R_i \cdot \cos(\theta)} d\theta \tag{3.36}$$

$$t_i = 2 \cdot |R_i| \cdot \tanh^{-1}\left(\frac{(a-b) \cdot \tan\left(\frac{1}{2}\theta\right)}{\sqrt{a^2 - b^2}}\right) \frac{1}{\sqrt{a^2 - b^2}}\Bigg|_{\theta_{0,i}}^{\theta_{f,i}}, \qquad \text{with} \quad a = -G_{lin,i} \cdot R_i, \quad b = G_{lin,i} \cdot z_{c,i} + c_{0,i} \tag{3.37}$$

Since the final position of the second ray is known, Equation (3.30) and Equation (3.31) is evaluated to determine the spreading loss TL_S in Equation (3.33).

Atmospheric Attenuation Loss.
Besides the spreading loss, the sound waves loses energy through internal friction by travelling through the air. To express this atmospheric absorption, typically the sound attenuation coefficient α is used. The coefficient defines the loss in Sound Pressure Level (SPL) per 100 m.

Generally, the attenuation coefficient is determined using the procedure described by the *ICAO* in [63] and is discussed in the next paragraph.

The expression used to determine the transmission loss due to atmospheric attenuation within one atmospheric layer is presented by Equation (3.38) in which T is the local air temperature in °C and RH is the local relative air humidity in %. An adjustment is made for frequencies higher than 4000 Hz, the so-called adjusted frequency f_a, to evaluate the attenuation coefficient. The adjustment to the 4, one-third octave frequency bands is presented in Table 3.3. Interpolation between the frequencies f is used to find the right adjusted frequency f_a for the Doppler frequency shifted frequencies. Lastly, the $\eta(\delta)$ is obtained from Table A1.5 in [63].

$$\begin{aligned} TL_A &= \frac{\alpha \cdot s}{100} \\ &\text{with:} \\ \alpha &= 10^{\left[2.05 \log_{10}\left(\frac{f_a}{1000}\right) + 1.1394 \cdot 10^{-3} T - 1.916984\right]} + \eta(\delta) \cdot 10^{\left[\log_{10}(f_a) + 8.42994 \cdot 10^{-3} T - 2.755624\right]} \\ \delta &= \sqrt{\frac{1010}{f_a}} 10^{\left[\log_{10} RH - 1.328924 + 3.179768 \cdot 10^{-2} T\right]} \cdot 10^{\left[-2.173716 \cdot 10^{-4} T^2 + 1.7496 \cdot 10^{-6} T^3\right]} \end{aligned} \tag{3.38}$$

Table 3.3: Adjusted frequency f_a to evaluate the atmospheric attenuation coefficient [63].

f [Hz]	f_a [Hz]
5000	4500
6300	5600
8000	7100
10000	9000

In the layered atmosphere, each layer has a different attenuation coefficient due to varying air temperature. As the local air temperature and humidity gradients within one layer is constant, the average temperature and relative humidity in the layer is used to calculate the attenuation coefficient. The summation of all TL_A in each layer result in the resulting transmission loss due to atmospheric attenuation.

To illustrate the difference in attenuation coefficient per air temperature, relative humidity and sound frequency combination, Figure 3.14 presents the atmospheric attenuation coefficient for different frequencies.

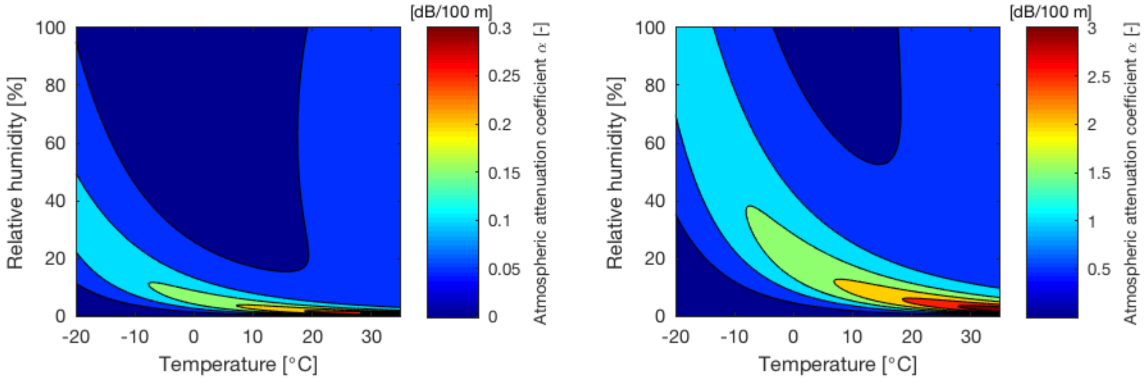

(a) f_a = 100 Hz. **(b)** f_a = 500 Hz.

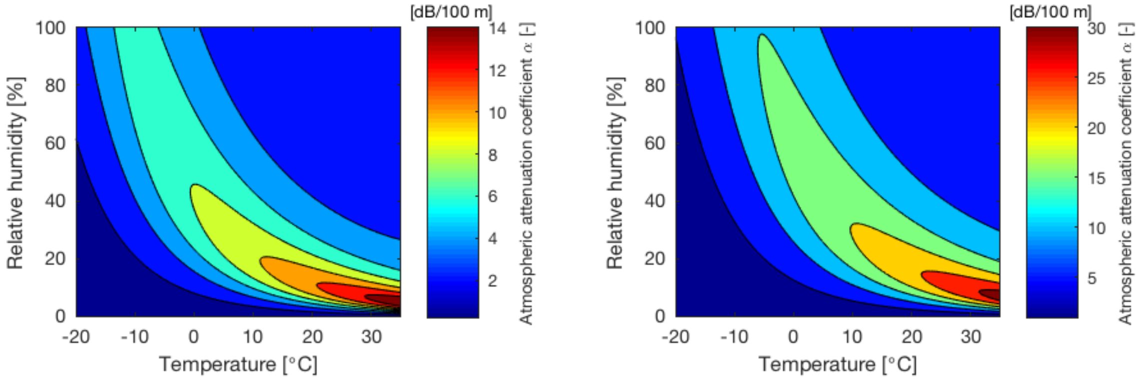

(c) f_a = 4500 Hz. **(d)** f_a = 9000 Hz.

Figure 3.14: Atmospheric attenuation coefficient α for varied temperature and relative humidity for adjusted frequency $f_a = 100, 1000, 4500$ and 9000 Hz. Note the difference in scale.

It is observed that the attenuation coefficient per frequency is generally the highest for a combination of high air temperature and low relative humidity. Once the relative humidity is below 1% the the attenuation coefficient is nearly 0 for any air temperature. With increasing frequency, the absolute value of the attenuation coefficient increases. Furthermore, the curve on which higher attenuation coefficients is found becomes steeper with increasing frequency.

In ISA conditions with sea level temperature of 15 °C and frequently employed relative humidity of 70%, a relatively low atmospheric attenuation is obtained. A higher attenuation coefficient for higher frequencies implies that the higher frequencies lose more of their energy with increasing distance compared to lower frequencies.

Ground Reflection.
Sound rays are reflected on the ground resulting in the observer receiving multiple sound rays. Depending on the phase difference and the amplitude of the direct and reflected ray, the sound is constructively or destructively interfered. To illustrate effect of rays arriving at different phases, the red wave in Figure 3.15 illustrates constructive interference, while the blue wave illustrates destructive interference.

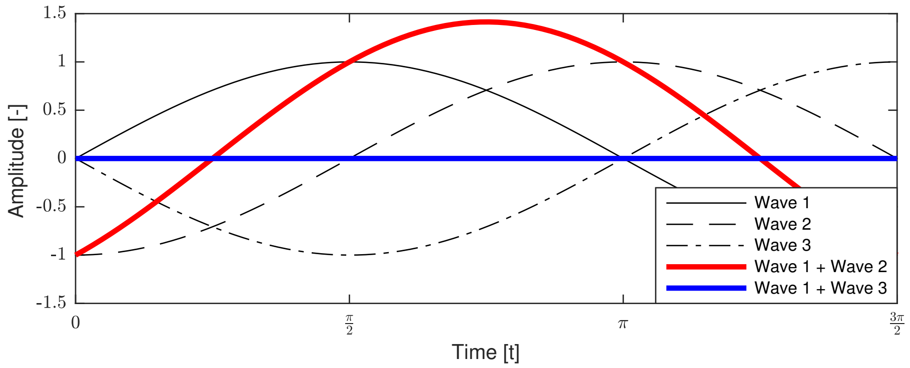

Figure 3.15: Constructive (red) and destructive (blue) interference of two sound rays arriving at the observer at different time instances.

In essence, the transmission loss due to the effect of ground interference TL_G is determined by subtracting the free field SPL from the actual received SPL. This is mathematically presented by Equation (3.39) [27]. The respective effective sound pressure is denoted as p_e.

$$\begin{aligned} TL_G(s,\theta) =& SPL_{actual}(s,\theta) - SPL_{free}(s,\theta) \\ =& 10\log_{10}\left(\frac{p^2_{e,actual}}{p^2_{e,0}}\right) - 10\log_{10}\left(\frac{p^2_{e,direct}}{p^2_{e,0}}\right) \end{aligned} \tag{3.39}$$

In order to determine the amplitude and phase difference between both rays, the geometry of the problem in a homogeneous atmosphere for a stationary source at height z_s for a flat ground surface with a small roughness length compared to the wavelength is presented in Figure 3.16. In the figure, z_r is the receiver height and s_1 is the direct ray distance determined by summing Equation (3.27) over each atmospheric layer. As the receiver height is relatively close to the ground, refraction over the reflected ray can be neglected resulting in Equation (3.40) to determine the indirect ray distance s_2.

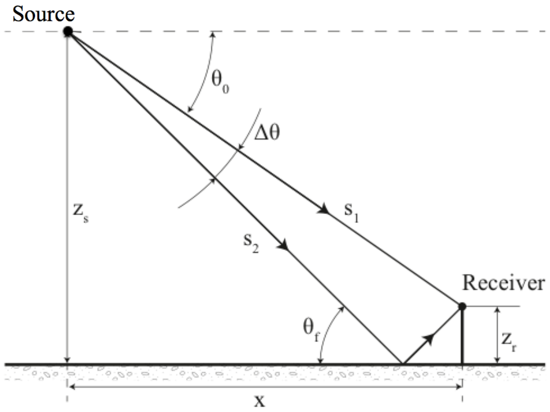

Figure 3.16: Ground reflection geometry. Adapted from [26].

$$s_2 = s_1 + 2\cdot z_r \cdot \sin\left(\theta_f\right) \tag{3.40}$$

The sound pressure received by the receiver is the summation of the sound pressure level of the direct and indirect ray and is presented as Equation (3.41) [27, 64]. In this expression A is the source strength or amplitude, ω is the angular velocity of the source ($= 2\cdot\pi\cdot f$) using the Doppler shifted frequency, c is the local speed of sound and Q is the reflection factor. Integrating Equation (3.41) over time and substituting $Q = |Q|e^{i\phi}$ in order to evaluate the amplitude and phase change, results in Equation (3.42): the effective sound pressure at the receiver.

$$p'(s,t) = \frac{A}{s_1}\cdot e^{i\cdot\omega\cdot\left(t-\frac{s_1}{c}\right)} + Q\cdot\frac{A}{s_2}\cdot e^{i\cdot\omega\left(t-\frac{s_2}{c}\right)} \tag{3.41}$$

$$p_e(s) = \sqrt{\frac{A^2}{2s_1^2} + |Q|^2\cdot\frac{A^2}{2s_2^2} + |Q|\cdot\frac{A}{s_1\cdot s_2}\cdot\cos\left(\omega\cdot\frac{s_2-s_1}{c}+\phi\right)} \tag{3.42}$$

The effective sound pressure of the direct ray is defined as $p_{e,direct}(s) = \frac{A}{s_1 \cdot \sqrt{2}}$ [64]. Substituting this into Equation (3.42), Equation (3.43) is obtained. This expression has a format which allows Equation (3.39) to be rewritten into Equation (3.44).

$$p_e(s) = p_{e,direct}(s) \cdot \sqrt{1 + \left(\frac{s_1}{s_2}\right)^2 \cdot |Q|^2 + 2 \cdot \frac{s_1}{s_2} \cdot |Q| \cdot \cos\left(\omega \cdot \frac{s_2 - s_1}{c} + \phi\right)} \tag{3.43}$$

$$TL_G(s,\theta) = 10 \cdot \log_{10}\left[1 + \left(\frac{s_1}{s_2}\right)^2 \cdot |Q|^2 + 2 \cdot \frac{s_1}{s_2} \cdot |Q| \cdot \cos\left(\omega \cdot \frac{s_2 - s_1}{c} + \phi\right)\right] \tag{3.44}$$

By resubstituting $|Q|e^{i\phi} = Q$, the final expression for the transmission loss due to ground interference TL_G is obtained and presented in Equation (3.45).

$$TL_G = 20 \cdot \log_{10}\left|1 + \frac{s_1}{s_2} \cdot Q \cdot e^{i \cdot k \cdot (s_2 - s_1)}\right| \quad \text{with} \quad k = \frac{\omega}{c} \tag{3.45}$$

The reflection coefficient Q is the last unknown to determine and is dependent on the surface impedance. The surface impedance Z_g is the ratio of the sound pressure p' to the velocity of the air particles v_g at one point on the surface [26]. Based on the surface impedance, *Chessell* [64] derived an expression for the reflection coefficient presented in Equation (3.46). In this expression, ρ_0 and c_0 are the respective density and speed of sound at the surface. This expression holds together with the assumption that the plane wave theory applies and that the ground can transmit sound in lateral direction as sound does in fluids.

For surfaces used in aviation noise modelling, it is assumed that the ground surface is locally reacting. This implies that the lateral component of propagation into the ground can be neglected [64] and the normal surface impedance Z_n can be used. This implies that the velocity of the air particles at the ground v_g and the resulting incidence angle into the ground θ_g, illustrated by Figure 3.17, is replaced by v_n and θ_n. The final expression obtained for Q is presented by Equation (3.47).

$$Q = \frac{\frac{Z_g}{\rho_0 \cdot c_0} \sin(\theta_f) - \sin(\theta_g)}{\frac{Z_g}{\rho_0 \cdot c_0} \sin(\theta_f) + \sin(\theta_g)} \tag{3.46}$$

$$Q = \frac{\frac{Z_n}{\rho_0 \cdot c_0} \sin(\theta_f) - 1}{\frac{Z_n}{\rho_0 \cdot c_0} \sin(\theta_f) + 1} \tag{3.47}$$

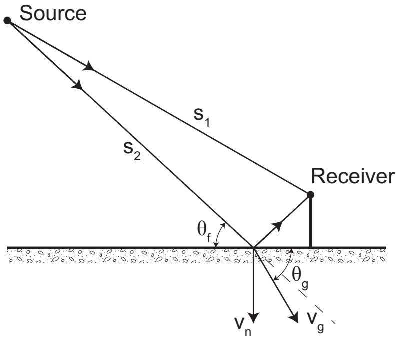

Figure 3.17: Reflection and refraction on a ground surface [26].

The specific normal acoustic impedance $\frac{Z_n}{\rho_0 \cdot c_0}$ is expressed as a function of effective flow resistivity σ and frequency f according to the relation presented by Equation (3.48) [65].

$$\frac{Z_n}{\rho_0 \cdot c_0} = 1 + 0.0511 \cdot \left(\frac{f}{\sigma}\right)^{-0.75} + i \cdot 0.0768 \cdot \left(\frac{f}{\sigma}\right)^{-0.73} \tag{3.48}$$

Example flow resistivity σ values is obtained from Table 1 of [66] and Table 3 of [67] and are presented in Table 3.4 to illiterate the magnitude for different ground surfaces.

Table 3.4: Flow resistivity of different terrains [66, 67].

Surface characteristics	**Flow resistivity** σ $[10^3 \cdot \mathrm{N{\cdot}s{\cdot}m^{-4}}]$
Snow	1-30
High crops, hedges and shrubs	40 - 50
Loose sand and dry cultivated soil	30 - 140
Tall grass on level ground	70 - 850
Wet and compact soil	4,000 - 8,000
Quarry dust	5,000 - 20,000
Asphalt	up to 30,000

Shadow Zones.

When sound rays are refracted downwards by the effect of the negative speed of sound gradient, shadow zones exists as is presented in Figure 2.2. No direct rays reach the shadow zone, however low SPLs are observed in the shadow zone. This is mainly caused by reflected rays by the ground surface, diffraction, and scattering due to turbulence.

The SPLs in the shadow zone is required to be evaluated to allow for continuity within the gradient-based optimisation scheme. To do so, first the boundary between the illuminated and shadow zone is identified. Next it is identified whether the observer is in the shadow zone or not. If so, the SPL in the shadow zone is determined.

At the boundary between the illuminated and shadow zone, the ray launched at launch angle θ_{sz} reaches a final incidence angle $\theta_f = 0$ at the receiver height z_r as is illustrated by Figure 3.18. The shadow zone starts beyond this point. The lowest atmospheric layer j determines where the boundary is exactly located.

Rewriting the ray equations of Equation (3.23) to Equation (3.27), an equation is derived that determines the launch angle within the atmospheric layer depending on the characteristics of the layer. The derived expression is presented by Equation (3.49). Starting from $\theta_{0,j}$, propagating upwards through the layers, the limiting launch angle θ_{sz} is obtained. Based on the launch angle θ_{sz}, the ray equations are evaluated again to determine the distance x_{sz} from the source where the shadow zone starts.

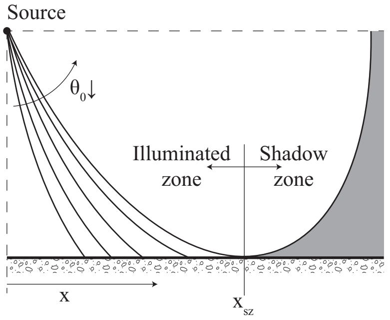

Figure 3.18: The boundary between the illuminated and shadow zone [26].

$$\theta_{0,i} = \cos^{-1}\left(\frac{\Delta z_i - \frac{c_i}{g_i}}{-\frac{c_i}{g_i}}\right) \tag{3.49}$$

If the receiver is in the shadow zone ($x_r > x_{sz}$), first the transmission losses due to spreading, atmospheric attenuation and ground reflection up to the shadow zone ($\left.\right|_{sz}, x = x_{sz}$) are determined using the methods described in the previous sections.

Within the shadow zone, losses are determined using a procedure described by [56]. When entering the shadow zone, a linear diffraction correction L_{sz} is added to the transmission losses up to the shadow zone. This loss correction only depends on the frequency and local gradient of the speed of sound in layer n, in between the receiver height z_r and the ground. The linear correction is introduced by Equation (3.50). The linear diffraction correction only accounts for the transition when entering the shadow zone and is bounded to a maximum loss of 30 dB [26].

$$L_{sz} = L_{d1} \cdot L_{d2}\,(x - x_{sz}), \quad \text{with:} \quad \begin{aligned} L_{d1} &= -\,0.0032 - 3.5 \cdot 10^{-5} \cdot f \\ L_{d2} &= 6.7 \cdot G_{lin,n} + 0.31 \end{aligned} \tag{3.50}$$

For the additional distance between the boundary of the shadow zone and the observer in the shadow zone, atmospheric attenuation loss is accounted for. The atmospheric loss in the shadow zone $TL_{A,sz}$ assumes that the ray travels parallel to the ground in layer n.

In case the diffraction correction L_{sz} exceeds the loss of 30 dB, instead of using the spreading loss up till the shadow zone $TL_S\Big|_{sz}$ and the atmospheric spreading in the shadow zone $TL_{A,sz}$, spherical spreading and atmospheric attenuation over the entire ground distance x is used to determine the loss together with a 30 dB diffraction correction loss [26]. This result in the final expression for the transmission loss in the shadow zone TL_{sz}, expressed by Equation (3.51).

$$TL_{sz} = \begin{cases} (TL_S + TL_A + TL_G)\Big|_{sz} + L_{sz} + TL_{A,sz}, & \text{if} \quad L_{sz} > -30\text{dB} \\ (TL_A + TL_G)\Big|_{sz} - 20 \cdot \log_{10}(x) + \frac{\alpha \cdot x}{100} - 30, & \text{if} \quad L_{sz} \leq -30\text{dB} \end{cases} \tag{3.51}$$

Total Noise Levels.
The addition of all transmission losses added to the initial source noise result in the observed sound levels. This is illustrated by Equation (3.52).

$$\begin{aligned} SPL(f) &= SPL(f)_A + TL_S + TL_A + TL_G, && \text{if observer is in the illuminated zone.} \\ SPL(f) &= SPL(f)_A + TL_{sz}, && \text{if observer is in the shadow zone.} \end{aligned} \tag{3.52}$$

As discussed in Section 2.2.2, the sensitivity of the human ear is not equally spread over the frequency domain. Thus an additional A-weighting correction is applied additionally to the losses. This expression is presented by Equation (3.54), in which L_A is the A-weighted sound level computed using Equation (3.53), in which f is the Doppler shifted frequency of the received sound [27].

$$\Delta L_A(f) = -145.528 + 98.262 \log_{10}(f) - 19.509(\log_{10}(f))^2 + 0.975(\log_{10}(f))^3 \tag{3.53}$$

The sound pressure level observed is expressed by Equation (3.52). The final A-weighted expression for the A-weighted sound level is presented by Equation (3.54).

$$L_A = 10 \cdot log_{10} \sum \left(10^{L_A(f)}\right), \quad \text{with} \quad L_A(f) = SPL(f) + \Delta L_A(f) \tag{3.54}$$

Assumptions and limitations to the propagation model.
With the implementation of the propagation model, assumptions are made and accordingly, there are limitations to the model. The following list summarises the limitations to the model.

- Flat Earth is assumed, resulting in ground reflection only by flat surfaces. Furthermore the ground can transmit sound in lateral direction. In mountainous areas, the ground reflected rays can be traced using ray equations presented by *Lamancusa* and *Daroux* [62]. However, this becomes increasingly difficult with mountains having erratic slopes.
- The simplification of the the wind velocity $V_W \approx 0$ near the ground used to determine the focusing and defocusing for the spreading loss only holds for wind velocities up to 15 kts. *Lamancusa* and *Daroux* discuss methods in which the simplifications are not made making it possible to evaluate (de)focusing for higher wind velocities [62]. However the method is more complex and for this study, the effect of the wind can be clearly distinguished. Furthermore, it can be assumed that a stronger wind will show a similar behaviour on sound propagation as when the wind is increased up to 15 kts.
- Plane wave theory is assumed meaning that the sound wave's wavefront are infinitely parallel.
- It is assumed that sound ray travels parallel to the ground in the atmospheric layer between the observer height z_r and the ground in the shadow zone.

3.5. Noise Impact Model

To quantify the noise impact due to the received noise on the ground, a noise impact model is employed. Several measures exist to quantify noise impact. Often used measures are the day-evening-night average sound level L_{den}, peak noise level $L_{A,max}$ and the Sound Exposure Level (SEL) which is the total sound exposure normalised to 1 s.

As the name suggests, L_{den} is the total sound level received divided over a 24 hour period. Noise levels in the evening and night time receive an additional penalty value added on top of the sound level to compensate for the increased annoyance. L_{den} is most suitable to analyse the total average sound received over a longer period of time. However, due to its average nature, loud and unacceptable noise events might be hiding within an acceptable L_{den} value. Furthermore, L_{den} does not apply to single noise events.

The peak noise value $L_{A,max}$ does not consider the duration of the sound exposure, whilst the SEL integrates the L_A value received during one noise event and normalises this value to 1 s. This allows for the comparison of noise events of different duration. It is very suitable for the comparison of different single noise events as both the peak value as well as the exposure time is contained within this metric. The normalisation of the L_A over time is illustrated by Figure 2.7, and is expressed by Equation (3.55).

$$SEL = 10\log_{10}\left(\frac{1}{t_{SEL}}\int_0^T 10^{\frac{L_A(t)}{10}}\,dt\right), \qquad \text{with } t_{SEL} = 1 \tag{3.55}$$

Previous studies using SEL as noise metric have minimised the noise contour areas for SEL values above a certain threshold, minimised the number of awakenings due to the noise event and minimised the total population exposed to SEL values above a certain threshold [16, 17, 26, 34, 35].

Minimising for the noise contour area resulted in optimised trajectories very close to the ground. Lateral attenuation ensured that only narrow bands of high noise contour areas reached the ground close to the aircraft. This implies large noise impact for a limited area, which is undesirable as a relative small area is encountering a high noise impact.

Expected awakenings are determined using dose-response relationships and are based on indoor SEL values. Often used dose-response relationships in research are the "maximum percent of the exposed population expected to be behaviourally awakened", determined by the Federal Interagency Committee on Aviation Noise (FICAN) [21]. The FICAN dose-response relation is presented in Equation (3.56) and is based on a field research and laboratory measurements of which the results are presented in Figure 3.19. The American National Standards Institute (ANSI) has since then published a revised version of this relationship [68, 69] and is presented in Equation (3.57). The ANSI dose-response relationship has a lower slope when compared to the FICAN dose-response relationship and indoor SEL values below 50 dB are disregarded. In a typical home with an average transmission loss, the indoor SEL is 20.5 dB lower than the outdoor SEL [16, 17].

The total number of awakenings N_A is the summation of the percentage awakenings A times the people living in the grid point p_n.

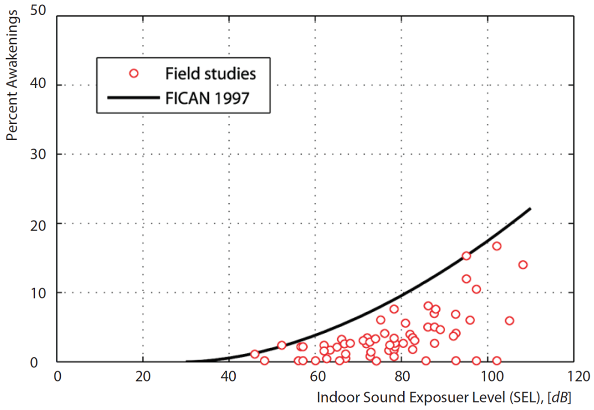

Figure 3.19: FICAN dose-response relationship [21].

$$A_{FICAN} = 0.0087 \cdot (SEL_{ind} - 30)^{1.79} \tag{3.56}$$

$$A_{ANSI} = \frac{1}{1+e^{-Z}}$$

with:

$$Z = (-6.884 + 0.04444 \cdot SEL_{ind}) \tag{3.57}$$

$$N_A = \sum_{n=1}^{N} A \cdot 100 \cdot p_n \tag{3.58}$$

With the revision of the FICAN dose-response to the ANSI dose-response curve, the American National Standards Institute advised the use of the ANSI dose-response curve to analyse existing trajectories for awakenings, and the use of the FICAN dose-response curve to assess noise impact for new trajectories. Whilst the FICAN dose-response results in the maximum percentage of expected awakenings, the ANSI dose-response results in a more realistic number of awakenings. However people tend to experience larger noise impact for new noise events to which they are not accustomed to. Thus the use of the higher expected awakenings is fair.

In this research, as non-existing trajectories will be evaluated, the FICAN dose-response relationship is used to evaluate the noise impact.

Implementation of Source Noise in GPOPS.
The number of awakenings is linked to the source noise level, which is again relate to the thrust level. The thrust level is a function of among others, the state variables altitude z and velocity V, and control variable thrust setting η. This implies that an additional derivative term is required to the awakenings derivative in the cost function.

The respective derivatives terms of the $\frac{dT_n}{dx}$ and $\frac{dT_n}{du}$ are automatically differentiated by the automatic differentiaton tool INTlab within MATLAB when the thrust level is determined. The additional derivatives $\frac{dA}{dT_n}$ is obtained from the propagation model. The resulting derivative of the awakenings over the state variables and control variables is presented in Equation (3.59).

$$\frac{dA}{d\bar{x}} = \begin{bmatrix} \frac{dA}{dx} \\ \frac{dA}{dy} \\ \frac{dA}{dz} + \frac{dA}{dT_n} \cdot \frac{dT_n}{dz} \\ \frac{dA}{dV} + \frac{dA}{dT_n} \cdot \frac{dT_n}{dV} \\ \frac{dA}{d\chi} \\ 0 \end{bmatrix}, \qquad \frac{dA}{d\bar{u}} = \begin{bmatrix} \left(\frac{dA}{dT_n} \cdot \frac{dTn}{d\eta} \right) \\ 0 \\ 0 \end{bmatrix} \tag{3.59}$$

3.6. Geographic Information System

In order to make the optimisation site-specific and include the population information in the optimisation, the Geographic Information System (GIS) provided by the Statistics Netherlands (Centraal Bureau voor de Statistiek (CBS)) is used. The GIS ensures that distinction is made between densely populated and rural areas. The framework makes use of population data of 2017 [70]. The total population count of the Netherlands is nearly 16.5 million.

The information provided by the CBS holds information regarding population, household income and other demographic information per 100 x 100 m cell. The coordinates of each cell is expressed in the local Dutch Rijksdriehoeks Cartesian coordinate system and ranges from $x = [13.8, ..., 277.2]$ km and $y = [306.9, ...611, 4]$ km. The coordinate system is set-up such that any point in the Netherlands has positive coordinates and the smallest y-coordinate is always larger than the largest x-coordinate.

In order to reduce computational time while maintaining the spread in decreasing population density of larger cities, the cells have been enlarged to cells of 1 x 1 km. The total population is combined into one point in the centre of the cell. An example of the population density of part of the Randstad of the Netherlands is presented in Figure 3.20. For illustration, the runways of Amsterdam Schiphol airport are depicted as well. Furthermore, large cities and their suburb can be clearly distinguished.

Evaluating the sound received at each cell is not necessary as the sound received for an aircraft taking off in northern direction for instance does not bother the population living in Rotterdam. The FICAN dose-response relationship holds a threshold SEL value of 50.5 dB as minimum sound level for awakenings.

Use is made of a filter that reduces the amount of cells to be evaluated based on the slant range between observer and aircraft and the amount of sound propagation losses received along the slant range. The latter varies per atmospheric condition, and reduces the total number of observers in a grid of 1 x 1 km with more than 1000 population, from 4324 to roughly 100 to 200 observers per evaluation.

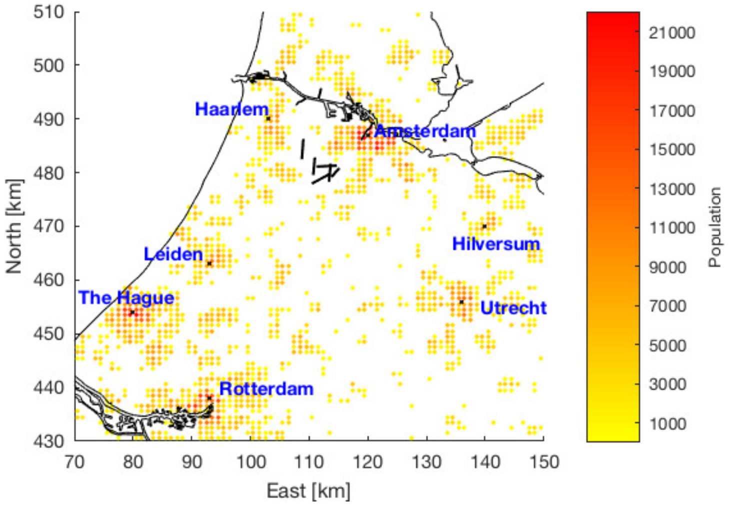

Figure 3.20: Population density of part of the Randstad of the Netherlands for a 1 x 1 km grid with population density larger than 1000 per 1 km^2.

3.7. Flow within the WAFORT framework

From a high-level perspective, the framework of WAFORT consists of four main blocks, as is presented by Figure 3.21. Within the core of the program, the GPOPS optimisation software ensures that all information received is translated into a problem definition and solves the problem. In the following paragraphs, each block is elaborated upon.

Problem statement. To define the problem statement, the case has to be set-up. This is performed by bounding the environment in which the optimisation is performed. Furthermore, the number of case parameters and phases are determined. If required, event and path constraints are generated. The initial guess is of importance as the optimisation algorithm starts its search for the minimum in the vicinity of the initial guess. To obtain physically feasible optimal state and control variables, both variable types are bounded.

Input data. Besides the problem statement, input data is required to obtain necessary information about the aircraft and cost function. With aircraft data as input, WAFORT is not limited to the evaluation of only aircraft type or configuration only. Depending on the aircraft type, the initial guess and the state and control bounds need to be reevaluated.

The cost function in the WAFORT model used for this research consists of awakenings and fuel as presented by Equation (3.60). The k values denote the weighting factor of each part to the cost function. Obviously, the noise impact is evaluated by the total number of expected awakenings of the local community. However, the airlines choose to fly the optimised trajectories. In order to obtain economically viable trajectories, a fuel usage parameter is included.

$$J = k_{noise} \cdot \text{awakenings} + k_{fuel} \cdot \int_0^{t_f} \dot{m}_{fuel} dt \tag{3.60}$$

In the cost function of Equation (3.60), the initial part of the awakenings form the Mayer form (Φ). The fuel usage is the Lagrange form ($\mathscr{L}$).

Models. Running the Aircraft Performance Model (APM) and the sound propagation model, the noise impact is evaluated using the Geographic Information System (GIS). Depending on the aircraft type and cost function, different results are obtained. This information is sent to the GPOPS to evaluate whether the optimal solution has been obtained. If not, a new trajectory to be evaluated by the models is received from the GPOPS.

Results. The optimal solution is divided into the optimal state, control and time vector. In the final block, these optimal vectors are translated into total number of awakenings, the optimal flight trajectory and the total fuel consumed.

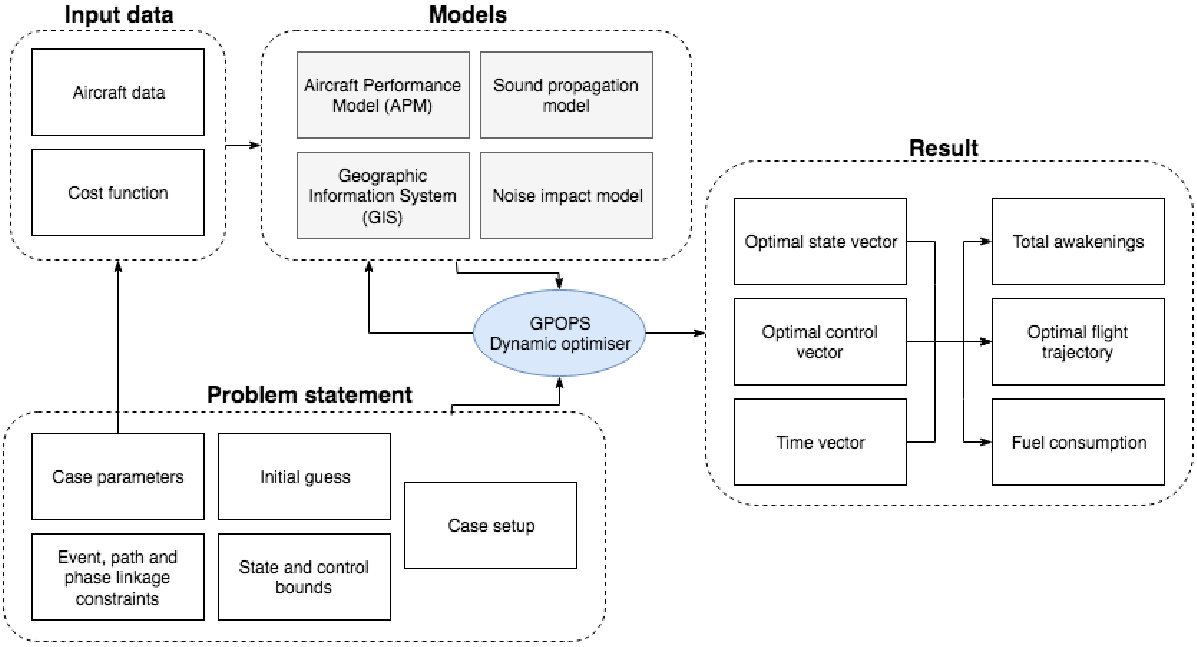

Figure 3.21: Flowchart within the Weather-Adaptive Flight Optimisation Research Tool.

3.8. Limitations of the WAFORT

With the introduction of the WAFORT model and its modelling, it is of importance to understand what problems the tool can be used for, and what limitations there are present. The following list summarises the limitations of the tool.

- The combined effect of the simplifications and assumptions taken in each model cannot be quantified. However since all models are verified and validated, the impact should be negligible.
- The APM is only dependent on temperature. In reality, the relative humidity also contribute to engine performance.
- Both aircraft and source noise are simplified to a point model, meaning that the aircraft is not a rigid body anymore. Difference with the rigid body model might be encountered when the aircraft is performing manoeuvres where both engine installation angle influences thrust and sound reflection on the aircraft might affect the sound propagation. However for this study, the accuracy of the point model is sufficient.
- The currently employed wind model is simple and does become obscure at higher altitudes. Once the model is used to evaluate higher altitudes than the 6000 ft used in this study, one might change the wind model to the Monin-Obukhov method [71] which is know to be more accurate at higher altitudes.
- To evaluate the increase in wind velocities with altitude, it is assumed that the boundary layer of the surface is not affected by obstacle turbulence. Obstacles are for example skyscrapers, forests and cities. Thus obstacles which could affect the horizontal wind profile are neglected.
- Use of awakenings to evaluate noise impact does not cover the annoyance during the day. However, no single-event noise evaluation criteria based on SEL exist. Noise during the day is mainly evaluated using multiple-event noise metrics, which take average noise levels over a certain period of time. The WAFORT model in its current form is not suitable to optimise for multiple-events.

4

Propagation Model Verification and Validation

4.1. Introduction

To investigate whether the behaviour of the sound propagation model is as expected in various different weather conditions, the obtained sound level and Sound Exposure Level (SEL) are analysed in more detail in Section 4.2. Since verification and validation are in this case closely related, they are discussed in parallel. The performance of the propagation model withing the total framework is discussed in Section 4.3.

4.2. Sound Level and Sound Exposure Level

The basis of the propagation model is based on the model developed by *Hartjes* [26] in which helicopter sound is propagated in non-standard atmosphere. In his work, *Hartjes* validated the propagation model against a ray tracing model [56], which was again validated against a Fast Field Program (FFP) in [57]. As there is no access to actual measurements, the results have not been compared against real data. In order to validate the adapted propagation model, the results are compared against the values obtained using the INM method [20]. As *Hartjes* modelled the helicopter sound up to frequencies of 560 Hz, it is of importance to identify how the larger frequencies behave in the propagation model. Furthermore the implementation of the Doppler frequency shift and its influence on the sound propagation is of interest to be identified.

In order to compare against the same atmospheric conditions, the temperature and relative humidity defined in the SAE-AIR-1845 are used in order to eliminate the acoustic impedance adjustment used in the INM [20]. Furthermore a constant velocity of 160 knots is used to eliminate the duration adjustment for exposure-based metrics.

First the L_A over time plots are analysed in Section 4.2.1 followed by the analysis of the SEL contours in Figure 4.2.2. The section is concluded by Section 4.2.3 commenting on the findings in the previous two sections.

4.2.1. Sound Level over Time

The L_A over time plots are used to evaluated the source noise levels and the sound level obtained by the WAFORT propagation model and the current standard using the INM. In order to compare both models, a straight flight is performed by a Boeing 737-300 aircraft model above flat ($z = 0$) grassland over a distance of 10 km with constant net corrected thrust T_n of 9500 lbf. This aircraft type is chosen as many previous studies on noise abatement have considered this aircraft type [16–19, 34, 35].

Furthermore, the same trajectory is flown at different aircraft velocities to identify the effect of the Doppler frequency shift. Validation is performed to identify what cause the difference in sound level received by the WAFORT propagation model and the INM model.

The INM propagation against WAFORT propagation. To test how the new propagation model in the WAFORT behaves against the INM L_A over time plots have been generated in Figure 4.1 for both propagation models for an observer at (0,0) and for different altitudes. The atmospheric conditions in the simulations match the assumptions taken in the INM.

The propagation model is validated by comparing the WAFORT propagation model against the INM. Three different altitudes are discussed in detail in order to discuss multiple phases of flight.

At 200 feet, Figure 4.1a, the observer is initially in the shadow zone. After 25 seconds, the observer enters the illuminated zone and starts to receive direct sound rays. INM does not consider a shadow zone and thus in the initial stage, the received L_A levels are much lower in the WAFORT propagation model.

The L_A levels for a straight fly over of an aircraft at 1000 ft is presented in Figure 4.1b. For both 200 and 1000 feet case, it is observed that the slope for the INM model is concave while the WAFORT propagation model has a more linear character in the illuminated zone. Furthermore, at the peak, some erratic behaviour is observed.

For the fly over at an altitude of 10000 ft, presented in Figure 4.1c, it is observed that the L_A levels in the WAFORT propagation model fluctuates on top of the L_A levels received. This is caused by the ground reflection, with reflected rays arriving in different phases at different moments in time. With decreasing altitude of the aircraft, the peaks concentrate near where the aircraft is directly overhead of the observer.

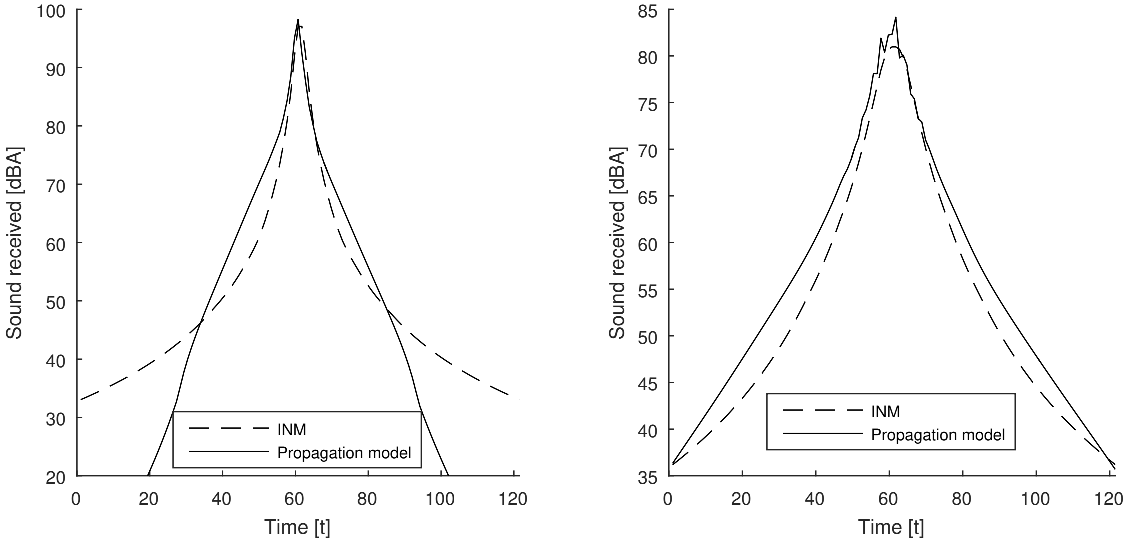

(a) $h = 200$ ft. **(b)** $h = 1000$ ft.

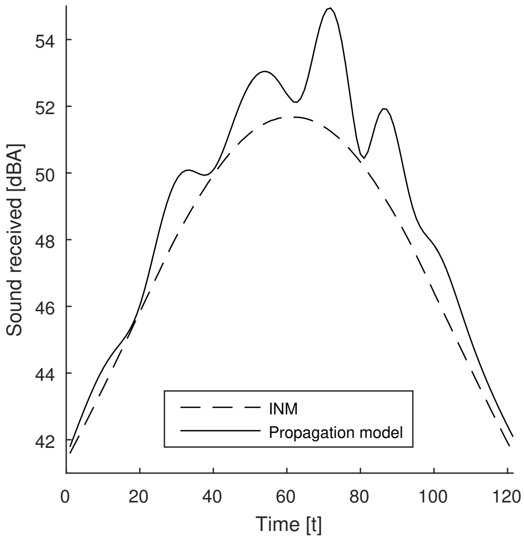

(c) $h = 10000$ ft.

Figure 4.1: Comparison of the INM and WAFORT propagation model of the L_A over time for a horizontal straight flight for different altitudes for an observer at (0,0) (v = 160 kts, T = 25°C, RH = 70%).

Source noise level. The implementation of the source noise level is tested by comparing the $L_{A,max}$ values of both propagation models as the source noise is obtained by manipulating the values in the ANP database, discussed in Section 3.4.1. The L_A over time plot in Figure 4.1 presents that the $L_{A,max}$ observed when the aircraft is directly overhead for the propagation model and the INM model are similar, except for the effect of the Doppler frequency shift and ground reflection.

Doppler effect. If the aircraft is flying towards the observer, the frequency of the sound increases, resulting in a higher atmospheric absorption loss. This implies that the noise received is lower when the aircraft is flying towards the observer, and higher if it flies away from the observer. The faster the aircraft is flying towards the observer, the higher the observed sound frequencies are.

To test the implementation of the Doppler frequency shift, the L_A over time for an aircraft at an altitude of 10000 ft for different aircraft velocities and different observer locations are analysed in Figure 4.2. 10000 ft is chosen as altitude as the effect of the frequency shift is larger with increasing altitude.

The frequency shift is clearly present when comparing the sound level at the start and the end of the fly over: the sound level for all observers are higher at the end of the fly over compared to the start. The influence of the difference in velocity is mainly noticeable due to the ground reflection as it is frequency dependant and thus also the ground reflection peaks are shifted with velocity. However the peaks are not larger as the ground surface is not altered. Thus lower total sound levels are obtained when the aircraft is flying faster.

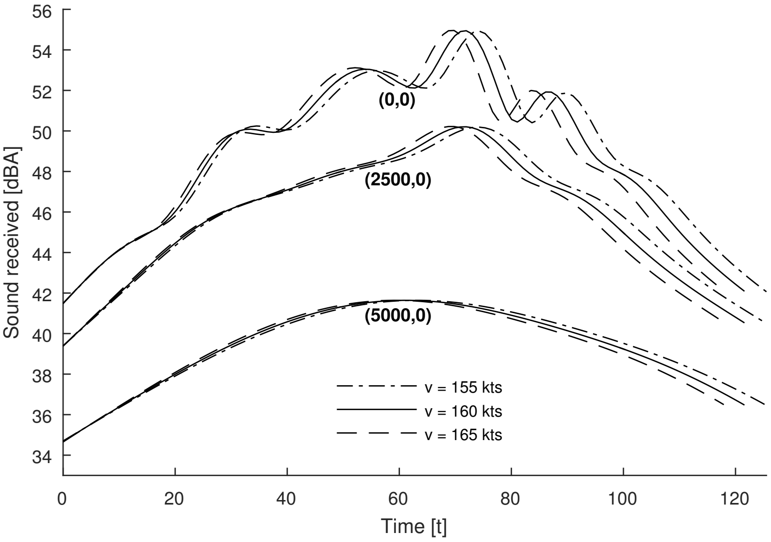

Figure 4.2: L_A over time received on the ground for a horizontal straight flight for different velocities and different observer locations (h = 10000 ft, T = 25°C, RH = 70%).

Validation of propagation model.
In nearly all cases when the observer is in the illuminated zone, the received L_A levels are higher in the WAFORT propagation model. This is caused by different modelling techniques for the ground reflection and due to the use of a different atmospheric attenuation coefficient. In order to understand what modelling differences exactly cause the different received sound levels, a detailed look is given for both the ground reflection and atmospheric attenuation in INM and the WAFORT propagation model.

Ground reflection. The INM incorporates the ground reflection as lateral attenuation adjustment and consists of ground reflection effects, refraction effects and aircraft shielding effects [20]. The ground is assumed to be flat. Furthermore, shielding effects are only present when the aircraft is banking. The correction factor is based on empirical parameters and the position of the aircraft with respect to the observer. The correction is limited to a maximum of 10.86 dB and is not a function of frequency. In the case of the observing standing underneath the flight path, the ground correction is 0.

In order to identify the influence of the ground reflection in the WAFORT propagation model, Figure 4.3 present the L_A over time plot with the inclusion and exclusion of ground reflection for a fly over at an altitude of 1000 and 10000 feet. The curves excluding ground reflection are smooth, and thus concluding that the peaks are caused by the ground reflection losses.

In Figure 4.3a it is observed that initially, the ground reflection loss increases the loss incurred. After 25 s until 85 s into the flight, the ground reflection loss is negative. A theoretical 6 dB increase can be noticed when two rays arrive exactly in phase at the observer. This implies that when the aircraft is flying straight to or from the observer, initially the complicated reflected ray traces increases the noise level received.

When the aircraft is travelling at a higher altitude, the ground loss is always negative as is illustrated by Figure 4.3b. With the increased altitude, the complicated reflected ray traces have expand over a larger area.

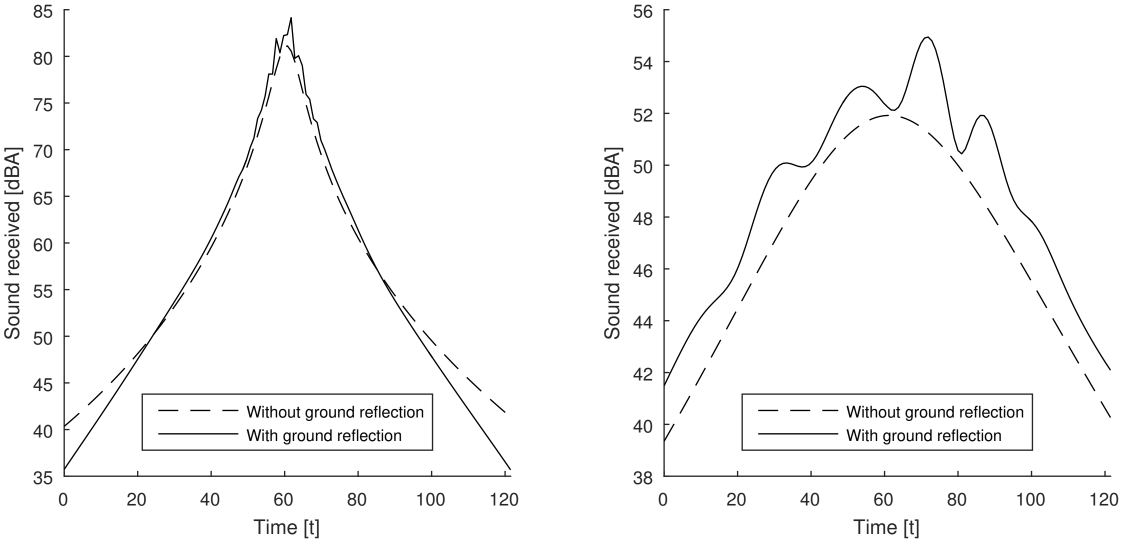

(a) h = 1000 ft. **(b)** h = 10000 ft.

Figure 4.3: L_A over time with and without the effect of ground reflection using the WAFORT propagation model for an observer at (0,0) (v = 160 kts, T = 25°C, RH = 70%).

While the effect of the ground reflection is now identified, this does however not answer why the propagation model used by the INM has a mainly concave slope while the WAFORT propagation model has a mainly linear slope. This difference is to be identified by analysing the atmospheric attenuation coefficient in more detail.

To analyse the influence of the ground surface type on the ground reflection, Figure 4.4 illustrates the sound levels received for multiple observers for grass and snow covered surfaces. A lower flow resistivity results in a higher ground reflection loss, and the peaks caused by constructive interference of different sound rays is smaller. Accordingly with increasing flow resistivity, a lower ground reflection loss and larger constructive interference is observed, which is theoretically limited to 6 dB.

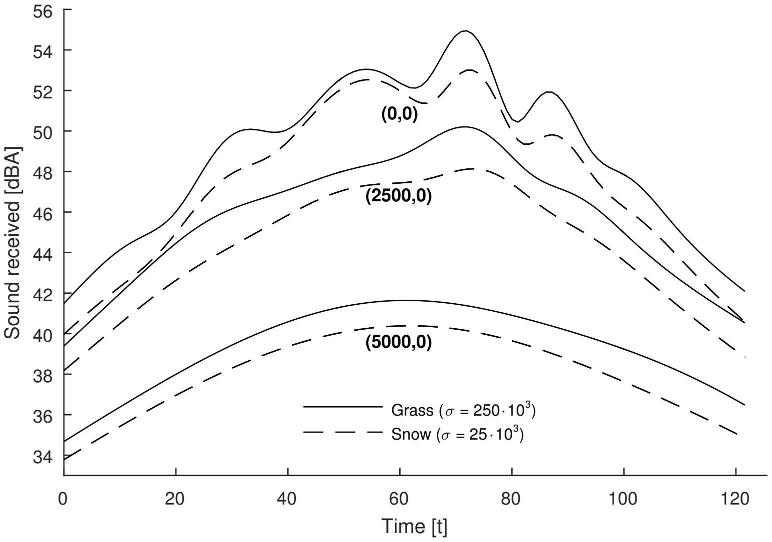

Figure 4.4: L_A over time received on the ground for a horizontal straight flight for different ground surface flow resistivity and different observer locations (h = 10000 ft, T = 25°C, RH = 70%).

Atmospheric attenuation. To analyse the difference in atmospheric attenuation losses, the modelling of the atmospheric attenuation coefficient α is analysed in more detail. Within INM, arithmetic averages of the attenuation coefficient are used to define the atmospheric absorption adjustment. These arithmetic values are presented in Table 3.2. On the other hand, within the WAFORT propagation model, the attenuation coefficients are determined using a procedure described by the *ICAO* [63] and is discussed in detail in Section 3.4.4.

The attenuation coefficients are compared by presenting them against increasing frequencies illustrated by Figure 4.5. Atmospheric conditions are taken such that the assumptions made in INM are met.

It is clearly noted in Figure 4.5a that the two approaches diverge from a frequency of 800 Hz and larger, with the arithmetic values in INM being greater. However, when analysing the frequencies up to 1000 Hz, illustrated by Figure 4.5b, it is noted that the arithmetic values increase piece wise around the values found in the WAFORT propagation model. This implies that for certain lower frequencies, the losses encountered by the WAFORT propagation model is higher than in INM.

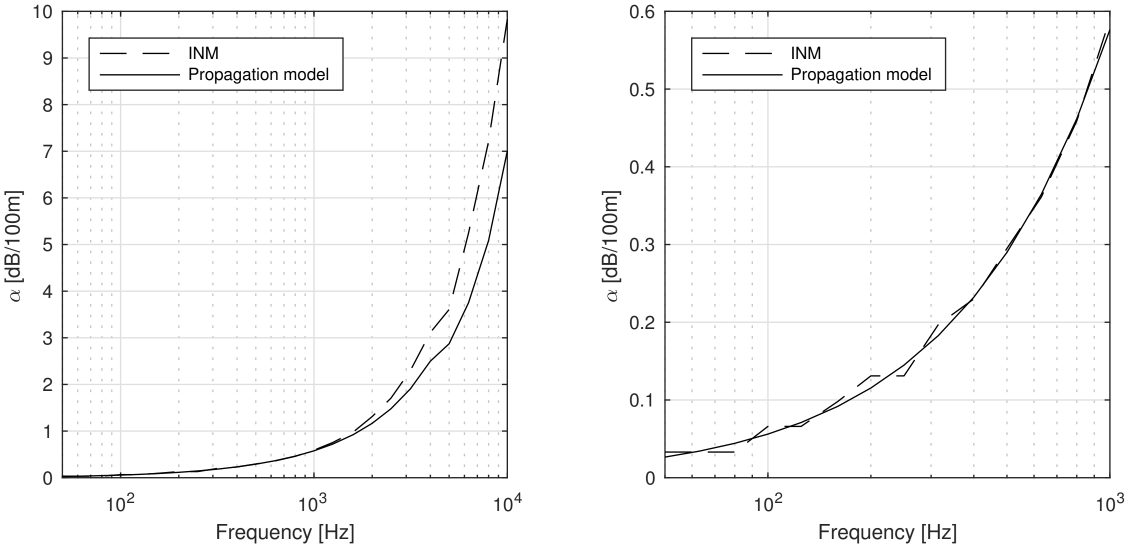

(a) Frequency interval of 50 to 10000 Hz.

(b) Frequency interval of 50 to 1000 Hz.

Figure 4.5: Comparison of the atmospheric attenuation coefficient α used by the propagation model in INM and in WAFORT for different frequency intervals (T = 25°C, RH = 70%).

WAFORT allows for the simulation of different temperature and relative humidity values and consists of a layered atmosphere. On the other hand, the INM is based on a homogeneous atmosphere. Generally, air temperature drops with increasing altitude. To analyse how the attenuation coefficient changes with increasing altitude, and how the changes stand with respect to the arithmetic attenuation coefficient used in INM, the attenuation coefficient in WAFORT for different temperature at constant humidity is compared against the arithmetic attenuation coefficients for increasing frequency in Figure 4.6.

As presented by Figure 3.14, at a relative humidity of 70%, generally for temperatures in the range of 10 to 30 °C, for decreasing temperatures the attenuation coefficient increases for higher frequencies as illustrated by Figure 4.6a, while the attenuation coefficient decreases for low frequencies as illustrated by Figure 4.6b. In comparison with the INM propagation model, main differences are observed at low frequencies.

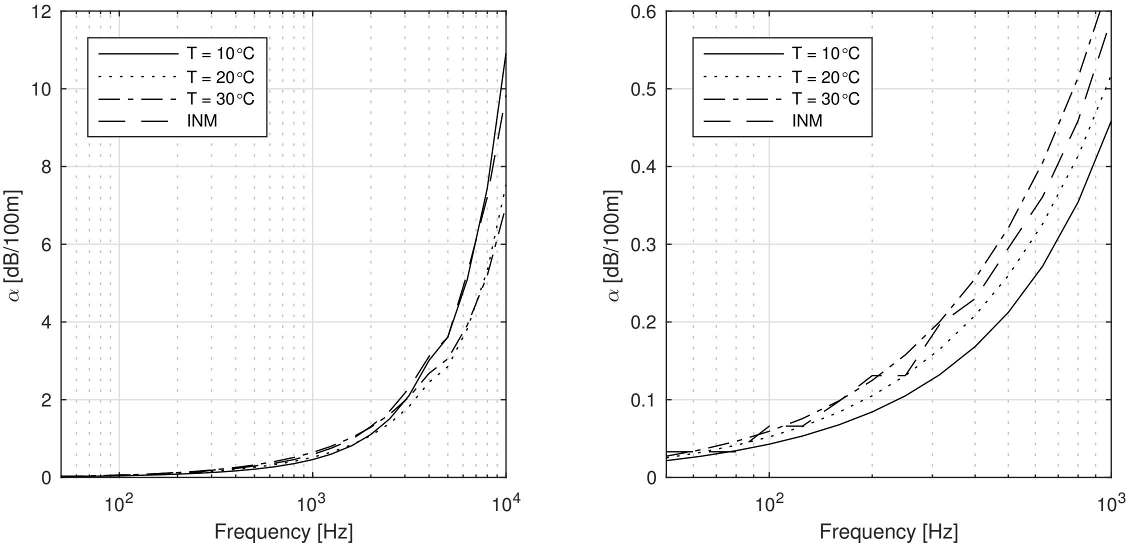

(a) Frequency interval of 50 to 10000 Hz. **(b)** Frequency interval of 50 to 1000 Hz.

Figure 4.6: Comparison of the atmospheric attenuation coefficient α used by the propagation model in INM and in WAFORT for different temperatures (RH = 70%).

To analyse whether these differences in attenuation coefficient in the low frequency domain results in the differences observed in Figure 4.1, it is required to analyse what frequency levels are dominant when propagating towards the observer. To do so, Figure 4.7 illustrates the spreading and absorption losses corrected to A-weighting, encountered as a function of slant range s for multiple frequencies. It is deduced that if the slant range between the observer and the aircraft is more than 2 km, all tones of the source noise have lost 75 dBA at the receiver. Furthermore, it is clearly observed that the atmospheric attenuation loss is dominant for high frequency tones, while spreading loss is dominant for low frequency tones up to 500 Hz.

Between 100 and 500 Hz, the amount of loss decreases for slant ranges up to 9 km. For frequencies greater than 500 Hz, the atmospheric attenuation losses increase the total loss again with increasing distances. From these findings it is concluded that the difference in atmospheric attenuation coefficient α between the propagation model in INM and in WAFORT cause the higher received sound levels in the WAFORT propagation model.

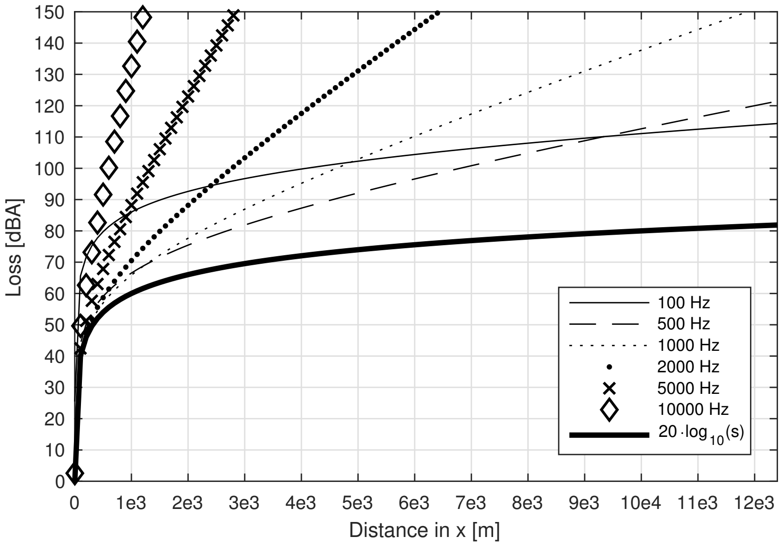

Figure 4.7: Comparison of the spreading and atmospheric attenuation loss with A-weight correction encountered for increasing distance for different frequencies (T = 25°C, RH = 70%).

4.2.2. Sound Exposure Level

As the noise impact is determined using the Sound Exposure Level (SEL), it is of interest how the SEL values for a grid of observers behaves. First the SEL values obtained by the WAFORT propagation model are compared against the values obtained by the INM model. This is followed by a comparison of the SEL of aircraft flying at different altitude, and the analysis of different weather conditions on the SEL values.

INM Against WAFORT Propagation.

Two-dimensional flight. In order to evaluate the difference in SEL received in a consistent manner between the two propagation models, the same integration technique is used to determine SEL from the L_A values observed. Thus no use is made of the NPD for SEL values at different thrust levels in the ANP database. The integration of L_A is performed using the trapezoidal rule.

The difference in SEL for a fly over between the two propagation models, in which the aircraft is flying from (0,-5000) to (0,5000) at a constant thrust level for different altitudes, is presented in Figure 4.8. As expected, the SEL values of the new propagation method are higher whenever the the observer is in the illuminated zone.

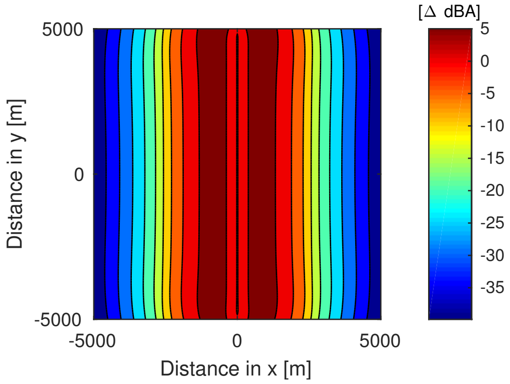

(a) $h = 200$ ft. Note the different scale with the other figures.

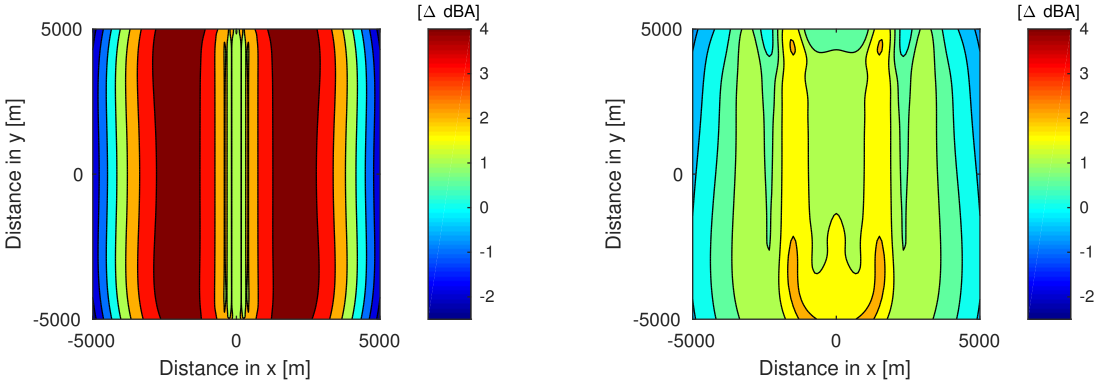

(b) $h = 1000$ ft.

(c) $h = 10000$ ft.

Figure 4.8: Difference in SEL (ΔSEL) received using the INM and the WAFORT propagation model for different altitudes and constant thrust level ($v = 160$ kts, T = 25°C, RH = 70%). Aircraft flies from (0,-5000) to (0,5000).

When the aircraft flies at 200 ft, the observers in the shadow zone are clearly distinguished by the gradually increasing negative Δ dBA values away from the aircraft ground track as illustrated by Figure 4.8a.

A similar pattern is observed in Figure 4.8b, when the aircraft is flying at 1000 ft. However, the shadow zone is not located within the range of the figure and thus the difference in SEL are not that large. Furthermore, thin bands of fluctuations in the Δ SEL values are observed perpendicular to the motion of the aircraft. This is caused by the ground reflection modelled in the WAFORT.

The effect of the ground reflection is more clearly illustrated by Figure 4.8c for a fly over at 10000 ft. The difference in received SEL values are not as large as for lower altitudes. However a combination of the Doppler frequency shift and the ground reflection induce non-symmetric Δ SEL values along the x-axis at (0,0).

Three-dimensional flight. In actual flight, velocity, thrust level and altitude changes. Figure 4.9 analyses the difference in SEL for a three-dimensional flight, in which Figure 4.9a illustrates The difference in SEL between the INM and the WAFORT propagation model and Figure 4.9b illustrates the thrust and velocity profile of the trajectory.

It is noticed that in a band of roughly 8 km perpendicular to the direction of flight the SEL values are around 3 dB larger in the WAFORT propagation model. Furthermore, the gradual reduction in SEL at the shadow zone, which is not modelled by INM, is clearly visible. The very fine, thin tubes of differences due to the ground reflection underneath the trajectory of the aircraft identified in Figure 4.8 is much less visible. This is mainly caused by the grid of observers not fine enough.

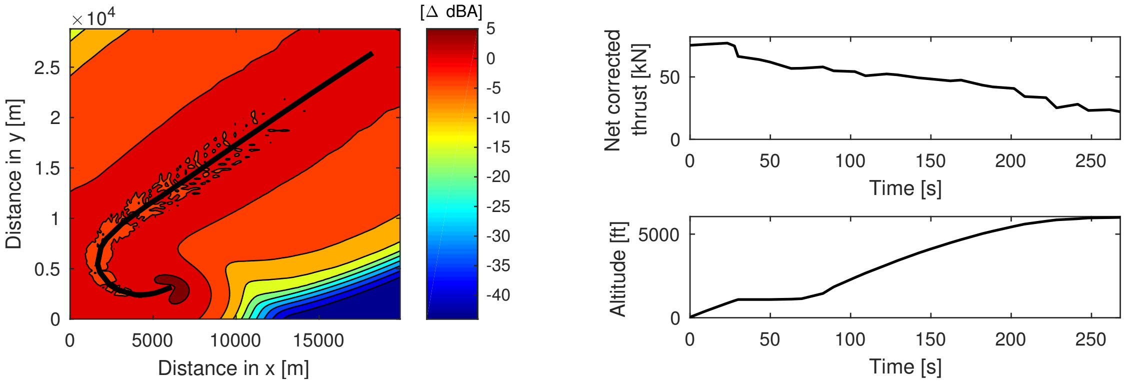

(a) Difference in SEL.

(b) Net corrected thrust T_n and altitude profile.

Figure 4.9: Difference in SEL (ΔSEL) received using the INM and the WAFORT propagation model in three-dimensional flight with varied thrust level (T = 25°C, RH = 70%).

With these comparisons, it is clear what the differences are of the different propagation modelling between INM and the WAFORT. It is concluded that while in the illuminated zone, the SEL values are larger in the WAFORT. Furthermore narrow, thin bands in which the SEL values change due to the ground reflection is observed in the WAFORT model.

In the following paragraphs, the influence of different weather conditions on the SEL values in the WAFORT propagation model are discussed.

The altitude. At lower altitudes, the shadow zone can be found more near to the aircraft and thus ensures that only a limited area is exposed to high noise levels. With increasing altitude, the shadow zone moves away from the aircraft and the sound energy is spread over an increased area. This results in lower sound levels over a larger area.

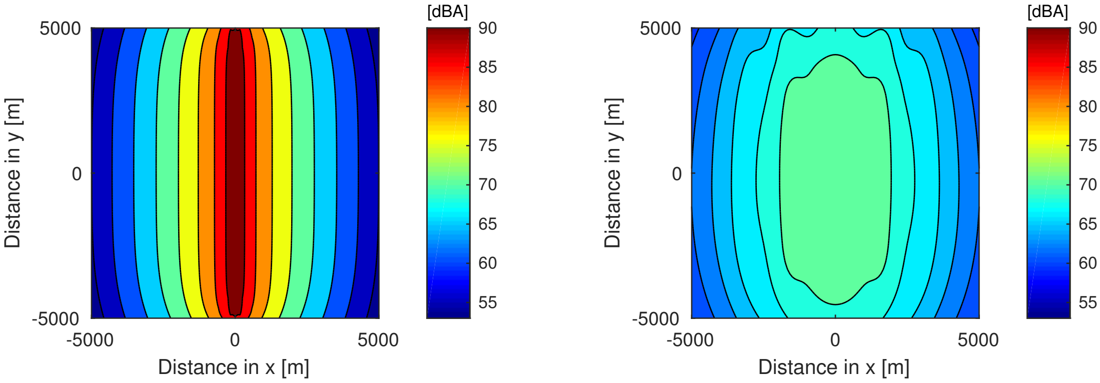

(a) h = 1000 ft.

(b) h = 10000 ft.

Figure 4.10: SEL received on the ground for a straight horizontal flight at different altitude in ISA conditions (v = 160 kts, T = 15°C, RH = 70%). Aircraft flies from (0,-5000) to (0,5000).

To test whether this is true, the SEL for a fly over at 1000 and 10000 ft is simulated and presented in Figure 4.10. It is observed that the higher the aircraft flies, the wider the noise contour and the lower the SEL values received by the observer.

The wind. Depending on whether the observer is up- or downwind of the aircraft influences the received sound levels. For upwind observer locations, the sound waves are bent up, while for the observer locations downwind, the sound waves are bent down. This results in a 'pushing' effect on the shadow zone, and is caused by varying effective speed of sound levels. The shadow zone upwind is pushed closer to the source while downwind, the shadow zone disappears.

The SEL received for a 10 kts eastern wind is presented for an aircraft at an altitude of 1000 and 10000 ft in Figure 4.11. Clearly, the effect of wind is present for the aircraft at 1000 ft, as illustrated by Figure 4.11a. Upwind, the shadow zone is much closer to the ground track of the aircraft, while downwind the shadow zone has disappeared when compared against the no wind conditions in Figure 4.10a. Similar behaviour is observed at lower wind speeds as well.

At higher altitudes, the boundary between the illuminated and shadow zones lies much further away when compared against lower altitudes. Furthermore the sound energy is spread over a larger area and wider noise contours are obtained. Considering this, the results obtained for an aircraft flying at 10000 ft presented in Figure 4.11b shows an expected pattern. The wind definitely has an influence on the SEL values, however over the grid distance taken in this simulation, the effects are hardly noticeable. Especially in the upwind corner points, lower SEL values are obtained when compared against the downwind corner points.

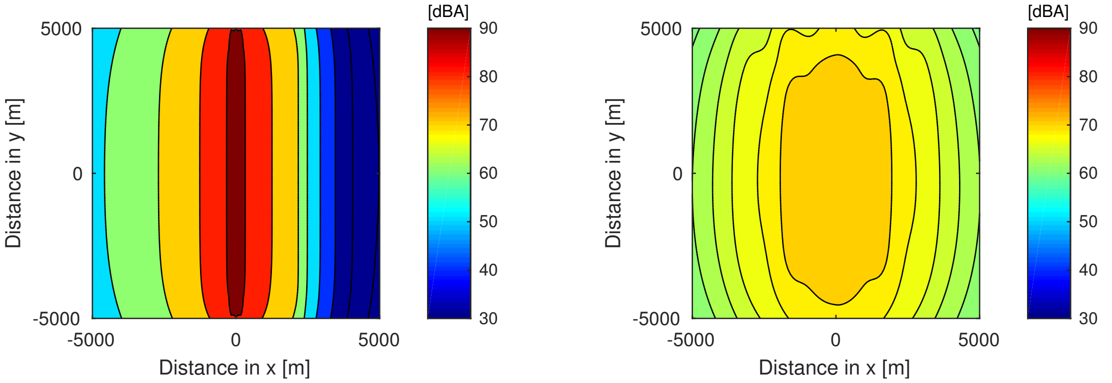

(a) $h = 1000$ ft. **(b)** $h = 10000$ ft.

Figure 4.11: SEL received on the ground for a straight horizontal flight with a 10 kts (≈ 5.1 m·s^{-1}) eastern wind ($v = 160$ kts, T = 15°C, RH = 70%). Aircraft flies from (0,-5000) to (0,5000).

Inverted atmosphere. In a cold atmosphere, the temperature lapse rate can invert. Sound waves are not bent upwards, but downwards as the speed of sound decreases with altitude and thus no shadow zones exist. The inverted atmosphere is modelled with a temperature below zero and a ground surface covered by snow. Snow has a factor 10 lower flow resistivity σ than grass. The reduced flow resistance dampens the ground reflection. Furthermore, in this particular atmosphere, for most frequencies the atmospheric attenuation coefficient α is slightly higher than in ISA conditions, resulting in higher atmospheric attenuation loss.

The difference in SEL between ISA conditions and the inverted atmosphere scenario is presented in Figure 4.12. The received SEL values are always larger in ISA conditions. In Figure 4.12a many narrow bands exists where the ground reflection causing the SEL in ISA conditions to be larger than in the inverted atmosphere conditions. Furthermore, since no shadow zone exist anymore, the difference becomes smaller when at the observer locations where the aircraft enters the shadow zone in ISA conditions. Asymmetry around the x-axis at (0,0) is caused by the effect of the Doppler frequency shift on the ground reflection.

With increasing altitude, the narrow bands caused by the ground reflection widens. Figure 4.12b illustrates the difference in SEL between ISA and the inverted atmosphere conditions for an aircraft flying at 10000 ft. The narrow bands have become quite wide. The general trend of the larger difference is caused by the higher attenuation coefficient and the larger distance covered by the rays.

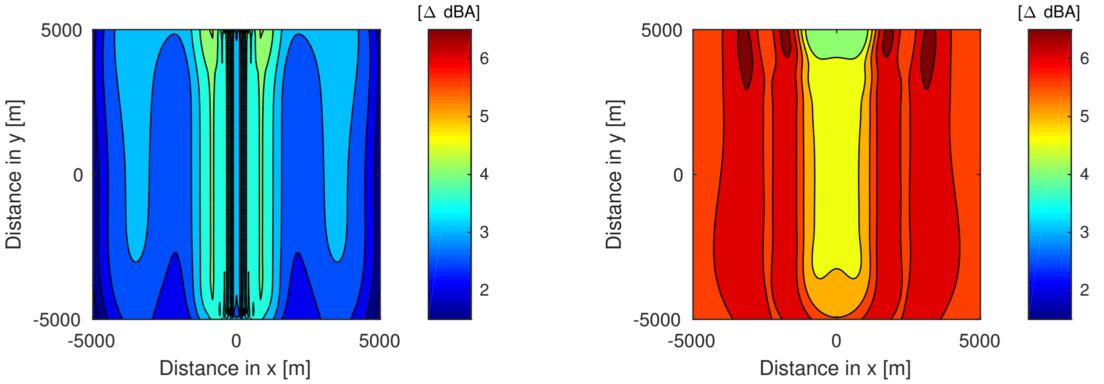

(a) h = 1000 ft.

(b) h = 10000 ft.

Figure 4.12: Difference in SEL received on the ground for a horizontal straight flight in a cold atmosphere with snow covered surface (T = -10°C, σ = 25e3, v = 160 kts, RH = 70%). Aircraft flies from (0,-5000) to (0,5000).

Atmospheric attenuation coefficient. The general trend in the atmospheric attenuation coefficient for different frequency, air temperature and relative humidity is discussed in Section 3.4.4. To test the degree of influence of a large atmospheric attenuation coefficient against propagation in ISA conditions, atmospheric conditions with high atmospheric attenuation conditions is simulated and presented by Figure 4.13.

The reduction in noise received in high absorption condition is clearly observed. For the aircraft flying at 1000 ft, the sound contour lines in Figure 4.10a move closer to each other and the peak value is lowered by more than 6 dB directly underneath the flight path of the aircraft. This difference diminishes once the observer is not in the illuminated zone. For the aircraft flying at 10000 ft, the sound contour changes in high atmospheric absorption conditions. The influence of the ground reflection clearly observed in Figure 4.10b diminished as the losses encountered are dominated by atmospheric attenuation losses, as illustrated by Figure 4.13b. Directly underneath the aircraft, the SEL is reduced by more than 12 dB. It is noticed that the opposite of the Doppler frequency shift is noticed: the SEL values at the observers to which the aircraft mainly flies towards is larger than for the observers the aircraft is flying from. Although the wave like peaks of the ground reflection is reduced there is still a small increase in SEL when the aircraft is flying away from the observer.

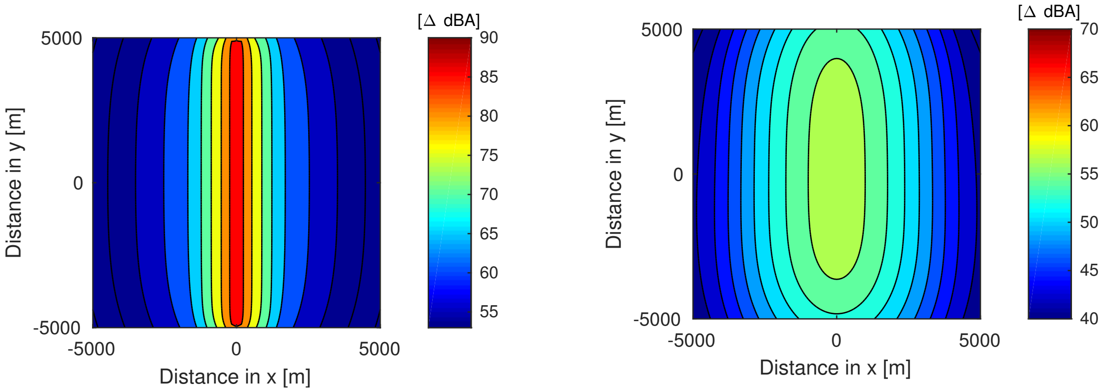

(a) h = 1000 ft.

(b) h = 10000 ft. Note the difference in scale with Figure 4.10b.

Figure 4.13: SEL received on the ground for a straight horizontal flight in high atmospheric attenuation conditions (T = 30°C, RH = 5%, v = 160 kts). Aircraft flies from (0,-5000) to (0,5000).

4.2.3. Conclusion

Instead of using correction factors, the WAFORT propagation model makes use of numerically determined frequency dependent ground reflection, atmospheric absorption that actually depend on the atmospheric conditions and numerically determined shadow zones. When compared to the propagation model in INM, the current standard for aircraft sound evaluation, lower sound levels arrive at the receiver. This is mainly caused by lower atmospheric attenuation coefficients in the WAFORT propagation model compared to the arithmetic values used by the SAE-AIR-1845 atmosphere used by the INM.

The Doppler frequency shift has a large influence on the ground reflection, Due to the wave-like nature of the ground reflection, fluctuating sound levels are observed when the observer is moved slightly in perpendicular direction of the motion of flight. The implementation of the wind and the effects of different atmospheric conditions result in expected behaviour.

4.3. Performance within the Optimisation Framework

This Section discuss the performance of the propagation model within the framework of the optimisation. All calculations are performed on a desktop with a 3.33 GHz CPU with a 4 Gb RAM and 4 available cores.

With the implementation of the propagation model in the GPOPS optimisation paradigm, there are multiple notable findings. As GPOPS uses a gradient-based optimisation technique to solve the minimisation problem, derivatives of the cost functional and constraints are required. So the gradients of the states used within the propagation model are required as well. The derivatives can be obtained numerically, or can be automatically obtained using an Automatic Differentiation (AD) program which repeatedly performs the chain rule over the arithmetic activities performed by the computer. This results in derivatives with machine precision.

Initially, the entire propagation model has been programmed in MATLAB to ensure coherency in modelling language in combination with the INTerval LABoratory (INTLab) [72] as AD. With increasing problem size, the number of derivatives to be stored in the memory increases. This resulted in the evaluation of one single fly over for 121 observers to take more than 7 hours. As multiple iterations have to be performed, the computational time is unacceptable.

As alternative, the propagation model has been translated to FORTRAN language in combination with AUTO_DERIV [73] as AD. FORTRAN is very efficient in memory allocation and the same problem as in MATLAB is solved in 10 s, which is an acceptable computational time for one fly over.

However, due to the machine precision of the derivatives, the convergence of the problem got affected. So it is determined to use Numerical Differentiation (ND) using the forward finite difference method to smooth the gradient function. Additionally, using numerical differentiation, less memory is required compared to automatic differentiation, resulting in a computational time of to 2.5 s for the fly over.

5
Case Studies

5.1. Introduction

The WAFORT tool is used to simulate real departure procedures at Amsterdam Airport Schiphol (AAS). Goal of the case studies is to formulate a conclusion on the following points:

- The influences of air temperature, relative humidity and wind on the fuel usage, the sound propagation and the resulting noise impact.
- The comparison of noise optimal departure procedures in International Standard Atmosphere (ISA) conditions and the weather-adaptive noise optimal departure procedures.
- The performance of the new propagation model withing the WAFORT framework.

The noise optimal trajectories are modelled after the Noise Abatement Departure Procedure (NADP). By optimising the trajectory, the model decides whether a NADP-I or NADP-II is the most noise friendly. The noise optimal trajectory in the different simulations are compared against their fuel optimal trajectory to analyse the reduction in noise impact.

Weather-adaptive noise optimal trajectories are compared against the noise optimal trajectory in ISA conditions as the actual Standard Instrument Departure (SID) is difficult to simulate in WAFORT in its current form. This is mainly due to varied state and control variables along the trajectory obtained in varied atmospheric conditions. Although the actual SIDs are not simulated, a previous study on trajectory optimisation identified that the fuel optimal trajectories are more fuel efficient than the actual SIDs [74]. Thus the increased fuel usage in the noise optimal trajectories does not necessarily imply that the fuel usage is higher than the current SIDs.

Before the simulations are performed, the cases are defined in Section 5.2. Three different types of cases are simulated in order to identify the different influences of the atmospheric conditions on the optimal noise trajectory. Case 1, which is discussed in Section 5.3, covers various limiting atmospheric conditions for the Spijkerboor 3K SID. Similarly, Section 5.4 discusses Case 2 in which similar atmospheric conditions as in Case 1 are discussed for the Arnem 3E SID. In Case 3, actual weather conditions observed in the past months are used to evaluate the noise optimal trajectories for the Spijkerboor and Arnem SID. Goal is to relate the findings obtained in Case 1 and Case 2 to actual weather conditions. The findings of all cases are discussed in Section 5.5.

5.2. Case Definition

The definition of the cases are described along with the different groups presented in the WAFORT framework as introduced in Section 3.7. First the problem statement is formulated, by defining the case setup, the constraints and the number of phases. Furthermore the problem size and a modelling limitation are introduced. Section 5.2.2 defines the cost functional and aircraft data resulting in a complete case definition.

5.2.1. Problem Statement of the Cases

To compare current noise optimised trajectories with weather-adaptive noise optimised trajectories, two different departure trajectories are simulated. The two trajectories are based on the SID published by the Air Traffic Control The Netherlands. Amsterdam Airport Schiphol (AAS) is used because of the availability of Geographic Information System (GIS) data of the Netherlands. However, the WAFORT can be used to evaluate different procedures at different airports as well. Appendix A elaborates on the runway configuration and arrival and departure charts of AAS.

Case Setup.
The first trajectory is the so-called Spijkerboor 3K departure towards way point ANDIK, located above the city of Andijk. The aircraft departs from runway 24 (Kaagbaan) and makes a sharp right turn over the highly populated area of Hoofddorp and Nieuw-Vennep, flying past Haarlem and Zaandam and overflying the city of Hoorn.

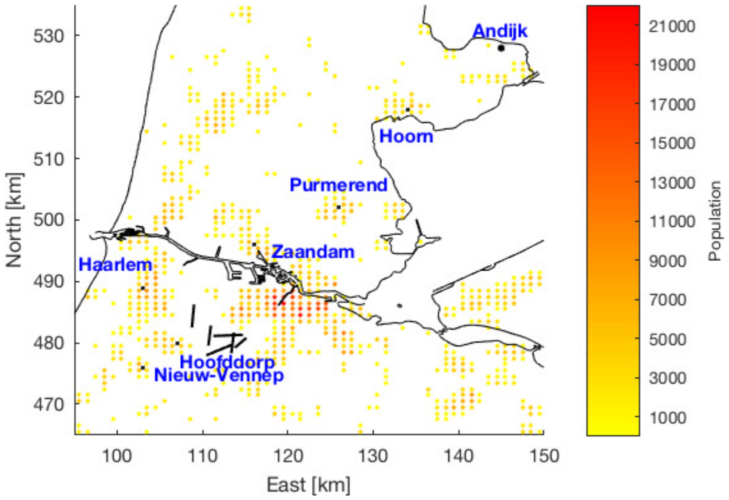

Figure 5.1: Population density around the Spijkerboor 3K SID.

The second trajectory is the so-called Arnem 3E departure towards way point IVLUT, located above the city of Laren. The aircraft departs in Southern direction from runway 18L (Aalsmeerbaan) where after it makes a left turn straight toward the way point. The trajectory flies past the cities of Aalsmeer, Uithoorn, Amstelveen and near the end of the trajectory, the cities of Hilversum and Laren.

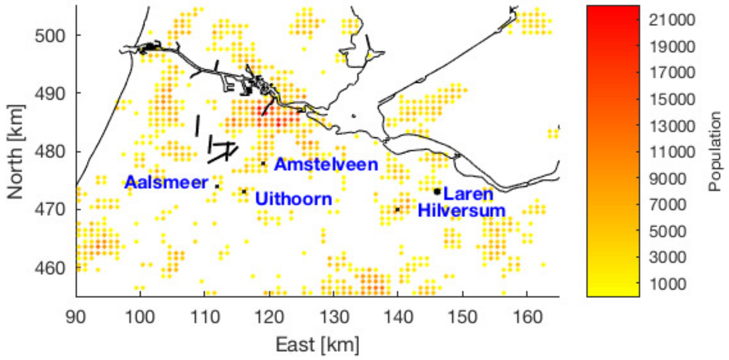

Figure 5.2: Population density around the Arnem 3E SID.

The two SIDs complement each other by flying over very different population densities. While the Spijkerboor 3K departure flies over many populated areas during most of its flight, the Arnem 3E departure mainly encounters population at the start and at the end of its trajectory and it covers a smaller distance. Thus two different kind of results are to be expected in which the Spijkerboor departure optimises for the ground track, swinging around populated areas, while the Arnem departure might more optimise in the vertical profile. The departure cases are summarised in Table 5.1.

As the goal of this research is to identify the influence of the different atmospheric conditions on the flown noise optimal trajectories, three different types of cases are performed. The fist two cases separately identify the effect of the different atmospheric conditions on the two different SIDs. The third case simulates real weather conditions occurred in the past few months, in which a combination of multiple atmospheric conditions are assessed. The atmospheric conditions used for each case are defined per case.

Table 5.1: Departure procedure characteristics.

	Departure runway	SID name	Final way point
Case 1	24	Spijkerboor 3K	ANDIK
Case 2	18L	Arnem 3E	IVLUT

Problem size. The trajectory is discretised over 71 segments, resulting in a problem with 663 variables divided over the state, control and time variables and 700 constraints divided over collocation, path, event and linkage constraints.

Limitation. It is assumed that the aircraft is in clean configuration during the entirety of the simulation. In reality, control surfaces and the landing gear are retracted. This limitation results in higher drag, resulting in weaker climb performance in the initial phases of flight.

Constraints and Phases.
During the entire simulation, the aircraft is not allowed to lose altitude. Furthermore, the bank angle constraint presented in Table 2.4 holds anytime. The resulting constraints are presented by Equation (5.1) and Equation 5.2.

$$\dot{z} \geq 0 \tag{5.1}$$

$$|\mu| \leq \mu_{max} \tag{5.2}$$

The maximum bank angle μ_{max} after take-off is dependent on the height above the ground, as presented in Table 2.4. In order to incorporate the change in bank angle as a constraint without adding extra phases and discontinuities, the maximum bank angles are approximated using switch functions. The switch functions are approximated using the arctangent presented by Equation (5.3), and is illustrated by Figure 5.3. Using the approximation, at different altitudes, a slightly larger or smaller bank angles are allowed resulting in small errors.

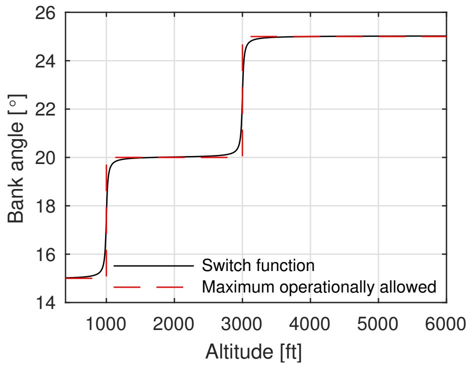

Figure 5.3: Switch function for the maximum bank angle.

$$\begin{aligned}
\mu_{max1} &= \frac{5}{2 \cdot \tan^{-1}(60)} \cdot \tan^{-1}\left(\frac{60}{305 \cdot z} - 60\right) + 17.5 \\
\mu_{max2} &= \frac{5}{2 \cdot \tan^{-1}(180)} \cdot \tan^{-1}\left(\frac{180}{915 \cdot z} - 180\right) + 2.5 \\
\mu_{max} &= \mu_{max1} + \mu_{max2}
\end{aligned} \tag{5.3}$$

In order to model realistic operations that fall within the flight procedures and regulations discussed in Section 2.4, at least 3 phases are required. In the first phase, the aircraft climbs to an altitude of 400 ft, where after it is allowed to turn. Phase 2 ends when the aircraft reaches an altitude of where the thrust is cut-back from take-off thrust to climb thrust and coincides with the altitude specified by the NADP. Phase 3 ends when the aircraft has reached its final point in the simulation. In the following paragraphs, phase specific constraints are defined.

Phase 1. The initial phase runs until the aircraft has obtain a height of 400 ft. In this phase, the aircraft is forced to use all energy to climb. Although the Procedure Design Gradient (PDG) of 3.3% to avoid obstacles after take-off is not evaluated, by not allowing the aircraft to increase its Calibrated Airspeed (CAS) until the altitude of 400 ft has been cleared, the aircraft will always climb as fast as possible. CAS is the indicated airspeed corrected for system errors. The constraint on the CAS is illustrated by Equation (5.4). During the entire phase, take-off thrust is used.

$$-0.001 \leq \dot{V}_{CAS} \leq 0.001 \tag{5.4}$$

Phase 2. The second phase runs until the aircraft has reached an altitude between 800 to 1500 ft. To follow the NADP procedure introduced in Section 2.4.2, during phase 2 the aircraft can reduces its climb gradient. The aircraft still maintains take-off thrust and is allowed to turn. In order for the model to be realistic and to prevent abrupt heading changes, the change in angular heading velocity is bounded by Equation (5.5).

$$-3 \leq \dot{\chi} \leq 3 \quad [^\circ] \tag{5.5}$$

Phase 3. Phase 3 runs until the final conditions are met. In this phase, climb thrust is used i.e. a thrust cut-back. The aircraft is not allowed to decrease velocity, but is free to increase it, as expressed by Equation (5.6).

$$\dot{V}_{CAS} \geq 0 \tag{5.6}$$

5.2.2. Input Data

Input data consists of the cost function and information regarding aircraft data.

Cost function. In order to compare different noise optimal trajectories, the optimal fuel trajectory in ISA conditions is used as reference trajectory. The cost function of Equation (3.60) is used with $k_{fuel} = 1$ and k_{noise} varying between 0 (optimal fuel) and the value until either the fuel usage or flight time has increased by 10% or until convergence difficulties does not allow for (local) optimal solutions to be found that meet the optimality and feasibility threshold of $\epsilon = 1 \cdot 10^{-6}$. The cost function is presented in Equation (5.7).

$$J = k_{noise} \cdot \text{awakenings} + \int_0^{t_f} \dot{m}_{fuel} dt \tag{5.7}$$

The results for different k_{noise} values are evaluated by plotting them to create a Pareto front for the number of awakenings against the fuel usage. Pareto fronts are used in multiple objective optimisation problems to illustrate to potential reduction in the number of awakenings with increasing fuel usage at higher k_{noise} values. Normalising the Pareto front, the results of different atmospheric conditions can be compared and evaluated.

Aircraft data. The aircraft type in the simulation is the Boeing 737-800. This aircraft type is part of the Boeing 737 Next Generation (NG) family, a narrowbody short- to medium-range passenger aircraft powered by two engines as depicted in Figure 5.4. Typical characteristics of the aircraft is presented in Table 5.2. At AAS, it is a very common aircraft type.

Figure 5.4: KLM Boeing 737-800 (©Bene Riobó).

Table 5.2: Boeing 737-800 characteristics. [55].

Dimensions	Length	39.5 m
	Height	12.5 m
	Wingspan	38.5 m
	Wing area	124.6 m^2
Weights	Operating Empty Weight (OEM)	41,413 kg
	Maximum Take-off Weight (MTOW)	79,016 kg
Capacity	Two-class	162 passengers
	One-class	189 passengers
Performance	Maximum Mach number	0.82
	Range	5,436 km
	Maximum thrust (both engines)	110 - 120 kN

The aircraft with winglets is certified to a maximum crosswind at take-off of 33 kts and tailwind of 10 kts [44]. However, no tailwind at take-off is simulated in any of the cases as certain limitations hold that does not make tailwind operations trivial, as is discussed in Section 2.4.3.

5.3. Case 1: Spijkerboor 3K Departure to ANDIK

Case 1 simulates the departure from runway 24 towards way point ANDIK. Goal of this case is to identify the influences of air temperature, relative humidity and wind on the fuel usage, the sound propagation and the resulting noise impact by comparing the fuel and the noise optimal trajectory. Furthermore, the noise optimal trajectories in non-ISA conditions are compared against the noise optimal trajectory in ISA conditions.

First the reference case in ISA conditions is discussed in Section 5.3.1, followed by a case with varied wind conditions discussed in Section 5.3.2. The analysis of different air temperature and relative humidity combinations is discussed in Section 5.3.3. Section 5.3.4 concludes on the findings and discusses the convergence performance of the new propagation model within WAFORT.

The results for all k_{noise} values simulated in between the fuel and noise optimal trajectory is presented in Section C.1. To illustrate the change in noise contour lines, the appendix also presents the noise contour lines of the fuel and noise optimal trajectories.

Before analysis of the cases, the atmospheric conditions and additional constraints that hold for this case are discussed.

Atmosphere. The atmospheric conditions simulated for Case 1 is presented in Table 5.3. Note that by the definition of the wind, the direction ψ_W is the direction the wind is blowing to. The numbering of the atmospheres are used when referring to simulations with a specific atmosphere.

Table 5.3: Atmosphere parameters for Case 1.

		T_0 [K]	λ [K·m^{-1}]	RH [%]	z_v [m]	$v_0(z_v)$ [kts]	ψ_W [°]	σ [N·s·m^{-4}]
Atm. 1	ISA	288.15	-0.0065	70	10	0	0	$250 \cdot 10^3$
Atm. 2	ISA,270/5	288.15	-0.0065	70	10	5	90	$250 \cdot 10^3$
Atm. 3	ISA,270/15	288.15	-0.0065	70	10	15	90	$250 \cdot 10^3$
Atm. 4	ISA,148/15	288.15	-0.0065	70	10	15	328	$250 \cdot 10^3$
Atm. 5	High α	303.15	-0.0065	5	10	0	0	$250 \cdot 10^3$
Atm. 6	Low α	263.15	-0.0065	5	10	0	0	$250 \cdot 10^3$

The first simulation, or the reference case, is performed in ISA conditions. The reference case is enhanced by wind in the subsequent three cases. Due to the runway configuration of Amsterdam Airport Schiphol (AAS) and the orientation of runway 24, only wind directions between 148° and 328° does not result in tailwind.

To analyse the effect of increasing wind velocities, a western wind of 5 and 15 kts at the reference height is simulated. The western wind diminishes the shadow zones near the highly populated area of Amsterdam and is a common wind direction over AAS. Furthermore to identify the effect of a different wind direction, a south-eastern, full crosswind of 15 kts in simulated. Although the maximum wind velocity at the reference height is limited to 15 kts due to modelling limitations, as discussed in Section 3.4.4, this is sufficient to identify the effect of wind on optimal trajectories.

For the last two simulations in Case 1, the air temperature and relative humidity are altered such that conditions in which very high and low atmospheric attenuation coefficients are obtained. These atmospheric conditions are experienced in desert like environments. The procedure to determine the atmospheric attenuation coefficient is presented in Section 3.4.4.

Figure 5.5 compares the atmospheric attenuation over the frequencies against the values obtained in ISA conditions. In high atmospheric attenuation conditions, larger attenuation coefficients are obtained for frequencies larger than 100 Hz. For the low attenuation coefficient conditions, lower attenuation coefficients start to occur for frequencies larger than 1000 Hz.

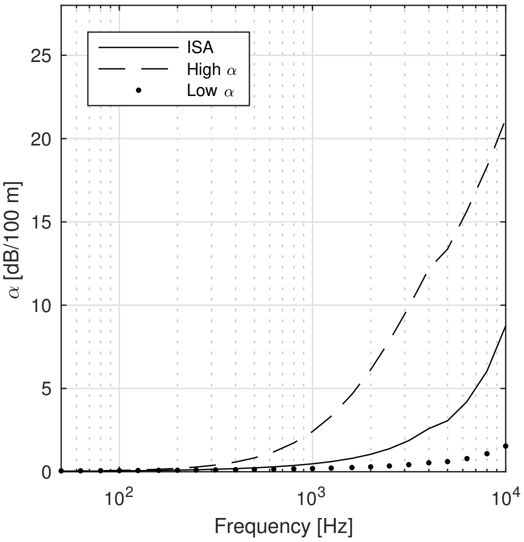

Figure 5.5: Atmospheric attenuation coefficient in ISA, high α and low α atmospheric attenuation conditions.

Constraints. The constraints for the Spijkerboor departure are defined by initial and final conditions for the position and velocity. Additionally, the initial heading is defined. The actual values of the boundary constraints are defined in Table 5.4.

The position is given in the Rijksdriehoeks Cartesian coordinate system and the initial xy coordinates matches the end of the runway. At the end of the runway, it is assumed that the aircraft has already gained some altitude. The initial velocity matches with the safe aircraft take-off velocity V2 + 10 kts. The final position coincides with the way point ANDIK. The final altitude and velocity are prescribed by the SID chart presented in Appendix A.2.

Table 5.4: Initial and final conditions for Case 1.

Constraint	Initial value	Final value	Unit
Position (x,y)	(110 658, 478 103)	(147 117, 528 012)	km
Altitude	35	6000	ft
Velocity	155	250	kts
Heading	238	free	°

5.3.1. Reference Case

To obtain the reference to which the various atmospheric conditions are compared against, the reference case in ISA conditions is simulated. The results of the optimal fuel and noise trajectory in atmosphere 1 is presented in Table 5.5. It is seen that for a relatively small increase in fuel usage and flight time, the awakenings can be reduced by more than 20%.

Table 5.5: Fuel and noise optimal trajectory characteristics of case C1.1.

Case	Objective	Fuel [kg]	ΔFuel [%]	Awakenings	ΔN_A [%]	Time [s]	ΔTime [%]
C1.1.1	Fuel	559.5	-	9904	-	525.8	-
C1.1.7	Fuel + 0.01 $\cdot N_A$	566.5	+1.26	7671	-22.55	535.3	+1.82

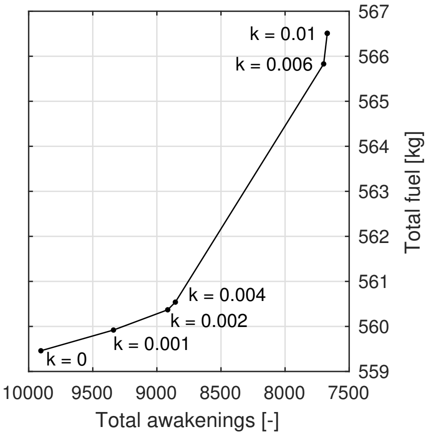

Figure 5.6: Total awakenings against total fuel usage for case C1.1. with according k_{noise} values.

Figure 5.6 presents the behaviour of the k_{noise} against the total awakenings and the fuel usage. It is clearly observed that a larger number of awakenings is reduced by implementing a small weighting factor. However, between the weighting factors of 0.006 and 0.01, a limited reduction in awakenings is related to a relatively large increase in fuel usage. Furthermore, larger k_{noise} values do not result in optimal solutions that satisfy both feasibility and optimality threshold. Thus the trajectory with $k_{noise} = 0.01$ is taken as the noise optimal trajectory.

To compare the fuel and noise optimal trajectories, Figure 5.7 presents the change in SEL level observed by the receivers on the ground. The noise optimal trajectory can be characterised as swinging past the populated areas to avoid direct fly overs. The aircraft relieves the densely populated area of Amsterdam by flying away from them and another small swing is observed around Hoorn.

By evading Amsterdam, new awakenings are obtained near Zaandam. Although the SEL values received by the population north of Haarlem increase by nearly 40 dB, no awakenings are observed due to the SEL not exceeding the threshold of 50.5 dB. It is noted that when overflying the population near Zaandam, the aircraft flies right over the least dense populated area.

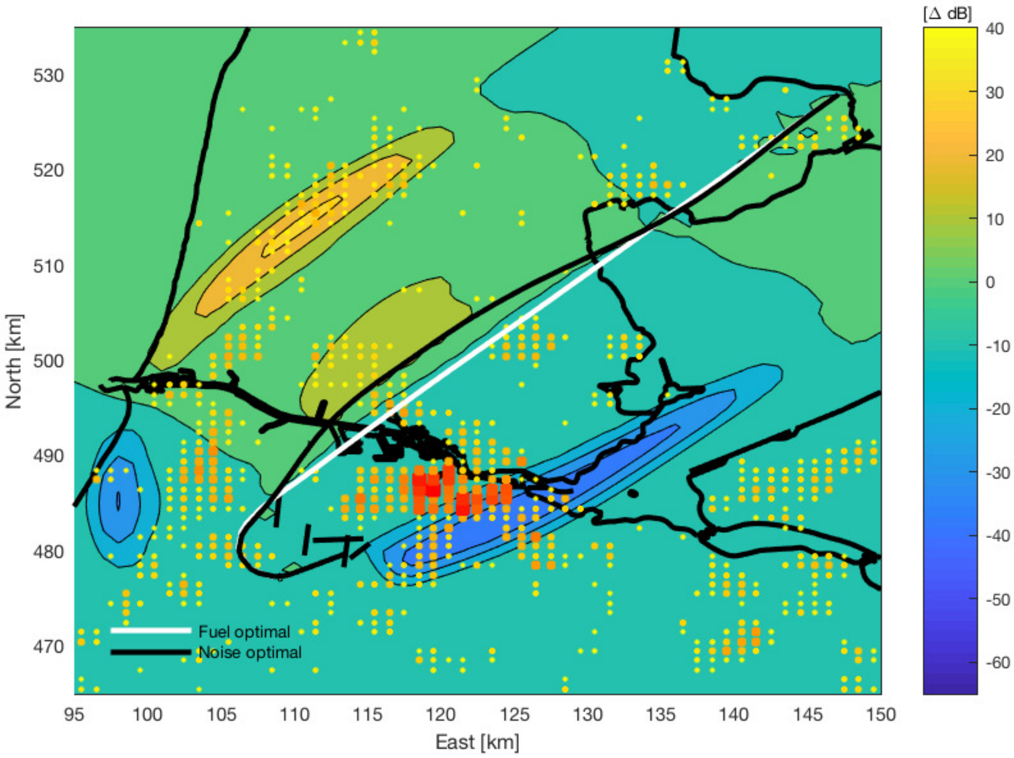

Figure 5.7: Difference in received SEL values between the noise and fuel optimal trajectories for case C1.1.

The trajectories are evaluated in more detail in Figure 5.8. Figure 5.8a illustrates the initial 200 s of the velocity, and the entire altitude and thrust setting profile of both trajectories. It is observed that the noise optimal trajectory uses a lower throttle setting and thus accelerate slower than the fuel optimal case. Two different accelerations are used to increase velocity of which the second is lower than the initial acceleration. Once the aircraft obtained its final velocity, climb is initiated and is less steep. Due to the lower thrust level, source noise is reduced. Furthermore by staying lower for a longer time period, narrow high value SEL bands are obtained using higher lateral attenuation compared to aircraft flying at higher altitude. This results is less noise further away from the aircraft.

Comparing the ground tracks in Figure 5.8b, the combination of a delayed climb and a slightly sharper initial turn over Hoofddorp result in a clearly noted reduction in SEL to the west of Haarlem.

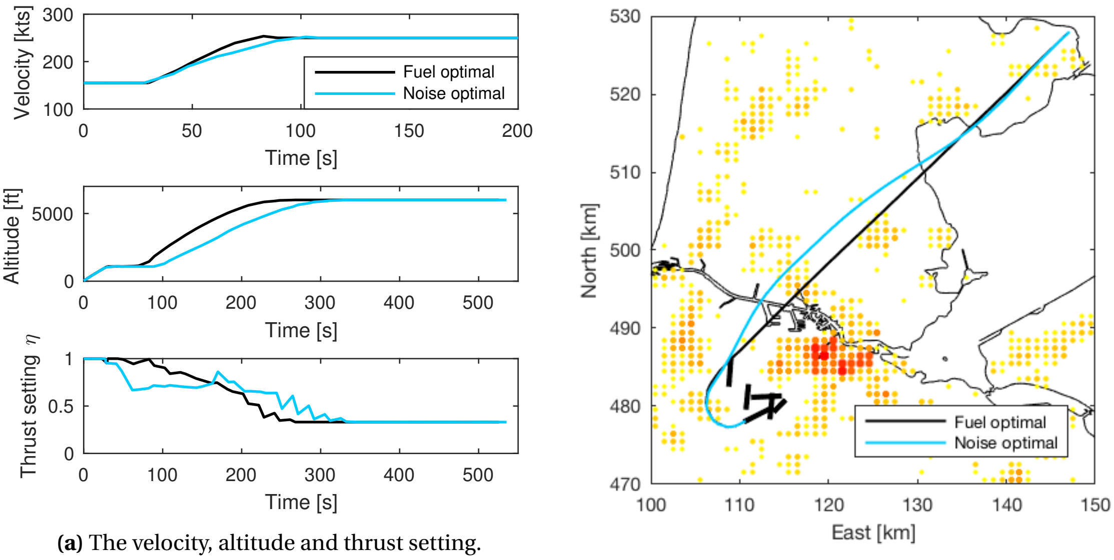

(**a**) The velocity, altitude and thrust setting.

(**b**) The ground track.

Figure 5.8: Comparison of the velocity, altitude and thrust setting and ground track of the fuel and noise optimal trajectory of case C1.1.

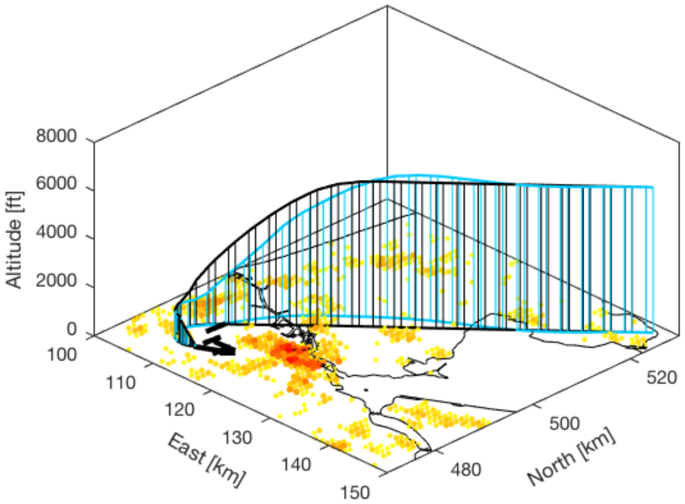

Figure 5.9: Comparison of the three dimensional trajectory of case C1.1.

Although the thrust setting is presented to analyse the trajectories, it is noted that in actual flight, the control variables are a result of flying the trajectory defined by the state variables. The saw tooth like pattern obtained for the thrust setting profile is caused by the discretisation of the trajectory.

The three-dimensional trajectory of the fuel and noise optimal trajectory is presented in Figure 5.9. It is observed that to reduce awakenings, the aircraft does not climb until the initial turn has finished and the aircraft is flying in a straight line.

As the fuel optimal trajectory in most atmospheric conditions is similar to the one presented in Figure 5.8, the analysis in the following sections will mainly focus on the differences between noise optimal trajectories in different atmospheric conditions.

Compared to previous studies using the non-weather-adaptive FORT model [16, 18], the aircraft tend to climb earlier in the WAFORT model. Climb is initiated after the final velocity has been obtained. One of the reason why the aircraft increases its velocity is that by doing so, it is more fuel efficient.

5.3.2. Varying Wind Conditions

To analyse how noise optimal trajectories make use of the wind to reduce noise impact, varied atmospheric conditions with different wind velocity and direction are simulated. The results obtained in atmosphere 2 with a 5 kts western wind, atmosphere 3 with a 15 kts western wind and atmosphere 4 with a 15 kts south-eastern wind is presented in Table 5.6.

As for the reference case, large reductions in the number of awakenings are obtained by adding a weighting function for the awakenings to the objective function. The wind profile has a large influence on the initial number of awakenings, fuel usage and flight time for the fuel optimal trajectories.

Table 5.6: Fuel and noise optimal trajectory characteristics of cases C1.2.-C1.4.

Case	Objective	Fuel [kg]	ΔFuel [%]	Awakenings	ΔN_A [%]	Time [s]	ΔTime [%]
C1.2.1	Fuel	551.7	-	9647	-	514.2	-
C1.2.7	Fuel + 0.01 $\cdot N_A$	557.1	+0.98	7196	-25.41	521.0	+1.32
C1.3.1	Fuel	537.5	-	9221	-	491.0	-
C1.3.6	Fuel + 0.008 $\cdot N_A$	545.1	+1.40	6350	-31.14	501.5	+2.12
C1.4.1	Fuel	573.4	-	8905	-	548.4	-
C1.4.7	Fuel + 0.01 $\cdot N_A$	580.8	+1.29	6628	-25.57	557.4	+1.64

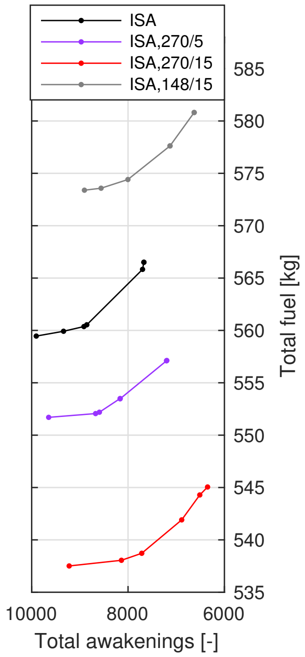

Figure 5.10: Total awakenings against total fuel usage for cases C1.1-C1.4.

The total awakenings against the total fuel usage for the atmospheres with different wind conditions and the reference case is illustrated by Figure 5.10. All curves have a similar shape albeit shifted. With respect to the fuel optimal trajectory of the reference case, with a 15 kts western wind, fuel usage is reduced by 22 kg and the flight time is reduced by 34 s. A southeastern wind of 15 kts result in an increase in fuel usage of 14 kg and flight time of 22 s. Furthermore, the wind creates shadow zones upwind, on the outside of the initial turn. This results in part of Nieuw-Vennep and Haarlem being relieved from awakenings. Wind from the southeast relieves the eastern half of Amsterdam from awakenings. Due to a slight headwind component, more fuel is used.

The curves in the figure present that for all cases, higher k_{noise} values will still result in a reduction in awakenings while not drastically increasing fuel usage. However, due to convergence difficulties, the higher weighting factor did not result in solutions that satisfy the optimality and feasibility threshold.

When analysing the difference in SEL values received between the fuel and noise optimal trajectories in different wind conditions, a large change in SEL values are noticed upwind of the aircraft. The wind moves the shadow zone closer to the aircraft upwind and diminishes the shadow zone downwind. Based on where the most densely populated area is located relative to the wind direction, the degree of swing around the most densely populated areas in the noise optimal ground track is obtained.

Comparing the noise optimal trajectories in the different wind conditions against the reference case in ISA conditions, it is noticed that wind has very limited influence on the noise optimal trajectory. No use is made of the wind direction to make use of larger tailwind at higher altitudes, or making use of lower headwind at lower altitudes. The ground track is only slightly different between the different noise optimal trajectories and varies around the ground track of the reference case. Due to these limited effects, a more detailed analysis of these simulations is presented in Appendix B.1.

5.3.3. Varying Atmospheric Absorption Conditions

To analyse how different noise levels obtained in high and low atmospheric attenuation conditions influence noise optimal trajectories, very high and low atmospheric absorption is simulated. The results obtained in atmosphere 5 with high atmospheric attenuation conditions and atmosphere 6 with low atmospheric attenuation conditions are presented in Table 5.7.

A large difference in the absolute number of awakenings is observed when comparing the fuel optimal trajectories in high and low atmospheric attenuation conditions. For the noise optimal trajectories in low absorption conditions, the number of awakenings is reduced by more than half. Percentage wise, the noise optimal trajectory in high absorption condition reduces the number of awakenings more than the reference case.

It is interesting to note the difference in fuel usage and flight time for the fuel optimal trajectories, which follows from the Aircraft Performance Model (APM). A more detailed analysis on the influence of air temperature on the APM is performed at the end of this section.

Table 5.7: Fuel and noise optimal trajectory characteristics of cases C1.5. and C1.6.

Case	Objective	Fuel [kg]	ΔFuel [%]	Awakenings	ΔN_A [%]	Time [s]	ΔTime [%]
C1.5.1	Fuel	556.2	-	2994	-	526.2	-
C1.5.8	Fuel + 0.02 $\cdot N_A$	563.5	+1.31	2021	-32.49	531.5	+1.00
C1.6.1	Fuel	565.2	-	22801	-	521.5	-
C1.6.9	Fuel + 0.016 $\cdot N_A$	597.3	+5.69	11350	-50.24	558.6	+7.11

The total number of awakenings against the total fuel usage of the reference case together with the high and low atmospheric absorption cases are presented in Figure 5.11. The air temperature influences the fuel usage and flight time. Furthermore, with deceasing atmospheric attenuation, the fuel usage and the number of awakenings increases. In high atmospheric attenuation conditions, for similar percentage of increase in fuel usage and flight time as in the reference condition, the number of awakenings is reduced by an additional 10%. In low atmospheric attenuation conditions, an increase of 6% in fuel usage and 7% in flight time result in the reduction of the number of awakenings by more than half. The reduction in the absolute number of awakenings reduces with increasing atmospheric attenuation, as is presented by the curve being more flat.

Analysing the curves, it is noted that for low atmospheric attenuation conditions the smoothness of the curve is as desired.

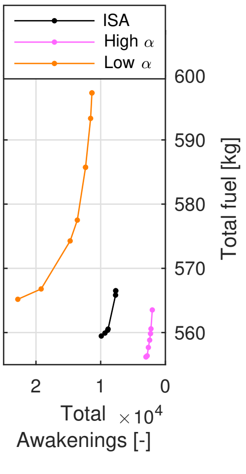

Figure 5.11: Total awakenings against total fuel usage for cases C1.1, C1.5. and C1.6.

The difference in SEL received for the fuel and noise optimal trajectories in high absorption attenuation conditions is presented in Figure 5.12. As with the reference case in Figure 5.7, a large increase in SEL is observed to the west of the trajectory, and a large reduction is observed to the east of it. Due to the high atmospheric attenuation loss, the fuel optimal trajectory does not create any awakenings in the most densely populated part of Amsterdam. However, together with the west of Haarlem, the SEL around Amsterdam is reduced the most.

The initial turn is tighter compared to the fuel optimal trajectory to relieve Hoofddorp, Nieuw-Vennep and part of Haarlem. Once the aircraft has reached its final altitude, no awakenings are made any more directly underneath the aircraft due to the high atmospheric attenuation. Thus after flying past Zaandam, the aircraft flies straight to the final position without making a swing around Hoorn.

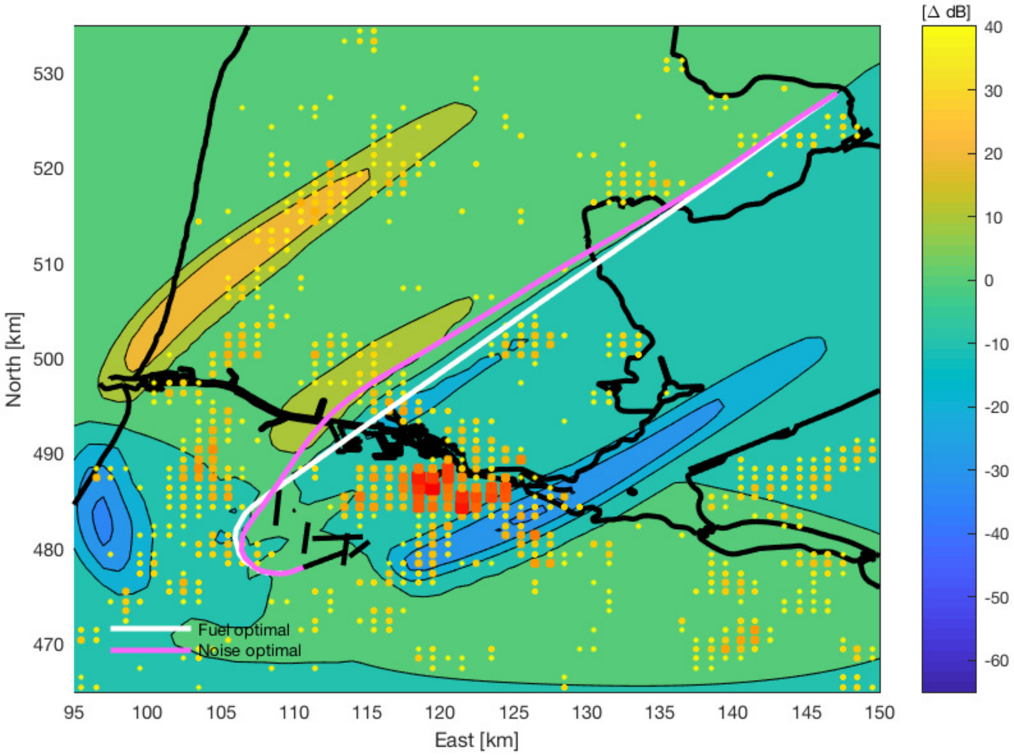

Figure 5.12: Difference in received SEL values between the noise and fuel optimal trajectories of case C1.5.

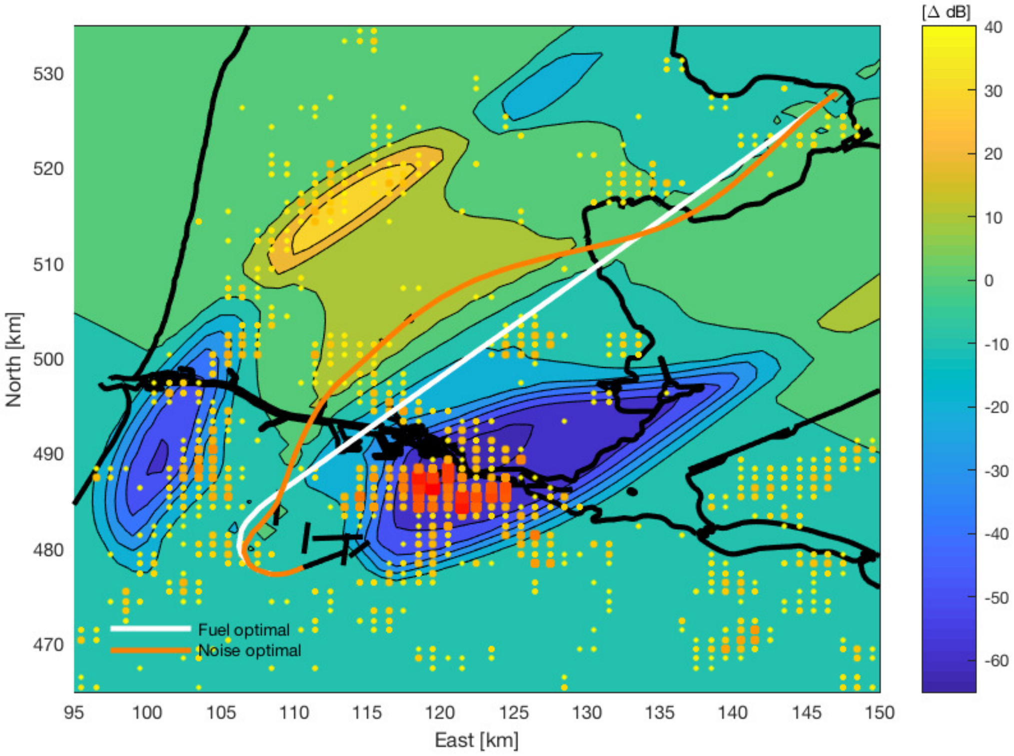

Figure 5.13: Difference in received SEL values between the noise and fuel optimal trajectories of case C1.6.

When analysing the difference in SEL for the fuel and noise optimal trajectories in low atmospheric attenuation conditions, it is clear that the SEL is reduced greatly for a large area as is illustrated by Figure 5.13. The main contribution to the 50% reduction in the number of awakenings is obtained by relieving Amsterdam. In exchange, the SEL values north of Zaandam increase by a lot. However the SEL observed is lower than the threshold to obtain awakenings.

To reduce the number of awakenings, the ground track has been optimised as much as possible. The result is a trajectory with large swings around Amsterdam and Hoorn.

The noise optimal trajectories in high and low atmospheric attenuation conditions together with the noise optimal trajectory of the reference case are analysed in more detail in Figure 5.14 for the initial 120 s of the velocity profile, and the entire altitude and thrust setting profile.

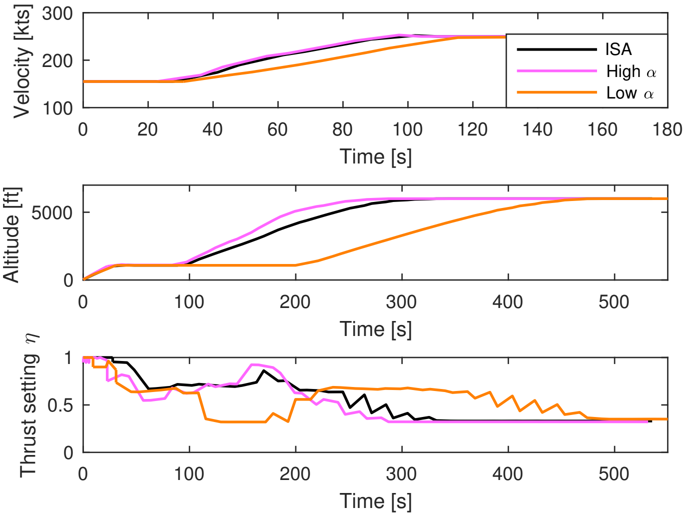

Figure 5.14: Comparison of the velocity, altitude and thrust setting of the noise optimal trajectories of cases C1.1., C1.5. and C1.6.

It is noticeable that different vertical trajectories are the most noise optimal. In low atmospheric attenuation conditions, it is optimal to stay at lower altitude with lower thrust setting to make use of lateral attenuation and obtain narrow noise contours. The velocity is also increased slightly later and at a lower acceleration rate. While the reference case initiates climb after 100 s, a slightly less steep climb is initiated after 200 s. On the other hand, in high atmospheric attenuation conditions, the aircraft climbs earlier and faster than the reference case. The velocity profile matches the reference case. The increased source noise level and the weaker effect of lateral attenuation is mainly diminished by the high absorption level.

Comparing the three-dimensional trajectories in Figure 5.15, it is observed that the climb in high atmospheric attenuation conditions is initiated at the same location as for the reference case. On the other hand, in low atmospheric attenuation conditions, the aircraft stays low until passing Zaandam. After passing west of Zaandam, thrust is increased to reach its final altitude before swinging past Hoorn.

The ground tracks of each noise optimal trajectory is presented in Figure 5.16. It is clearly observed that in low atmospheric attenuation conditions, the ground track is optimised to reduce the noise impact. A sharper initial turn is made to initially fly away from populated areas followed by large swings around Amsterdam and Hoorn. On the other hand, the noise optimal trajectory in high atmospheric attenuation is similar to the reference case. However, the trajectory consists of more straight segments.

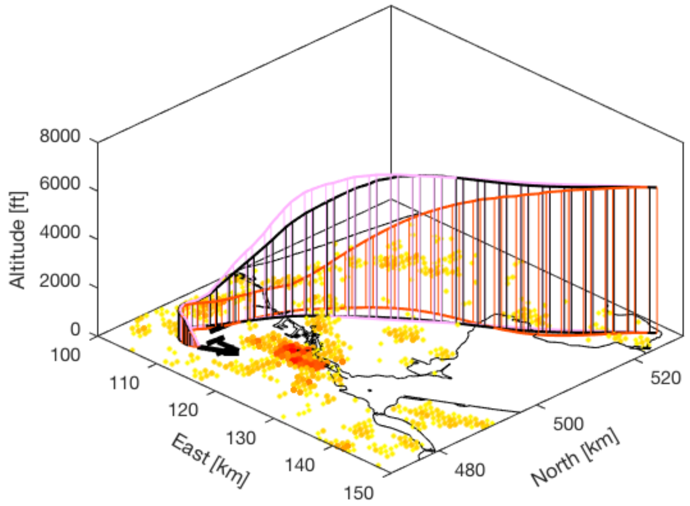

Figure 5.15: Comparison of the three dimensional trajectories of cases C1.1., C1.5. and C1.6.

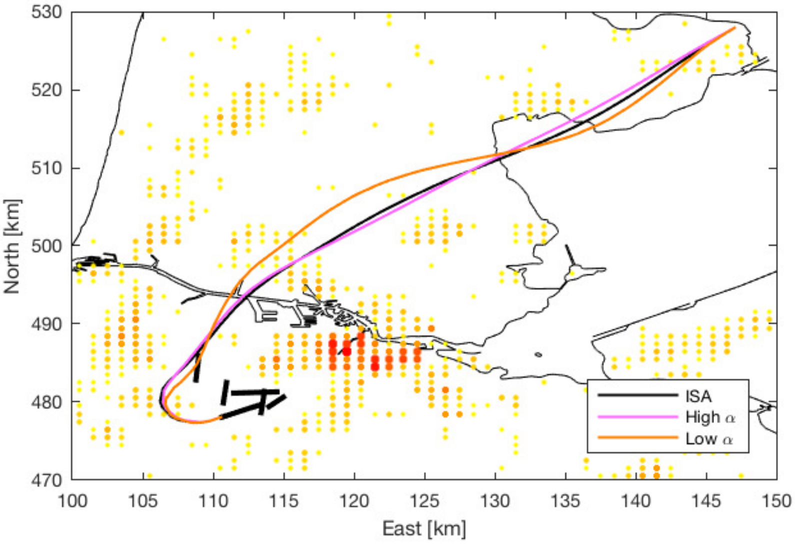

Figure 5.16: Comparison of the ground track of the noise optimal trajectories of cases C1.1., C1.5. and C1.6.

Effect of air temperature on the aircraft performance model. It is noticed that in high atmospheric attenuation conditions, the noise optimal thrust setting is in general lower than in the other trajectories in the initial phase of flight where all trajectories fly the same trajectory.

The APM makes use of the pressure and temperature ratios in an off-standard atmosphere in order to obtain the pressure altitudes. Table 5.8 analyses the thrust and drag at full take-off throttle setting with equal velocity and mass of the aircraft in ISA conditions, in 30°C in high atmospheric attenuation conditions and in -10°C in low atmospheric attenuation. It is noticed that 16% more thrust is available, with an increase of 8% in drag resulting in a 22% larger excess thrust in higher temperature conditions compared to ISA conditions.

In colder temperatures, the aircraft operates at higher pressure altitudes. However, with resulting larger density, lower aerodynamic forces of thrust, lift and accordingly drag are obtained. This is caused by a smaller Reynolds number $Re = \frac{\rho \cdot V \cdot l}{\mu}$, in which ρ is the air density, V the airspeed, l the characteristic length of the airfoil and μ the dynamic viscosity coefficient. The dynamic viscosity coefficient reduces with air temperature, resulting in larger Reynolds number [75]. The aerodynamic coefficients are obtained by comparing it to a $\frac{1}{Re}$-term, meaning that with larger Reynolds number, the aerodynamic coefficient will decrease.

Table 5.8: Comparison of excess power for cases C1.1, C1.5. and C1.6..

	Time [s]	**Thrust setting** η [-]	**Thrust** [kN]	**Drag** [kN]	**Excess thrust** [kN]
ISA/15°C	1	1	162.1	63.7	98.3
High α/30°C	1	1	188.6	68.6	120.0
Low α/-10°C	1	1	160.1	56.8	103.3

The 22% increase is large but is a result of the APM and results from the temperature and pressure ratio. As this value cannot be verified, it can be speculated that the BADA might not be the optimal tool to simulate non-ISA conditions.

5.3.4. Conclusion and Discussion

Case 1 was defined to identify the influence of various weather conditions on the noise impact and the noise optimal trajectory for a departure procedure characterised by flying over densely populated areas. Simulations using ISA conditions, the ISA conditions enhanced with wind, and conditions in which the atmospheric absorption is higher and lower than in ISA conditions were performed. The noise optimal trajectory in ISA condition is used as reference condition to compare the noise optimal trajectory in different weather conditions.

In ISA conditions, more than 20% of awakenings are reduced with less than 2% increase in both fuel usage and flight time. Once the aircraft obtains the final velocity, climb is initiated. The climb is initiated just after the initial turn. The ground track makes a wider swing around the most populated areas.

With the inclusion of wind, the number of awakenings for the fuel optimal cases varies a with the wind direction and velocity. Furthermore, the fuel usage and flight time is influenced depending on whether head- or tailwind is encountered. The inclusion of wind does not alter velocity and vertical profile of the noise optimal trajectories much compared to the reference case. For the ground track, the wideness of the initial turn and varies wind direction if a tail wind can be obtained in the turn. when flying past the most densely populated area, the ground track varies around the ground track in ISA conditions. The variation is obtained in the direction upwind of the aircraft as shadow zones are located there. Increasing the wind velocity, the variation converges with the noise optimal ISA ground track.

The influence of air temperature and relative humidity is analysed using the atmospheric attenuation coefficient. With increasing atmospheric attenuation conditions, the number of awakenings decrease. Compared to the reference case, a steeper climb and a ground track that consists of more straight segment is flown. on the other hand, the velocity profile matches the reference case.

On the contrary, with decreasing atmospheric coefficients, the number of awakenings increase. Compared to the reference case, the aircraft accelerates at a lower rate, stays at a lower altitude for a longer time period and the ground track is mainly optimised to reduce the noise. This results in large swings around the densely populated area are made.

At higher temperatures where the engine operates in the flat rating, lower thrust settings are used to obtain similar thrust levels as in ISA conditions. This results in lower fuel usage, and source noise levels.

To analyse the weather conditions in which the most awakenings are reduced with respect to the fuel usage, the Pareto front in each atmospheric condition is normalised and presented in Figure 5.17. Furthermore the figure is used to analyse convergence.

Analysing the figure, it can be concluded that only in low atmospheric attenuation conditions, a satisfactory convergence is obtained. Except in ISA and in ISA conditions with a southeastern wind, all other conditions follow a similar trend as in low atmospheric attenuation conditions. These conditions show a possibility to be optimised for a larger k_{noise} value, however convergence issue encountered in the propagation model is limiting this value.

Figure 5.17b presents the normalised Pareto front without the low atmospheric attenuation conditions. The increase in fuel usage for the different conditions are similar, except for the 5 kts Western wind. There is no relation to be identified between the wind speed or wind direction resulting in a larger reduction in awakenings or increase in fuel usage. The second largest reduction in awakenings is obtained in high atmospheric attenuation conditions.

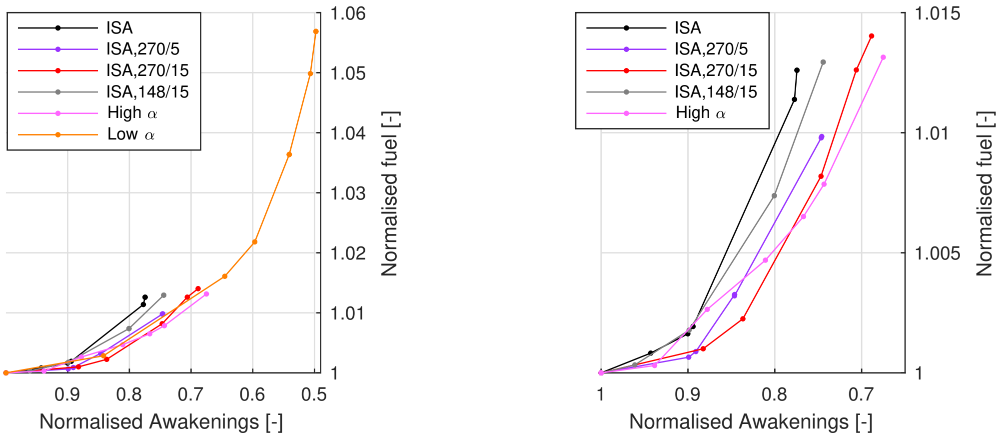

(a) All atmospheres.

(b) All atmospheres except 6.

Figure 5.17: Normalised Pareto front of all atmospheres considered in Case 1.

5.4. Case 2: Arnem 3E Departure to IVLUT

Case 2 simulates the departure from runway 18L towards way point IVLUT. The goal of this case is the same as for Case 1. The difference between Case 1 is that this departure procedure flies over less densely populated areas and the population is concentrated at the initial and final point of this procedure. Furthermore, the trajectory is shorter implying lower flight time.

Similar to Case 1, the reference case in ISA conditions is analysed in Section 5.4.1, followed by the analysis of the inclusion of wind in ISA conditions in Section 5.4.2 and the analysis of different air temperature and relative humidity combinations in Section 5.4.3.

The results for all k_{noise} values simulated in between the fuel and noise optimal trajectory is presented in Section C.2. To illustrate the change in noise contour lines, the appendix also presents the noise contour lines of the fuel and noise optimal trajectories.

Before the analysis of the simulations, the atmospheric conditions and additional constraints that hold for this case are discussed.

Atmosphere. To relate the noise optimal trajectories between the Spijkerboor departure and Arnem departure, similar atmospheric conditions as in Case 1 are simulated and are presented in Table 5.9. For the orientation of the wind, a southwestern wind direction is simulated in order to diminish the shadow zones around the densely populated areas around Amsterdam. As Case 1 presented the effect of an increasing wind velocity, one wind velocity of 15 kts is simulated.

Table 5.9: Atmosphere parameters for Case 2.

		T_0 [K]	λ [K·m^{-1}]	RH [%]	z_v [m]	$v_0(z_v)$ [kts]	ψ_W [°]	σ [N·s·m^{-4}]
Atm. 1	ISA	288.15	-0.0065	70	10	0	0	250·10^3
Atm. 5	High α	303.15	-0.0065	5	10	0	0	250·10^3
Atm. 6	Low α	263.15	-0.0065	5	10	0	0	250·10^3
Atm. 7	ISA,210/15	288.15	-0.0065	70	10	15	30	250·10^3

Constraints. Again, the initial and final conditions for the position and velocity, and the initial heading are constrained. The position coordinates and heading match the departure from runway 18L and way point IVLUT and are tabulated in Table 5.10.

Table 5.10: Initial and final conditions for Case 2.

Constraint	Initial value	Final value	Unit
Position (x,y)	(113 384, 478 299)	(146 075, 472 799)	km
Altitude	35	6000	ft
Velocity	155	250	kts
Heading	183	free	°

5.4.1. Reference Case

The results of the optimal fuel and noise trajectories for the reference case in atmosphere 1 is presented in Table 5.11. Compared to the percentage reduction in awakenings observed for the Spijkerboor departure procedure, a much lower percentage is obtained. This effect is expected as most population lives near the initial or final position of the aircraft, reducing optimisation possibilities.

Table 5.11: Fuel and noise optimal trajectory characteristics of case C2.1.

Case	Objective	Fuel [kg]	ΔFuel [%]	Awakenings	ΔN_A [%]	Time [s]	ΔTime [%]
C2.1.1	Fuel	381.0	-	4612	-	277.0	-
C2.1.8	Fuel + 0.02 $\cdot N_A$	386,6	+1.48	4352	-5.64	284.7	+2.78

Figure 5.18 presents the number of awakenings against the fuel usage curve. It is noted that again a relative large reduction in awakenings is obtained with the implementation of small k_{noise} in the cost functional. Large jumps in k_{noise} values are observed. One of the reasons of this behaviour is the location of the population at both initial and final position in combination with the short departure procedure. Reducing sound levels at take-off reduces the range of the state and control variables as the final conditions still have to be satisfied.

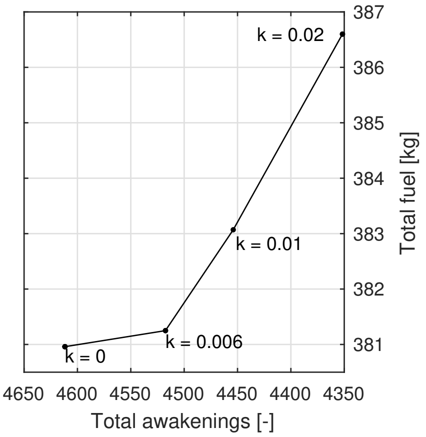

Figure 5.18: Total awakenings against total fuel usage for case C2.1. with according k_{noise} values.

The difference in SEL observed by the receivers for the fuel and noise optimal trajectory is presented in Figure 5.19. It is noted that the greatest reduction in SEL is obtain in the most highly populated area of Amsterdam and south of Uithoorn. This is achieved by a making a southern swing in the noise optimal trajectory where in the fuel optimal trajectory, the segment is straight. Near the end of the trajectory, Hilversum is relieved as much as possible by swinging to the north.

The trajectories are evaluated in more detail in Figure 5.20. Figure 5.20a illustrates the initial 200 s of the velocity, and the entire altitude and thrust setting profile of both trajectories. It is noted that the aircraft in the noise optimal trajectory accelerates slower. Once reaching the final velocity, the climb is initiated. The acceleration is decreased once a velocity of 200 kts is reached. This enables lower thrust settings and accordingly a lower source noise. Wide swings away from the inhabited areas are made in order to reduce the sound level in the most densely populated areas.

Figure 5.21 presents the three-dimensional trajectories of the fuel and noise optimal trajectories. As was observed in Figure 5.9 for the Spijkerboor departure, the aircraft start climbing once it has completed the initial turn in the noise optimal trajectory. The final altitude is reached just before arriving at the final position. This implies that the trajectory reduces the number of awakenings by staying at lower altitude, making use of stronger lateral attenuation until it is required to climb in order to reach the final altitude with reasonable thrust settings.

As in Case 1, for the following atmospheric conditions, no separate analysis of the fuel and noise optimal trajectories is performed as in most atmospheric conditions similar trajectories are obtained to the one presented in Figure 5.20.

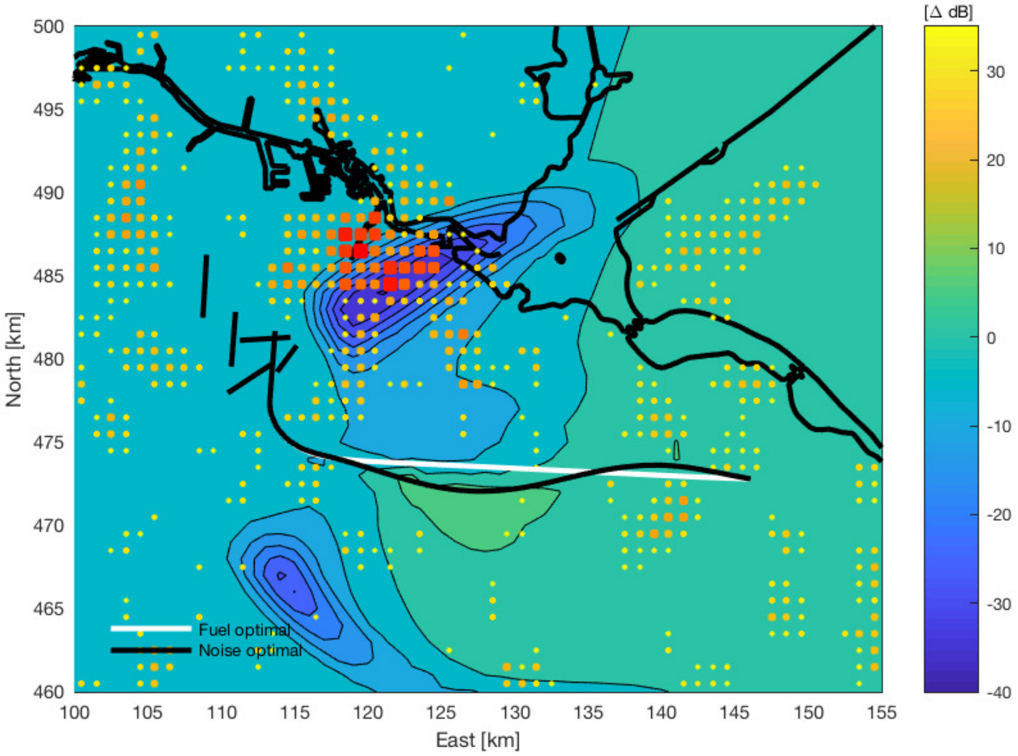

Figure 5.19: Difference in received SEL values between the noise and fuel optimal trajectories for case C2.1.

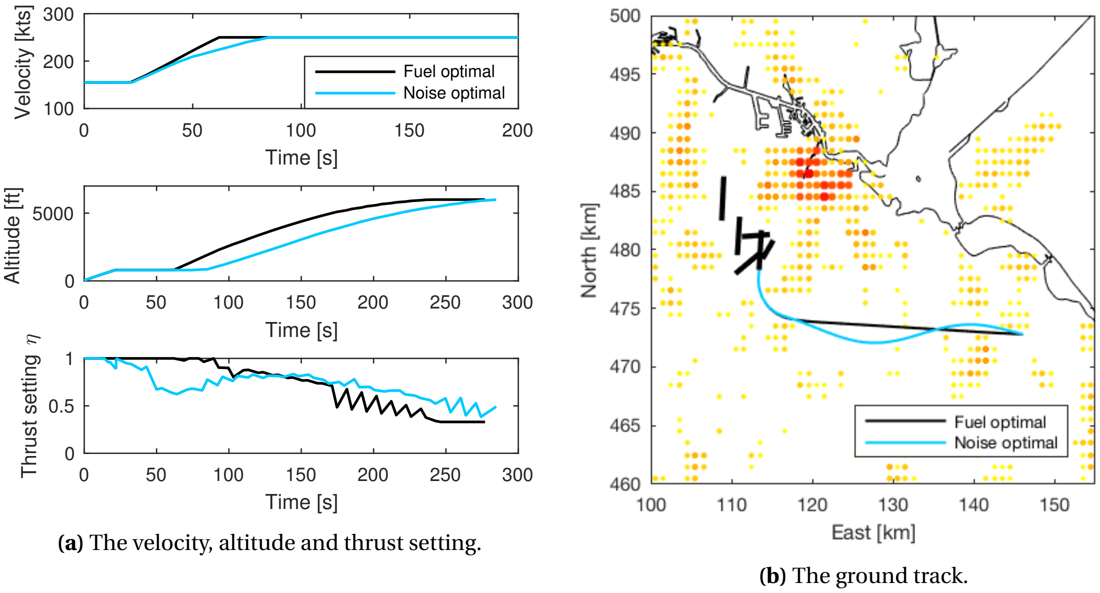

(a) The velocity, altitude and thrust setting.

(b) The ground track.

Figure 5.20: Comparison of the velocity, altitude and thrust setting and ground track between the noise optimal trajectories of case C2.1.

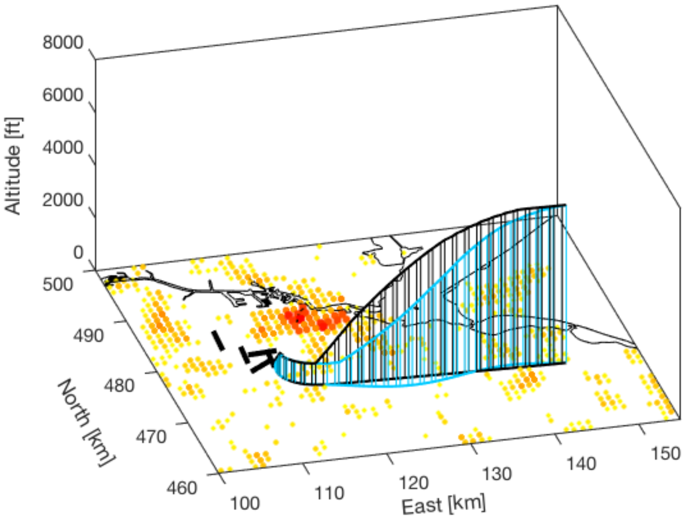

Figure 5.21: Comparison of the three dimensional trajectories of case C2.1.

5.4.2. Wind Conditions

In the Spijkerboor departure, it was noticed that the influence of wind velocity and direction does not influence the noise optimal trajectory much. To analyse the influence of wind for the Arnem departure, a 15 kts southwestern wind blowing towards the most densely populated area, denoted as atmosphere 7, is simulated. A similar percentage in reduction of the number of awakenings is achieved as presented by Table 5.12, with minimal increase in fuel usage and flight time compared to the reference case.

Table 5.12: Fuel and noise optimal trajectory characteristics of case C2.7.

Case	Objective	Fuel [kg]	ΔFuel [%]	Awakenings	ΔN_A [%]	Time [s]	ΔTime [%]
C2.7.1	Fuel	402.6	-	4406	-	305.4	-
C2.7.7	Fuel + 0.01 $\cdot N_A$	403,4	+0.18	4150	-5.80	306.6	+0.40

Analysing the number of awakenings against the total fuel usage curves in Figure 5.22, it is noted that in this particular wind direction and velocity, convergence difficulties for larger k_{noise} values arise after an initial relatively large reduction in awakenings. One of the reason of this behaviour might be the location of the shadow zone upwind over Aalsmeer and Uithoorn. In order to reduce the noise impact in this region, while not creating new awakenings in Amsterdam, this part of the trajectory is constrained. However, a similar reduction in the number of awakenings is obtained as for the reference case. The curve is shifted to the right with increasing fuel usage due to head wind during the initial phase of flight. With respect to the fuel optimal trajectory of the reference case, fuel usage is increased by 21 kg and the flight time is increased by 28 s.

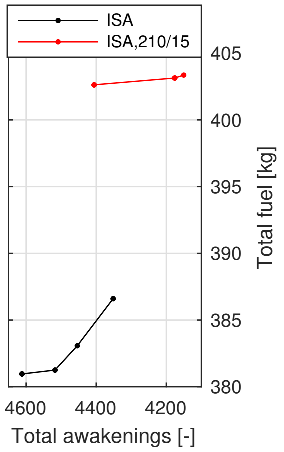

Figure 5.22: Total awakenings against total fuel usage for cases C2.1. and C2.7.

The difference in SEL observed is not very large as is presented by Figure 5.23. In the fuel optimal trajectory, only awakenings are obtained in the southern part of Amsterdam. The reduction in SEL is mainly in this area and in Uithoorn. Due to the effect of the wind, the reduction in SEL observed in the reference case in Figure 5.19 to the south of Uithoorn has shifted along with the wind. Hilversum is passed by slightly to the north of the fuel optimal trajectory as the wind shifts the shadow zones closer to the aircraft for observers upwind.

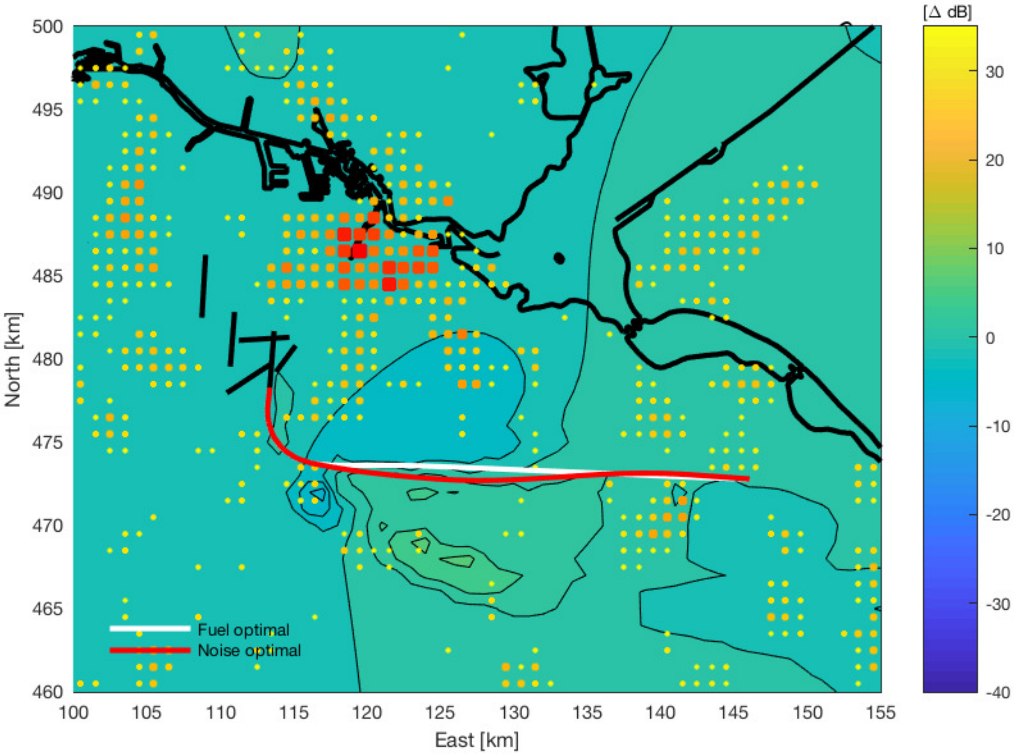

Figure 5.23: Difference in received SEL values between the noise and fuel optimal trajectories for case C2.7.

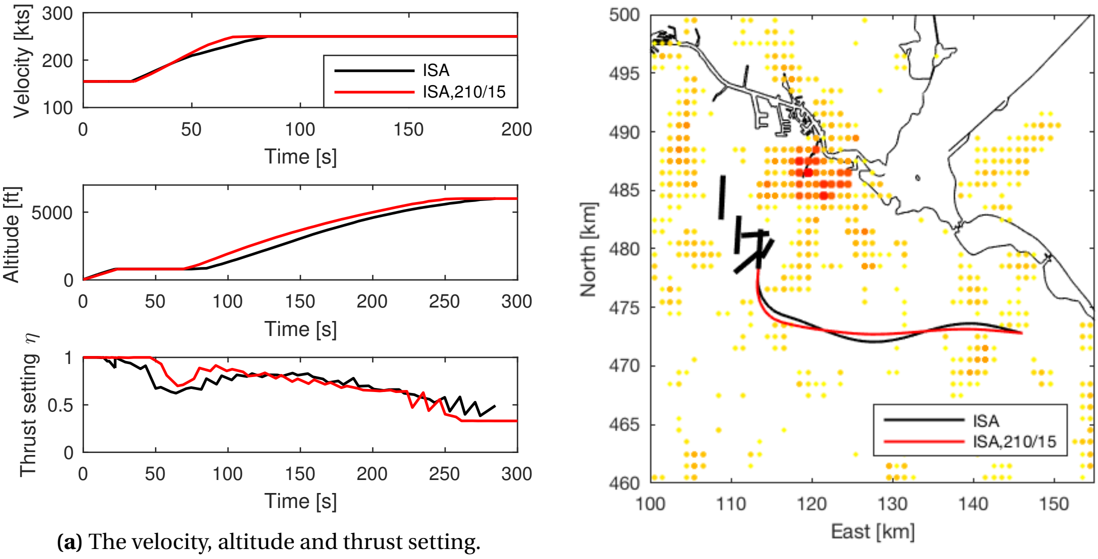

(a) The velocity, altitude and thrust setting.

(b) The ground track.

Figure 5.24: Comparison of the velocity, altitude and thrust setting and ground track between the noise optimal trajectories of cases C2.1. and C2.7.

The trajectories are evaluated in more detail in Figure 5.24. Figure 5.24a illustrates the initial 200 s of the velocity, and the entire altitude and thrust setting profile of both trajectories. The noise optimal trajectory in wind conditions shows more similarities to the fuel optimal trajectory of the reference case presented in Figure 5.20 than the noise optimal trajectory. This is a result of the lower noise contribution to the objective function. Near the final position, when passing Hilversum, the aircraft can fly by at a lower thrust setting, as illustrated by Figure 5.24b.

5.4.3. Varying Atmospheric Absorption Conditions

To analyse the influence of air temperature and relative humidity, the results of the high atmospheric attenuation conditions in atmosphere 5 and low atmospheric attenuation conditions in atmosphere 6 are presented in Table 5.13.

As observed in the previous case, very little awakenings are obtained in the high atmospheric attenuation conditions while very many awakenings are obtained in low atmospheric attenuation conditions. Furthermore, in colder temperatures a higher fuel usage is observed. However, the flight time shows a different behaviour. Unlike the Spijkerboor departure procedure, the flight time in warmer air temperature of atmosphere 5 result in lower flight time. The percentage wise reduction for both conditions are larger than in the reference case. This time, the highest reduction is observed in the high atmospheric attenuation conditions.

Table 5.13: Fuel and noise optimal trajectory characteristics of cases C2.5. and C2.6.

Case	Objective	Fuel [kg]	ΔFuel [%]	Awakenings	ΔN_A [%]	Time [s]	ΔTime [%]
C2.5.1	Fuel	378.0	-	1251	-	274.3	-
C2.5.8	Fuel + 0.05 $\cdot N_A$	383,4	+1.44	902	-27.94	280.4	+2.21
C2.6.1	Fuel	384.7	-	10107	-	275.2	-
C2.6.12	Fuel + 0.02 $\cdot N_A$	392.3	+1.98	9241	-8.57	287.5	+4.49

The total number of awakenings against the fuel usage for the Arnem departure is presented in Figure 5.25. The shift in the different curves is similar to the ones obtained in the Spijkerboor departure, as illustrated by Figure 5.11. In high atmospheric attenuation conditions, for similar percentage of increase in fuel usage and flight time, the number of awakenings is reduced by 28%. In low atmospheric attenuation conditions, an increase of 2% in fuel usage and 5% in flight time result in the reduction of the number of awakenings by 9%.

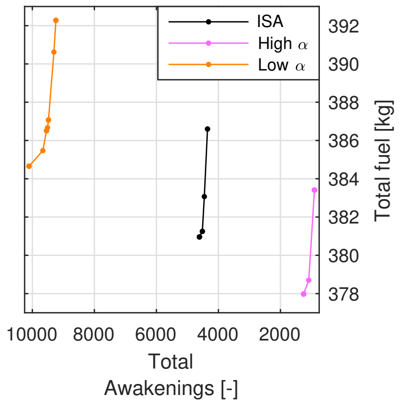

Figure 5.25: Total awakenings against total fuel usage for cases C2.1., C2.5. and C2.6.

When analysing the difference in SEL received by the observers for the fuel and noise optimal trajectory in high atmospheric attenuation conditions, it is clearly seen that Amsterdam, Uithoorn and Hilversum are mainly relieved of sound as illustrated by Figure 5.26. Main reduction is obtained by changing the ground track slightly. Although the SEL value is reduced by a lot in Amsterdam, in fact no awakenings are obtained in the fuel optimal trajectory.

A very different figure is presented in Figure 5.27, in which the difference in SEL for the fuel and noise optimal trajectory is compared for the low atmospheric attenuation conditions. Again, the densely populated centre of Amsterdam does not receive awakenings as the shadow zone location does not change due to a variation in absorption conditions. Main reduction in awakenings is obtained south of Amsterdam and in Amstelveen.

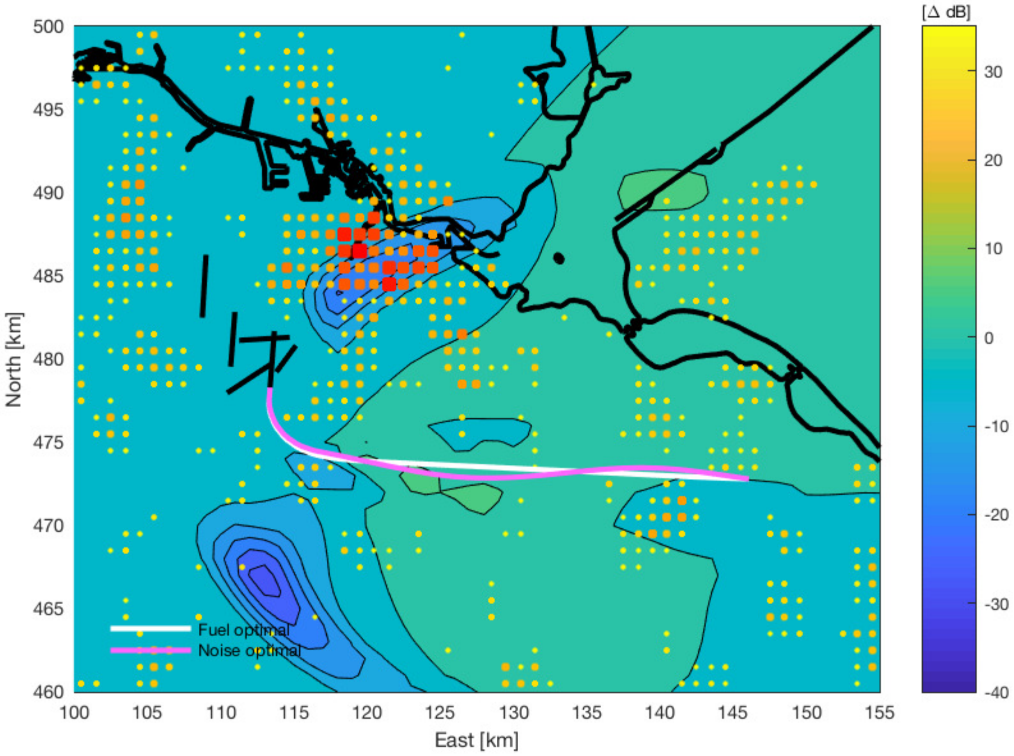

Figure 5.26: Difference in received SEL values between the noise and fuel optimal trajectories for case C2.5.

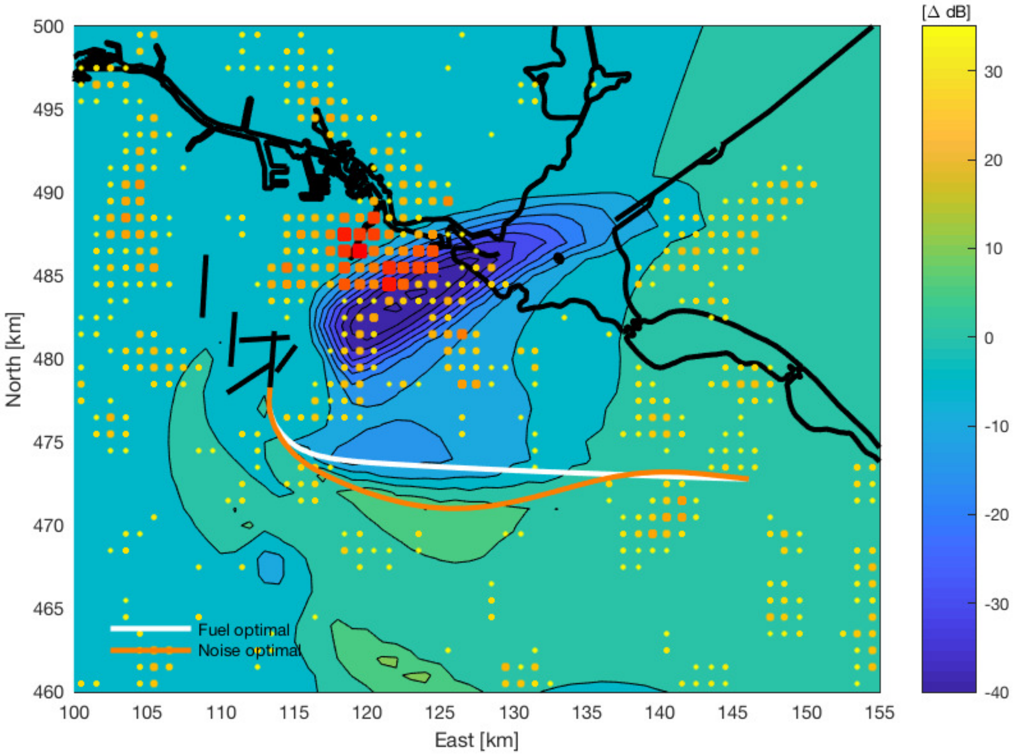

Figure 5.27: Difference in received SEL values between the noise and fuel optimal trajectories for case C2.6.

Analysing the noise optimal trajectories in more detail for the velocity for the initial 120 s, and the entire altitude and thrust settings profile in Figure 5.28, it is noted that the reference case and the low atmospheric attenuation conditions show large similarities in altitude and thrust settings profile. For the velocity profile, the low atmospheric attenuation conditions reaches the final velocity slightly earlier by having a greater acceleration.

On the other hand, in high atmospheric attenuation conditions the aircraft climbs at a greater climb gradient, while the velocity profile matches the reference case. The larger climb gradient can be achieved due to the high atmospheric attenuation resulting in larger propagation losses and thus lower SEL received on the ground. Furthermore, this is achieved by the increased performance in higher air temperature conditions in the APM, as discussed at the end of Case 1. This is clearly illustrated by analysing the thrust setting for the initial 50 s of flight, in which the trajectory flown is equal for all three simulations.

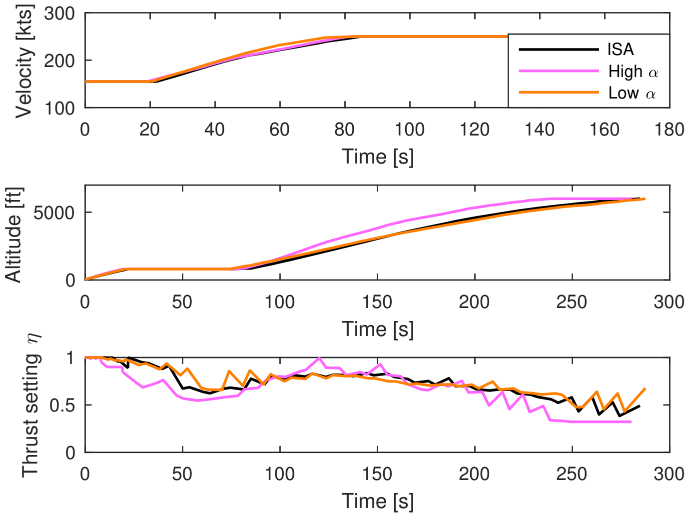

Figure 5.28: Comparison of the velocity, altitude and thrust setting between the noise optimal trajectories of cases C2.1., C2.5. and C2.6.

The three-dimensional trajectories are presented in Figure 5.29. While the climb is initiated at similar moment in time after the initial turn for all three cases, the actual location differs. It is clearly identified that the steeper climb of the trajectory in high atmospheric attenuation conditions result in the arrival at the final altitude before flying past Hilversum.

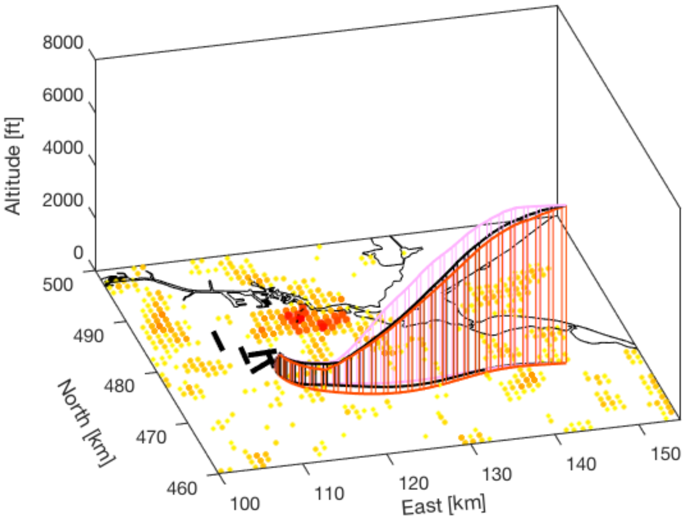

Figure 5.29: Comparison of the three dimensional trajectories of cases C2.1., C2.5. and C2.6.

Comparing the ground track of the different noise optimal trajectories in Figure 5.30, it is observed that with lower the atmospheric attenuation conditions, a wider initial turn is made. Subsequently, the second swing around Hilversum becomes less wide.

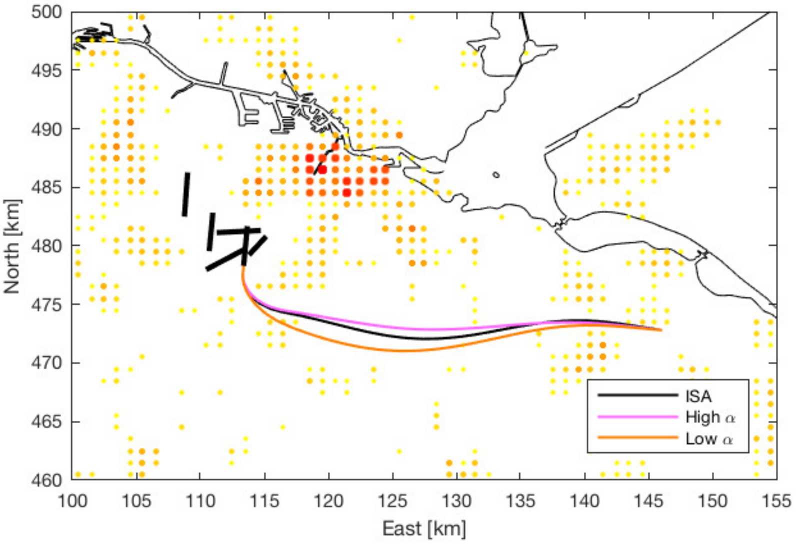

Figure 5.30: Comparison of the ground track between the noise optimal trajectories of cases C2.1., C2.5. and C2.6.

5.4.4. Discussion and Conclusion

Case 2 was defined to identify the influence of various weather conditions on the noise impact and the noise optimal trajectory for a departure procedure characterised by most of the population located at the initial and final position of the trajectory. As in Case 1, cases are simulated using ISA conditions, the ISA conditions enhanced with wind, and conditions in which the atmospheric absorption is higher and lower than in ISA conditions. Again, the noise optimal trajectory in ISA condition is used as reference condition.

In this section, only the findings not observed in Case 1 for the Spijkerboor departure are discussed.

In ISA conditions slightly more than 5% of the awakenings are reduced with an increase of less than 2% in fuel usage and 3% in flight time. Compared to the Spijkerboor departure, this is a much lower reduction in awakenings.

With the inclusion of a 15 kts southwestern wind, convergence difficulties arose for larger k_{noise} values, resulting in a noise optimal trajectory similar to the fuel optimal trajectory in the reference case. However, similar reduction in the number of awakenings is obtained as for the reference case with a lower fuel usage and flight time increase.

The air temperature and relative humidity influence the atmospheric attenuation conditions. With decreasing atmospheric attenuation, the initial turn is taken wider and a larger swing to the south of the ground track is observed. In low atmospheric attenuation conditions, faster acceleration and a similar climb as in the reference case is noticed. The largest reduction percentage wise is obtained in high absorption conditions.

To analyse the performance in different atmospheric conditions and to comment on the performance of the propagation model within the WAFORT, Figure 5.31 presents the normalised Pareto front for the different atmospheres.

In general, for the Arnem departure the awakenings are reduced by around 6%. Similar to the Spijkerboor departure procedure, the lowest reduction in percentage awakenings is observed in the reference case in ISA conditions. A remarkable reduction in awakenings is observed in the high atmospheric attenuation conditions. ISA conditions enhanced with a southeastern wind results in a very efficient reduction.

Again, in low atmospheric attenuation conditions, the normalised curve shows a desired shape. Implying that enough k_{noise} values have been run to obtain the noise optimal trajectory. ISA conditions are also satisfactory, but the ISA enhanced with wind and conditions in high atmospheric attenuation conditions show potential to obtain noise optimal trajectories at higher k_{noise} values.

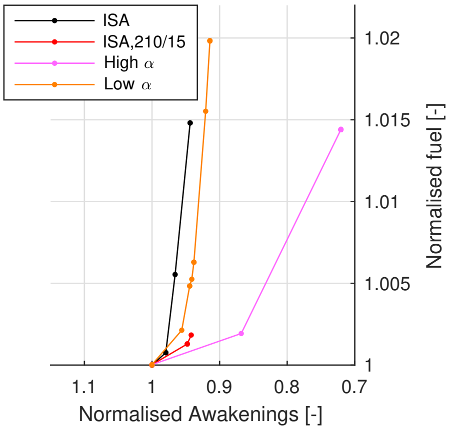

Figure 5.31: Normalised Pareto front of all atmospheres considered in Case 2.

5.5. Case 3: Real Day Simulation

With the separate effects on the noise optimal trajectories in ISA, varied wind conditions and varied atmospheric attenuation conditions defined in Case 1 and 2, it is of interest how much of an influence the atmospheric conditions have on daily operations. And if so, it is of interest of this research to conclude on whether the influences are large enough to implement weather-adaptive noise abatement procedures.

Daily operations are simulated by three different weather conditions encountered during the course of a year at Amsterdam Airport Schiphol (AAS): ISA-like, warm and cold weather conditions. The weather data is obtained from actual weather data collected by the University of Wyoming[1] and the website Time and Date[2].

The weather characteristics of the different dates are summarised in Table 5.14. Due to the orientation of the runways, no northern wind is simulated. An additional cold weather condition is simulated as an eastern wind results in tailwind departures from runway 24.

Table 5.14: Weather characteristics of the real day simulations.

Case	Date	Temperature [°C]	Relative Humidity [%]	Wind [$\text{m}\cdot\text{s}^{-1}$]	Wind direction
ISA	22 April 2018	20	88	4	W (260 - 280)
Warm	26 July 2018	29	15	3	S (170)
Cold	2 March 2018	-2	58	6	E (90)
Cold	16 March 2018	-1	100	2	SSW (225)

The following sections discus the different weather conditions and their noise optimal trajectory. In Section 5.5.1 the ISA-like condition is discussed, followed by Section 5.5.2 discussing the findings in warm weather conditions. The cold condition is discussed last in Section 5.5.3. In each section, first the Spijkerboor departure is evaluated, followed by the Arnem departure. In cold weather conditions, also an analysis is performed on the influence of different ground surfaces as in cold conditions, snow might cover the ground.

For the Arnem departure, limited new findings have been obtained performing the simulations. Thus a brief discussion is presented for each atmospheric conditions in their respective section, and an elaborate analysis is performed in Appendix B.2.

5.5.1. International Standard Atmosphere-Like Weather Conditions

The weather on April 22 is characterised as nice weather in the Netherlands. The temperature and relative humidity are a little bit higher than in ISA conditions and a gentle western breeze from the North Sea blows over AAS. The atmospheric parameters for this case are defined in Table 5.15. The wind results in a tailwind component during most of the flight for both departure procedures.

---

[1] http://weather.uwyo.edu/surface/meteorogram/europe.shtml

[2] https://www.timeanddate.com/weather/@2747542/historic

Table 5.15: Atmosphere parameters for Case 3 in ISA-like weather conditions.

		T_0 [K]	λ [K·m^{-1}]	RH [%]	z_v [m]	$v_0(z_v)$ [kts]	ψ_W [°]	σ [N·s·m^{-4}]
Atm. 8	20°C,88%,260-280/4	293.15	-0.0065	88	10	4	80-100	250·10^3

To evaluate the influence of the air temperature and relative humidity, Figure 5.32 presents the atmospheric attenuation coefficient α of atmosphere 8 against the previously discussed atmospheres in ISA conditions, high atmospheric attenuation conditions and low atmospheric attenuation conditions. For the frequencies up to 3000 Hz, the attenuation coefficient is nearly identical to the coefficients obtained in ISA conditions. For higher frequencies, the coefficient is slightly lower.

As the attenuation coefficient is slightly lower, the ISA conditions and low atmospheric attenuation conditions are used to evaluate the noise optimal trajectory in ISA-like conditions.

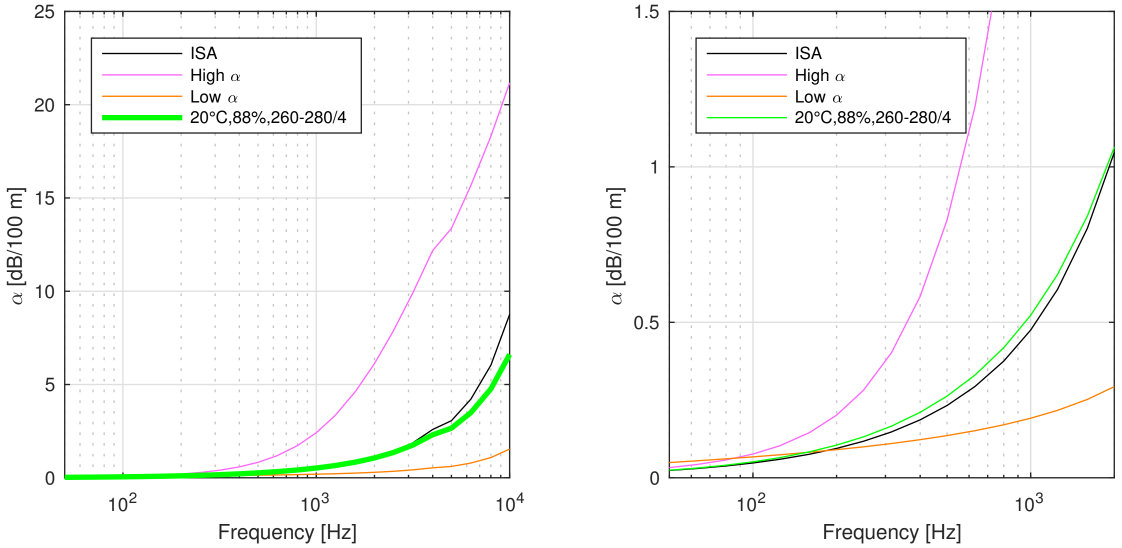

(a) Frequency range of 50 to 10000 Hz. **(b)** Frequency range of 50 to 2000 Hz.

Figure 5.32: Atmospheric attenuation coefficient α for different atmosphere for case C3.8.

Table 5.16: Fuel and noise optimal trajectory characteristics of cases C3.SPY.8., C1.1, C1.5. and C1.6.

(a) Case C3.SPY.8.

Case	Objective	Fuel [kg]	ΔFuel [%]	Awakenings	ΔN_A [%]	Time [s]	ΔTime [%]
C3.SPY.8.1	Fuel	547.6	-	8293	-	506.6	-
C3.SPY.8.7	Fuel + 0.014 $\cdot N_A$	566,6	+3.47	5415	-34.70	528.4	+4.31

(b) Case C1.1., C1.5. and C1.6.

Case	Objective	Fuel [kg]	ΔFuel [%]	Awakenings	ΔN_A [%]	Time [s]	ΔTime [%]
C1.1.1	Fuel	559.5	-	9904	-	525.8	-
C1.1.7	Fuel + 0.01 $\cdot N_A$	566.5	+1.26	7671	-22.55	535.3	+1.82
C1.5.1	Fuel	556.2	-	2994	-	526.2	-
C1.5.8	Fuel + 0.02 $\cdot N_A$	563.5	+1.31	2021	-32.49	531.5	+1.00
C1.6.1	Fuel	565.2	-	22801	-	521.5	-
C1.6.9	Fuel + 0.016 $\cdot N_A$	597.3	+5.69	11350	-50.24	558.6	+7.11

Spijkerboor. The results of the fuel and noise optimal trajectory in atmosphere 8, as well as the previous results in ISA conditions in atmosphere 1, high atmospheric attenuation conditions in atmosphere 5 and low atmospheric attenuation conditions in atmosphere 6 are presented in Table 5.16. The total awakenings for the fuel optimal case is less than the number observed in atmosphere 1 due to the wind relieving the population upwind of the initial turn and Haarlem. The wind is not strong enough to obtain SEL values higher than the threshold in the densely populated area of Amsterdam. The slightly larger atmospheric attenuation over the lower frequencies might also contribute in the lower number of awakenings. Furthermore the effect of the tailwind on the fuel usage for the fuel optimal case is evident.

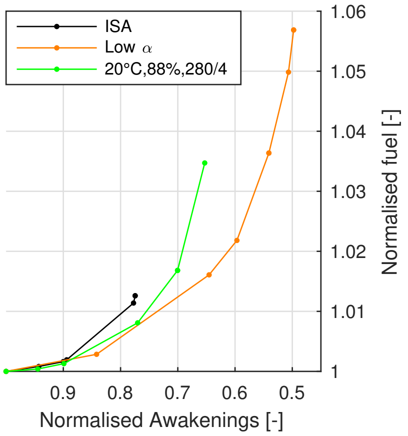

Figure 5.33: Normalised awakenings against fuel usage for cases C1.1., C1.6. and C3.SPY.8.

The normalised Pareto front for case C3.SPY.8. together with the ones obtained in case C1.1. in ISA conditions and in case C1.6. in low atmospheric attenuation conditions are presented in Figure 5.33. It is observed that in ISA-like conditions the flattening in reduction of awakenings is observed with increasing k_{noise} values. Both decrease in awakenings as increase in fuel usage lies in between the two other atmospheric conditions.

The noise optimal trajectories are analysed in more detail in Figure 5.34 for the initial 120 s for the velocity profile, and the entire altitude and thrust settings profile. Analysing the velocity profile, the ISA-like conditions is nearly identical to the ISA conditions.

In the vertical profile, it is observed that the trajectory shows similar characteristics as is observed in the trajectory in low atmospheric attenuation conditions. However, this time a three-step climb is performed. The first climb after take-off is to clear the initial climb prescribed by the NADP. In the second climb, the aircraft climbs an additional 500 ft at the same moment when the trajectory in ISA conditions initiates its climb towards the final altitude, as observed in the three-dimensional trajectories of the different cases illustrated by Figure 5.35. The final climb is initiated at the same moment when the climb in low atmospheric attenuation conditions is initiated. From these observations, for this specific departure procedure and GIS combination, there seems to be two points when climb can be initiated where the the impact on the awakenings due to the increased thrust to climb is minimal. In between these optimal points, aircraft will not climb due to their vicinity to populated areas.

The thrust setting is a combination of both ISA and low atmospheric attenuation conditions in which first the ISA condition setting is followed, succeeded by the low atmospheric attenuation condition setting. No use is made of the increased wind velocity at higher altitudes to increase ground speed without increasing the thrust.

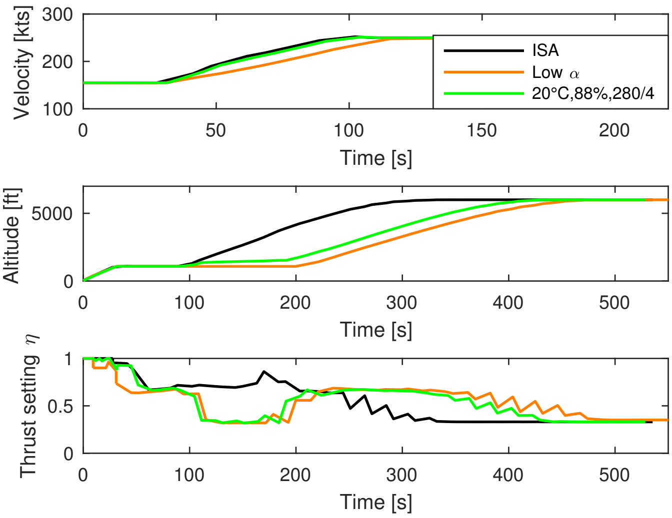

Figure 5.34: Comparison of the velocity, altitude and thrust setting between the noise optimal trajectories of cases C1.1., C1.6. and C3.SPY.8.

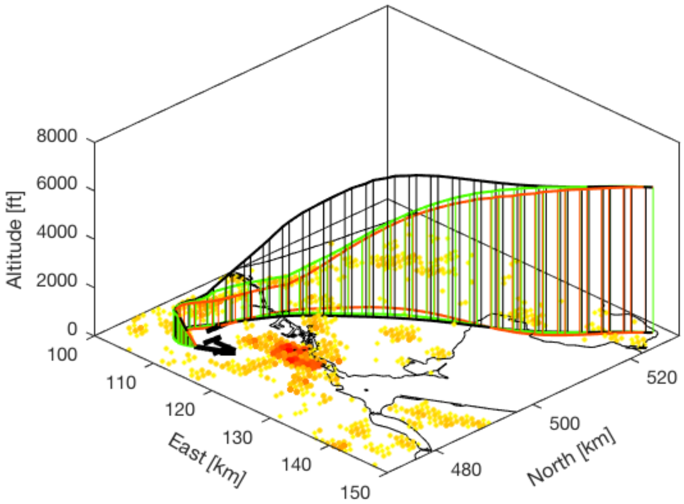

Figure 5.35: Comparison of the three dimensional trajectories of cases C1.1., C1.6. and C3.SPY.8.

The comparison in ground track is presented in Figure 5.36, together with the optimal noise trajectory obtained for different wind profiles discussed in Section 5.3.2. It is observed that the ground track is more similar to the ground track obtained in different wind profiles than to the ground track in low atmospheric attenuation conditions. This matches the conclusion made in Section 5.3.2, that the ground track with the inclusion of wind and in ISA conditions does not differ much.

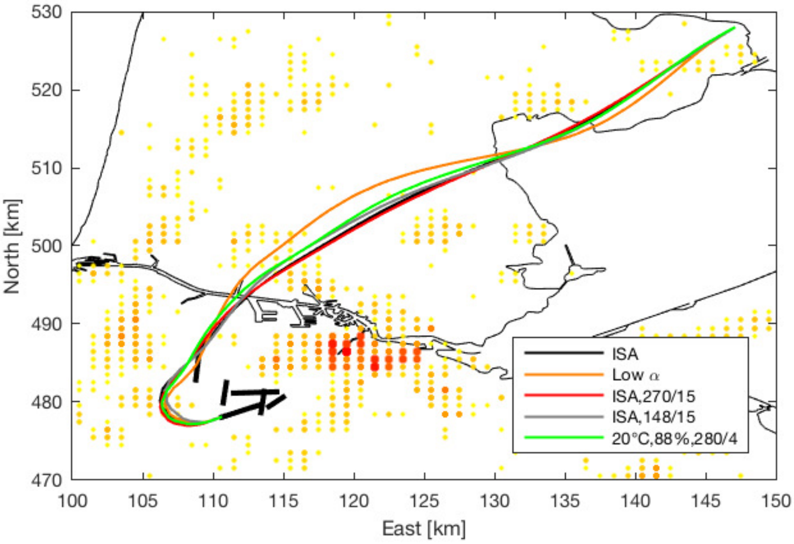

Figure 5.36: Comparison of the ground track between the noise optimal trajectories of cases C1.1., C1.6., C1.3., C1.4. and C3.SPY.8.

Arnem. The results of the noise optimal trajectories obtained in ISA-like conditions as well as in ISA conditions in atmosphere 1, low atmospheric attenuation conditions in atmosphere 6 and in ISA conditions enhanced with a 15 kts southwestern wind in atmosphere 7 are presented in Table 5.17. In the ISA-like conditions, the western wind relieves some population living to the west of the initial straight segment after take-off. Combined with the slightly higher atmospheric attenuation for the lower frequencies, this results in lower number of awakenings for the fuel optimal case compared to the reference case. As is observer in ISA conditions enhanced by wind, the wind ensures that with a minimal amount of increase in fuel usage, a relatively large reduction in the percentage of awakenings is obtained.

Table 5.17: Fuel and noise optimal trajectory characteristics of cases C3.ARN.8., C2.1., C2.6. and C2.7.

(a) Case C3.ARN.8.

Case	Objective	Fuel [kg]	ΔFuel [%]	Awakenings	ΔN_A [%]	Time [s]	ΔTime [%]
C3.ARN.8.1	Fuel	380.5	-	3862	-	278.9	-
C3.ARN.8.5	Fuel + 0.04 $\cdot N_A$	382,6	+0.56	3620	-6.28	282.1	+1.13

(b) Case C2.1., C2.6. and C2.7.

Case	Objective	Fuel [kg]	ΔFuel [%]	Awakenings	ΔN_A [%]	Time [s]	ΔTime [%]
C2.1.1	Fuel	381.0	-	4612	-	277.0	-
C2.1.8	Fuel + 0.02 $\cdot N_A$	386,6	+1.48	4352	-5.64	284.7	+2.78
C2.6.1	Fuel	384.7	-	10107	-	275.2	-
C2.6.12	Fuel + 0.02 $\cdot N_A$	392.3	+1.98	9241	-8.57	287.5	+4.49
C2.7.1	Fuel	402.6	-	4406	-	305.4	-
C2.7.7	Fuel + 0.01 $\cdot N_A$	403,4	+0.18	4150	-5.80	306.6	+0.40

The normalised Pareto fronts for the different cases are presented in Figure 5.37. It is observed that in the ISA-like condition the Pareto front of low atmospheric attenuation conditions is followed. However the curve stops midway, not having the same smoothness as in low atmospheric conditions. Furthermore, the percentage reduction in awakenings is similar to the other cases.

The noise optimal trajectory in ISA-like weather conditions show large similarities with the noise optimal trajectory in ISA conditions with a southwestern wind, discussed in Section 5.4.2. Only the noise optimal ground track differs slightly, in which the initial turn matches the noise optimal ground track in ISA conditions without wind. A more elaborate discussion is presented in Appendix B.2.1.

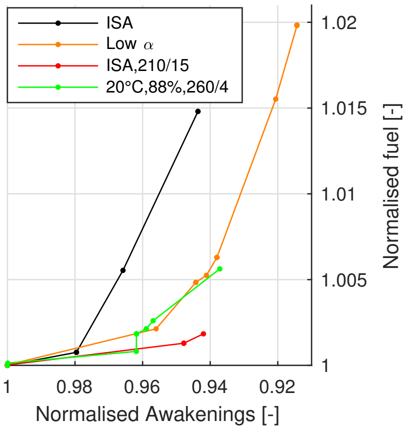

Figure 5.37: Normalised awakenings against fuel usage for cases C2.1., C2.6., C2.7. and C3.ARN.8.

Conclusion. The ISA-like weather condition is characterised by a gentle breeze from southeastern direction. The atmospheric attenuation up to 2000 Hz is slightly larger than the values obtained in ISA conditions, where after it is slightly smaller than the values obtained in ISA conditions for larger frequencies. A combination of the wind direction and the larger atmospheric attenuation over the lower frequency results in lower awakenings for the fuel optimal case for both departure procedures.

For the Spijkerboor departure, tailwind result in lower fuel usage and flight time. The velocity profile of the noise optimal trajectory is identical to the noise optimal trajectory in ISA conditions. However, the vertical profile consists of a three step climb in which the aircraft stays at a lower altitude for the initial 200 s. The ground track is dominated by the wind, while it does not differ too much from the ground track in ISA conditions. Satisfactory convergence is obtained.

For the Arnem departure, effect of tailwind component observed in the lower fuel usage in the fuel optimal trajectory compared to the reference case. However, as headwind is experienced in the initial part of the flight, the flight time is increased. The velocity and altitude profile of the noise optimal trajectory matches that the of the atmosphere with wind in Case 2. The ground track makes a tighter initial turn as a combination of favourable winds and as Case 2 concluded that for higher atmospheric attenuation, a tighter initial turn is more noise-optimal.

5.5.2. Warm Weather Conditions

July 26 is characterised by high temperatures with low relative humidity conditions. The atmospheric conditions of this day are translated to variables of interest to the WAFORT in Table 5.18. A light breeze blowing from the southeast results in a crosswind component for the Spijkerboor departure, while the Arnem departure experiences a headwind component during the entire trajectory.

Table 5.18: Atmosphere parameters for Case 3 in warm weather conditions.

		T_0 [K]	λ [K·m^{-1}]	RH [%]	z_v [m]	$v_0(z_v)$ [kts]	ψ_W [°]	σ [N·s·m^{-4}]
Atm. 9	29°C,15%,170/6	302.15	-0.0065	15	10	6	350	250·10^3

To analyse the level of atmospheric absorption of this atmosphere, the atmospheric attenuation coefficient is compared against the coefficient found in ISA conditions, high atmospheric attenuation conditions and low atmospheric attenuation conditions in Figure 5.38. It is clear that the atmospheric absorption of atmosphere 9 falls in-between the ISA and the high atmospheric attenuation conditions, and is always larger than in ISA conditions. Thus for both departure procedures, the ISA and high atmospheric attenuation conditions are used to analyse the results.

In high air temperatures, the aircraft engine operates in the temperature rated area meaning reduced absolute thrust levels. According to the APM, the Boeing 737-800 will operate at temperature rating once the outside local air temperature deviates by more than 20 °C from the ISA conditions [55]. As this is not the case for this simulation, the engine is always operated at its flat rating.

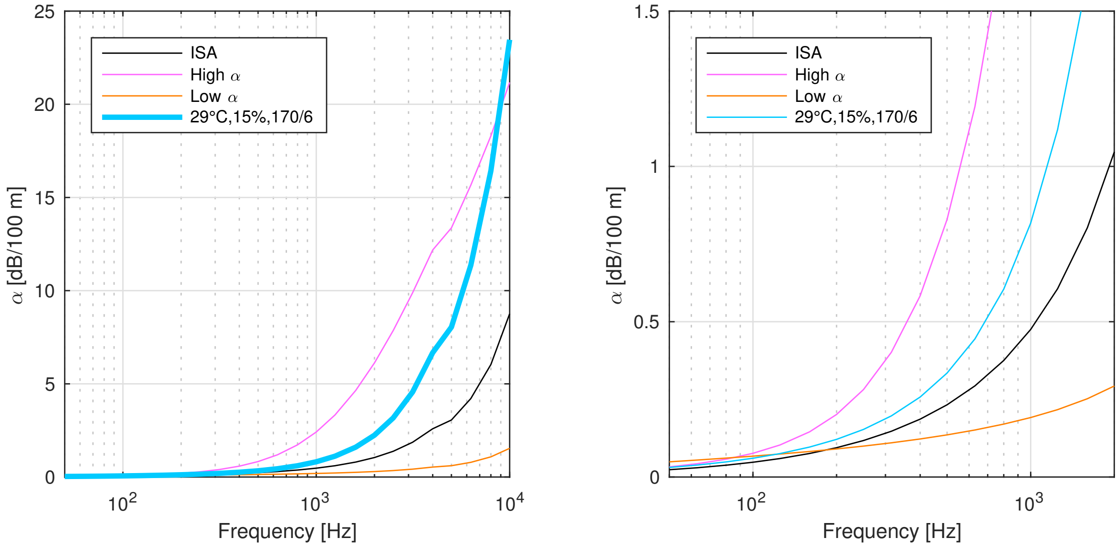

(a) Frequency range of 50 to 10000 Hz.

(b) Frequency range of 50 to 2000 Hz.

Figure 5.38: Atmospheric attenuation coefficient α for different atmosphere for case C3.9.

Spijkerboor. Table 5.19 presents the fuel and noise optimal trajectories in warm weather conditions, in ISA conditions of atmosphere 1, in ISA conditions enhanced with a 15 kts southeastern crosswind of atmosphere 4 and in high absorption conditions of atmosphere 5. The wind direction in warm weather conditions blows more from the south albeit the velocity is lower.

Analysing the results for the fuel optimal trajectory, the effect of the higher atmospheric attenuation in the warm weather condition is clearly observed by the lower number of awakenings compared to the conditions in ISA and ISA enhanced with wind. Furthermore, the lower fuel usage due to higher air temperature is observed.

When analysing the normalised Pareto front for warm weather conditions and the other cases in Figure 5.39, it is observed that initially the curve for warm weather conditions follows the same curve as in ISA conditions and in ISA enhanced by wind conditions. The total reduction in awakenings is similar to ISA enhanced by wind conditions, although relatively more fuel is used. The shape of the curve is similar to the other atmospheric conditions.

Table 5.19: Fuel and noise optimal trajectory characteristics of cases C3.SPY.9., C1.1., C1.4. and C1.5.

(a) Case C3.SPY.9.

Case	Objective	Fuel [kg]	ΔFuel [%]	Awakenings	ΔN_A [%]	Time [s]	ΔTime [%]
C3.SPY.9.1	Fuel	557.3	-	6237	-	525.4	-
C3.SPY.9.5	Fuel + 0.018 $\cdot N_A$	565,8	+1.52	4549	-27.07	534.4	+1.72

(b) Case C1.1., C1.4. and C1.5.

Case	Objective	Fuel [kg]	ΔFuel [%]	Awakenings	ΔN_A [%]	Time [s]	ΔTime [%]
C1.1.1	Fuel	559.5	-	9904	-	525.8	-
C1.1.7	Fuel + 0.01 $\cdot N_A$	566.5	+1.26	7671	-22.55	535.3	+1.82
C1.4.1	Fuel	573.4	-	8905	-	548.4	-
C1.4.7	Fuel + 0.01 $\cdot N_A$	580.8	+1.29	6628	-25.57	557.4	+1.64
C1.5.1	Fuel	556.2	-	2994	-	526.2	-
C1.5.8	Fuel + 0.02 $\cdot N_A$	563.5	+1.31	2021	-32.49	531.5	+1.00

To compare the noise optimal trajectory in warm weather conditions against the other atmospheres, the initial 100 s of the velocity profile, and the first 400 s of the altitude and thrust setting profile is presented in Figure 5.40a. It is observed that the velocity profile does not change much compared to the other cases, while the altitude profile is in between the altitude profile in ISA conditions and in high atmospheric attenuation conditions. A similar lower thrust setting is observed in warm weather conditions as for the high atmospheric attenuation conditions due to the higher temperature and thus larger excess thrust.

The ground track of the different noise optimal trajectories for the different atmospheres are compared in Figure 5.40b. From this figure, it can be deduced that the difference in ground track are small for all atmospheric conditions.

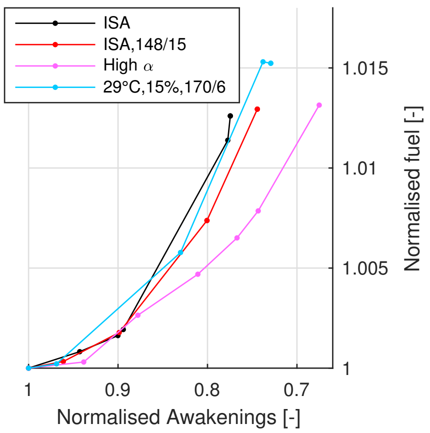

Figure 5.39: Normalised awakenings against fuel usage for cases C1.1., C1.4., C1.5. and C3.SPY.9.

Arnem. For the Arnem departure procedure, atmosphere 1 in ISA conditions and atmosphere 5 in high atmospheric attenuation conditions are used to evaluate the noise optimal trajectory in warm weather conditions. The characteristics of the fuel and noise optimal trajectories of the three different simulations are presented in Table 5.20. As holds for the Spijkerboor departure procedure, the total number of awakenings for the fuel optimal trajectory and the percentage reduction in awakenings obtained is in between the two atmospheric conditions. The headwind component along the trajectory results in a clear increase in fuel usage.

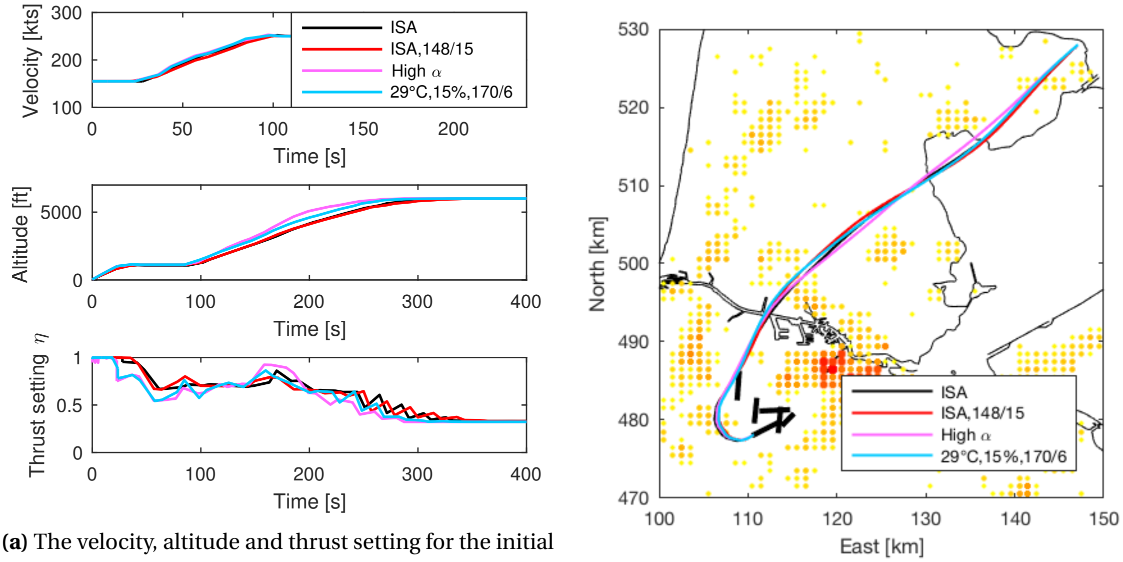

(a) The velocity, altitude and thrust setting for the initial 400 seconds of flight.

(b) The ground track.

Figure 5.40: Comparison of the velocity, altitude and thrust setting and ground track between the noise optimal trajectories of cases C1.1., C1.4., C1.5. and C3.SPY.9.

Table 5.20: Fuel and noise optimal trajectory characteristics of cases C3.ARN.9., C2.1. and C2.5.

(a) Case C3.ARN.9.

Case	Objective	Fuel [kg]	ΔFuel [%]	Awakenings	ΔN_A [%]	Time [s]	ΔTime [%]
C3.ARN.9.1	Fuel	386.6	-	2936	-	284.4	-
C3.ARN.9.8	Fuel + 0.016 $\cdot N_A$	390,4	+0.98	2497	-14.96	289.1	+1.65

(b) Case C2.1. and C2.5.

Case	Objective	Fuel [kg]	ΔFuel [%]	Awakenings	ΔN_A [%]	Time [s]	ΔTime [%]
C2.1.1	Fuel	381.0	-	4612	-	277.0	-
C2.1.8	Fuel + 0.02 $\cdot N_A$	386,6	+1.48	4352	-5.64	284.7	+2.78
C2.5.1	Fuel	378.0	-	1251	-	274.3	-
C2.5.8	Fuel + 0.05 $\cdot N_A$	383,4	+1.44	902	-27.94	280.4	+2.21

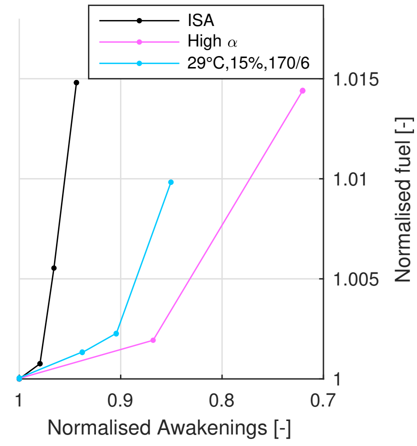

Figure 5.41: Normalised awakenings against fuel usage for cases C2.1., C2.5. and C3.ARN.9.

Figure 5.41 presents the normalised Pareto front in ISA conditions, high atmospheric attenuation conditions and warm weather conditions. The curve flattens out in the warm weather conditions, resulting in better performance as compared to high atmospheric attenuation condition.

The noise optimal trajectory in warm weather conditions show large similarities to the noise optimal trajectory in high atmospheric attenuation conditions, discussed in Section 5.4.3. This is mainly caused by the higher temperature and thus similar performance achieved through the aircraft performance model. Due to theses similarities with the previously simulated case, Appendix B.2.2 presents a more elaborate discussion of the trajectories.

Conclusion. The warm weather conditions is characterised by a light breeze from the south. The atmospheric attenuation coefficient is larger than in ISA conditions for all frequencies. A combination of the wind direction and the larger atmospheric attenuation over the lower frequency results in lower awakenings for the fuel optimal case for both departure procedures compared to ISA conditions. Lower fuel usage is obtained due to the higher outside temperature.

For the Spijkerboor departure, the tailwind results in a slightly positive influence on the flight time compared to the fuel optimal trajectory in high atmospheric attenuation conditions. The velocity profile of the noise optimal trajectory is similar to the noise optimal trajectory in ISA conditions but it reaches its final velocity slightly earlier. The vertical profile is in between the ISA and high atmospheric attenuation conditions. Slightly earlier in time, a climb with a similar climb gradient as in ISA is initiated. The ground track is dominated by wind, although not much difference is observed compared to the noise optimal ground track in ISA conditions.

For the Arnem departure, flight time for the fuel optimal trajectory is increased by the headwind component compared to the fuel optimal trajectory in ISA conditions. The acceleration for the noise optimal trajectory is reduced at 220 kts instead of 200 kts observed in ISA conditions. This results in an earlier climb with less steep climb gradient as in the noise optimal trajectory in high atmospheric attenuation conditions. Due to the wind and the lower atmospheric attenuation compared to the value observed in the high atmospheric attenuation conditions, a wider turn is initiated where after the ground track merges with the noise optimal ground track in the high atmospheric attenuation conditions.

5.5.3. Cold Weather Conditions

For the cold weather conditions, two different dates are selected. Atmosphere 10 is modelled after the 16th of March, a day with high relative humidity and a light south-southwestern breeze. Atmosphere 11 represents the 2nd of March and is characterised by a moderate eastern breeze. Atmosphere 10 is used for the Spijkerboor departure procedure as the eastern wind in atmosphere 11 results in tailwind for the Spijkerboor departure procedure. The atmospheric parameters of interest are presented in Table 5.21.

Table 5.21: Atmosphere parameters for Case 3 in cold weather conditions.

		T_0 [K]	λ [K·m^{-1}]	RH [%]	z_v [m]	$v_0(z_v)$ [kts]	ψ_W [°]	σ [N·s·m^{-4}]
Atm. 10	-1°C,100%,225/4	272.15	+0.00001	100	10	4	45	$250\cdot10^3$
Atm. 11	-2°C,58%,90/12	271.15	+0.00001	58	10	12	270	$250\cdot10^3$

Both dates are characterised by temperatures below zero and due to the cold temperature, an inverted atmosphere is modelled with a slightly positive temperature lapse rate. This implies that with increasing altitude, the temperature increases resulting in the speed of sound gradient to be always positive. This results in the refracting of the sound rays to be always downwards, diminishing all shadow zones.

On March 16, the surface was covered with snow. In order to identify the influence of different ground surfaces on the SEL received, noise optimal trajectories for the Spijkerboor departure procedure is also simulated for grass, snow, asphalt and a hard surface with varying flow resistivity levels.

In order to evaluate the atmospheric attenuation of the two cold weather conditions, Figure 5.42 presents the atmospheric attenuation coefficient α against the frequency in ISA, high atmospheric attenuation and low atmospheric attenuation conditions. Both cold atmospheres have higher atmospheric attenuation coefficients at higher frequencies. The attenuation coefficient is lower for frequencies up to 1000 Hz in atmosphere 10, while this is only the case for frequencies up to 40 Hz in atmosphere 11.

This section first discusses the influence of the cold weather conditions on the noise optimal trajectory for the Spijkerboor and Arnem departure procedure. This is followed by an analysis on the influence of different ground surfaces for the Spijkerboor departure procedure.

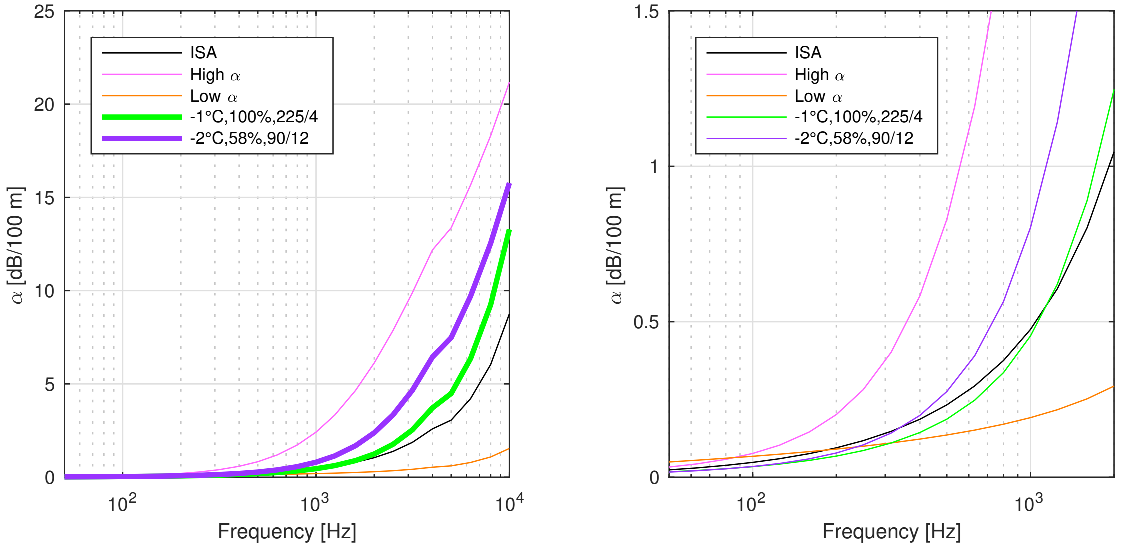

(a) Frequency range of 50 to 10000 Hz.

(b) Frequency range of 50 to 2000 Hz.

Figure 5.42: Atmospheric attenuation coefficient α for different atmosphere for cases C3.10. and C3.11.

Table 5.22: Fuel and noise optimal trajectories characteristics of cases C3.SPY.10., C1.1., C1.5. and C1.6.

(a) Case C3.SPY.10.

Case	Objective	Fuel [kg]	ΔFuel [%]	Awakenings	ΔN_A [%]	Time [s]	ΔTime [%]
C3.SPY.10.1	Fuel	556.9	-	12008	-	514.4	-
C3.SPY.10.7	Fuel + 0.018 $\cdot N_A$	576,1	+3.44	7589	-36.80	538.6	+4.71

(b) Case C1.1., C1.5. and C1.6.

Case	Objective	Fuel [kg]	ΔFuel [%]	Awakenings	ΔN_A [%]	Time [s]	ΔTime [%]
C1.1.1	Fuel	559.5	-	9904	-	525.8	-
C1.1.7	Fuel + 0.01 $\cdot N_A$	566.5	+1.26	7671	-22.55	535.3	+1.82
C1.5.1	Fuel	556.2	-	2994	-	526.2	-
C1.5.8	Fuel + 0.02 $\cdot N_A$	563.5	+1.31	2021	-32.49	531.5	+1.00
C1.6.1	Fuel	565.2	-	22801	-	521.5	-
C1.6.9	Fuel + 0.016 $\cdot N_A$	597.3	+5.69	11350	-50.24	558.6	+7.11

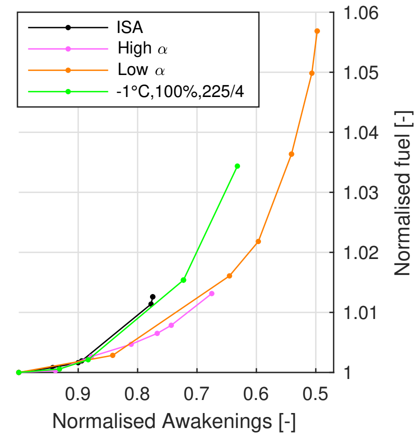

Figure 5.43: Normalised awakenings against fuel usage for cases C1.1., C1.5., C1.6. and C3.SPY.10.

Spijkerboor. The results of the Spijkerboor departure procedure in an inverted atmosphere is presented in Table 5.22 together with the results obtained in ISA conditions of atmosphere 1, high atmospheric attenuation conditions in case 5 and low atmospheric attenuation conditions in case 6. The diminishing of the shadow zones induced by the inverted atmosphere results in the total number of awakenings for the fuel optimal case to be a third larger than the value obtain in ISA conditions. The tailwind result in lower flight time and the air temperature mainly affects fuel usage.

Analysing the normalised Pareto front in Figure 5.43, the initial front matches the front in ISA conditions, while obtaining the same percentage in reduction of the awakenings as in high atmospheric attenuation conditions. The curve flattens out, however, not as much as the curve in low atmospheric attenuation conditions.

Analysing the initial 130 s of the velocity profile, and the entire altitude and thrust setting profile in Figure 5.44, it is noted that the velocity and altitude profile of the noise optimal trajectory is found in between the noise optimal trajectory in ISA and in low atmospheric attenuation conditions. As the inverted atmosphere creates relatively larger number of awakenings, it is observed that the noise optimal trajectory shows similarities to the low atmospheric attenuation conditions. However where the thrust setting in the low atmospheric attenuation conditions is reduced after reaching the final velocity, climb is initiated in cold weather conditions with a constant thrust setting.

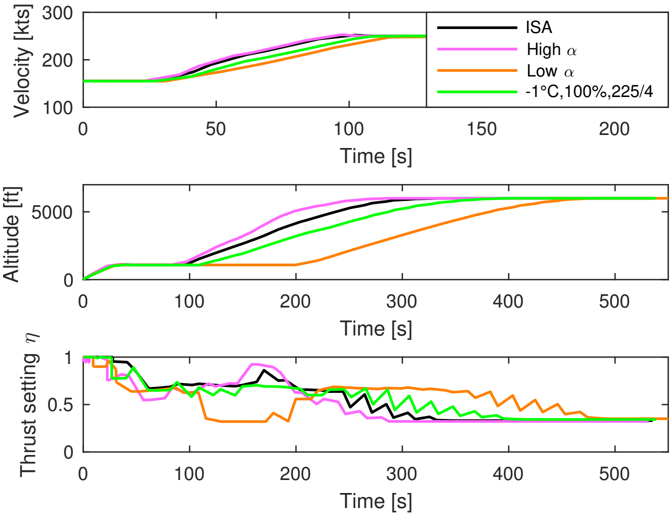

Figure 5.44: Comparison of the velocity, altitude and thrust setting between the noise optimal trajectories of cases C1.1., C1.5., C1.6. and C3.SPY.10.

The three-dimensional trajectories of the cases is presented by Figure 5.45. In cold atmospheres, it is seen that the climb is initiated slightly later than in ISA and high atmospheric attenuation conditions as velocity is increased with a smaller acceleration.

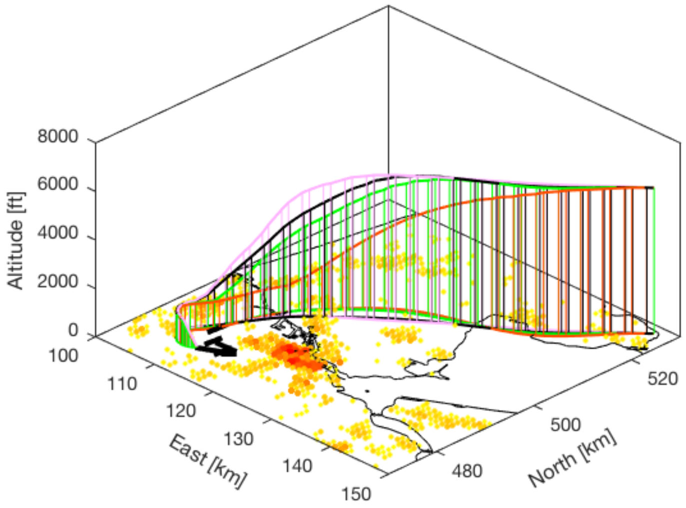

Figure 5.45: Comparison of the three dimensional trajectories of cases C1.1., C1.5., C1.6. and C3.SPY.10.

Figure 5.46 compares the noise optimal ground track of the different cases. The ground track also show large similarities to the noise optimal ground track in low atmospheric attenuation conditions, however the swing around densely populated areas is smaller in cold weather conditions as the atmospheric attenuation is higher.

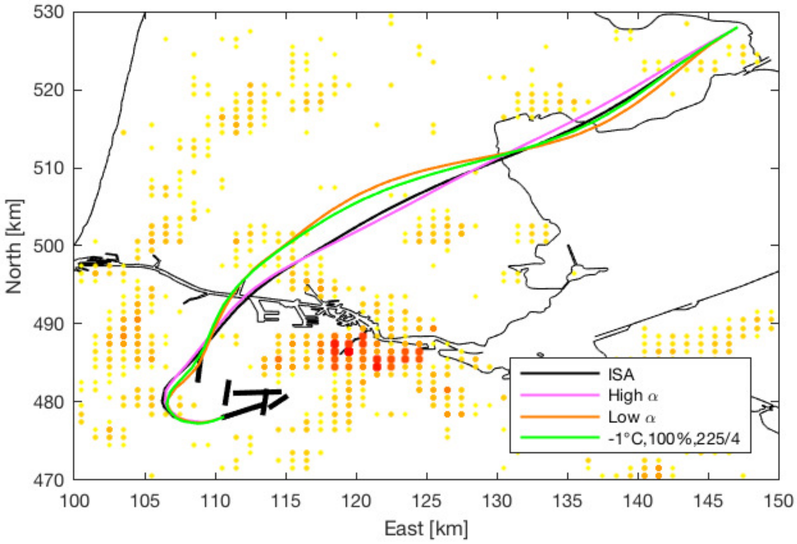

Figure 5.46: Comparison of the ground track between the noise optimal trajectories of cases C1.1., C1.5., C1.6. and C3.SPY.10.

Arnem. For the Arnem departure procedure, the atmospheric absorption coefficient α is most of the time higher than the coefficients in ISA conditions, as illustrated by Figure 5.42b. When comparing the atmospheric attenuation coefficient against the values obtained in warm weather condition in atmosphere 9, similar values are obtained for lower frequencies. For higher frequencies, the coefficient is smaller. The wind in atmosphere 11 blows from the east, resulting in headwind for most of the flight. It is of interest whether the optimal noise trajectory changes with the aircraft subjected to this headwind component for most of the flight.

The results of the fuel and noise optimal trajectories are presented in Table 5.23 together with the results obtained in the ISA-like weather conditions of atmosphere 8 with a western wind and in warm weather conditions of atmosphere 9 with a southern wind.

The effect of head wind along the straight segment towards the final position and the cold temperature result in higher fuel usage.

Table 5.23: Fuel and noise optimal trajectory characteristics of cases C3.ARN.11., C3.ARN.8. and C3.ARN.9.

(a) Case C3.ARN.11.

Case	Objective	Fuel [kg]	ΔFuel [%]	Awakenings	ΔN_A [%]	Time [s]	ΔTime [%]
C3.ARN.11.1	Fuel	383.0	-	3707	-	273.3	-
C3.ARN.11.6	Fuel + 0.01 $\cdot N_A$	384,2	+0.32	3507	-5.39	275.5	+0.83

(b) Case C3.ARN.8. and C3.ARN.9.

Case	Objective	Fuel [kg]	ΔFuel [%]	Awakenings	ΔN_A [%]	Time [s]	ΔTime [%]
C3.ARN.8.1	Fuel	380.5	-	3862	-	278.9	-
C3.ARN.8.5	Fuel + 0.04 $\cdot N_A$	382,6	+0.56	3620	-6.28	282.1	+1.13
C3.ARN.9.1	Fuel	386.6	-	2936	-	284.4	-
C3.ARN.9.8	Fuel + 0.016 $\cdot N_A$	390,4	+0.98	2497	-14.96	289.1	+1.65

Figure 5.47 illustrates the normalised Pareto front for the different trajectories in different wind conditions. It is noted that in warm weather conditions and a southern wind, the largest reduction in the percentage of

awakenings is obtained. Furthermore the eastern and western wind result in similar percentage of reduction in awakenings. Due tot the population spread around the trajectory, awakenings can be reduced more for northern and southern winds than for wind from the east and west. The convergence performance for higher k_{noise} values in cold weather conditions and an inverted atmosphere do not show any flattening, meaning that there is still potential to reduce awakenings with limited increase in fuel usage.

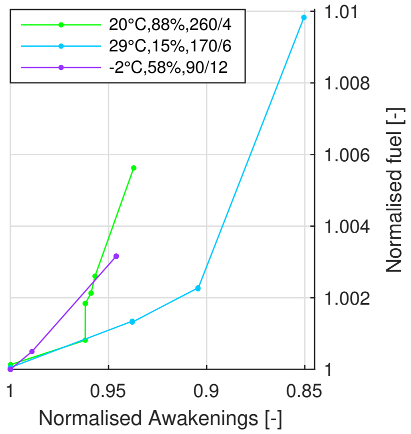

Figure 5.47: Normalised awakenings against fuel usage for cases C3.ARN.8., C3.ARN.9. and C3.ARN.11.

When analysing the noise optimal trajectories for wind from the west, south and east in very different atmospheric conditions, it is noticed that both the noise optimal velocity, altitude and thrust profile, and the noise optimal ground track are identical. So compared to no wind conditions, the noise optimal trajectory differs. However once wind is included, the noise optimal trajectory for the Arnem departure does not change. For a more elaborate analysis, please refer to Appendix B.2.3.

Spijkerboor - Different ground surface. In the cold weather conditions simulated in the Spijkerboor departure in atmosphere 10, the relative humidity is 100%. In these weather conditions, often precipitation is experienced. On this particular day, fresh snow covered the ground. In order to analyse the influence of different ground surface types, the ground is modelled as grass in atmosphere 10, snow in atmosphere 12 and asphalt in atmosphere 13 according to the effective flow resistivity obtained by *Embleton et. al* [66]. A smaller flow resistivity results in an increased damping of the reflected rays, as discussed in Section 3.4.4.

Table 5.24: Atmosphere parameters for Case 3 in cold weather conditions and varied ground surfaces.

		T_0 [K]	λ [K·m^{-1}]	RH [%]	z_v [m]	$v_0(z_v)$ [kts]	ψ_W [°]	σ [N·s·m^{-4}]
Atm. 10	Grass	272.15	+0.00001	100	10	4	45	250·10^3
Atm. 12	Snow	272.15	+0.00001	100	10	4	45	25·10^3
Atm. 13	Asphalt	272.15	+0.00001	100	10	4	45	30·10^6
Atm. 14	Variable hard surfacee	272.15	+0.00001	100	10	4	45	(5 to 30)·10^6

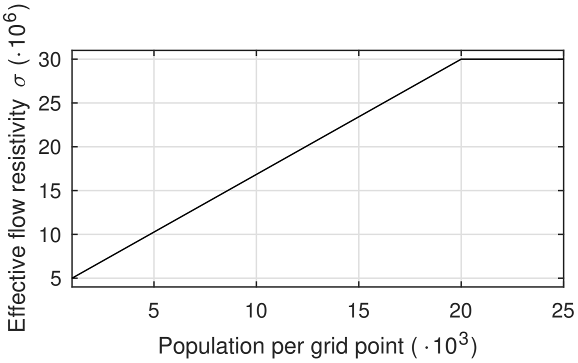

Figure 5.48: Population against effective flow resistivity σ in case C3.14.

As the SEL is determined in populated area, not every grid point in reality have the same flow resistivity. For example, in large cities the ground might be modelled as a hard surface due to the existence of many buildings. On the other hand, often the suburbans of the city have more trees and grasslands, reducing the hardness of the ground surface. In order to investigate the influence of a dynamic flow resistivity, the flow resistivity σ is linearly increased with increasing population between 1,000 and 20,000 in atmosphere 14 according to the relation presented in Figure 5.48. The minimum population of 1,000 is based on the grid point containing at least 1,000 people per km^2, while the maximum value is based on the maximum population of 22,000 in one grid point. The atmospheric parameters of the different atmospheres is presented in Table 5.24. Please note the difference in the order of the flow resistivity for atmosphere 13 and 14.

The result of the different cases are presented in Table 5.25. As the effective flow resistivity only affects the ground reflection, it is noted than the fuel optimal cases are identical for all cases. It is interesting to note that with a snow covered surface, more awakenings are obtained in the fuel optimal trajectory. With increasing flow resistivity, the number of awakenings increases in the noise optimal trajectory.

Table 5.25: Fuel and noise optimal trajectory characteristics of case C3.SPY.10., C3.SPY.12.-C3.SPY.14.

Case	**Objective**	**Fuel [kg]**	**ΔFuel [%]**	**Awakenings**	**ΔN_A [%]**	**Time [s]**	**ΔTime [%]**
C3.SPY.10.1	Fuel	556.9	-	12008	-	514.4	-
C3.SPY.10.7	Fuel + 0.018 $\cdot N_A$	576,1	+3.44	7589	-36.80	538.6	+4.71
C3.SPY.12.1	Fuel	556.9	-	12568	-	514.5	-
C3.SPY.12.6	Fuel + 0.016 $\cdot N_A$	566,6	+3.47	5415	-34.70	528.4	+4.31
C3.SPY.13.1	Fuel	556.9	-	15090	-	514.7	-
C3.SPY.13.6	Fuel + 0.022 $\cdot N_A$	572,0	+2.71	11858	-21.4	536.3	+4.19
C3.SPY.14.1	Fuel	556.9	-	15002	-	514.4	-
C3.SPY.14.7	Fuel + 0.012 $\cdot N_A$	568,9	+2.15	11674	-22.18	532.2	+3.45

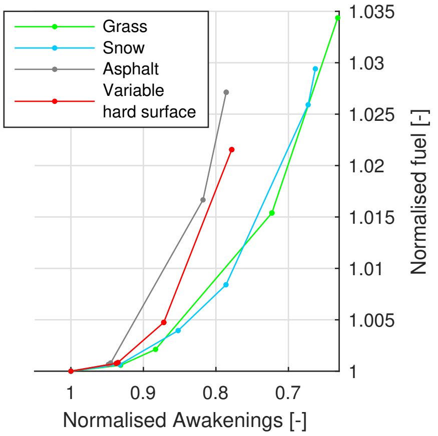

Figure 5.49: Normalised awakenings against fuel usage for cases C3.SPY.10., C3.SPY.12.-C3.SPY.14.

When comparing the normalised Pareto front of the different cases in Figure 5.49, it is clearly identified that there are two different solutions obtained: one for lower flow resistivity, and one for higher resistivity. The lower resistivity hold for atmosphere 10 and 12 for respective grass and snow surfaces. The larger flow resistivity hold for atmosphere 13 and 14 for asphalt and a varying hard surface respectively. Both for lower and higher resistivity, it is observed that the two atmospheres results in noise optimal trajectories with similar increase in fuel usage and a similar amount of reduction in awakenings. All surfaces except for the variable surface show a flattening with increasing k_{noise} values.

The initial 100 s of the velocity profile, and the entire altitude and thrust setting profile are presented in Figure 5.50. Again the two different types of noise optimal trajectories are identified in lower and higher flow resistivity conditions. All trajectories accelerate at the same moment, where the acceleration is lower in lower flow resistivity conditions. Both accelerations are reduced after reaching 200 kts, with the acceleration in lower flow resistivity conditions being slightly smaller than in higher flow resistivity conditions. Accordingly, climb is initiated earlier in higher flow resistivity conditions. On a grass surface, a slightly steeper noise optimal climb is performed compared to snow surface. The high flow resistivity profiles are very similar. For the thrust setting profile, two similar patterns for both the low and high flow resistivities are identified.

When analysing the noise optimal ground tracks in Figures 5.51, it is noted that the initial turn is taken more widely in the high flow resistivity atmospheres. After the turn, all trajectories are within roughly a km distance from each other. In the lowest flow resistivity conditions, the most direct noise optimal ground track is taken. The noise optimal ground track with the largest swings around the populated area is observed in the highest flow resistivity conditions. The ground track for an asphalt surface show large similarities with the noise optimal ground track for low atmospheric attenuation conditions.

When a variable flow resistivity is simulated, the noise optimal ground track initially follows the trajectory of the high flow resistivity conditions, where after it converges with the trajectory simulated using grass as ground surface when the impacted population density reduces. Thus having variable ground surface types per observer, the number of awakenings and the noise optimal trajectory will change.

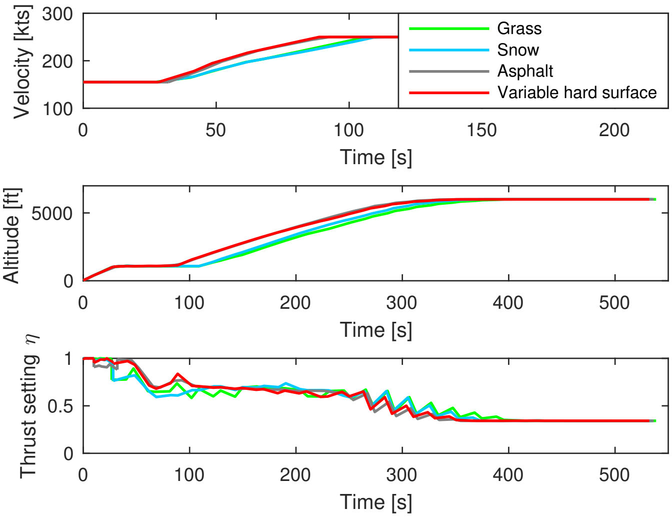

Figure 5.50: Comparison of the velocity, altitude and thrust setting between the noise optimal trajectories of cases C3.SPY.10., C3.SPY.12.-C3.SPY.14.

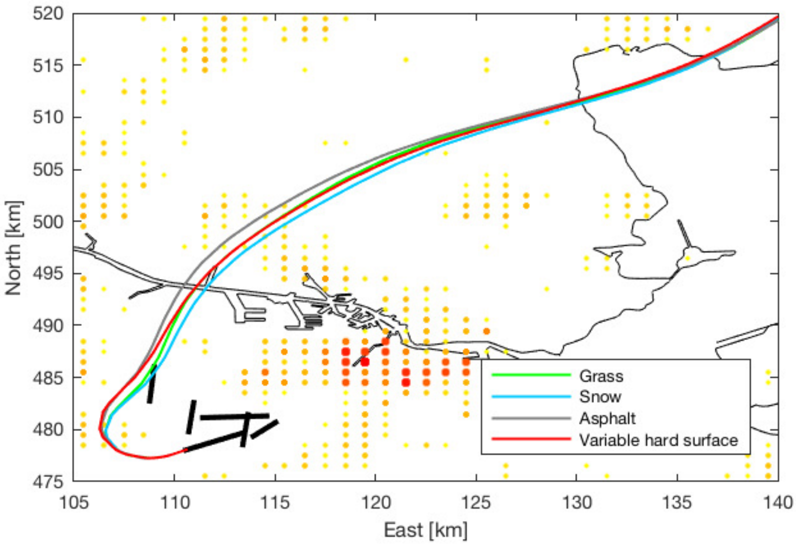

Figure 5.51: Comparison of the ground track between the noise optimal trajectory of cases C3.SPY.10., C3.SPY.12.-C3.SPY.14.

The influence of an increasing flow resistivity on the noise optimal trajectories are that aircraft accelerate faster and climb earlier. With higher flow resistivity, the ground reflection losses reduce and peaks observed by the receiver increase, resulting in higher sound levels at the receiver as discussed in Section 4.2.1. The peaks flatten out with increasing altitude. To lower the sound level received, it is best to gain altitude.

Conclusion. For each departure procedure, different cold weather conditions are simulated as the wind direction induced a tailwind departure for the Spijkerboor departure if simulated with the cold weather condition of the Arnem departure. For both departure procedures, The lower temperature increase the fuel usage. Furthermore, an inverted atmosphere induced more awakenings.

The cold weather condition in the Spijkerboor departure is characterised by a headwind at take off and lower atmospheric attenuation for frequencies up to 1000 Hz compared to ISA conditions. The influence of the tailwind is clearly observed in the flight time and fuel usage. Due to the higher number of awakenings, the velocity and the altitude profile of the noise optimal trajectory is found in between ISA and in low atmospheric attenuation conditions. Where the noise optimal thrust setting of in low atmospheric attenuation conditions is reduced to delay its climb, the noise optimal thrust setting in cold weather conditions is kept constant and climb is initiated 100 s earlier. The noise optimal ground track show large similarities with the low atmospheric attenuation conditions with smaller swings around the populated areas.

The cold weather condition in the Arnem departure is characterised by a cross wind at take off and tailwind along most of the flight. The atmospheric attenuation is mainly higher than the values observed in ISA conditions. Main goal was to analyse the different noise optimal trajectory in different weather conditions with wind blowing from various directions. Although the awakenings and fuel usage is affected by the weather conditions, the noise optimal trajectory does not change.

Different ground surface types for the Spijkerboor departure procedure resulted in different noise optimal trajectories. With larger flow resistivity for harder surfaces, the noise optimal trajectory accelerates faster and initiates climb earlier. Awakenings increase with harder surfaces as a lower ground reflection loss is observed.

5.6. Conclusion and Discussion of the Cases

In the first two cases, the influence of air temperature, relative humidity and wind has been analysed separately against ISA conditions for two different departure trajectories. The third case analysed the noise optimal trajectories and related the findings of the first two cases in actual weather conditions.

It turned out that the difference in fuel usage, noise propagation and the noise impact in different atmospheric conditions can be predicted with respect to the values obtained in ISA conditions. However, the noise optimal trajectory is a trade-off between fuel usage and noise impact performed by the optimisation. Especially in the Spijkerboor departure, different trajectories as expected are obtained when air temperature, relative humidity and wind are combined.

To conclude and discuss upon all the simulations performed in this chapter, the goal of the case studies are evaluated. Based on the conclusions of each case performed in the previous sections, the influence of air temperature, relative humidity, wind and the ground surface on the fuel usage, sound propagation and the resulting noise impact are discussed.

Fuel usage Head- or tailwind components along the trajectory influence fuel usage. Higher temperature generally results in higher thrust and drag. Generally, this results in larger excess thrust compared to ISA conditions at the same throttle setting as long as the engine operates in flat rating, as determined by the BADA APM. Thus lower thrust settings are used to achieve the same performance, resulting in lower fuel usage and source noise levels at higher air temperatures. On the contrary, at colder temperatures, the thrust and drag is lower. Depending on the exact atmospheric conditions, also larger excess thrust is obtained.

Sound propagation and noise impact. Wind direction and velocity influence noise impact depending on their orientation. Besides the increased shadow zones upwind and the diminishing of shadow zones downwind, the wind has a large influence on the sound level contours up- and downwind of a turn in turning flight.

The air temperature and relative humidity are represented by the atmospheric absorption and immediately relate to noise impact. The lower the atmospheric absorption, the larger the noise impact and thus more awakenings. For the atmospheric attenuation coefficient, the frequencies up to 1000 to 2000 Hz mainly affect whether the atmosphere is of high or low absorption conditions with respect to ISA conditions.

Furthermore, in an atmosphere with inverted temperature lapse, also known as an inverted atmosphere, the number of awakenings is mainly increased. Different ground surfaces primarily influence the total number of awakenings, with increasing awakenings with increasing flow resistivity observed by harder surfaces.

Noise optimal trajectory. In every simulation, with minimal fuel increase, several percentages of awakenings are reduced. Furthermore the aircraft always accelerates first before climb is initiated. This mainly reduces fuel usage and the Doppler frequency shift results in lower sound levels when the aircraft is flying faster.

The noise optimal trajectory, both in horizontal and vertical direction, is very much bounded by the spreading of the population. Around Amsterdam Airport Schiphol, the largest population density is found around Amsterdam. All simulations make sure that the SEL received in Amsterdam is lower for the noise optimal trajectory with respect to the fuel optimal trajectory. Furthermore, better use of the thrust setting is made to reduce source noise.

When the atmospheric attenuation condition is higher than in ISA condition, a steeper climb and a ground track that consists of more straight segment is flown. The velocity profile generally match the reference case in ISA conditions. With different wind velocities and directions, no use is made of increased tailwind velocities at higher altitudes by climbing faster or the reduced headwind component at lower altitudes.

For the Spijkerboor departure, different wind directions only influence the noise optimal ground track. The wideness with respect to the reference case of the initial turn varies with the wind direction. The variation is caused by the location of the shadow zone upwind. When flying over densely populated areas, use is made of lateral attenuation by flying at a lower altitude in weather conditions were relatively many awakenings are obtained. Furthermore, with increasing awakenings the ground track is optimised to reduce awakenings.

For the Arnem departure, where most of the population located at the initial and final position of the trajectory, there is not much room to optimise for the ground track. Furthermore as the departure procedure is shorter, the period in which use is made of stronger lateral attenuation is limited to allow for a climb with reasonable thrust setting. Thus the aircraft accelerates faster to make use of the Doppler frequency shift to reduce awakenings.

When the ground surface is modified, two types of trajectories are obtained: one for low flow resistivity surfaces such as grass and snow and one for high resistivity surface such as asphalt. The higher the flow resistivity, the faster the aircraft accelerates and initiate its climb in order to reduce peak noise levels caused by ground reflection.

Performance of gradient-based optimisation. When analysing convergence behaviour, it is seen that for atmospheric conditions in which higher sound levels are observed, k_{noise} values have been increased until the normalised Pareto fronts show a satisfactory curve in which awakenings are only slightly decreased with large increase in fuel usage. This holds for the low atmospheric attenuation conditions for both departure procedures and for the Spijkerboor departure, in ISA-like conditions and asphalt as ground surface.

One reason for this behaviour might be the shape of the objective function. The higher sound levels are penalised more due to the increased gradient and the number of awakenings, as depicted in Figure 3.19.

At lower sound levels, the optimisation might be deceived by the influence of the ground reflection. The influence of the ground reflection can theoretically increase the sound levels by 6 dB or cancel out the entire sound level. This is depicted by the narrow bands with different sound levels observed in Figure 4.8. In the optimisation, this translates into a very negative gradient in the objective function. In the next iteration, a small step is taken in the direction of the negative gradient. However, the objective function might now result in a positive gradient due to the narrow bands in which the sound levels changes due to ground reflection. Once the optimisation is stuck in this phenomena, no optimal trajectory satisfying the threshold for feasibility and optimality is obtained. With increasing k_{noise} values, this effect is strengthen.

Another reason applicable for simulations with the inclusion of wind, is the shadow zone. When entering the shadow zone, initially the sound level drops linearly as elaborated in Section 3.4.4. Although the loss is modelled continuously, the second order derivative, the Hessian, is not continuous. In case of stronger wind velocities, the shadow zone upwind of the aircraft moves closer towards the aircraft due to the change in local speed of sound. When densely populated grid points are located near the boundary of the illuminated and shadow zone, the cost functional can be reduced by a relative large amount by ensuring the population does not receive 50.5 dB of sound. Once the optimisation scheme focuses on this particular part of the trajectory, the not continuous Hessian might cause difficulties to the convergence.

Furthermore the set-up of the cases influence the convergence. As the Arnem departure is very restricted by the population spread, noise optimal trajectories with lower k_{noise} value are also the noise optimal trajectory for larger k_{noise} values. This limits the number of data points on the Pareto front, resulting in non-smooth normalised Pareto fronts.

The optimal trajectory found by the WAFORT tool is based on the initial guess. Initial guesses of trajectories flying around cities with larger population density, such as Haarlem to the west, converges towards either the solution presented in the specific case or the threshold of feasibility or optimally could not be obtained.

Due to the convergence issues with higher weighing functions in the gradient-based optimisation, not entire new trajectories have been obtained. However, as noise impact is greatly reduced by the application of weather-adaptive noise abatement procedures while incrementally increasing fuel usage over the fuel optimal trajectory, the adaptations to the noise optimal trajectory in ISA conditions has shown its potential.

6

Conclusions and Recommendations

With the results obtained for different cases with varying weather variables in the previous chapter, conclusions for this research can be drawn. Section 6.1 presents a concise overview of the conclusions of the research. This is followed by Section 6.2 in which the limitations and consequent recommendations and possible future work is discussed.

6.1. Conclusions

Main goal of this thesis is to assess the influence of weather on optimised noise abatement departure procedures for one fly over, by developing an optimisation tool that allows for the synthesis of weather-adaptive noise abatement procedures within the Terminal Manoeuvring Area (TMA).

For this purpose, the Weather-Adaptive Flight Optimisation Research Tool (WAFORT) has been developed. Within this framework, an Aircraft Performance Model (APM), sound propagation model, noise impact model and Geographic Information System (GIS) is combined in the dynamic optimisation software GPOPS. Based on the problem statement, aircraft data, cost functional and initial guess, the noise optimal trajectory with the minimised maximum number of expected awakenings is obtained using the gradient-based optimisation technique Optimal Control Theory (OCT).

Weather variables that influence sound propagation are the air temperature, relative humidity and the wind.

The APM is modelled using BADA 4.0. The BADA holds a data base with performance characteristics of aircraft types. Furthermore the aerodynamic forces are related to the pressure and air temperature ratios to account for different atmospheric conditions. The aircraft mechanics is modelled as a point mass, reducing the number of variables in the optimisation.

The source noise level of the aircraft is derived from the ANP database. Combined with the Doppler frequency shift, the sound is propagated towards the observer. Sound propagation is modelled using geometric ray tracing. Ray tracing is independent of frequency, reducing computational time. Refraction is modelled by dividing the atmosphere is logarithmic spaced atmospheric layers. With the inclusion of wind, rays may be refracted upwards upwind of the aircraft due to decreasing effective speed of sound levels. Downwind, rays are bent downwards diminishing all shadow zones. The losses accounted for in the propagation model include spreading loss, atmospheric attenuation loss and ground reflection. Atmospheric attenuation loss is influenced by air temperature and relative humidity, with larger atmospheric attenuation loss at higher atmospheric attenuation coefficients. The atmospheric attenuation coefficient is frequency dependent. Ground reflection is influenced by the ground surface type and is frequency dependent as well. The shadow zones are modelled to ensure continuity for all observers, which is required for the gradient-based optimisation scheme.

Noise impact is evaluated using the FICAN dose-response relationship, relating Sound Exposure Level (SEL) to the maximum number of expected awakenings. The analysis is made site-specific by the GIS, using the latest data from 2017 published by Statistics Netherlands (CBS).

A gradient-based optimisation technique is used as it has a superior run time over other optimisation techniques. Using optimal control theory, one composite objective function is evaluated within a couple seconds to minutes. An initial guess is required to start the optimisation.

Verification and validation of the sound propagation model was performed by comparing the sound levels against the sound levels obtained using the Integrated Noise Model (INM), the current standard to evaluate aircraft noise. The new propagation model results in larger sound levels. This is caused by the different atmospheric attenuation loss obtained in each atmospheric layers. INM employs a constant, arithmetic atmosphere which does not take into account different atmospheric layers. Furthermore since INM does not model the shadow zone, large differences in sound levels are observed when the receiver is in the shadow zone.

In the new propagation model, larger sound levels are observed when the aircraft is flying away from the observer due to the Doppler frequency shift. Furthermore the shift in the shadow zone location is clearly observed with the inclusion of wind. Thin, narrow bands with varied sound levels are observed due to the ground reflection, caused by secondary sound rays interfering constructively or destructively with the direct sound ray. With softer ground surfaces, the effect of ground reflection is damped, resulting in lower overall sound levels and smaller ground reflection peaks.

The gradients of the noise impact model are obtained using the forward finite difference method as automatic derivatives with machine precision resulted in convergence difficulties.

To analyse the influence of the weather variables, simulations in various wind and atmospheric attenuation conditions have been performed on two different Standard Instrument Departure (SID) procedures from Amsterdam Airport Schiphol (AAS):

- *Spijkerboor 3K departure to way point ANDIK.* - Departure from runway 24 in southwestern direction, where after a sharp turn towards the right is made to continue flight in northeastern direction.
- *Arnem 3E departure to way point IVLUT.* - Departure from runway 18L in southern direction, followed by a left turn towards the east.

The two departure procedure differ mainly in the population density spread around the departure track and in length. Nearly all around the ground track of the Spijkerboor departure there is population while for the Arnem departure, the population is mainly located at the initial and final position of the simulation. The Arnem departure is also shorter in length, meaning reduced flight time.

To analyse the separate influences of the weather variables on the fuel usage, the sound propagation and the noise impact, first the weather variables have been analysed separately. The results obtained for the two departure procedures were compared to the results obtained in International Standard Atmosphere (ISA) conditions.

Air temperature has an influence on the APM. Compared to ISA conditions, depending on the excess thrust level at the same throttle setting when operating the engine in flat rating, different thrust levels result in the same performance. As the source noise is directly related to thrust level, lower thrust level reduces source noise and fuel usage. The air temperature and relative humidity are represented by the atmospheric absorption and immediately relate to noise impact. For the atmospheric attenuation coefficient, the frequencies up to 1000 to 2000 Hz mainly affect whether the atmosphere is of high or low absorption conditions with respect to ISA conditions. The lower the atmospheric absorption, the larger the noise impact and thus more awakenings are obtained. Furthermore, in an atmosphere with an inverted temperature lapse, the number of awakenings is mainly increased.

Head- or tailwind components along the trajectory influence fuel usage. Wind direction and velocity influence noise impact depending on their orientation. Besides the increased shadow zones upwind and the diminishing of shadow zones downwind, the wind has a large influence on the sound level contours up- and downwind of a turn in turning flight.

Different ground surfaces primarily influence the total number of awakenings, with increasing awakenings with increasing flow resistivity observed for harder surfaces.

Following the separate weather variable influences, an analysis of actual weather conditions observed in the past months has been performed which combines the different weather conditions.

It turned out that the difference in fuel usage, noise propagation and the noise impact in different atmospheric conditions can be predicted with respect to the values obtained in ISA conditions. However, the noise optimal trajectory is a trade-off between fuel usage and noise impact performed by the optimisation. Especially for the Spijkerboor departure, unexpected trajectories were obtained when the different weather variables were combined.

In every simulation, with minimal fuel increase, several percentages of awakenings are reduced. Furthermore the aircraft always accelerates first before climb is initiated. This mainly reduces fuel usage and the Doppler frequency shift results in lower sound levels when the aircraft is flying faster. The noise optimal trajectory, both in horizontal and vertical direction, is very much bounded by the spreading of the population. Around Amsterdam Airport Schiphol, the largest population density is found around Amsterdam. All simulations make sure that the SEL received in Amsterdam is lower for the noise optimal trajectory with respect to the fuel optimal trajectory. Furthermore, better use of the thrust setting is made to reduce source noise.

When the atmospheric attenuation condition is higher than in ISA condition, a steeper climb and a ground track that consists of more straight segment is flown. The velocity profile generally match the reference case in ISA conditions.

With different wind velocities and directions, no use is made of increased tailwind velocities at higher altitudes by climbing faster or the reduced headwind component at lower altitudes.

When the ground surface is modified, with increasing hardness and thus increasing flow resistivity, the faster the aircraft accelerates and initiate its climb in order to reduce peak noise levels caused by ground reflection.

Differences in noise optimal trajectories are observed for the two procedures.

For the Spijkerboor departure, different wind directions only influence the noise optimal ground track. The wideness with respect to the reference case of the initial turn varies with the wind direction. The variation is caused by the location of the shadow zone upwind. When flying over densely populated areas, use is made of lateral attenuation by flying at a lower altitude in weather conditions were relatively many awakenings are obtained. Furthermore, with increasing awakenings the ground track is optimised to reduce awakenings.

For the Arnem departure, where most of the population located at the initial and final position of the trajectory, there is not much room to optimise for the ground track. Furthermore as the departure procedure is shorter, the period in which use is made of stronger lateral attenuation is limited to allow for a climb with reasonable thrust setting. Thus the aircraft accelerates faster to make use of the Doppler frequency shift to reduce awakenings.

Convergence difficulties for higher weighting values for the noise impact in the objective function, k_{noise}, resulted in not entirely new noise optimal trajectories. Most of the obtained noise optimal trajectories can be considered as slight adaptations on the horizontal, vertical and velocity profile in ISA conditions.

The initial search range of the optimisation is based on the initial guess. Initial guesses of trajectories flying around cities with larger population density, converges towards either the solution presented in the specific case or the threshold of feasibility or optimally could not be obtained.

When analysing convergence behaviour, it is observed that for atmospheric conditions in which relatively high sound levels are obtained, the weighting value of noise in the objective function k_{noise} has been increased until the normalised Pareto fronts show a satisfactory curve in which awakenings are only slightly decreased with large increase in fuel usage. One reason for this behaviour might be the shape of the objective function. The higher sound levels are penalised more due to the increased number of awakenings in the objective function.

At lower sound levels, the optimisation might be deceived by the increased sound levels due to ground reflection. The ground reflection induces thin narrow bands with increasing or decreasing sound levels. When a large population grid point is located exactly within the peaks, the optimisation is stuck and convergence difficulties arise. With increasing k_{noise} values, this effect is strengthened.

For simulations with the inclusion of wind, the shadow zone might also be a source of the convergence difficulties. When entering the shadow zone, initially the sound level drops linearly. Although the loss is modelled continuously, the second order derivative, the Hessian, is not continuous. In case of stronger wind velocities, the shadow zone upwind of the aircraft moves closer to the aircraft due to the change in local speed of sound. Again when a large population grid point is located near the boundary of the illuminated and shadow zone, convergence issues might be encountered.

Furthermore the set-up of the cases influence the convergence. As the Arnem departure is very restricted by the population spread, noise optimal trajectories with lower k_{noise} value are also the noise optimal trajectory for larger k_{noise} values. This limits the number of data points on the Pareto front, resulting in non-smooth normalised Pareto fronts.

Based on these findings, it is concluded that the weather-adaptive noise abatement procedures will benefit the local community. It is noted that the fuel optimal trajectory evaluated in this study is more fuel efficient than the current procedures. Thus the limited increase in fuel usage over the fuel optimal trajectory does not necessarily increase the current fuel usage. Furthermore as no entire new trajectories are obtained, the implementation of weather-adaptive noise abatement procedures should not introduce many difficulties for both pilots and air navigation service providers.

6.2. Recommendation and Future Work

Based on the research, modelling limitations, modelling improvements and future work have been identified.

Modelling limitations.

Multiple modelling limitations are identified for this research and consists of: the analysis of one aircraft type only, no actual measurements in the field have been performed, the use of FICAN dose-response relationship as noise criterion, and the use of gradient-based optimisation in combination with an initial guess to start the optimisation.

Analysis based on one aircraft type. In order to present the differences in the noise optimal trajectories, simulations for one aircraft type with the same mass at the start of the simulation and in clean configuration for the entire duration is used. This limits the conclusion to one aircraft type only.

Due to the versatile APM, different aircraft types can be easily implemented. Furthermore, the APM holds different dag coefficients, in order to model different configurations of the aircraft along the trajectory. In general, the addition of the landing gear and control surfaces will result in a slower climb for the initial phase of the flight. If the aircraft type is changed to a larger type different performance and source noise levels are obtained. In the same atmosphere considered in this study, this implies different noise-optimal trajectories.

With the same reasoning, it is of interest how much quieter the new generation aircraft like the Boeing 737MAX, 787; Airbus A320NEO, A350 actually are in similar conditions as is considered in this research. A large portion of the aircraft fleet in the future will consist out of these aircraft types and will be doing so for at least the coming 20 to 30 years until they are succeeded by their evolution.

No measurements in the field. No field research has been performed to measure the sound level received on the ground or to the number of awakenings. As the dose-response relationship is recognised by the American National Standards Institute (ANSI), there is no need to do a field research again, as this has already been performed by others to determine this dose-response relationship.

Noise impact criterion. To evaluate the noise, the maximum number of expected awakenings determined by the FICAN dose-response relationship is used. Although the ANSI prescribes the use of the FICAN dose-response relationship when analysing the noise impact for new aircraft procedures, the actual number of awakenings is a fictional number: it does not represent the actual number of awakenings. In order to present noise impact to outsiders, a non-fictional number might increase the impact and awareness to certain sound levels observed.

Gradient-based optimisation. The optimal trajectory found by the WAFORT tool is based on an initial guess. Although an optimal solution is found, using optimal control theory as optimisation scheme, it is not sure whether this solution is the global optimum. In order to analyse whether the solution is the global optimum, multiple initial guesses have to be tested and analysed whether the same optimal solution is obtained.

With increasing value of the weighting function for the awakenings in the cost functional, increasing convergence problems were encountered. Furthermore an accurate initial guess did not necessarily improve convergence nor run time of the optimisation. To improve convergence, a filter might be applied on the gradients of the objective function. However with increased weight of the noise impact in the objective function, it is expected that the convergence difficulties will be obtained again.

Modelling improvements.

Improvements that can be made to the WAFORT include more accurate and flyable trajectories, more accurate modelling of the atmosphere and atmospheric properties respectively, modelling of the aircraft and sound source as rigid models and the modelling of more accurate flow resistivity per ground surface type.

Fly ability of the trajectories. In order to improve fly ability of the trajectories, Area Navigation (RNAV) can be introduced. With RNAV the trajectory can be limited to straight segments and constant radius turns. Within the current form of WAFORT, fly ability is limited by constraining the flight performance within realistic bounds. However no analysis has been performed on the fly ability of each noise optimal trajectory and according change in workload for the pilots and the air navigation service providers. The use of RNAV will result in more realistic and accurate trajectories which result in more flyable trajectories.

More advanced modelling of the atmosphere Within the WAFORT framework, straightforward atmospheric conditions are evaluated. To compare the influence of weather against ISA conditions, this is sufficient. In order to enhance the evaluation of different weather conditions, improvements and additional models can be included in the modelling domain due to the modular structure of the WAFORT. For example, the two-dimensional wind can be enhanced in order to obtain a three-dimensional wind field or a relative humidity lapse rate can be added.

Rigid body modelling. Both aircraft and sound source are modelled as a point mass and point source in order to reduce parameters in the optimisation. It might be of interest to compare the differences in sound levels received on the ground when the aircraft is modelled as a rigid body and if multiple directional sound sources are used. However, this increases the computational intensity which might not be desired.

Flow resistivity level. This study presented how noise optimal trajectories change when the flow resistivity of the ground surface at the observer is varied accordingly with population density. Research in this field in order to identify a relation between population density and ground surface type might result in new insights regarding the noise received and accordingly the influence on the noise optimal trajectories.

Future work.
The development of the WAFORT and the results found in this study can be used and improved in future work in multiple different applications. Examples are the enhancement of the optimisation scheme with an evolutionary algorithm to obtain the global minimum, the definition of a multiple noise event problem and the creation of a runway allocation problem from an airport perspective.

Global optimum using evolutionary algorithm. In a future application the WAFORT in its current form can be used to analyse the potential for noise abatement procedures in certain atmospheric conditions. If there is potential, the WAFORT enhanced with an evolutionary algorithm can obtain the noise optimal trajectories for higher k_{noise} values. Depending on the work load for the pilots and air navigation service providers, one noise optimal trajectory out of a set of trajectories can be chosen to fly.

Multiple noise event problem. This study focused on optimising for a single noise event. The total noise level received during one day of operations has not been considered. An interesting future study might be to look at the difference in noise impact for an entire day of operations with different types of aircraft. The problem is thus adapted from a single event to a multiple noise event problem.

Runway allocation problem for airports. As observed by the difference in the number of absolute awakenings in different weather conditions, the noise optimal procedure in certain conditions result in much lower or higher awakenings. This implies that in certain weather conditions, the use of a runway creates more awakenings on a particular day.

An entire different, interesting future study is to analyse the number of awakenings from an airport perspective. A runway allocation problem can be set up in which the total number of awakenings per runway is minimise over a season or a year. By doing so, the total noise impact of the airport is minimised. Use can be made of the different weather conditions to operate a runway with relatively many awakenings in ISA conditions, but which induces much lower number of awakenings in for example favourable wind conditions.

Bibliography

[1] Air Transport Action Group (ATAG). Aviation benefits beyond borders. online, 2016. Powering global economic growth, employment, trade links, tourism and support for sustainable development through air transport, accessed on 3 December 2017.

[2] Airbus. Global market forecast 2017 - 2036. online, 2017. Growing Horizons, accessed on 3 December 2017.

[3] The Boeing company. Current market outlook 2017-2036. online, 2017. Accessed on 3 December 2017.

[4] J.E. Penner, D. Lister, D.J. Griggs, D.J. Dokken, and M. McFarland. *Aviation and the Global Atmosphere*. Cambridge University Press, 1999. Interngovernmental Panel on Climate Change.

[5] M. Basner, W. Babisch, A. Davis, M. Brink, C. Clark, S. Janssen, and S. Stansfeld. Auditory and non-auditory effects of noise on health. *Lancet*, 383:1325 – 1332, 2014.

[6] S.A. Stansfeld and M.P. Matheson. Noise pollution: non-auditory effects on health. *British Medical Bulletin*, 68:243 – 257, 2003.

[7] L. Fritschi, A. Brown, R. Kim, D. Schwela, and S. Kephalopoulos. Burden of disease from environmental noise. online, 2011. World Health Organization, accessed on 4 December 2017.

[8] E.A.M. Franssen, C.M.A.G. van Wiechen, N.J.D. Nagelkerke, and E. Lebret. Aircraft noise around a large international airport and its impact on general health and medication use. *Occupational and Environmental Medicine*, 61:405 – 413, 2004.

[9] A.L. Bristow and M. Wardman. A comparative analysis of annoyance from aircraft noise at three european airports. online, 2004. Association of European Transport, accessed 4 December 2017.

[10] J.E.C. Dekkers and W.J. van der Straaten. Monetary valuation of aircraft noise: A hedonic analysis around Amsterdam airport. *Ecological Economics*, 68:2850 – 2858, 2009.

[11] D.L. Huff. NASA Glenn's contributions to aircraft engine noise research. *Journal of Aerospace Engineering*, 26(2):218–250, 2013.

[12] F. Netjasov. Contemporary measures for noise reduction in airport surroundings. *Applied Acoustics*, 73:1076 – 1085, 2012.

[13] International Civil Aviation Organization (ICAO). Review of noise abatement procedure research & development and implementation results. online, 2007. Discussion on survey results, accessed on 3 December 2017.

[14] International Civil Aviation Organization (ICAO). Procedures for air navigation services, aircraft operations. online, 2006. Volume I Flight Procedures, Doc 8168, accessed on 3 December 2017.

[15] U. Ingard. A review of the influence of meteorological conditions on sound propagation. *The Journal of the Acoustical Society of America*, 25(3):405 – 411, 1953.

[16] H.G. Visser and R.A.A. Wijnen. Optimization of noise abatement departure trajectories. *Journal of Aircraft*, 38(4):620 – 627, 2000.

[17] H.G. Visser and R.A.A. Wijnen. Optimization of noise abatement arrival trajectories. *The Aeronautical Journal*, 107:607 – 615, 2003.

[18] S. Hartjes, H.G. Visser, and S.J. Hebly. Optimisation of RNAV noise and emission abatement standard instrument departures. *The Aeronautical Journal*, 114(1162):757 – 767, 2010.

[19] R.H. Hogenhuis, S.J. Hebly, and H.G. Visser. Optimization of area navigation noise abatement approach trajectories. *Proceedings of the Institution of Mechanical Engineers, Part G: Journal of Aerospace Engineering*, 225:513 – 521, 2010.

[20] E.R. Boeker, E. Dinges, B. He, G. Fleming, C.J. Roof, P.J. Gerbi, A.S. Rapoza, and J. Hemann. *Integrated Noise Model (INM) version 7.0 technical manual.* Federal Aviation Administration (FAA) Office of Environment and Energy, 2007. Washington DC, USA. Accessed on 2 December 2017.

[21] Federal Interagency Committee on Aviation Noise (FICAN). *Effects of Aviation Noise on Awakenings from Sleep*, 1997. Accessed on 2 December 2017.

[22] L.J.J. Erkelens. Research into new noise abatement procedures for the 21st century. In *Proceedings of the AIAA Guidance, Navigation and Control Conference and Exhibit*, 14–17 August 2000. AIAA-2000-4474.

[23] J-P.B. Clarke. Systems analysis of noise abatement procedures enabled by advanced flight guidance technology. *Journal of Aircraft*, 37(2):266 – 273, 2000.

[24] J. Huber, J-P.B. Clarke, and S. Maloney. Aircraft noise impact under diverse weather conditions. In *Proceedings of the 9th AIAA/CEAS Aeronautics Conference and Exhibit*, 12–14 May 2003. AIAA-2000-3276.

[25] L. Ren and J-P.B. Clarke. Development and application of separation analysis methodology for noise abatement approach procedures. In *Proceedings of the AIAA 5th Aviation Technology Integration and Operations Conference*, 26–28 September 2005. AIAA-2005-7397.

[26] S. Hartjes. *An Optimal Control Approach to Helicopter Noise and Emissions Abatement Terminal Procedures.* PhD thesis, Delft University of Technology, 2015.

[27] G.J.J. Ruijgrok. *Elements of Aviation Acoustics.* VSSD, second edition, 2007.

[28] S. Hartjes and H.G. Visser. Efficient trajectory parameterization for environmental optimization of departure flight paths using a genetic algorithm. *Journal of Aerospace Engineering*, 23:1115 – 1123, 2017.

[29] F.J. Vormer, M. Mulder, M.M. Van Paassen, and J.A. Mulder. Optimization of flexible approach trajectories using a genetic algorithm. *Journal of Aircraft*, 43(4):941 – 952, 2006.

[30] H. Yu, E van Kampen, and J.A. Mulder. An optimization paradigm for arrival trajectories using trajectory segmentation and state parameterization. In *Proceedings of the AIAA Guidance, Navigation and Control Conference*, 4–8 January 2016. AIAA-2016-1872.

[31] K. Deb. *Multi-Objective Optimization using Evolutionary Algorithms.* Wiley-Interscience. John Wiley & Sons, Ltd., Systems and Optimization, 2001.

[32] J.T. Betts. Survey of numerical methods for trajectory optimization. *Journal of Guidance, Control, and Dynamics*, 21(2):193–207, 1998.

[33] H.G. Visser. Aircraft performance optimization. Technical report, Delft University of Technology, 2014.

[34] H.G. Visser. Generic and site-specific criteria in the optimization of noise abatement trajectories. *Transportation Research Part D*, 10:405 – 419, 2005.

[35] R.A.A. Wijnen and H.G. Visser. Optimal departure trajectories with respect to sleep disturbance. *Aerospace Science and Technology*, 7:81 – 91, 2003.

[36] S.J. Franke and G.W. Swenson, Jr. A brief tutorial on the Fast Field Program (FFP) as applied to sound propagation in the air. *Applied Acoustics*, 27:203 – 215, 1989.

[37] X. Yang. *Computational Atmospheric Acoustics*, book section 7 in Atmospheric Acoustics, pages 220–270. De Gruyter, 2015.

[38] G.H. Spencer and M.V.R.K. Murty. General ray-tracing procedure. *Journal of the Optical Society of America*, 52(6):672—678, 1962.

[39] J.E. Rosenbaum. *Enhanced Propagation Modeling of Directional Aviation Noise: A Hybrid Parabolic Equation-Fast Field Program Method.* PhD thesis, Pennsylvania State University, 2011.

[40] J.E. Rosenbaum and E. Boeker. Enhanced propagation of aviation noise in complex environments: A hybrid approach. *Aeroacoustics*, 13(5–6):463 – 476, 2014.

[41] W.E. Zorumski. Aircraft noise prediction program theoretical manual. Report, National Aeronautics and Space Administration, 1982. NASA TM-83199-PT-1 and PT-2, accessed on 7 December 2017.

[42] M.J. White and K.E. Gilbert. Application of the parabolic equation to the outdoor propagation of sound. *Applied Acoustics*, 27:227 – 238, 1989.

[43] M. West, K. Gilbert, and R.A. Sack. A tutorial on the Parabolic Equation (PE) model used for long range sound propagation in the atmosphere. *Applied Acoustics*, 37:31 – 49, 1992.

[44] Delta Air Lines Inc. and the Boeing company. Boeing 737NG Operations Manual Volume I. Airplane Flight Manual, Delta Air Lines, June 2008. Accessed on 5 August 2018.

[45] Continental Airlines and the Boeing company. Boeing 777 Flight Manual. Airplane Flight Manual, Continental Airlines, November 2002. Accessed on 5 August 2018.

[46] G.W.H. van Es, P.J. van der Geest, and M.H. Nieuwpoort. Safety aspects of aircraft operations in crosswind. Report, National Aerospace Laboratory NLR, 2001. Accessed on 6 August 2018.

[47] A.V. Rao, D.A. Benson, C. Darby, M.A. Patterson, C. Francolin, I. Sanders, and G.T. Huntington. Algorithm 902: GPOPS, a MATLAB software for solving multiple-phase optimal control problems using the Gauss pseudospectral method. *ACM Transactions on Mathematical Software*, 37(2):22.1–22.39, 2010.

[48] G.T. Huntington. *Advancement and Analysis of a Gauss Pseudospectral Transcription for Optimal Control.* PhD thesis, Massachusetts Institute of Technology, 2007.

[49] K. Saß. *Modelling and Optimization of Tilt-Rotor Aircraft Flight Trajectories.* Msc thesis, Delft University of Technology, 2018.

[50] P.E. Gill, W. Murray, and M.A. Saunders. User's guide for SNOPT version 7: Software for large-scale nonlinear programming. Report, Stanford University, 2008. Accessed on 28 May 2018.

[51] H.G. Visser. Minimax optimal control analysis of lateral escape maneuvers for microburst encounters. *Journal of Guidance, Control, and Dynamics*, 20(2):370–376, 1997.

[52] G.M. Masters. *Wind Power Systems*, book section 6, page 307 — 384. John Wiley & Sons, Inc., Hoboken, NJ, USA, 2004.

[53] J.L.J. Herpers. *Optimization of Weather Adaptive Noise Abatement Trajectories.* Msc thesis, Delft University of Technology, 2014.

[54] A. Nuic. *User Manual for the Base of Aircraft Data (BADA) Revision 3.12.* Eurocontrol, 3.12 edition, 2014. EEC Technical/Scientific Report No. 14/04/24-44, accessed on 3 December 2017.

[55] A. Nuic and V. Mouillet. *User Manual for the Base of Aircraft Data (BADA) Family 4.* Eurocontrol, 1.2 edition, 2014. EEC Technical/Scientific Report No. 12/11/22-58, accessed on 8 May 2018.

[56] M. Arntzen, S.A. Rizzi, H.G. Visser, and D.G. Simons. A framework for simulation of aircraft flyover noise through a non-standard atmosphere. In *Proceedings of the 18th AIAA/CEAS Aeroacoustics Conference (33rd AIAA Aeroacoustics Conference)*, 4–8 June 2012. AIAA-2012-2079.

[57] Engineering Sciences Data Unit (ESDU). Prediction of sound attenuation in a refracting turbulent atmosphere with a Fast Field Program (FFP). ESDU Data Item, 2004. ESDU 04011, accessed on 3 December 2017.

[58] Society of Automotive Engineers Committee A-21 on Aircraft Noise. Procedure for the calculation of airplane noise in the vicinity of airports. online, 1986. AIR-1845, accessed on 7 December 2017.

[59] European Civil Aviation Conference/Conference Europeenne De L'aviation Civile (ECAC/CEAC). Report on standard method of computing noise contours around civil airports. online, 2016. ECAC.CEAC Doc 29, accessed on 4 December 2017.

[60] International Civil Aviation Organization (ICAO). Recommended method for computing noise contours around airports. online, 2008. Doc 9911, accessed on 3 December 2017.

[61] E.R. Boeker and E. Dinges et. al. *Aviation Environmental Design Tool (AEDT) version 2c technical manual.* Jointly prepared by USDOT Volpe National Transportation System Center, ATAC Corporation, Metron Aviation, CSSI, Federal Aviation Administration (FAA) Office of Environment and Energy, 2016. Washington DC, USA, accessed on 4 December 2017.

[62] J.S. Lamancusa and P.A. Daroux. Ray tracing in a moving medium with two-dimensional sound-speed variation and application to sound propagation over terrain discontinuities. *The Journal of the Acoustical Society of America*, 93(4):1716–1726, 1993.

[63] International Civil Aviation Organization (ICAO). Annex 16 environmental protection: Aircraft noise. Report, International Civil Aviation Organization, 2008.

[64] C.I. Chessell. Propagation of noise along a finite impedance boundary. *The Journal of the Acoustical Society of America*, 62(4):825–834, 1977.

[65] M.E. Delany and E.N. Bazley. Acoustical properties of fibrous absorbent materials. *Applied Acoustics*, 3(2):105–116, 1970.

[66] T.F.W. Embleton, J.E. Piercy, and G.A. Daigle. Effective flow resistivity of ground surfaces determined by acoustical measurements. *The Journal of the Acoustical Society of America*, 74(4):1239–1244, 1983.

[67] K. Attenborough. Ground parameter information for propagation modeling. *Journal of the Acoustical Society of America*, 92(1):418–427, 1992.

[68] American National Standard Quantities and Procedures for Description and Measurement of Environmental Sound — Part 6: Methods for Estimation of Awakenings Associated with Outdoor Noise Events Heard in Homes. online, 2008. Acoustical Society of America, standard: ANSI/ASA S12.9 Part 6, accessed on 4 December 2017.

[69] N.P. Miller and P.D. Schomer. How many people will be awakened by noise tonight? *Acoustics Today*, 2009.

[70] N. van Leeuwen, T. Guldemond, and F. Faqiri. Statistische gegevens per vierkant en postcode. Report, Centraal Bureau voor de Statistiek (Statistics Netherlands), 2017. Accessed on 26 July 2018.

[71] A.S. Monin and A.M. Obukhov. Basic laws of turbulent mixing in the surface layer of the atmosphere. *Contributions of the Geophysical Institute of the Academy of Sciences of the USSR*, 24(151):163 — 187, 1954.

[72] S.M. Rump. INTLAB - INTerval LABoratory. online, 1999. `http://www.ti3.tu-harburg.de/rump/`, accessed on 10 July 2018.

[73] S. Stamatiadis and S.C. Farantos. AUTO_DERIV: Tool for automatic differentiation of a Fortran code. *Computer Physics Communications*, 181(10):1818–1819, 2010.

[74] S.J. Heblij and H.G. Visser. Advanced noise abatement departure procedures: Custom optimized departure profiles. In *AIAA Guidance Navigation and Control Conference and Exhibit*, 18–21 August 2008.

[75] G.J.J. Ruijgrok. *Elements of Airplane Performance.* VSSD, second edition, 2009.

A
Airport Data

This appendix elaborates on airport data at Amsterdam Airport Schiphol (AAS). Section A.1 elaborates on the runway characteristics, while Section A.2 presents the current Standard Instrument Departure (SID) charts in use for the runways of interest of this research.

A.1. Runway Characteristics

AAS is the largest airport of the Netherlands. Due to varying wind along the Dutch coast, the airport consists of 5 main runways and 1 additional runway, oriented in various directions. The runways are generally named after the neighbouring cities that aircraft fly over when using the runway. The runway characteristics are tabulated in Table A.1.

Table A.1: Runway characteristics at Amsterdam Airport Schiphol.

Direction	Length [m]	Name	Usage
04/22	2014	Oostbaan	Primary general aviation
18L/36R	3400	Aalsmeerbaan	Main
06/24	3500	Kaagbaan	Main
09/27	3453	Buitenveldertbaan	Main
18C/36C	3300	Zwanenburgbaan	Main
18R/36L	3800	Polderbaan	Main, only Northerly take-off and Southerly landing

Departing aircraft from AAS proceed to an altitude of 6000 ft and to a certain way point, before the en-route climb is performed. A maximum velocity of 250 kts is persevered below 10,000 ft to ensure the workload of air traffic controllers are manageable.

A.2. Standard Instrument Departure Charts

The SID charts for AAS is published by the Air Traffic Control The Netherlands[1].

---

[1] http://www.ais-netherlands.nl/aim/2018-08-02-AIRAC/html/index-en-GB.html, accessed on 15 January 2018

Departure chart for runway 24

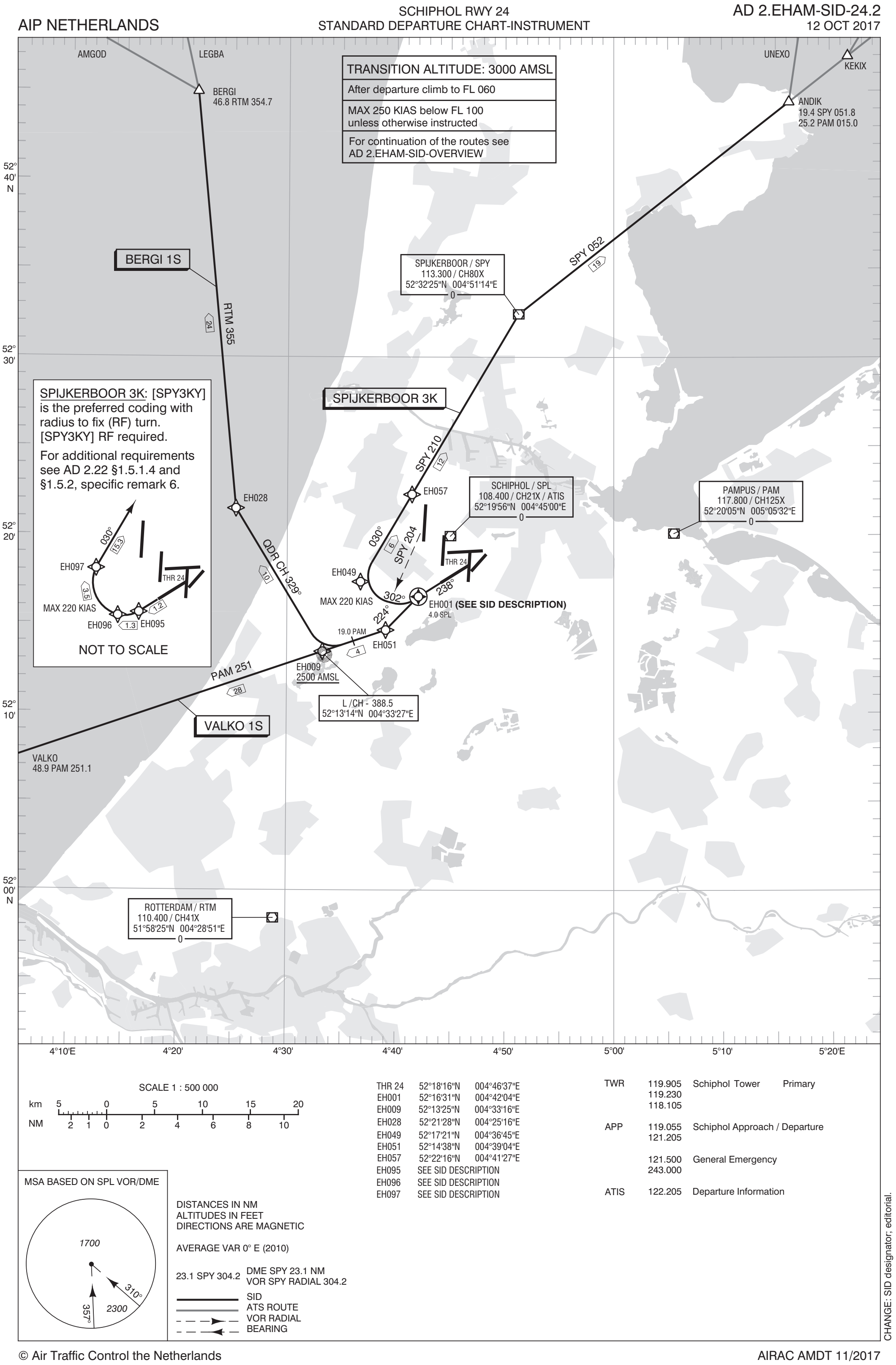

AIP NETHERLANDS

SCHIPHOL RWY 24
STANDARD DEPARTURE CHART-INSTRUMENT

AD 2.EHAM-SID-24.2
12 OCT 2017

TRANSITION ALTITUDE: 3000 AMSL

After departure climb to FL 060

MAX 250 KIAS below FL 100
unless otherwise instructed

For continuation of the routes see
AD 2.EHAM-SID-OVERVIEW

SPIJKERBOOR 3K: [SPY3KY] is the preferred coding with radius to fix (RF) turn. [SPY3KY] RF required.

For additional requirements see AD 2.22 §1.5.1.4 and §1.5.2, specific remark 6.

NOT TO SCALE

THR 24	52°18'16"N	004°46'37"E
EH001	52°16'31"N	004°42'04"E
EH009	52°13'25"N	004°33'16"E
EH028	52°21'28"N	004°25'16"E
EH049	52°17'21"N	004°36'45"E
EH051	52°14'38"N	004°39'04"E
EH057	52°22'16"N	004°41'27"E
EH095	SEE SID DESCRIPTION	
EH096	SEE SID DESCRIPTION	
EH097	SEE SID DESCRIPTION	

TWR	119.905 119.230 118.105	Schiphol Tower	Primary
APP	119.055 121.205	Schiphol Approach / Departure	
	121.500 243.000	General Emergency	
ATIS	122.205	Departure Information	

DISTANCES IN NM
ALTITUDES IN FEET
DIRECTIONS ARE MAGNETIC

AVERAGE VAR 0° E (2010)

23.1 SPY 304.2 DME SPY 23.1 NM
VOR SPY RADIAL 304.2

CHANGE: SID designator; editorial.

AIRAC AMDT 11/2017

Departure chart for runway 18L

AIP NETHERLANDS

SCHIPHOL RWY 18L
STANDARD DEPARTURE CHART-INSTRUMENT

AD 2.EHAM-SID-18L
22 JUN 2017

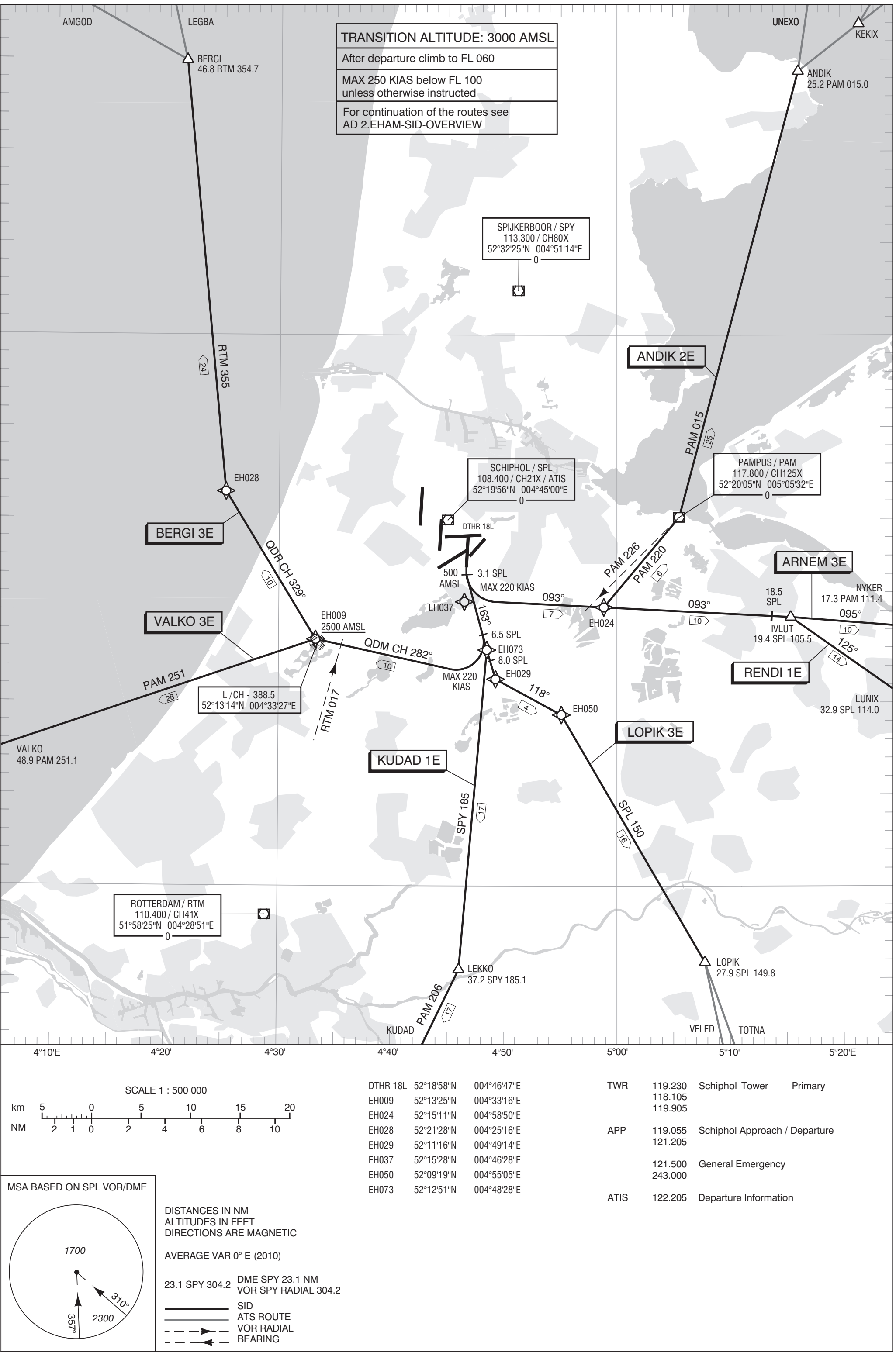

DTHR 18L	52°18'58"N	004°46'47"E
EH009	52°13'25"N	004°33'16"E
EH024	52°15'11"N	004°58'50"E
EH028	52°21'28"N	004°25'16"E
EH029	52°11'16"N	004°49'14"E
EH037	52°15'28"N	004°46'28"E
EH050	52°09'19"N	004°55'05"E
EH073	52°12'51"N	004°48'28"E

TWR	119.230 118.105 119.905	Schiphol Tower	Primary
APP	119.055 121.205	Schiphol Approach / Departure	
	121.500 243.000	General Emergency	
ATIS	122.205	Departure Information	

DISTANCES IN NM
ALTITUDES IN FEET
DIRECTIONS ARE MAGNETIC

AVERAGE VAR 0° E (2010)

23.1 SPY 304.2 — DME SPY 23.1 NM VOR SPY RADIAL 304.2

SID
ATS ROUTE
VOR RADIAL
BEARING

CHANGE: SID designators; editorial.

AIRAC AMDT 07/2017

B
Supporting Case Study Results

This appendix presents supporting results of the case studies performed in Chapter 5, that resulted in limited new conclusions. Appendix B.1 elaborates further upon varied wind conditions of Case 1. Appendix B.2 discusses all Arnem departure simulations performed in Case 3.

B.1. Case 1: Varying Wind Conditions

In varying wind conditions, three different combinations of wind direction and velocity are simulated, with the temperature and humidity matching International Standard Atmosphere (ISA) conditions.

- Atmosphere 2: wind from 270°, 5 kts.
- Atmosphere 3: wind from 270°, 15 kts.
- Atmosphere 4: wind from 148°, 15 kts.

With the inclusion of a western wind, the difference in SEL received in the fuel and noise optimal trajectories for atmosphere 2 and atmosphere 3 are presented in respectively Figure B.1 and Figure B.2.

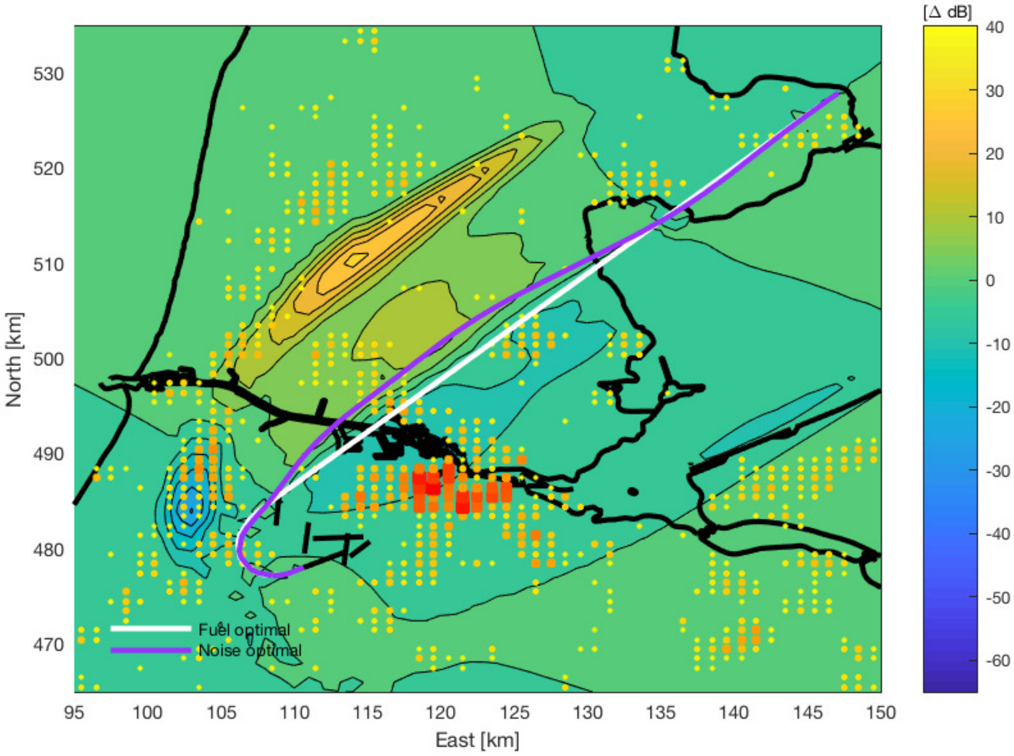

Figure B.1: Difference in received SEL values between the noise and fuel optimal trajectories for case C1.2.

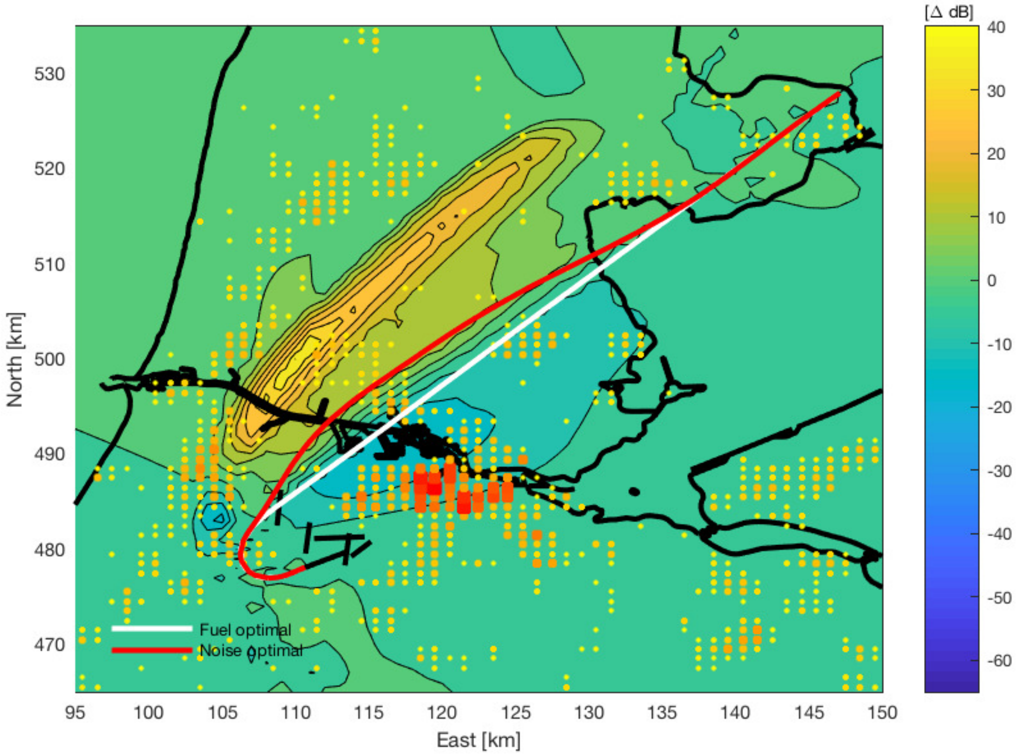

Figure B.2: Difference in received SEL values between the noise and fuel optimal trajectories for case C1.3.

The wind moves the shadow zone closer to the aircraft upwind and diminishes the shadow zone downwind. When analysing the difference in SEL values received between the fuel and noise optimal trajectories in different wind conditions, a large change in SEL values are noticed upwind of the aircraft. The increase in SEL observed north of Haarlem in the reference case, presented in Figure 5.7, has moved along with the wind to the east. It is now located more to the north of Zaandam. Furthermore, a similar decrease in SEL observed to the west of the initial turn has now moved to the east as well. It is now positioned directly over Haarlem.

Downwind, the shadow zone has diminished and the clear reduction is SEL as observed in the reference case is not present anymore. Without shadow zones, the propagation loss is mainly increased by increased ray path lengths. This clarifies the larger swing around Amsterdam. With increasing western wind, no swing around Hoorn is observed in the ground track.

To analyse the effect of wind from the east on the SEL received, the difference in SEL received between the fuel and noise optimal trajectories is presented in Figure B.3. When compared to the reference case in Figure 5.7, the reduction in SEL to the east of Amsterdam has shifted closer to the aircraft. Furthermore, the shadow zone downwind has diminished, resulting in the diminishing of the large increase in SEL values. Due to the eastern wind, a sharper initial turn is made in order to reduce sound levels in Hoofddorp, Nieuw-Vennep and Haarlem as much as possible.

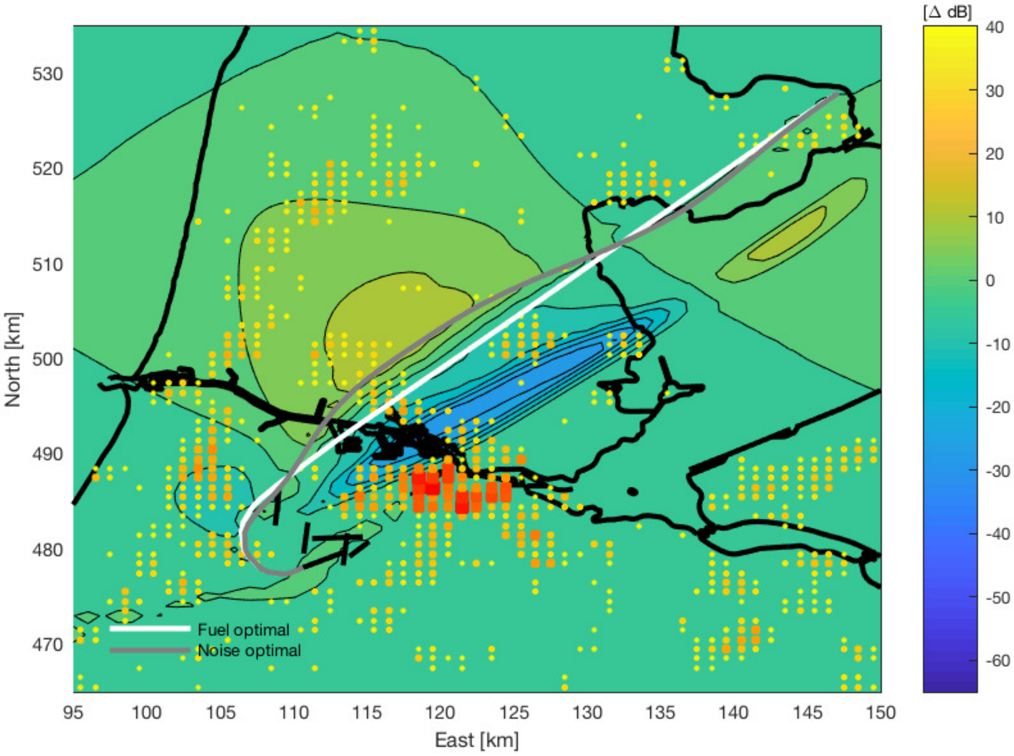

Figure B.3: Difference in received SEL values between the noise and fuel optimal trajectories for case C1.4.

The initial 100 s for the velocity and 400 s for the other profiles are presented in Figure B.4a. Although simulated in different wind profiles, the trajectory profiles look very much alike. Acceleration is initiated slightly earlier for a southeastern wind and is constant. This is likely performed to reduce the thrust setting and by doing so, relieving the population living in Hoofddorp, Nieuw-Vennep and Hoofddorp as much as possible as the southeastern wind prevents them of being in the shadow zone. No use is made of the wind to make use of larger tailwind at higher altitudes, or making use of lower headwind at lower altitudes.

Comparing the noise optimal ground tracks until flying past the city of Hoorn, as illustrated by Figure B.4b, it is noted that wider turns are made with a western wind. This is related to the shadow zone located upwind. Flying past Zaandam, it is noted that the trajectories are spread over a distance of roughly 2 km in the x-direction for the different trajectories. It is observed that a weak western wind allows for more eastern trajectories over Zaandam with respect to the reference case, while this diminishes with increasing wind velocities. With a southeastern wind, slightly more western trajectories with respect to the reference case are obtained. However, these differences are small.

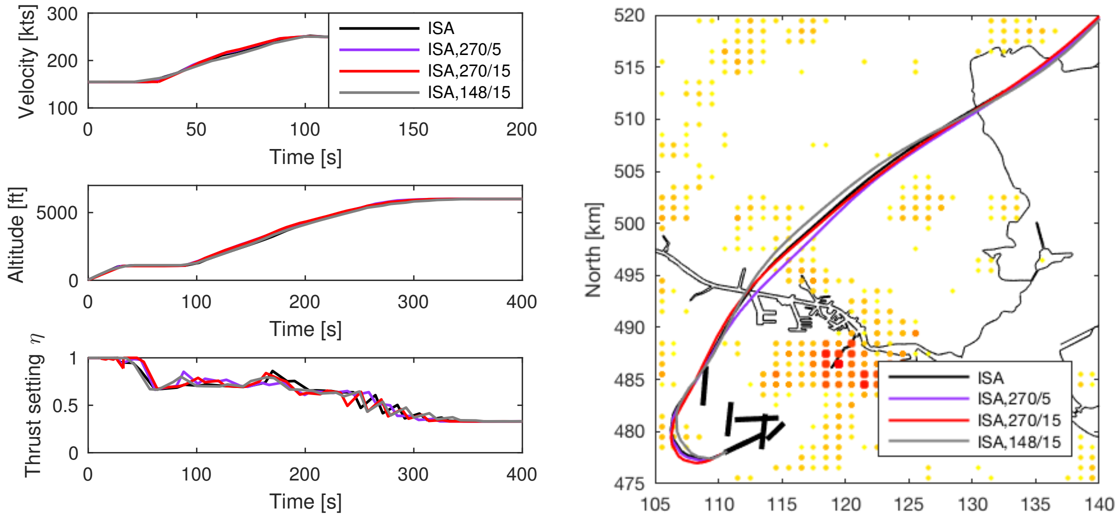

(a) The velocity, altitude and thrust setting.

(b) The ground track.

Figure B.4: Comparison of the velocity, altitude and thrust setting and ground track of the fuel and noise optimal trajectories of cases C1.1.-C1.4.

B.2. Case 3: Arnem Departure Procedures

The influence of actual weather conditions on the Arnem departure procedure resulted in noise optimal trajectories which are resembled by the simulations performed in Case 2, discussed in Section 5.4. These limited new findings are presented in this section. Following the order in the report, first the ISA-like weather conditions are discussed in Section B.2.1. This is followed by Section B.2.2 discussing ... and Section B.2.3 discussing ...

B.2.1. International Standard Atmosphere-Like Weather Conditions

In ISA-like weather conditions, the following atmospheric conditions are simulated.

- Atmosphere 8: temperature of 20°C, relative humidity of 88% and wind from 260°, 4 kts.

The initial 100 s for the velocity profile and the other profiles of the noise optimal trajectories are presented in Figure B.5a. In Case 2 it was observed that with the inclusion of a southwestern wind, the aircraft tend to increase altitude earlier than the reference case in ISA conditions. Both velocity and altitude profile in ISA-like conditions show large similarities to the noise optimal trajectory in ISA conditions with a southwestern wind. However, the acceleration is initiated earlier in the ISA-like conditions and consists of two accelerations rather than one constant acceleration. As the final velocity is obtained later, the climb is also initiated later. However, the climb rate is initially larger, resulting in the convergence of both trajectories towards each other.

The different ground tracks of the noise optimal trajectories are presented in Figure B.5b. The initial turn performed by the noise optimal trajectory in ISA-like conditions matches the turn performed in ISA conditions. After the turn, the noise optimal trajectory in ISA-like conditions converges towards the noise optimal trajectory in ISA conditions with wind. As the south western wind velocity is lower, a tighter turn can be made without increasing noise impact.

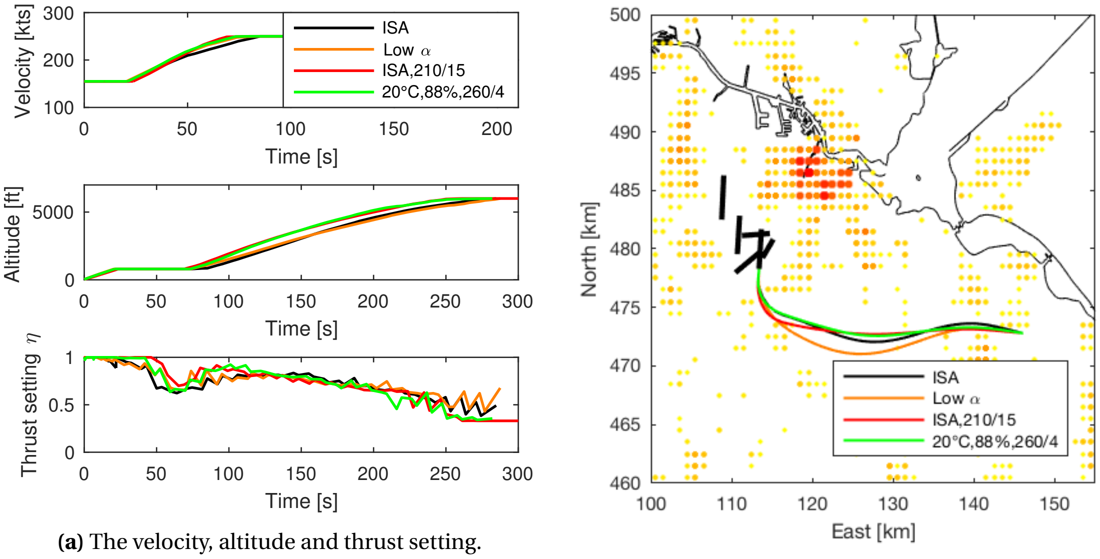

(a) The velocity, altitude and thrust setting.

(b) The ground track.

Figure B.5: Comparison of the velocity, altitude and thrust setting and ground track of the fuel and noise optimal trajectories of cases C2.1., C2.6., C2.7. and C3.ARN.8.

B.2.2. Warm Weather Conditions

In warm weather conditions, the following atmospheric conditions are simulated.

- Atmosphere 9: temperature of 29°C, relative humidity of 15% and wind from 170°, 6 kts.

The initial 100 s for the velocity profile and the other profiles of the noise optimal trajectories are presented in Figure B.6a. It is observed that the noise optimal trajectory in high atmospheric attenuation conditions and in warm weather conditions exactly match the altitude profile. This is induced by a combination between the increased performance at higher temperatures and higher atmospheric attenuation compared to ISA conditions. All three accelerations consist of two steps, in which the initial acceleration is larger in warm weather conditions. The latter acceleration is smaller and is initiated at the same moment in time as in ISA conditions.

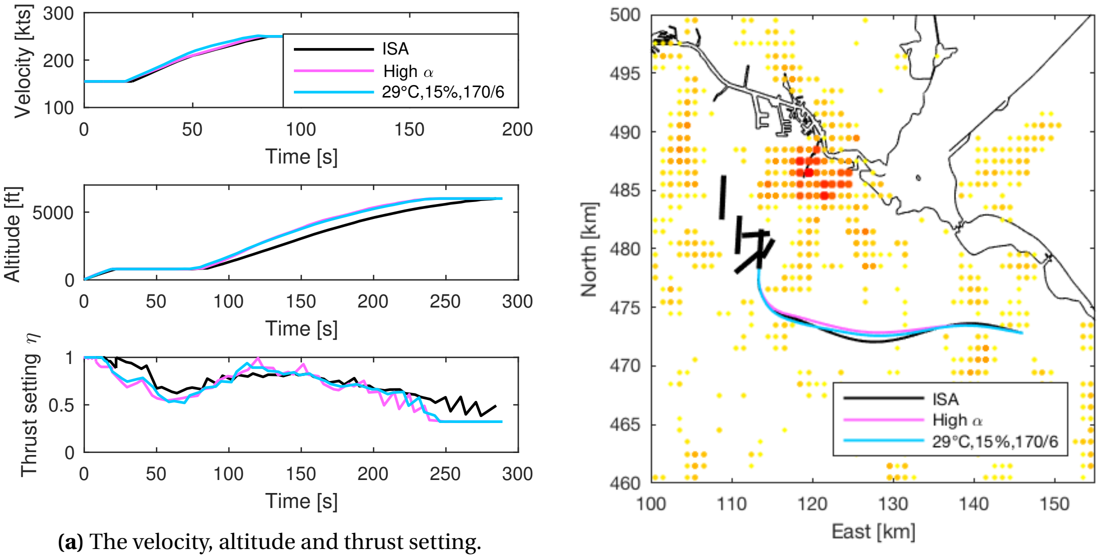

(a) The velocity, altitude and thrust setting.

(b) The ground track.

Figure B.6: Comparison of the velocity, altitude and thrust setting and ground track of the fuel and noise optimal trajectories of cases C2.1., C2.5. and C3.ARN.9.

The ground track of the noise optimal trajectories are presented in Figure B.6b. Due to the southern wind, a slightly more southern noise optimal trajectory is obtained in the warm weather conditions compared to the noise optimal trajectory in high atmospheric attenuation conditions.

B.2.3. Cold Weather Conditions

The cold weather condition is simulated in order to identify the influence of different weather conditions and different wind directions on the noise optimal trajectories for the Arnem departure. In cold weather conditions, the following atmospheric conditions are simulated.

- Atmosphere 11: temperature of -2°C, relative humidity of 58% and wind from 90°, 12 kts.

The initial 100 s for the velocity profile and the other profiles of the noise optimal trajectories are presented in Figure B.7a. It is noted that besides the length of the simulation, very minor differences are observed. A much lower thrust settings profile is observed for the trajectory in high air temperature. In higher temperatures, the aircraft can obtain equal excess power with lower thrust setting as long as the engine does not operate in the temperature rated area.

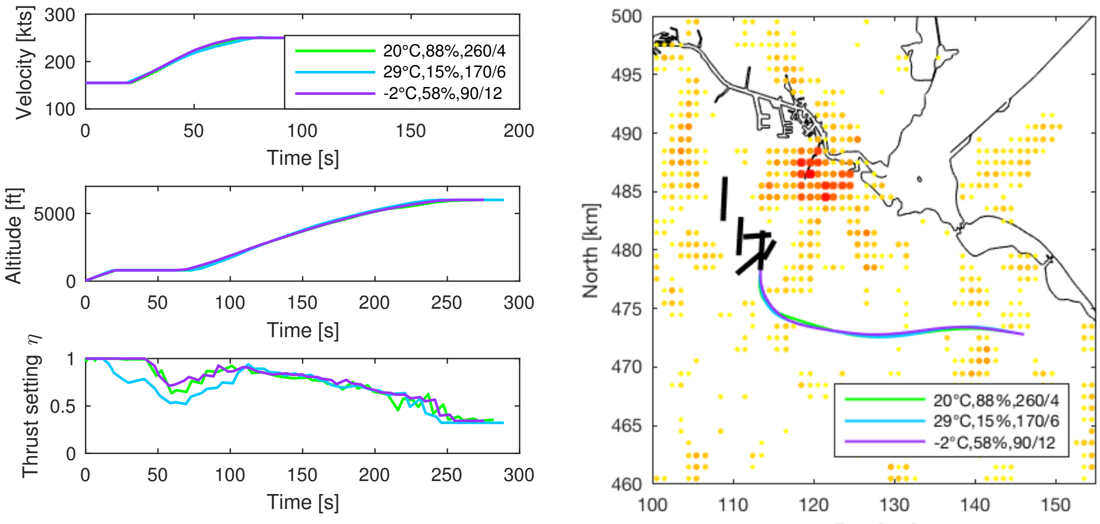

(a) The velocity, altitude and thrust setting.

(b) The ground track.

Figure B.7: Comparison of the velocity, altitude and thrust setting and ground track between the noise optimal trajectories of cases C3.ARN.8., C3.ARN.9. and C3.ARN.11.

The ground track, presented in Figure B.7b, show very high commonality for all cases.

Thus it is concluded that for the Arnem departure, the inclusion of wind from any direction and varied velocities does not result in different noise optimal trajectories. However, compared to the noise optimal trajectory in ISA conditions without wind, the noise optimal trajectory is different.

C

Results and Noise Contour Lines of Case 1 and Case 2

This Appendix presents the results of all k_{noise} values run for all cases presented in Section 5.3 and Section 5.4. Furthermore the noise contour lines for the fuel and noise optimal trajectory is presented to illustrate how noise contours change with different trajectories.

The results for the Spijkerboor departure procedure of Case 1 is presented in Section C.1. Section C.2 presents the results of the Arnem departure procedure performed in Case 2.

C.1. Case 1

Reference case.

The results of case C1.1. is presented in Table C.1.

Table C.1: Results of case C1.1.

Case	Objective	Fuel [kg]	ΔFuel [%]	Awakenings	ΔN_A [%]	Time [s]	ΔTime [%]
C1.1.1	Fuel	559.5	-	9904	-	525.8	-
C1.1.2	Fuel + 0.001 $\cdot N_A$	559.9	+0.08	9338	-5.72	526.8	+0.20
C1.1.3	Fuel + 0.002 $\cdot N_A$	560.4	+0.16	8915	-9.99	527.7	+0.37
C1.1.4	Fuel + 0.004 $\cdot N_A$	560.5	+0.19	8856	-10.59	527.9	+0.40
C1.1.5	Fuel + 0.006 $\cdot N_A$	565.8	+1.14	7699	-22.27	533.9	+1.55
C1.1.6	Fuel + 0.008 $\cdot N_A$	566.5	+1.26	7671	-22.55	535.3	+1.82
C1.1.7	Fuel + 0.01 $\cdot N_A$	566.5	+1.26	7671	-22.55	535.3	+1.82

Figure C.1 presents the noise contour for the fuel optimal trajectory. The contour lines illustrate the effect of the turn immediately after take-off: The population living on the outside of the turn receive less noise as the aircraft turns away from them and increasing the distance between the aircraft and the observer. The noise contours become nearly symmetrical in the fuel optimal trajectory once the aircraft starts to fly straight towards its final position.

Figure C.2 presents the noise contour for the noise optimal trajectory. The effect of flying lower and the resulting larger 70 dB contour directly under the flight path is clearly identified.

Atmosphere 1 - ISA

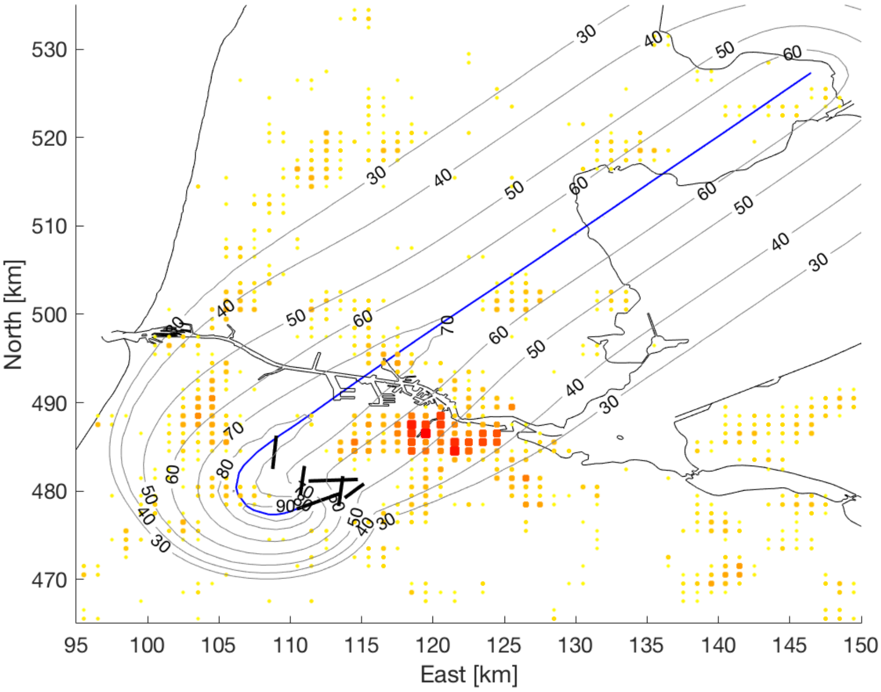

Figure C.1: Ground track and noise contour lines in SEL for the fuel optimal case of C1.1.

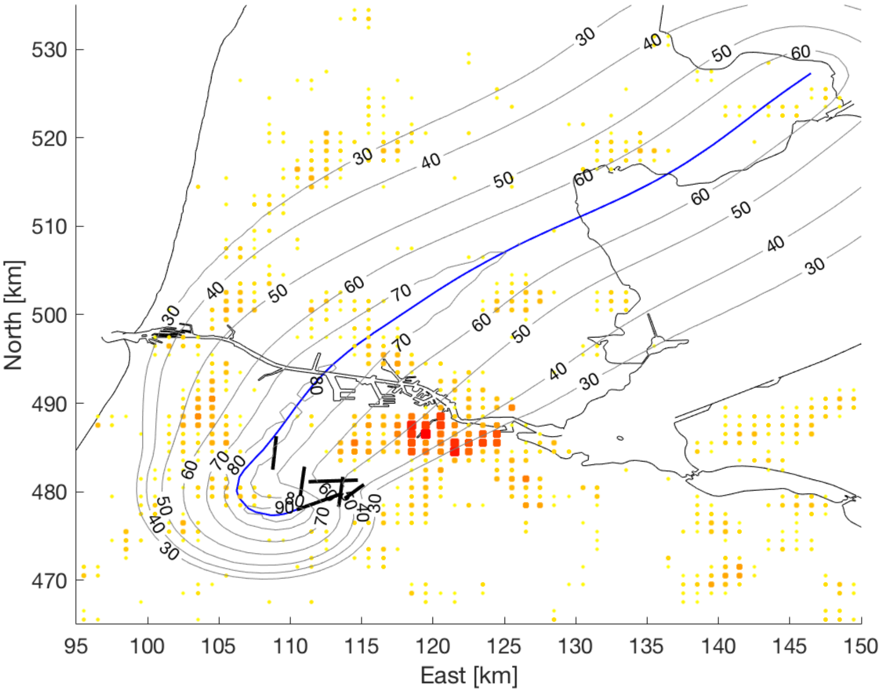

Figure C.2: Ground track and noise contour lines in SEL for the noise optimal case of C1.1.

Varying wind conditions.

In varying wind conditions, three different combinations of wind direction and velocity are simulated, with the temperature and humidity matching International Standard Atmosphere (ISA) conditions.

- Atmosphere 2: wind from 270°, 5 kts.
- Atmosphere 3: wind from 270°, 15 kts.
- Atmosphere 4: wind from 148°, 15 kts.

The result of cases C1.2. to C1.4. are presented in Table C.2.

Table C.2: Results of cases C1.2., C1.3. and C1.4.

Case	Objective	Fuel [kg]	ΔFuel [%]	Awakenings	ΔN_A [%]	Time [s]	ΔTime [%]
C1.2.1	Fuel	551.7	-	9647	-	514.2	-
C1.2.2	Fuel + 0.001 $\cdot N_A$	552.1	+0.07	8674	-10.09	514.1	-0.03
C1.2.3	Fuel + 0.002 $\cdot N_A$	552.2	+0.09	8594	-10.91	514.2	-0.01
C1.2.4	Fuel + 0.004 $\cdot N_A$	553.5	+0.33	8164	-15.38	515.9	+0.33
C1.2.5	Fuel + 0.006 $\cdot N_A$	553.5	+0.32	8165	-15.36	515.9	+0.32
C1.2.6	Fuel + 0.008 $\cdot N_A$	557.1	+0.98	7202	-25.34	521.0	+1.31
C1.2.7	Fuel + 0.01 $\cdot N_A$	557.1	+0.98	7196	-25.41	521.0	+1.32
C1.3.1	Fuel	537.5	-	9221	-	491.0	-
C1.3.2	Fuel + 0.001 $\cdot N_A$	538.1	+0.10	8137	-11.76	492.4	+0.29
C1.3.3	Fuel + 0.002 $\cdot N_A$	538.7	+0.16	7716	-16.33	493.3	+0.47
C1.3.4	Fuel + 0.004 $\cdot N_A$	541.9	+0.82	6887	-25.32	497.3	+1.29
C1.3.5	Fuel + 0.006 $\cdot N_A$	544.3	+1.26	6511	-29.39	500.6	+1.95
C1.3.6	Fuel + 0.008 $\cdot N_A$	545.1	+1.40	6350	-31.14	501.5	+2.12
C1.4.1	Fuel	573.4	-	8905	-	548.4	-
C1.4.2	Fuel + 0.001 $\cdot N_A$	573.6	+0.03	8559	-3.88	548.6	+0.04
C1.4.3	Fuel + 0.002 $\cdot N_A$	574.4	+0.18	8003	-10.13	549.4	+0.18
C1.4.4	Fuel + 0.004 $\cdot N_A$	577.6	+0.74	7219	-19.94	553.8	+0.98
C1.4.5	Fuel + 0.006 $\cdot N_A$	577.6	+0.74	7219	-19.94	553.8	+0.98
C1.4.6	Fuel + 0.008 $\cdot N_A$	580.8	+1.29	6628	-25.57	557.4	+1.64
C1.4.7	Fuel + 0.01 $\cdot N_A$	580.8	+1.29	6628	-25.57	557.4	+1.64

In general, the effect of wind on the noise contours are clearly identified by the noise contours being closer to each other. Effect of increasing wind velocity in atmosphere 3 and atmosphere 4 mainly observed upwind of the initial turn and the larger 30 dB contour downwind. Underneath the aircraft, minimal difference in SEL values are observed between the different wind conditions. Also, on the straight segment, there is no large difference between the SEL contours larger than 50 dB between the different wind conditions.

Atmosphere 2 - 5 kts western wind

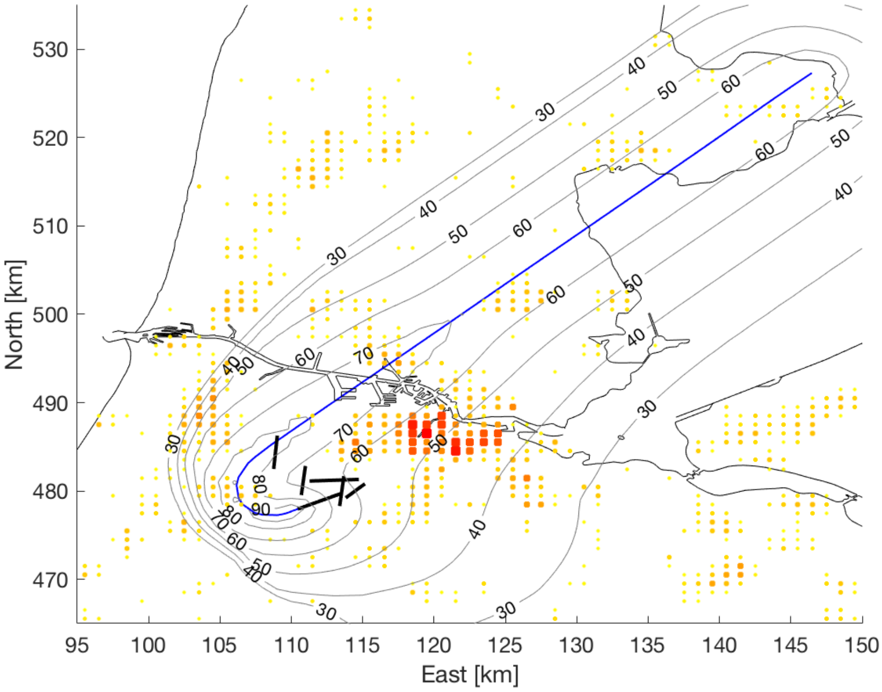

Figure C.3: Ground track and noise contour lines in SEL for the fuel optimal case of C1.2.

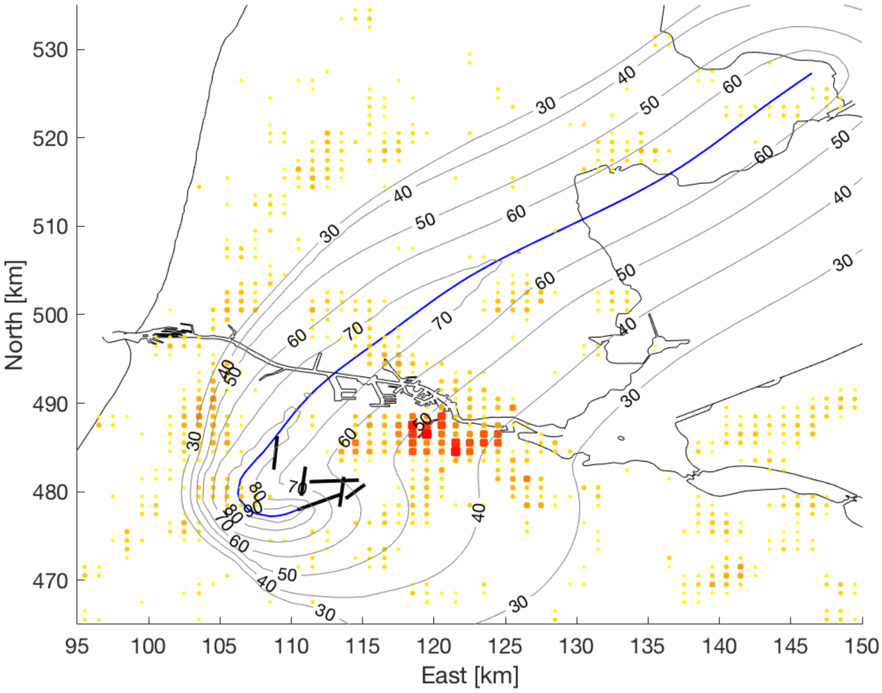

Figure C.4: Ground track and noise contour lines in SEL for the noise optimal case of C1.2.

Atmosphere 3 - 15 kts western wind

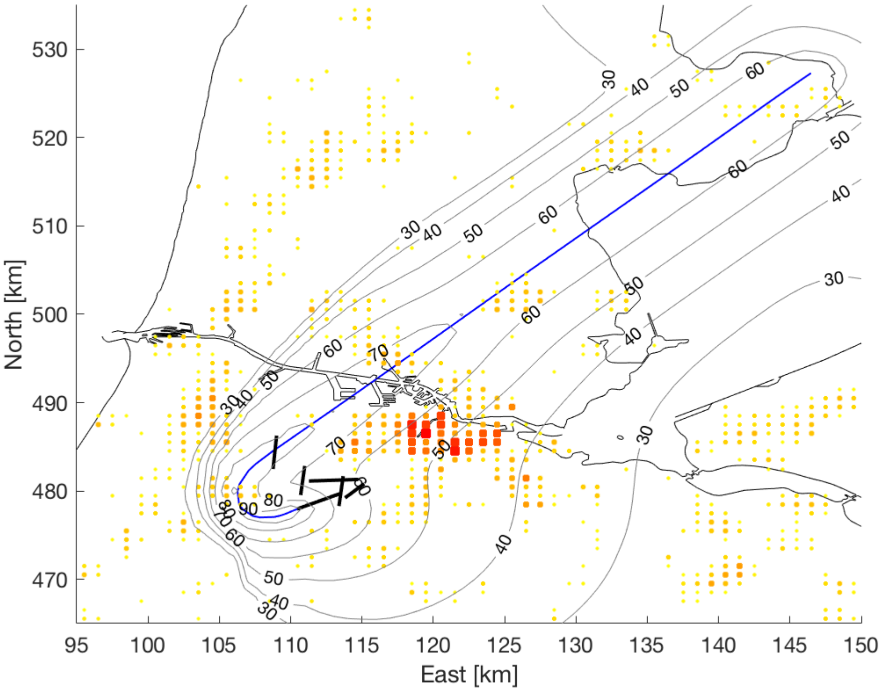

Figure C.5: Ground track and noise contour lines in SEL for the fuel optimal case of C1.3.

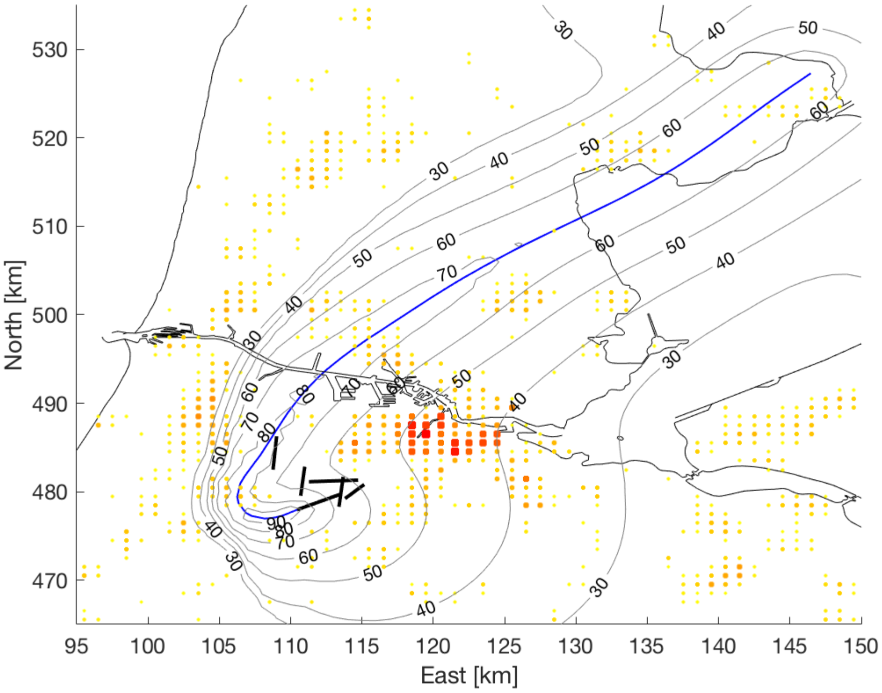

Figure C.6: Ground track and noise contour lines in SEL for the noise optimal case of C1.3.

Atmosphere 4 - 15 kts southeastern wind

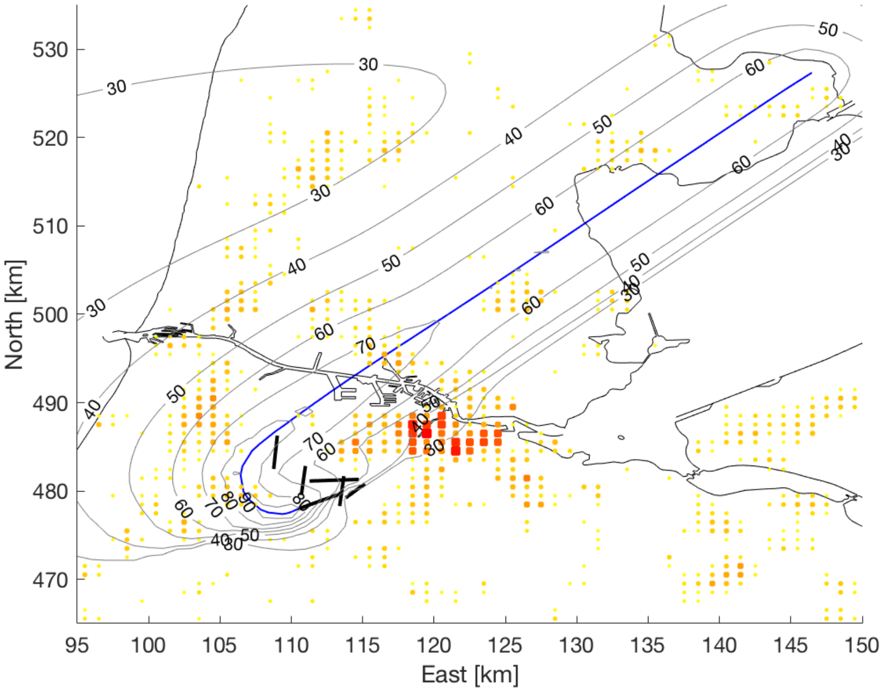

Figure C.7: Ground track and noise contour lines in SEL for the fuel optimal case of C1.4.

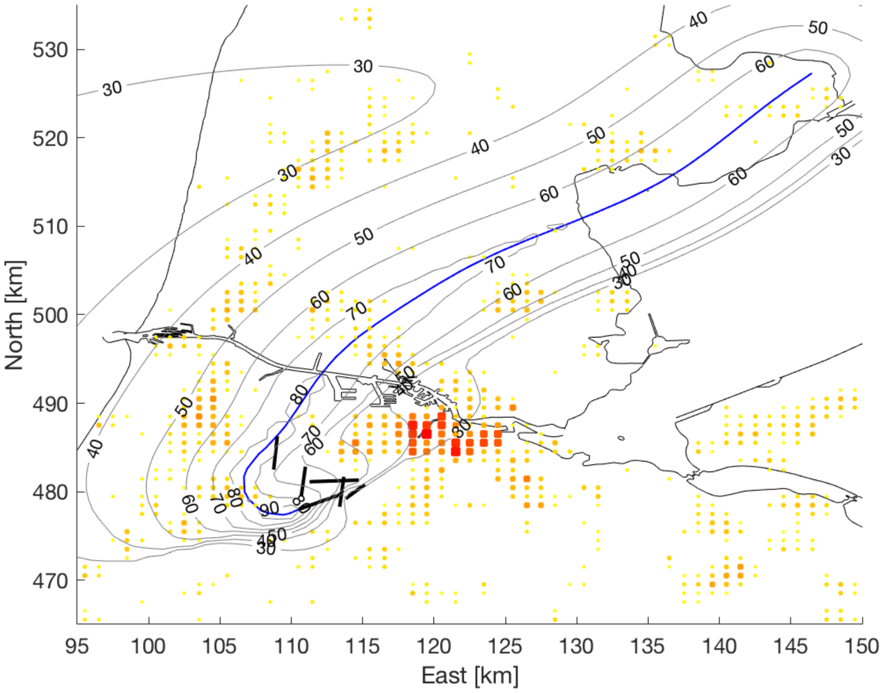

Figure C.8: Ground track and noise contour lines in SEL for the noise optimal case of C1.4.

Varying atmospheric attenuation coefficient.

In varying atmospheric absorption conditions, a high and a low atmospheric attenuation conditions are simulated by varying the air temperature and relative humidity.

- Atmosphere 5: 30°C air temperature, 5% relative humidity.
- Atmosphere 6: -10°C air temperature, 5% relative humidity.

The result of the cases C1.5. and C1.6. is presented in Table C.3. Although C1.6.10 results in lower awakenings, this trajectory is not considered as noise optimal as the ΔTime is larger than 10%.

Table C.3: Results of cases C1.5. and C1.6.

Case	Objective	Fuel [kg]	ΔFuel [%]	Awakenings	ΔN_A [%]	Time [s]	ΔTime [%]
C1.5.1	Fuel	556.2	-	2994	-	526.2	-
C1.5.2	Fuel + 0.001 $\cdot N_A$	556.2	+0.00	2994	-0.01	526.2	+0.00
C1.5.3	Fuel + 0.002 $\cdot N_A$	556.4	+0.03	2809	-6.16	526.4	+0.02
C1.5.4	Fuel + 0.004 $\cdot N_A$	557.7	+0.26	2628	-12.22	526.2	-0.01
C1.5.5	Fuel + 0.006 $\cdot N_A$	558.8	+0.32	2427	-18.92	527.5	+0.24
C1.5.6	Fuel + 0.008 $\cdot N_A$	559.8	+0.65	2296	-23.30	528.2	+0.38
C1.5.7	Fuel + 0.01 $\cdot N_A$	560.6	+0.79	2225	-25.67	529.3	+0.57
C1.5.8	Fuel + 0.02 $\cdot N_A$	563.5	+1.31	2021	-32.49	531.5	+1.00
C1.6.1	Fuel	565.2	-	22801	-	521.5	-
C1.6.2	Fuel + 0.001 $\cdot N_A$	566.8	+0.28	19203	-15.81	524.7	+0.61
C1.6.3	Fuel + 0.002 $\cdot N_A$	574.3	+1.61	14719	-35.47	533.2	+2.24
C1.6.4	Fuel + 0.004 $\cdot N_A$	577.5	+2.18	13611	-40.33	536.7	+2.91
C1.6.5	Fuel + 0.008 $\cdot N_A$	585.7	+3.64	12338	-45.91	546.2	+4.73
C1.6.6	Fuel + 0.01 $\cdot N_A$	585.7	+3.64	12337	-45.91	546.2	+4.73
C1.6.7	Fuel + 0.012 $\cdot N_A$	593.4	+4.98	11556	-49.34	553.8	+6.20
C1.6.8	Fuel + 0.014 $\cdot N_A$	597.3	+5.69	11350	-50.24	558.6	+7.11
C1.6.9	Fuel + 0.016 $\cdot N_A$	597.3	+5.69	11350	-50.24	558.6	+7.11
C1.6.10	Fuel + 0.018 $\cdot N_A$	617.2	+9.20	9331	-59.09	578.7	+10.96

Figure C.9 and Figure C.10 present the noise contours for high absorption conditions of atmosphere 5. The contour lines are very much smaller than in ISA conditions of atmosphere 1. Even in the fuel optimal trajectory, no awakenings are made in Amsterdam. It is noted that for both figures, the 30 dB contour lines are located at similar distance away from the aircraft. Even in the illuminated zone, sound levels lower than 30 dB are obtained.

Figure C.11 and Figure C.12 present the noise contours for low absorption conditions of atmosphere 6. Much higher noise levels are obtained compared to high absorption conditions. However the noise contours are not wider than the ones observed in ISA conditions of atmosphere 1 as the shadow zone has not moved. For the fuel optimal trajectory, awakenings are made in the most densely populated area of Amsterdam and Haarlem. The noise optimal trajectory clearly relieves the Amsterdam area and reduces the noise received in Haarlem.

Atmosphere 5 - Low absorption

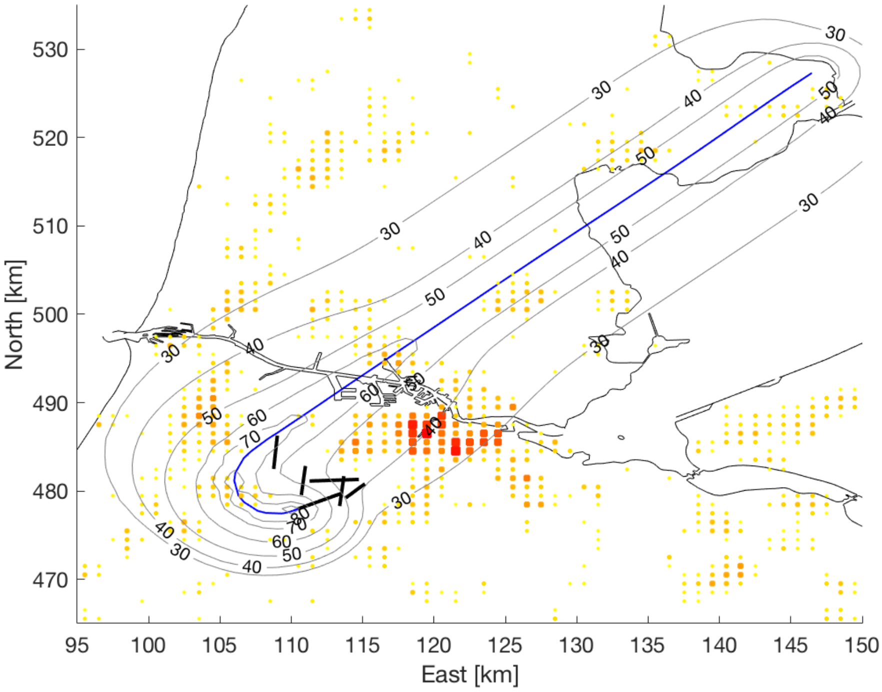

Figure C.9: Ground track and noise contour lines in SEL for the fuel optimal case of C1.5.

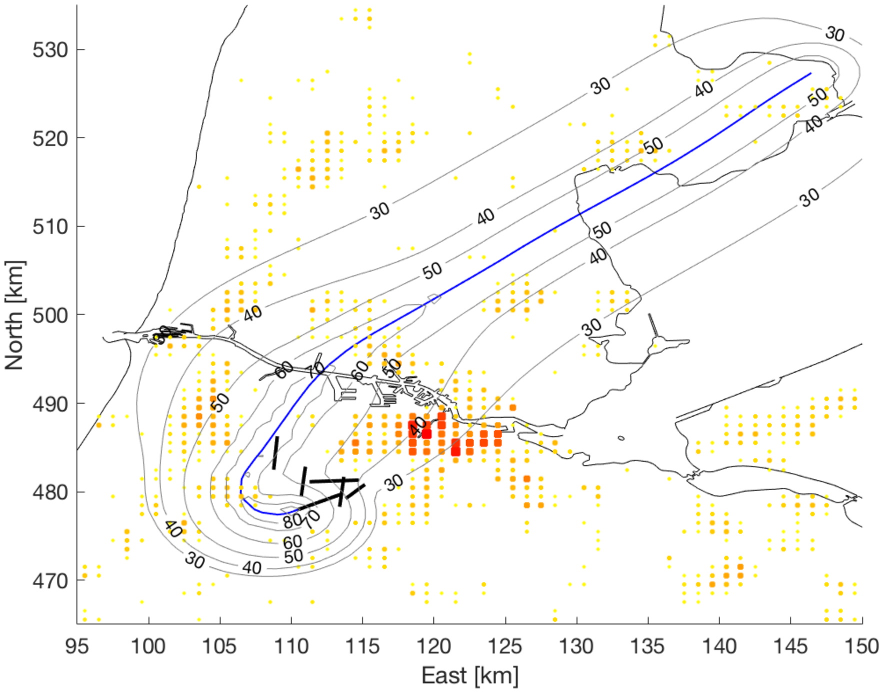

Figure C.10: Ground track and noise contour lines in SEL for the noise optimal case of C1.5.

Atmosphere 6 - High absorption

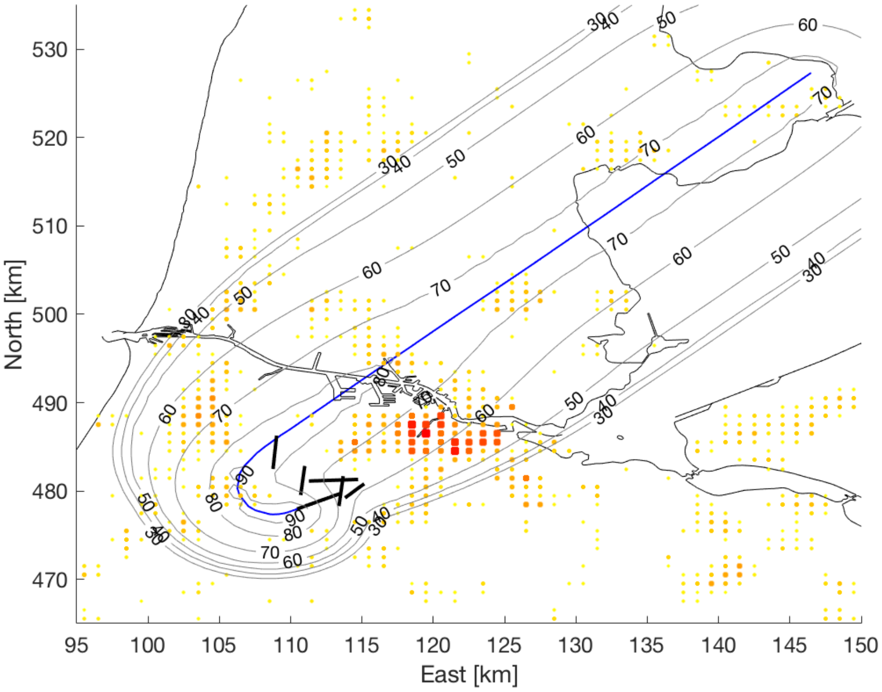

Figure C.11: Ground track and noise contour lines in SEL for the fuel optimal case of C1.6.

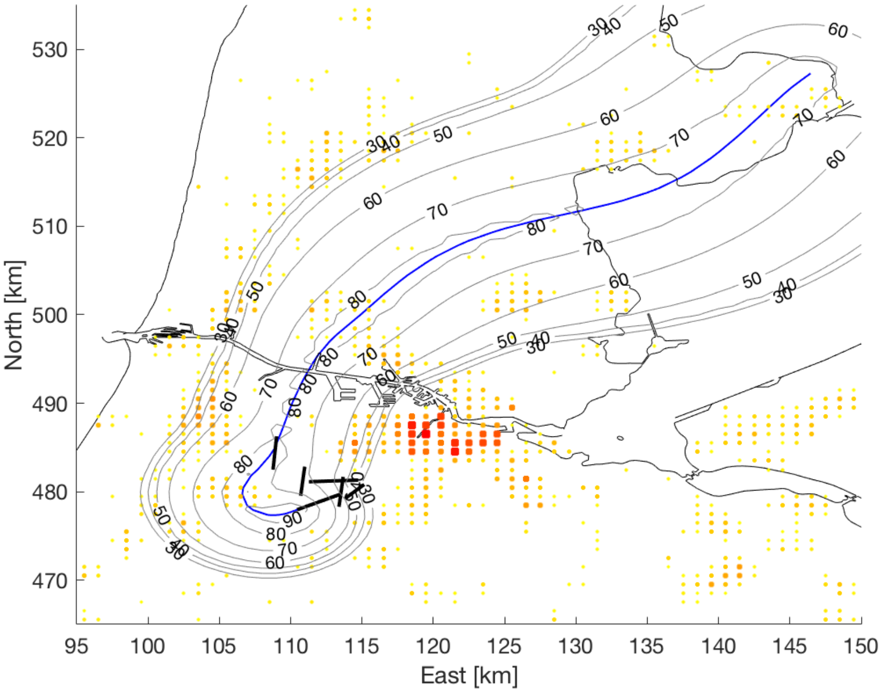

Figure C.12: Ground track and noise contour lines in SEL for the noise optimal case of C1.6.

C.2. Case 2

Reference case.

The results of case C2.1. is presented in Table C.3. As is observed multiple times for the cases for the Arnem departure procedure, one trajectory holds as optimal trajectory for multiple k_{noise} values.

Table C.4: Results of case C2.1.

Case	Objective	Fuel [kg]	ΔFuel [%]	Awakenings	ΔN_A [%]	Time [s]	ΔTime [%]
C2.1.1	Fuel	381.0	-	4612	-	277.0	-
C2.1.2	Fuel + 0.001 $\cdot N_A$	381.0	0.00	4612	0.00	277.0	0.00
C2.1.3	Fuel + 0.002 $\cdot N_A$	381.0	0.00	4612	0.00	277.0	0.00
C2.1.4	Fuel + 0.004 $\cdot N_A$	381.0	0.00	4612	0.00	277.0	0.00
C2.1.5	Fuel + 0.006 $\cdot N_A$	381,3	+0.08	4517	-2.04	277.9	+0.31
C2.1.6	Fuel + 0.008 $\cdot N_A$	381,3	+0.08	4518	-2.04	277.9	+0.31
C2.1.7	Fuel + 0.01 $\cdot N_A$	383,1	+0.55	4454	-3.42	280.6	+1.29
C2.1.8	Fuel + 0.02 $\cdot N_A$	386,6	+1.48	4352	-5.64	284.7	+2.78
C2.1.9	Fuel + 0.03 $\cdot N_A$	386,6	+1.48	4352	-5.64	284.7	+2.78
C2.1.10	Fuel + 0.04 $\cdot N_A$	386,6	+1.48	4352	-5.64	284.7	+2.78
C2.1.11	Fuel + 0.05 $\cdot N_A$	386,6	+1.48	4352	-5.64	284.7	+2.78

Figure C.13 and Figure C.14 presents the noise contour lines of the fuel and noise optimal trajectory in ISA conditions of atmosphere 1. Large SEL values are received surrounding the initial turn. However, these cannot be mitigated and thus are also observed in the noise optimal trajectory.

Atmosphere 1 - ISA

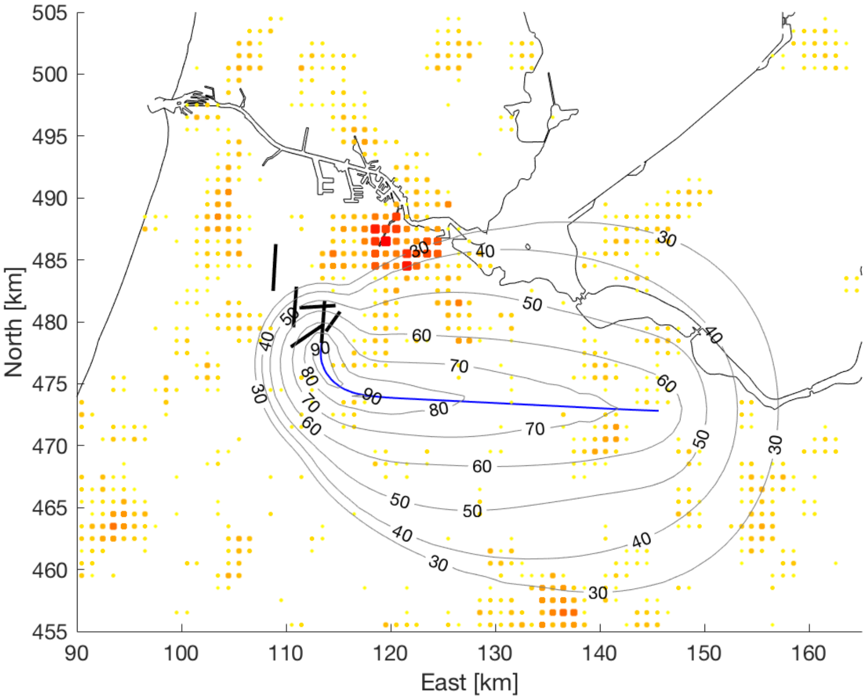

Figure C.13: Ground track and noise contour lines in SEL for the fuel optimal case of C2.1.

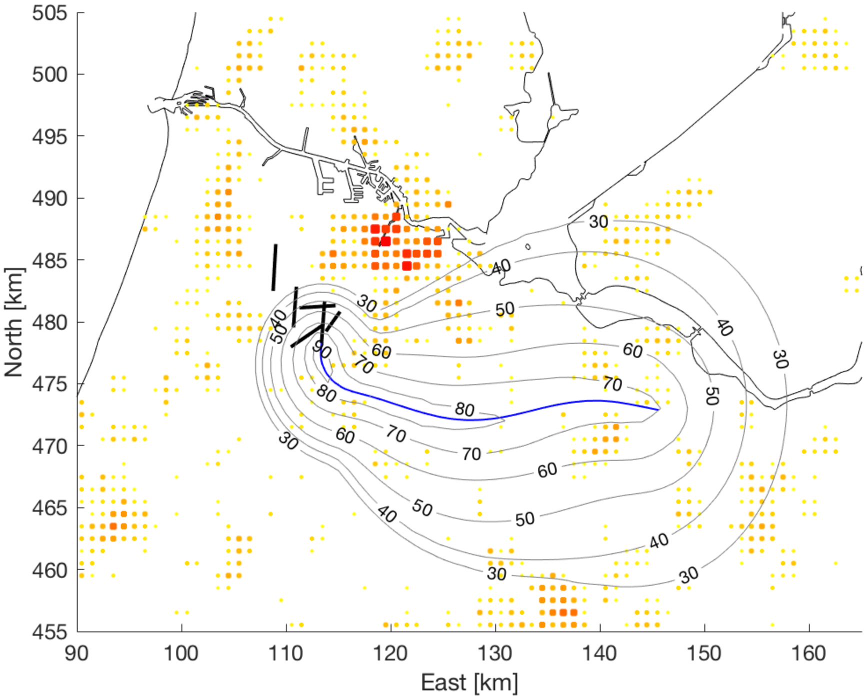

Figure C.14: Ground track and noise contour lines in SEL for the noise optimal case of C2.1.

Wind conditions.

The ISA conditions is enhanced by a wind from the southwest.

- Atmosphere 7: wind from 210°, 15 kts.

The results of case C2.7. is presented in Table C.5.

Table C.5: Results of case C2.7.

Case	Objective	Fuel [kg]	ΔFuel [%]	Awakenings	ΔN_A [%]	Time [s]	ΔTime [%]
C2.7.1	Fuel	402.6	-	4406	-	305.4	-
C2.7.2	Fuel + $0.001 \cdot N_A$	402.6	+0.01	4406	+0.01	305.4	+0.00
C2.7.3	Fuel + $0.002 \cdot N_A$	402.6	+0.00	4406	+0.00	305.4	+0.00
C2.7.4	Fuel + $0.004 \cdot N_A$	403.1	+0.13	4176	-5.22	306.3	+0.31
C2.7.5	Fuel + $0.006 \cdot N_A$	403,1	+0.13	4176	-5.22	306.3	+0.31
C2.7.6	Fuel + $0.008 \cdot N_A$	403,1	+0.13	4176	-5.22	306.3	+0.31
C2.7.7	Fuel + $0.01 \cdot N_A$	403,4	+0.18	4150	-5.80	306.6	+0.40

With the inclusion of wind, compared to ISA conditions in atmosphere 1, the wind has a large influence on the noise received upwind of the initial turn. Due tot the change in speed of sound profile, the shadow zone has moved much closer to the aircraft. However, even in the fuel optimal case, the wind is not strong enough to reach the densely populated area of Amsterdam.

Atmosphere 7 - 15 kts southwestern wind

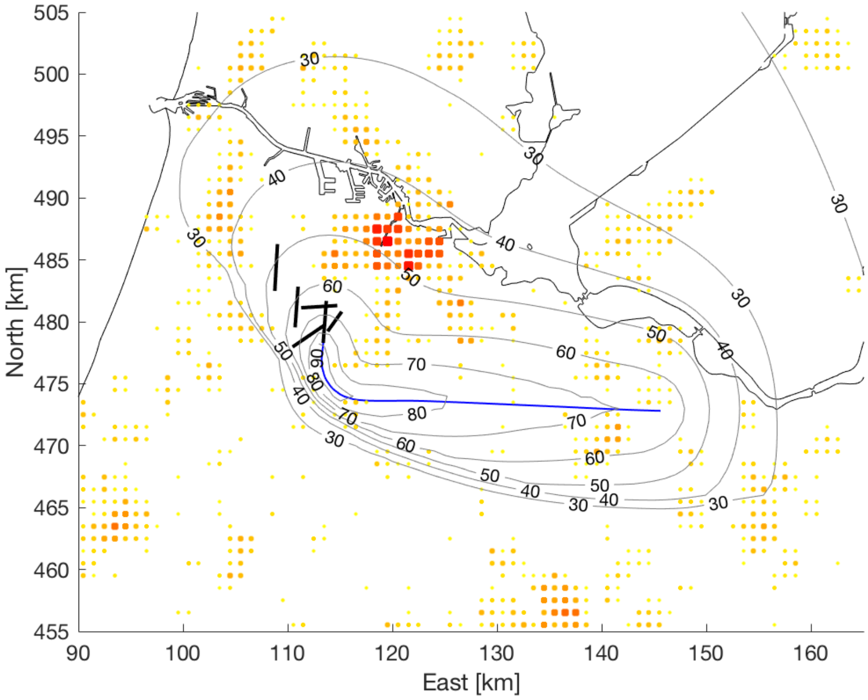

Figure C.15: Ground track and noise contour lines in SEL for the fuel optimal case of C2.7.

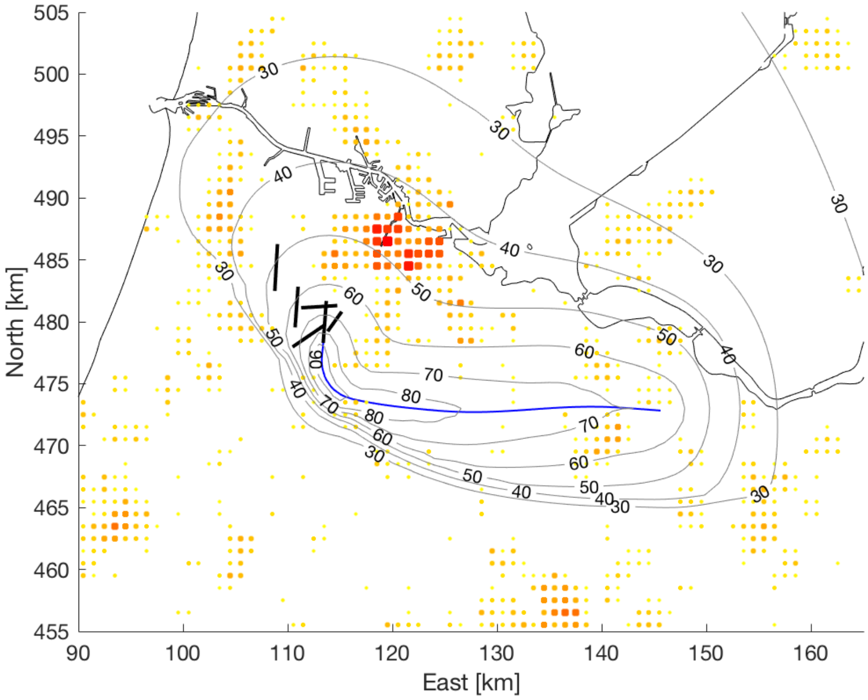

Figure C.16: Ground track and noise contour lines in SEL for the noise optimal case of C2.7.

Varying atmospheric absorption.

The same high and low atmospheric conditions as for the varying atmospheric absorption conditions for the Spijkerboor departure is simulated for the Arnem departure.

- Atmosphere 5: 30°C air temperature, 5% relative humidity.
- Atmosphere 6: -10°C air temperature, 5% relative humidity.

The result of cases C2.5. and C2.6. are presented in Table C.6.

Table C.6: Results of cases C2.5. and C2.6.

Case	Objective	Fuel [kg]	ΔFuel [%]	Awakenings	ΔN_A [%]	Time [s]	ΔTime [%]
C2.5.1	Fuel	378.0	-	1251	-	274.3	-
C2.5.2	Fuel + 0.001 $\cdot N_A$	378.0	+0.00	1251	-0.00	274.3	+0.00
C2.5.3	Fuel + 0.002 $\cdot N_A$	378.0	+0.00	1251	-0.00	274.3	+0.00
C2.5.4	Fuel + 0.004 $\cdot N_A$	378.0	+0.00	1251	-0.00	274.3	+0.00
C2.5.5	Fuel + 0.006 $\cdot N_A$	378.0	+0.00	1251	-0.00	274.3	+0.00
C2.5.6	Fuel + 0.008 $\cdot N_A$	378.0	+0.00	1251	-0.00	274.3	+0.00
C2.5.7	Fuel + 0.01 $\cdot N_A$	378,7	+0.19	1086	-13.20	275.8	+0.52
C2.5.8	Fuel + 0.05 $\cdot N_A$	383,4	+1.44	902	-27.94	280.4	+2.21
C2.5.9	Fuel + 0.06 $\cdot N_A$	383,4	+1.44	902	-27.94	280.4	2.21
C2.5.10	Fuel + 0.07 $\cdot N_A$	383,4	+1.44	902	-27.94	280.4	2.21
C2.5.11	Fuel + 0.08 $\cdot N_A$	383,4	+1.44	902	-27.95	280.4	2.22
C2.5.12	Fuel + 0.09 $\cdot N_A$	383,4	+1.44	902	-27.95	280.4	2.22
C2.5.13	Fuel + 0.1 $\cdot N_A$	383,4	+1.44	902	-27.95	280.4	+2.22
C2.6.1	Fuel	384.7	-	10107	-	275.2	-
C2.6.2	Fuel + 0.001 $\cdot N_A$	384.7	+0.00	10107	-0.00	275.2	+0.01
C2.6.3	Fuel + 0.002 $\cdot N_A$	384.7	+0.00	10108	-0.00	275.1	+0.01
C2.6.4	Fuel + 0.004 $\cdot N_A$	385,5	+0.21	9662	-4.40	277.4	+0.83
C2.6.5	Fuel + 0.006 $\cdot N_A$	386.5	+0.48	9544	-5.57	279.1	+1.42
C2.6.6	Fuel + 0.008 $\cdot N_A$	386.5	+0.48	9544	-5.57	279.1	+1.42
C2.6.7	Fuel + 0.01 $\cdot N_A$	386.7	+0.53	9512	-5.89	279.2	+1.46
C2.6.8	Fuel + 0.012 $\cdot N_A$	387.1	+0.63	9481	-6.20	279.8	+1.68
C2.6.9	Fuel + 0.014 $\cdot N_A$	387.1	+0.63	9481	-6.20	279.8	+1.68
C2.6.10	Fuel + 0.016 $\cdot N_A$	387.1	+0.63	9481	-6.20	279.8	+1.68
C2.6.11	Fuel + 0.018 $\cdot N_A$	390.6	+1.55	9305	-7.94	285.4	+3.72
C2.6.12	Fuel + 0.02 $\cdot N_A$	392.3	+1.98	9241	-8.57	287.5	+4.49
C2.6.13	Fuel + 0.026 $\cdot N_A$	392.3	+1.98	9241	-8.57	287.5	+4.50
C2.6.14	Fuel + 0.03 $\cdot N_A$	392.3	+1.98	9241	-8.57	287.5	+4.50

Figure C.17 and Figure C.18 present the noise contours for high absorption conditions of atmosphere 5. As for the Spijkerboor departure, the contour lines are very much smaller than in ISA conditions of atmosphere 1. Furthermore the same characteristics are observed as for the Spijkerboor procedure.

Figure C.19 and Figure C.20 present the noise contours for low absorption conditions of atmosphere 6. Much larger noise contour lines are obtained. In the noise optimal trajectory, the effect of the aircraft flying at a lower altitude for an increased amount of time is clearly observed by the increased 80 dB contour line underneath the aircraft.

Atmosphere 5 - Low absorption

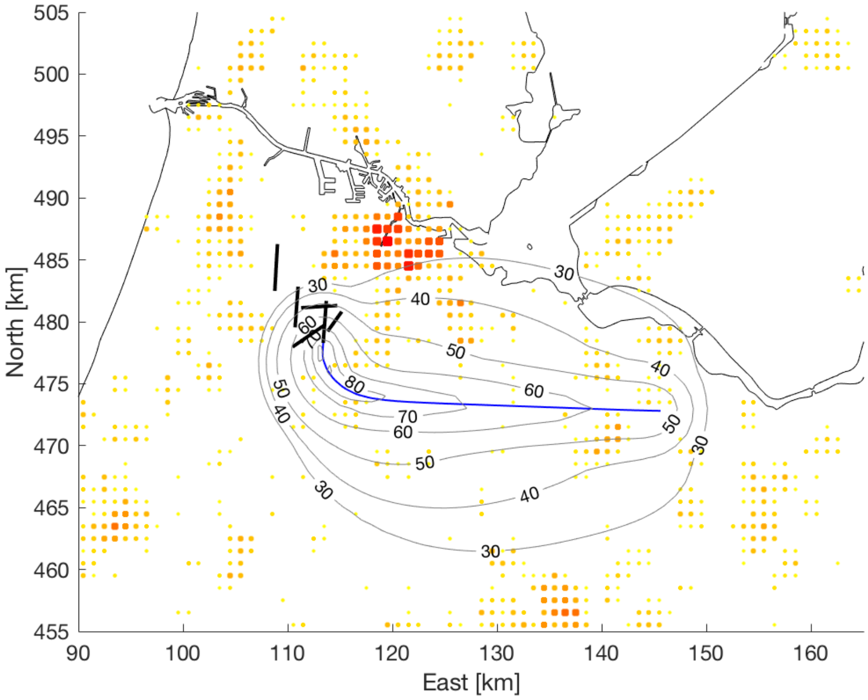

Figure C.17: Ground track and noise contour lines in SEL for the fuel optimal case of C2.5.

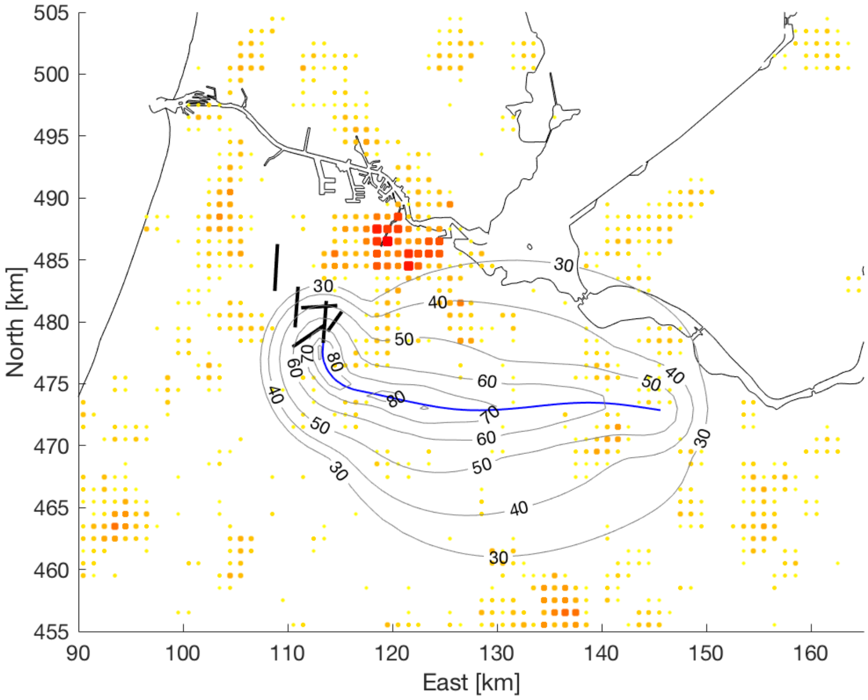

Figure C.18: Ground track and noise contour lines in SEL for the noise optimal case of C2.5.

Atmosphere 6 - High absorption

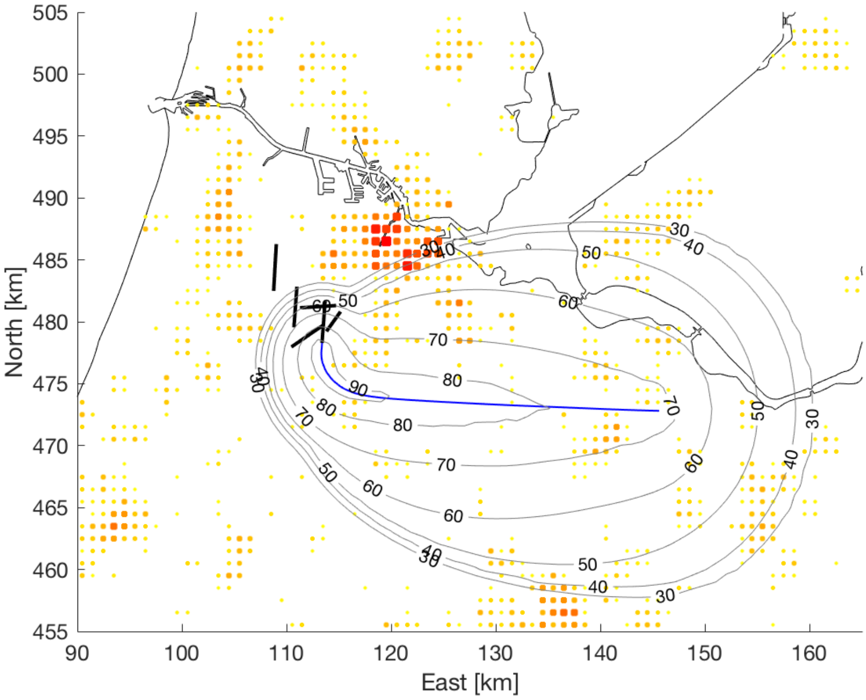

Figure C.19: Ground track and noise contour lines in SEL for the fuel optimal case of C2.6.

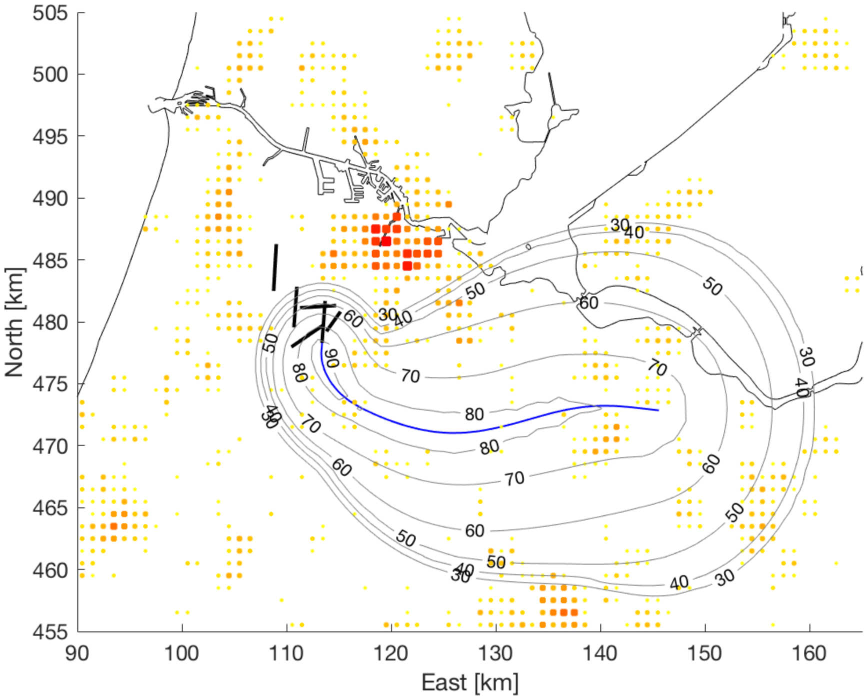

Figure C.20: Ground track and noise contour lines in SEL for the noise optimal case of C2.6.